UNIVERSITE BRETAGNE LOIRE MATHSTIC

UNIVERSITÉ DE RENNES 1

THESE DE DOCTORAT DE

L'UNIVERSITE DE RENNES 1
COMUE UNIVERSITE BRETAGNE LOIRE

ECOLE DOCTORALE N° 601
Mathématiques et Sciences et Technologies de l'Information et de la Communication
Spécialité : *Electronique*

présentée par

François Doucet

Continuous Parallel Plate Waveguide Lenses for Future Low Cost and High Performances Multiple Beam Antennas

Thèse présentée et soutenue à Rennes, le 25 Février 2019
Unité de recherche : IETR – UMR CNRS 6164, Institut d'Electronique et des Télécommunications de Rennes – Université de Rennes 1

Rapporteurs avant soutenance :

George GOUSSETIS — Professeur des universités, Heriot-Watt University, Edimbourg, Ecosse
Jean-Yves DAUVIGNAC — Professeur des universités, Université de Nice/Sophia Antipolis, Nice, France

Composition du Jury :

Président :
Examinateurs : George GOUSSETIS — Professeur des universités, Heriot-Watt University, Edimbourg, Ecosse
Jean-Yves DAUVIGNAC — Professeur des universités, Université de Nice/Sophia Antipolis, Nice, France
Brigitte LOISEAUX — Ingénieur de Recherche, Thales TRT, Palaiseau, France

Dir. de thèse : Ronan SAULEAU — Professeur des universités, Université de Rennes 1, Rennes, France
Encadrants : Nelson FONSECA — Ingénieur de Recherche, ESA, Noordwijk, Pays-Bas
Etienne GIRARD — Ingénieur de Recherche, Thales Alenia Space, Toulouse, France

Invité(s)
Gilles QUAGLIARO — Ingénieur de Recherche, Thales SIX, Gennevilliers, France

Remerciements

En remontant un peu moins de trois ans en arrière je me remémore les quelques moments passés à me demander si ce choix était le bon. Mais nul doute désormais, la thèse reste une expérience riche professionnellement mais également et surtout humainement. D'une manière générale et même si quelques lignes ne suffiront jamais, je souhaite adresser mes sincères remerciements à l'ensemble des personnes m'ayant accompagné de près ou de loin durant cette période.

Je tiens à remercier avant tout l'ensemble de mes encadrants, sans eux tout ce travail n'aurait pas pu être possible.

Merci à mon directeur de thèse Ronan Sauleau pour m'avoir permis de réaliser cette thèse au sein de l'IETR, pour le suivi et les conseils promulgués au cours de ces trois ans.

Je tiens à remercier chaleureusement Nelson Fonseca, co-encadrant à l'ESA, pour avoir travaillé près de moi durant cette période. Merci pour la disponibilité, la patience et le temps passé à m'éclairer sur les différentes études que l'on a menées ensemble. Je reste admiratif devant les qualités de rigueur scientifiques et techniques qui m'ont été transmises et qui me serviront sans aucun doute dans les prochaines années. Merci également pour son accueil pendant mon séjour à Noordwijk ainsi qu'à Peter de Maagt et à l'ensemble de la section Antenne de l'ESTEC.

Merci à Etienne Girard, co-encadrant chez Thales Alenia Space, pour m'avoir également suivi de très près pendant ces trois ans. Merci sincèrement pour les nombreuses discussions constructives que l'on a pu avoir ainsi que pour la positivité vis-à-vis de l'ensemble des travaux réalisés. Les encouragements et les conseils donnés durant nos nombreuses conversations téléphoniques auront été plus qu'importants.

Je tiens également à remercier Hervé Legay qui m'a donné l'opportunité de faire cette thèse après être passé au sein du département R&T de Thales Alenia Space pour mon projet de fin d'études, ainsi que pour le suivi accordé à mes travaux. J'y inclus également Renaud Chiniard et Jean-Philippe Fraysse avec qui j'ai pu avoir une première expérience particulièrement enrichissante pendant ces 6 mois de stage.

Mes remerciements vont également à Georges Goussetis, Professeur à l'Université d'Herriot Watt à Edimbourg et Jean-Yves Dauvignac, Professeur à l'Université de Nice/Sophia Antipolis pour avoir acceptés d'être rapporteurs sur cette thèse. J'ai apprécié l'intérêt porté vis-à-vis de mes travaux et également les discussions avant et pendant la soutenance. Merci également à Brigitte Loiseaux, Ingénieur chez Thales TRT à Palaiseau et Gilles Quagliaro, Ingénieur chez Thales SIX GTS à Gennevilliers pour les échanges que l'on a pu avoir.

Je n'oublie pas l'ensemble de mes collègues et amis de l'IETR. Merci tout d'abord à l'équipe administrative Nathalie, Martine et en particulier Noëlle. Je ne pourrai résumer en quelques mots l'aide et le soutien apporté au cours de ces trois ans, je retiendrai une personne avec des qualités humaines exceptionnelles. Merci à Xavier Morvan, Laurent Le Coq sans qui de nombreux résultats n'auraient pu être obtenus et également pour les nombreuses choses apprises en travaillant à leurs côtés. Merci également aux différents enseignants-chercheurs que j'ai pu côtoyer, Mauro, David, Benjamin, Olivier, Stéphane, Maria. Un remerciement spécial pour Franck et les nombreuses discussions, grâce à qui sans doute j'ai pu commencer à apprécier l'En Avant Guingamp (pas trop quand même), merci également pour l'aide accordée vis à vis de l'après thèse.

Merci à l'ensemble des doctorants et pour certains désormais docteurs, avec qui j'ai pu partager de nombreux moments pendant ces trois ans et à qui j'adresse tous mes vœux dans leurs projets personnels. Merci en particulier à Francesco pour son aide lors de mon arrivée, Antoine pour les nombreuses discussions et son dynamisme au sein du labo, Vincent pour les conseils apportés avant et tout au long de la thèse. Merci également à Tuyen et Alvaro pour avoir égayés nos longues journées de bureau et enfin Jorge pour sa bonne humeur au quotidien (bon courage Pélo !).

Je terminerai en adressant mes remerciements à l'ensemble de ma famille et amis pour leur indéfectible soutien, et tout particulièrement à mes parents de m'avoir permis de faire ces études et de m'avoir toujours encouragés dans mes choix.

Enfin et surtout, merci à Morgane pour son soutien et son aide au quotidien.

Amicalement,

Résumé

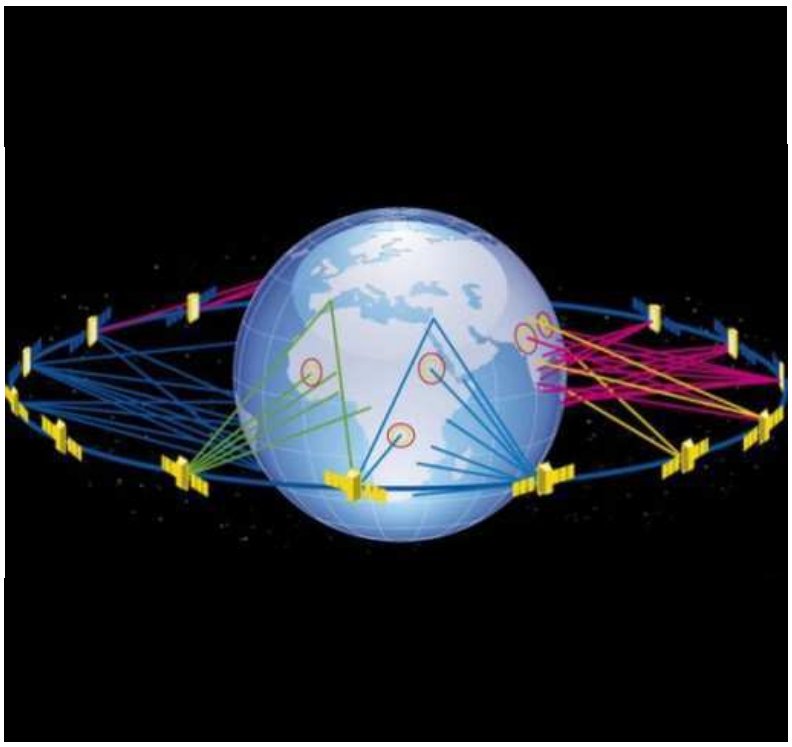

Figure 1: Exemple d'application en orbite basse ou intermédiaire (LEO/MEO) avec la constellation O3b [1].

Les missions satellitaires à multiple faisceaux ont rapidement émergés ces dernières années, proposant des couvertures faites d'un grand nombre de spots, supportant les bandes de fréquence en réception (sol/satellite) et en transmission (satellite/sol).

Une approche multi-faisceaux offre une capacité augmentée en comparaison à une couverture classique. Une exploitation plus élevée du spectre en fréquence est opérée, réutilisant les bandes de fréquences et la polarisation sur les différents faisceaux. Au début des années 2000, des couvertures régulières formées de 50 à 100 faisceaux fixes depuis des satellites géostationnaires (GEO) étaient proposées mais de nos jours, la capacité attendue augmente avec le nombre d'utilisateurs et les opérateurs de satellites demandent une plus grande flexibilité des systèmes de télécommunications. Des couvertures régulières avec un plus grand nombre de faisceaux ou irrégulière avec une combinaison de faisceaux de différentes tailles sont étudiées.

Les applications en orbite basse (LEO) ou intermédiare (MEO) viennent également fortement concurrencer les configurations classiques en orbite géostationnaire. Ces orbites présentent l'avantage d'être beaucoup plus proche du globe terrestre et peuvent proposer des temps de latence beaucoup moins importants (5-10 ms en LEO comparé à environ 250 ms en GEO). Actuellement, ce temps de latence n'est pas un réel problème mais ce critère risque de devenir de plus en plus essentiel notamment par rapport à la demande croissante de services multimédias et interactifs dans les années à venir. Ces orbites basses nécéssitent par contre l'utilisation de plusieurs satellites pour pouvoir couvrir efficacement une surface donnée, expliquant l'émergence des constellations. De nombreux projets proposants typiquement 10 à 100 satellites ont émergés ces dernières années ou sont en cours de dévelopemment, proposant des services de télécommunication et d'internet. Un exemple est donné en Fig. 1, avec la constellation O3b [1] composée de 20 satellites déployés sur une orbite circulaire à 8063 km d'altitude (MEO). Le déploiement de Méga-constellations (1000 satellites et plus) voit également le jour, poussant l'industrie satellitaire à réduire fortement les coûts de fabrication.

Ces applications potentielles et nouvelles nécessitent le développement de nouveaux systèmes antennaires à faisceaux multiples et à bas coût, permettant de couvrir des secteurs angulaires larges et variés tout en fonctionnant sur de larges bandes de fréquence. Au cours des dernières années, les formateurs de faisceaux quasi-optique sont apparus comme étant des solutions prometteuses pour répondre à certaines de ces applications. Ils proposent une conception mécanique simplifiée tout en maintenant potentiellement de hautes performances RF, particulièrement attendues lorsque des applications spatiales sont visées.

Un nouveau concept de formateur quasi-optique a récemment émergé d'une collaboration entre l'ESA/ESTEC, Thales Alenia Space et l'IETR dans le cadre du programme TRP (Technology Research Programme) de l'ESA. La solution proposée, transforme une onde cylindrique issue d'une source primaire et se propageant dans un guide d'onde à plans parallèles, en un front d'onde plan rayonné dans l'espace libre par un cornet. La conversion du front d'onde est assurée par une lentille formée d'une lame et d'une cavité transversale. La conception de cette lentille est similaire à celle d'une lentille contrainte (lentille de Rotman) sans la complexité et les limitations ajoutées par la discrétisation de la lentille et l'utilisation de lignes de transmission. Un prototype en bande Ku, servant de point de départ au concept, a été proposé et validé par la mesure. Des propriétés de dépointage sur une large bande de fréquence ont été démontrées. Cette solution est mécaniquement simple et peut répondre à des contraintes de coût tout en proposant de hautes performances RF, avec notamment une approche purement métallique particulièrement adaptée aux applications à forte puissance. Cependant, la démarche initiale basée sur

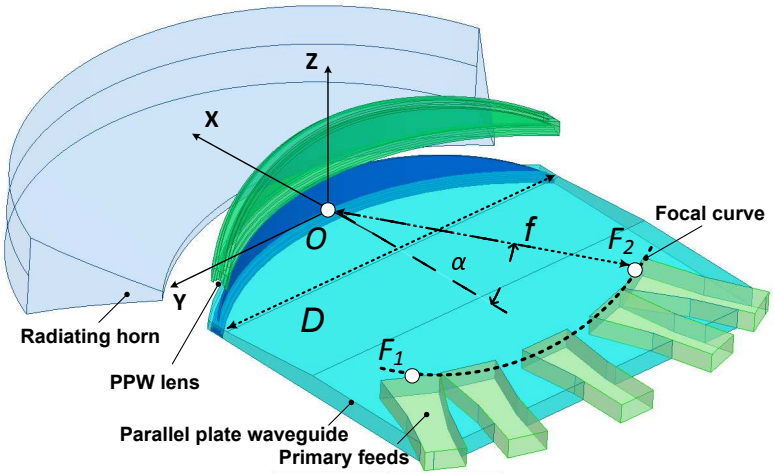

(a) Vue 3D

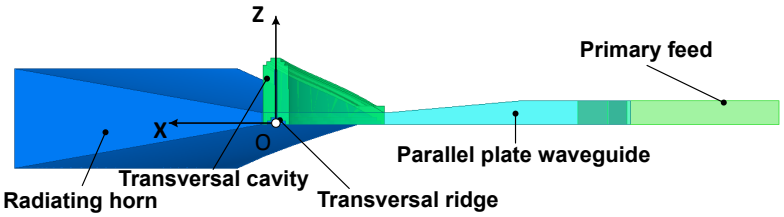

(b) Vue en coupe dans le plan $(O, \overrightarrow{X}, \overrightarrow{Z})$

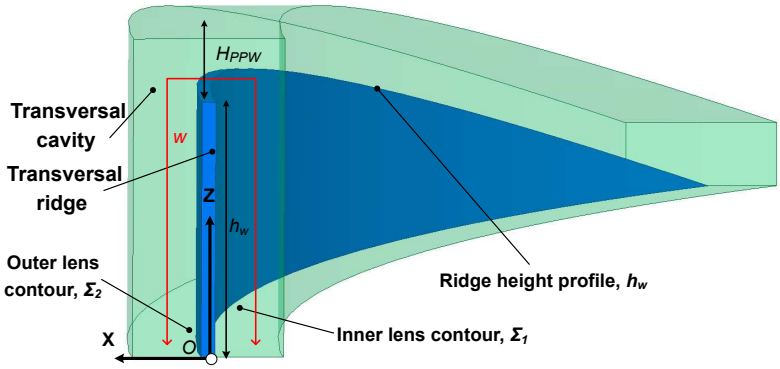

(c) Zoom sur la cavité transversale et la lame (le tracé en rouge décrivant le chemin de propagation dans la partie transversale)

Figure 2: Formateur de faisceaux quasi-optique basé sur une lentille continue en guide d'ondes à plans parallèles.

l'utilisation du logiciel commercial Ansoft HFSS requiert des temps de calcul et d'optimisation élevés. Ce type de procédure est difficilement applicable pour des lentilles de plus larges dimensions.

Le principal objectif de la thèse est d'étudier et de développer les aspects théoriques essentiels au concept. La mise en place d'un outil d'analyse rapide et précis, est nécessaire pour pouvoir optimiser des designs répondant à des spécifica-

tions données. Des évolutions du concept sont également à étudier, afin d'améliorer les performances en dépointage ou alors viser des solutions plus compactes. Cette solution proposée peut trouver plusieurs applications dans le domaine spatial, à bord des satellites géostationnaires mais également pour les terminaux antennes sol. Même si ce concept trouve principalement sa place dans des applications de télécommunication, il peut aussi avoir un potentiel pour des activités scientifiques et d'observation de la terre où des antennes à multiple faisceaux sont recherchées. Les principales parties de la thèse sont décrites ci-dessous.

Outil d'analyse pour l'étude de lentilles continues en guide d'onde à plans parallèles

Un outil d'analyse basé sur l'optique géométrique est proposé au Chapitre 2. Un premier modèle de lentille bifocal contrainte est étudiée, avec pour objectif la définition d'un point de départ pertinent et proche du concept proposé. Afin de définir ce modèle, la propagation dans la cavité transversale est simplifiée par l'utilisation des lignes de transmissions idéales. Ceci permet de définir deux profils principaux elliptiques, caractérisant respectivement un contour interne et une hauteur pour la lame et la cavité transversale.

Basée sur le modèle bifocal précédemment étudié, une procédure de tracé de rayons spécifique est définie afin de caractériser la propagation du front d'onde dans la cavité transversale. Elle finalise l'outil d'analyse et les premières performances en aberrations de phase sont étudiées et comparées à celles obtenues avec des formateurs de faisceaux biens connus dans la littérature (lentille de Rotman, antenne Pillbox).

Les performances en rayonnement sont ensuite analysées. Le front d'onde cylindrique rayonné par la source primaire est discrétisé suivant un pas angulaire régulier conduisant à une discrétisation spécifique du contour interne de la lentille. Les distributions de phase et d'amplitude obtenues en chaque point du contour externe de la lentille sont respectivement calculées à l'aide du tracé de rayons précédemment présenté et du rayonnement associé au cornet primaire. Le diagramme de rayonnement dans le plan de la lentille est calculé à l'aide d'une sommation d'éléments discrets auxquels une valeur de phase et amplitude est associée.

Les diagrammes de rayonnement obtenues sont validés avec le logiciel commercial Ansoft HFSS, démontrant une excellente prédiction des performances (

de pointage, ouverture à mi- puissance, lobes secondaires), comme on peut le voir en Fig. 3. On obtient une réduction considérable du temps de calcul, 1/2 s, comparé à 4/5 min avec l'approche commerciale, elle-même dépendante des dimensions de la lentille considérée.

Les performances finales de l'outil sont finalement analysées au travers de différentes spécifications (diamètre, distance focal, dépointage), confirmant les

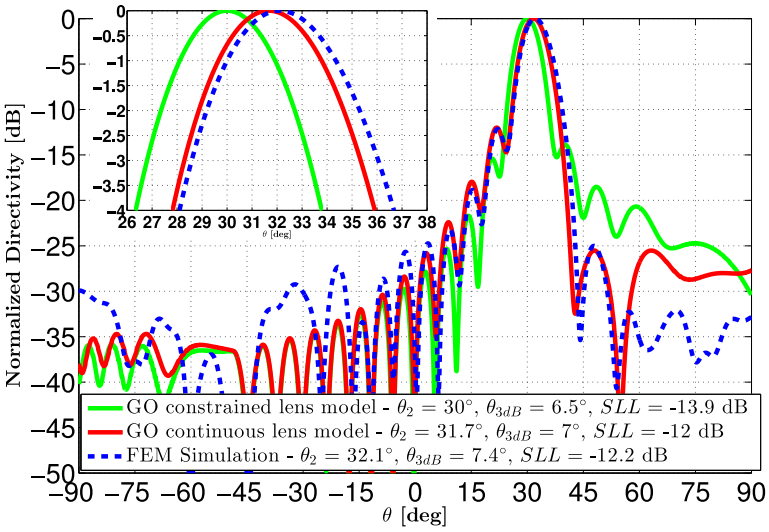

Figure 3: Diagramme de rayonnement dans le plan H d'une lentille continue de diamètre 10λ, avec une distance focale $f = 0.7D$ et une position angulaire de la source $\theta_1 = 30°$. En vert la prédiction donnée à l'aide du modèle bifocal initialement proposé, en rouge la prédiction finale fournie par l'outil d'analyse (optique géométrique). Une validation est proposée avec le diagramme simulé à l'aide du logiciel Ansoft HFSS.

capacités de prédiction de l'outil. Cette approche valide la possibilité de le combiner avec des procédures d'optimisations locales ou globales dans le but de répondre à des spécifications diverses.

Combinaison avec un outil d'optimisation, analyse de performance pour des applications antennes à multiple faisceaux

Le Chapitre 3 introduit la combinaison de l'outil d'analyse précédemment réalisé avec une procédure d'optimisation basée tout d'abord sur la minimisation des aberrations de phase dans l'ouverture de la lentille, et ensuite sur une méthode directe basée sur le diagramme de rayonnement. Un algorithme génétique, basé sur une méthode d'évolution différentielle (DE), est utilisé en tant que procédure d'optimisation globale.

L'outil d'analyse travaille avec des profils elliptiques. L'optimisation consiste à former ces profils de la cavité transversale pour le faisceau le plus dépointé. Un arc focal circulaire est ensuite optimisé pour définir les performances des faisceaux centraux et intermédiaires.

La minimisation des aberrations de phase démontre le potentiel du concept, avec des performances en dépointage intermédiaire à la lentille contrainte de Rotman et au concept Pillbox. Cependant, les diagrammes en rayonnement obtenus démontrent un déséquilibre résiduel des premiers lobes secondaires, caractérisant des aberrations de phase persistantes. Ce constat est confirmé par la procédure d'optimisation

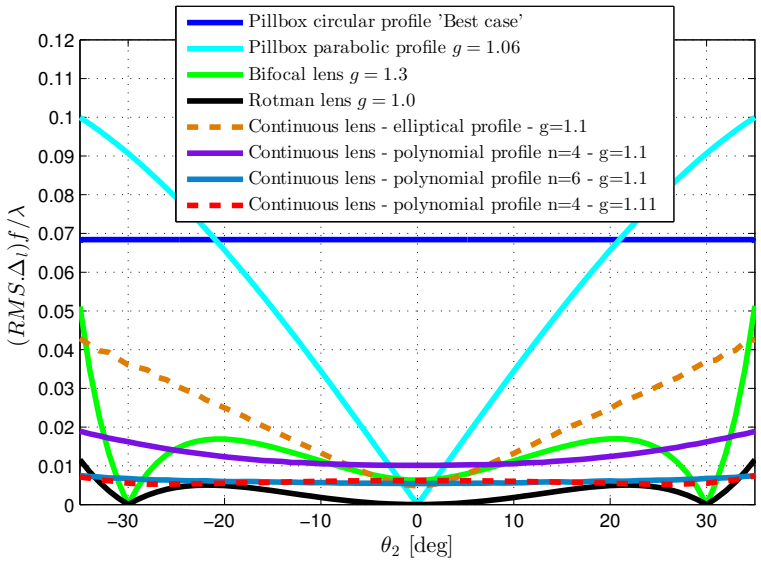

Figure 4: Performances en aberrations de phase du concept avec des profils elliptiques et polynomiaux. En comparaison avec les formateurs de faisceaux de type lentille contrainte (lentille de Rotman, bifocal), des performances similaires sont démontrées sur une large plage angulaire.

basée sur le diagramme de rayonnement, où ce déséquilibre est également présent. Les performances obtenues sont validées par le même logiciel commercial Ansoft HFSS. Elles démontrent les limites de cette première approche, issue du modèle de lentille bifocal contrainte et basée exclusivement sur des profils elliptiques.

Afin d'introduire des degrés de liberté supplémentaires pour le contrôle des distributions de phase et d'amplitude, des contours internes et externes indépendants sont définis. Ceci introduit une propagation additionnelle suivant l'épaisseur de la lame. Les performances en rayonnement obtenues sont améliorées, avec une réduction du déséquilibre des lobes secondaires précédemment observée. Cependant, la prédiction de l'outil d'analyse est dégradée par rapport à la précédente approche. L'épaisseur de la lentille réduit également les performances en compacité de la structure complète.

Une approche finalement basée sur des profils de lentille polynomiaux est introduite et analysée. La méthode de minimisation des aberrations de phase démontre d'excellentes performances en dépointage, proche de celles obtenues avec des modèles contraints simplifiés (Lentille de Rotman et Bifocal) sur un large secteur angulaire, comme prouvé en Fig. 4. Les performances en rayonnement démontrent une amélioration significative par rapport à l'approche elliptique. Des niveaux de lobes secondaires faibles et équilibrés sont obtenus. Ces développements sont validés dans les chapitres suivants au travers la définition et la réalisation de prototypes dans le bande Ka.

Design d'une lentille continue formée à multiple faisceaux dans la bande Ka

Au Chapitre 4 on propose une validation des performances en dépointage, démontrée avec l'utilisation de profils polynomiaux. La fabrication et la mesure d'un prototype dans la bande Ka en réception ([27.5-31] GHz) sont ainsi réalisées.

Le design vise 11 faisceaux rayonnés sur une large plage angulaire $[-28.5° \ 31.5°]$ avec un espacement de 6° entre chacun. L'ouverture à mi- puissance recherchée dans le plan de la lentille (plan H) est de 3°, tout en minimisant les niveaux de lobes secondaires. Cette lentille seule ne permet pas d'obtenir un recoupement à mi-puissance entre chacun des faisceaux, sachant que la minimisation des lobes secondaires conduit à la définition d'une dimension minimum des cornets primaires. On définit alors une configuration antenne avec deux lentilles superposées. Ces deux lentilles sont identiques, et une rotation de 180° est opérée entre les deux, de manière à obtenir une couverture complète de 22 faisceaux avec le niveau de recoupement recherché. On a ici l'avantage de pouvoir fabriquer et mesurer une seule lentille pour caractériser la configuration finale.

Une optimisation basée sur le diagramme de rayonnement est opérée. Les deux profils polynomiaux formant la lentille sont optimisés pour atteindre les performances désirées sur le faisceau le plus dépointé (31.5°). La forme de l'arc focal circulaire est ensuite considérée pour optimiser les performances des faisceaux intermédiaires. Les diagrammes de rayonnements obtenus démontrent une stabilité des performances en dépointage. L'analyse est premièrement effectuée en considérant des conditions de type PML sur les bords de la lentille puis pour le design final, purement métallique. Cette approche simplifie la fabrication et évite l'utilisation d'absorbants. Les dégradations sont observées pour des niveaux de puissance très faibles par rapport au maximum de rayonnement et sont sans conséquences notables sur les performances recherchées.

La fabrication du prototype à l'aide d'un usinage jet d'eau de deux blocs d'aluminium est ensuite mise en oeuvre, comme on peut le voir en Fig. 5. Les mesures valident les performances en rayonnement dans le plan de la lentille et présentent un excellent accord (direction de pointage, ouverture à mi- puissance, niveaux de lobes secondaires) avec la simulation finale du prototype menée à l'aide d'Ansoft HFSS. Le bon accord présenté est maintenu sur toute la plage angulaire ($[-90° \ 90°]$), jusqu'à des niveaux de l'ordre 30 dB sous le maximum de puissance rayonnée. Ceci démontre également la précision de la fabrication menée à l'IETR.

La stabilité des performances attendue sur la bande de fréquence ([27.5-31] GHz) est validée par la mesure. De hautes efficacités de rayonnement, attendues avec cette solution purement métallique, sont également démontrées (95% à 30 GHz pour la source dépointant à 31.5°). Les performances en paramètres S obtenues présentent

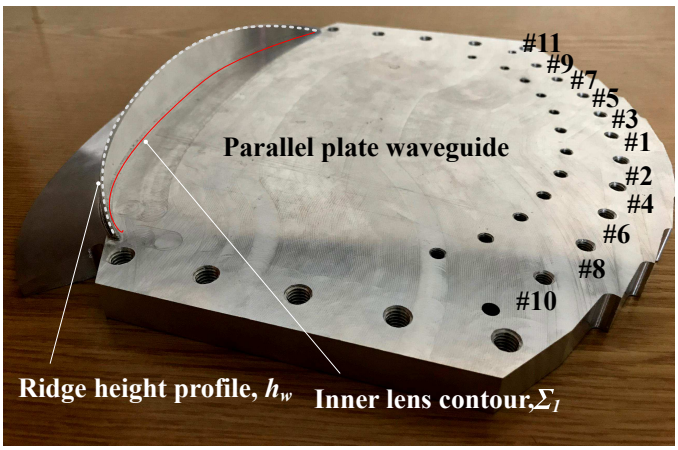

(a)

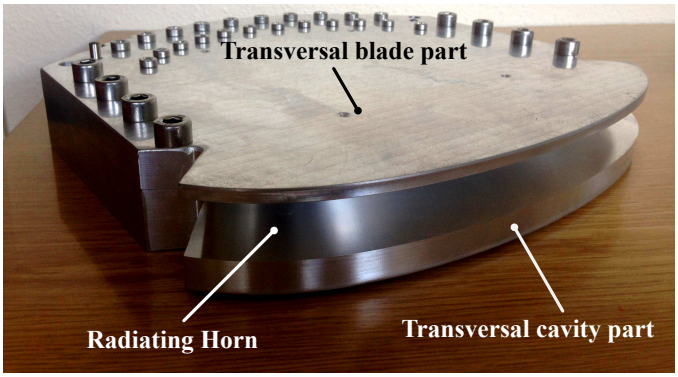

(b)

Figure 5: Prototype d'une lentille continue dans la bande Ka, [27.5-31] GHz. (a) Partie inférieure du formateur avec la lame, (b) design final assemblé.

des niveaux inférieurs à -19 dB en adaptation, et -22 dB en couplage mutuel, sur l'ensemble de la bande de fréquence. La simplicité de réalisation du concept est une nouvelle fois mise en avant, prouvant son potentiel pour des applications multi-faisceaux à bas coût et à haute performance.

Design d'une lentille continue formée et compacte à multiple faisceaux dans la bande Ka

Les performances en compacité sont particulièrement recherchées pour répondre à certaines contraintes d'intégration bien spécifiques. La cavité transversale du concept étudié, limite la réduction en hauteur de l'antenne. Ainsi, au Chapitre 5, ces aspects sont visés ainsi que l'étude d'un prototype dans la même bande Ka ([27.5-31] GHz).

Le design proposé dans ce chapitre a pour objectif des performances similaires à la première lentille précédemment mesurée dans la bande Ka ([27.5-31] GHz). Le diamètre est identique, 11 faisceaux sont rayonnés sur la même plage angulaire ($[-28.5°\ \ 31.5°]$).

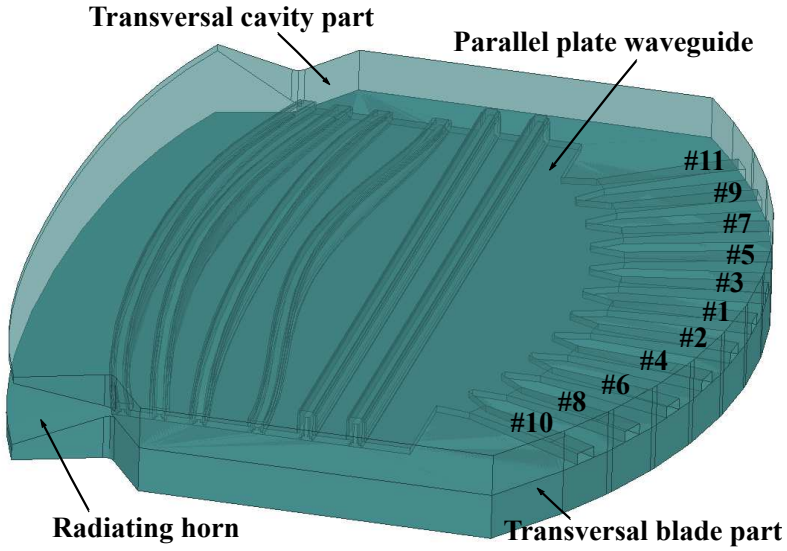

(a)

Figure 6: Design final du second prototype dans la bande Ka. On reconnait les différentes cavités et lames mises en place dans l'approche proposée.

Les lentilles compactes sont optimisées pour atteindre les performances désirées sur le faisceau le plus dépointé (31.5°) mais également sur le faisceau central (1.5°), de manière à imposer un arc focal circulaire tel que $g = 1$. Cette valeur permet d'éviter les effets de blocages entre les sources intermédiaires et également une réduction de la dimension longitudinale. Le processus d'optimisation est répété de manière à minimiser la hauteur finale du design, tout en maintenant les performances en rayonnement recherchées.

La compacité suivant la dimension transverse est dans un premier temps recherchée. On considère 4 lames et 4 cavités, disposées entre les sources primaires et le cornet rayonnant, afin de réduire la hauteur finale. Chaque lentille est définie par deux profils polynomiaux et une distance minimale égale à la longueur d'onde définie à la fréquence basse est spécifiée entre les différents contours internes. Cette contrainte est mise en place dans le but de limiter les réflexions multiples entre les différentes transitions adaptées.

Une réduction d'un facteur 2.7 de la hauteur des cavités transverses est finalement obtenue par rapport au premier design présenté au Chapitre 4. Les diagrammes de rayonnement sont comparés et une analyse de précision de l'outil d'optique géométrique est effectuée. On opère dans un second temps une réduction de la dimension longitudinale, deux cavités droites sont définies en repliant le guide d'onde réalisant une réduction de 27 mm.

Les performances en rayonnement et en paramètres S sont étudiées dans un cas idéal considérant des conditions PML sur les bords, évitant l'impact des effets des réflexions dans l'analyse souhaitée. Une comparaison avec le design premièrement

proposé est réalisée. Les valeurs de directivité, d'ouverture à mi- puissance et de niveaux de lobes secondaires pour l'ensemble des faisceaux rayonnés, et enfin les paramètres S (adaptation et couplage mutuel) sont étudiées.

Le design final avec des conditions métalliques sur les bords est finalement présenté en Fig. 6. Les dernières performances sont comparées aux résultats de simulation du prototype finale réalisé et mesuré précédemment au Chapitre. 4. Les performances en rayonnement (directivité, ouverture à mi-puissance, niveaux de lobes secondaires) démontrent des performances similaires au premier design fabriqué et mesuré. La dégradation des paramètres S, due aux différentes transitions adaptées reste limitée. Les niveaux des coefficients de réflexion et de couplage mutuel restent respectivement inférieurs à -17 et -18 dB. Ce second prototype doit être fabriqué prochainement à l'IETR et mesuré à l'ESA/ESTEC.

Abstract

Nowadays, there is a strong demand for high-performance yet low-cost multiple beam antennas for future satellite communication systems (GEO, LEO constellations). Over the past few years, the use of quasi-optical beamformers in combination with a continuous line source appears as a very promising solution since they provide a wide band of operation and avoid undesired effects such as propagation cut-off and grating lobes. Their simpler mechanical aspect is also quite attractive.

A new concept of continuous parallel plate waveguide (PPW) beamformer came out of a recent research activity between ESA/ESTEC, Thales Alenia Space and IETR in the frame of the Technology Research Programme (TRP) of ESA. The design approach is based on a constrained lens design but removing the aperture discretization and the complex transmission lines used to create the wave front transformation. In this respect, the proposed solution resembles the pillbox antenna, while providing significantly improved performance. The proposed solution transforms the cylindrical wave launched by one of the feed horns and propagating inside the PPW section into a nearly plane wave radiating in free space by the radiating horn (vice-versa), using a PPW lens made of a transversal ridge and cavity. The proposed concept can be manufactured using only metallic parts, providing a solution compatible with high-power applications. The simplicity of the mechanical design is also expected to enable low-cost antennas without compromising performance. A proof-of-concept has been developed and tested by TAS in the frame of the aforementioned TRP activity. A large scanning range ($[-30^\circ\ 30^\circ]$) has been demonstrated over the entire Ku-band dedicated to satellite communications and the measurements of the corresponding prototype, proved to be in very good agreement with simulation results. However, this design was based on a time consuming full-wave implementation; this approach cannot be applied to propose design and optimization processes in order to cope with different scenarios with specific requirements (scanning range, number of beams, frequency band). This work aims to develop the main theoretical aspects to study the concept. Evolutions of the solutions to improve the scanning capabilities or the performance in compactness have to be studied.

An efficient analytical tool based on geometrical optics (GO) is first developed. A fast and accurate prediction of the radiation performance is provided. The

procedure proposed relies on geometrical optics (GO) to characterize the wave front propagation into the PPW section but also in the transversal cavity, working as a delay lens. The results computed with the GO tool are compared successfully to full-wave results obtained with Ansoft HFSS.

The numerical tool developed has been combined with optimization procedures, based on the minimization of the phase aberrations along the radiating aperture and also based on a direct pattern optimization to account for both phase and amplitude errors in the aperture. Additional degrees of freedom, making use of polynomial profiles, have been introduced to shape the PPW lens. Phase aberrations similar to those obtained with simplified constrained lens designs (Rotman or Bifocal lens), where true focal points exist, are demonstrated. In line with this aspect, a stability of the radiation pattern performances (HPBW, SLL, scan loss) with the scanning angle is shown.

A breadboard operating over the Ka-band up-link ([27.5-31] GHz) has been proposed in order to validate the expected scanning capabilities. A full metal solution has been manufactured using a classical milling process. An excellent agreement is demonstrated between the FEM simulation and the measurement. The scanning properties are validated including a stability of the performances over the frequency band. We demonstrate again the capability to propose a low-cost approach. High radiation efficiencies are also demonstrated, which is particularly suitable for space applications.

The performance in compactness has been then studied in order to fulfill stringent integration requirements, or propose a stack of beamformers to produce a planar array. The transversal cavity, working as a delay lens, is the main limitation for the reduction of the beamformer height. A second prototype, working over the same fraction of the Ka-band ([27.5-31] GHz) and targeting the same RF performances is proposed. In this case, multiple PPW delay lenses are optimized in order to reduce the antenna size. With the final FEM model, the reduction of the longitudinal and transversal dimensions is significant while proposing similar simulated RF results. This prototype should be manufactured soon at IETR and tested in an anechoic chamber.

Contents

List of Figures

List of Tables

1 Introduction and State of the Art

1.1 Multi-beam antennas for space applications

Multiple beam broadband missions have emerged those last years, providing coverages made of a large number of spot beams, supporting down-link (satellite to ground) and up-link (ground to satellite) communications, often referred to as transmission (Tx) and reception (Rx) from a satellite system perspective.

A multibeam approach offers an increased capacity as compared to a classical contoured beam coverage. An increased spectral utilization is achieved through frequency and polarization re-use over the different beams. An increased antenna is also obtained, due to the smaller beamwidth, resulting in a higher effective radiated power for the down-link and higher gain to noise temperature for the up-link.

1.1.1 GEO configurations

Geostationary spacecrafts were first considered to propose such multibeam antenna systems, as they travel in the same direction as the rotation of the Earth and have the ability to stay in a stationary position relative to the Earth.

In the early 2000's, a regular grid of 50 to 100 regular cells in the range 0.5° to 0.7° in beamwidth was first considered as a compromise between antenna performances, payload power, satellite capabilities and link budget in order to cope with the ground user terminals. Then, in order to enlarge the area (up to full Earth coverage) in relation with accommodation requirements on board of spacecrafts, beams of different sizes in the range 0.4° to 1.5° have been considered.

More recently, as the system user capacity demand increases, the number of beams is more prominent, as compared the antenna efficiency. The requirements

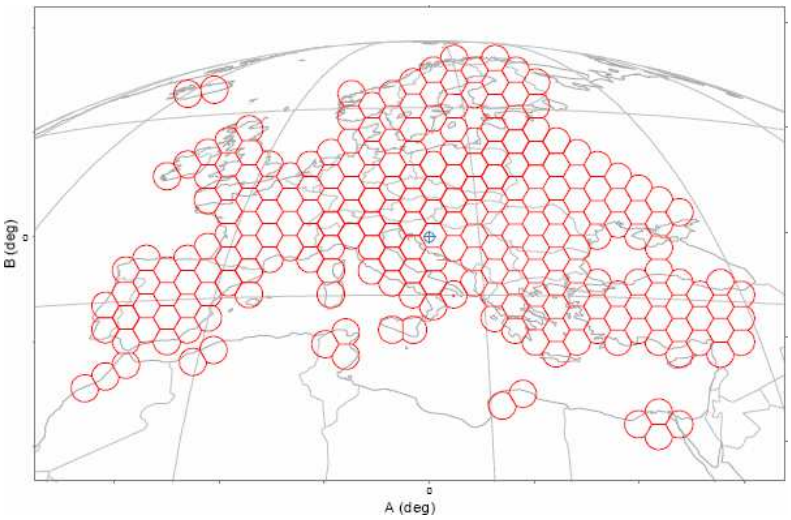

Figure 1.1: Typical coverage of 240 regular cells of 0.26° over Europe and neighboring countries [2].

are now to propose beams of size 0.20° to 0.35° on a regular lattice [2], as shown in Fig. 1.1, possibly combined with larger cells for less populated areas.

Satellite operators would like to have telecommunication systems adapted to the population maps. Considering this approach, antenna performances have to be optimized in a point to point approach. The main consequence of very narrow beams is that they imply a large number of cells to cover a given geographical area and a significant number of gateways. Those new potential applications request large and high power spacecrafts able to embark a large number of payload equipments.

For all above considerations, satellite prime contractors often consider Single Feed Per Beam (SFPB) antenna systems, with each beam defined by a single feed horn in a reflector-based antenna configuration. This solution works with at least 3 reflectors and Rx/Tx feed chains to propose multiple beam coverage with frequency and polarization reuse. A typical configuration is shown in Fig. 1.2 with the high throughput THD satellite, studied and delivered by Thales Alenia Space [3].

The major drawback of the SFPB architecture is the accommodation to embark other missions. Moreover, when required beams size are extremely low, spill-over effects are significant, due to the reflector size, limited by the fairing of the launcher.

To overcome those limitations, the Multi-feed per beam (MFPB) concept was introduced more recently. Each beam is generated by a cluster of horns, some of them being shared with adjacent clusters to provide an adjacent beam with the same frequency band but opposite polarizations. Thanks to the physical overlap of feed apertures, the number of reflectors can be reduced and only two reflectors are potentially needed to provide multiple beam capabilities. MFPB

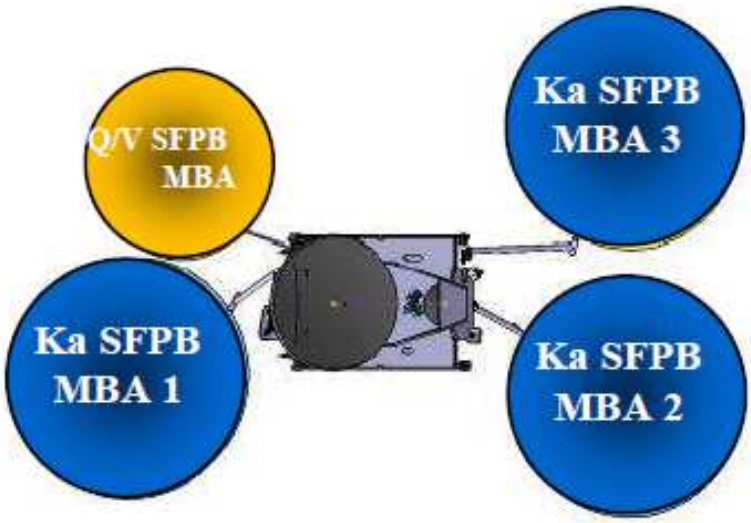

Figure 1.2: Example of High Throughput satellite for a GEO application: THD sat with SFPB antenna configuration (3 Ka offset reflectors of 3.5m + 2.4m Q/V reflector) [3].

antenna configurations proposed by Thales Alenia Space are described in [4]. The MFPB approach offer great advantages for small satellites, where it is difficult to accommodate four large reflectors using a SFPB approach or when a small number of beams is needed (e.g. secondary payload missions). This solution is also applicable for low frequency bands applications, typically at C-band where a SFPB solution would be quite heavy and bulky.

1.1.2 LEO/MEO challenges

GEO solutions for broadband missions are now challenged by lower orbit solutions. Low Earth Orbits (LEO), like Medium Earth Orbits (MEO), are significantly closer to the Earth. Thus, the main benefit of using LEO or MEO satellites is the low latency, which is typically between 5 and 10 ms for a LEO application, as compared to more than 250 ms with a classical GEO configuration.

Actually, GEO satellite latency has limited impact on user experience with more conventional satellite services (e.g. Direct To Home TV, broadcasting) but with the increase of multimedia services including Voice over IP and gaming, this aspect becomes more and more essential. LEO satellites require less power and thus tend to be smaller in size as compared to GEO satellites. However, more spacecrafts must work together to offer continuous coverage of a given location, explaining the deployment of a large number of satellites working in constellation.

Several constellations, made of 10 to 100 satellites, have been launched those last years or are currently under development. As an example, Thales Alenia Space

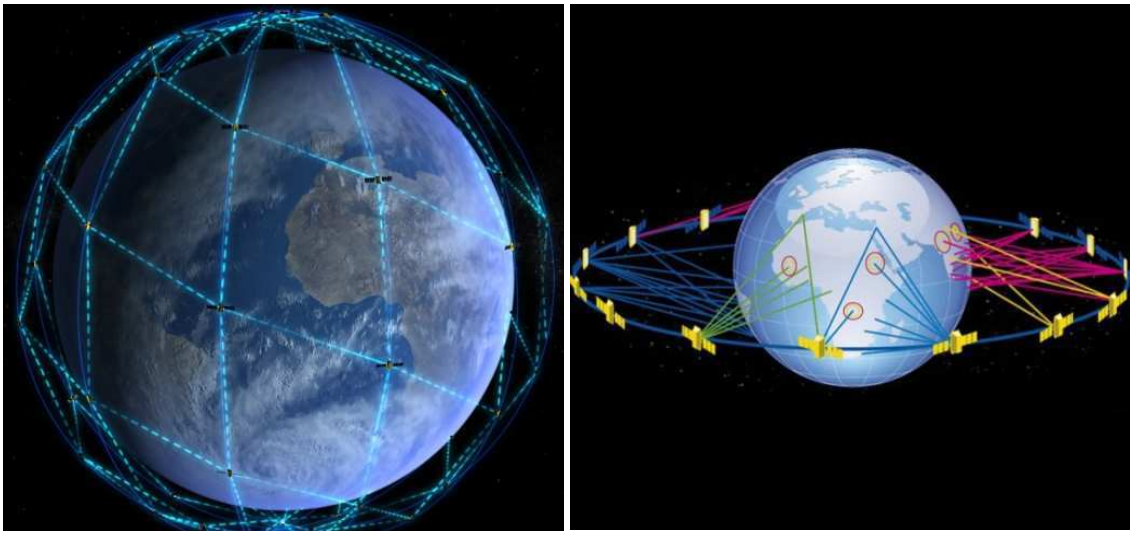

(a) (b)

Figure 1.3: Example of satellite constellations. (a) Iridium NEXT [5] and (b) O3B [1].

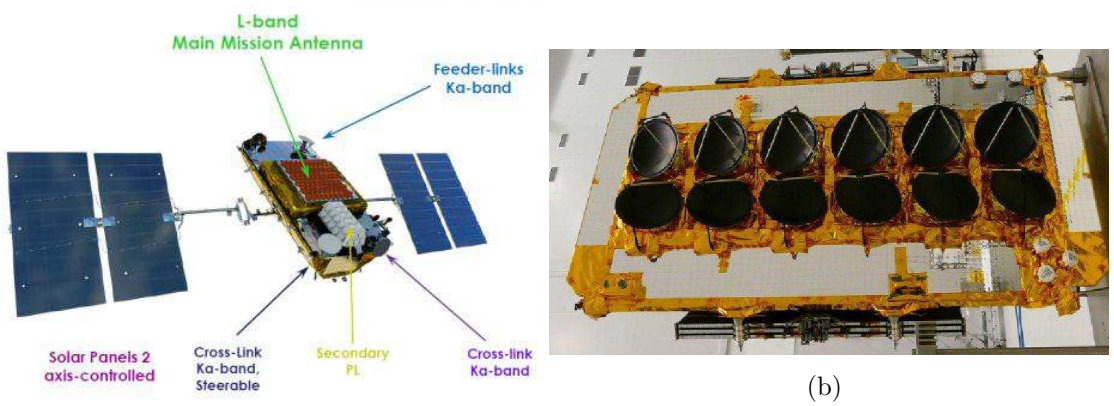

(a) (b)

Figure 1.4: (a) Iridium NEXT [5] and (b) O3B [1] satellites with their respective antenna systems. Pictures provided by Thales Alenia Space.

was involved in Iridium NEXT [5] and O3b [1], respectively illustrated in Fig. 1.3a and 1.3b, providing telecommunication and internet services. Iridium NEXT is made of 66 satellites connected and exploited from a LEO altitude of 780 km. Each satellite carries a single 48-beam transmit/receive L-band phased array antenna, as shown in Fig. 1.4a, in order to cover a circular service area on the Earth's surface with a diameter of 4700 km. O3b is made of 20 satellites, deployed in a circular orbit along the equator at an altitude of 8063 km (MEO). Each satellite is equipped with twelve fully steerable antennas, made by fully steerable mechanically controlled reflector antennas (Fig. 1.4b), targeting a field of view of $\pm 50°$ and working over both up and down-links of the Ka-band.

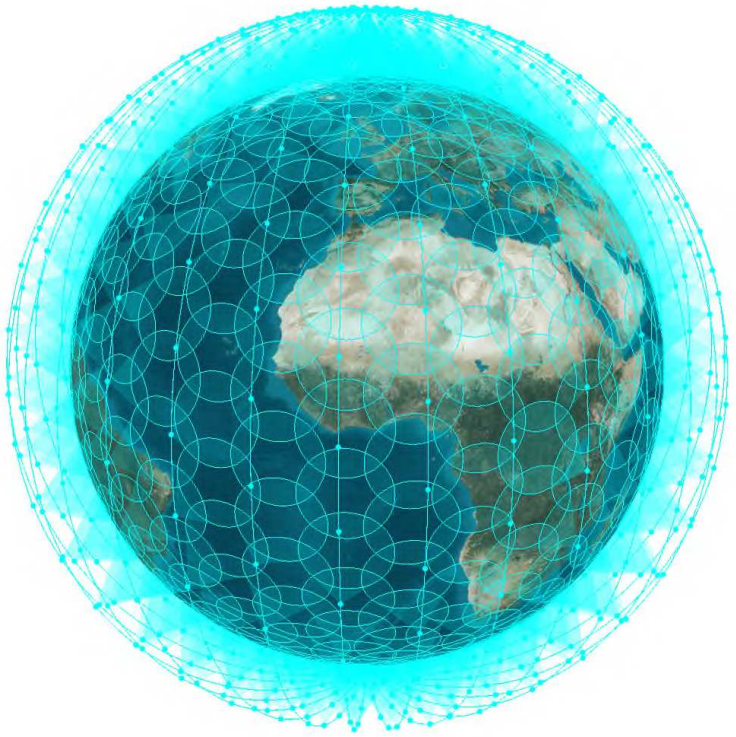

Figure 1.5: OneWeb satellites covering the entire Earth's surface (Simplified circular footprints are shown for each satellite) [6].

Since 2014, Mega-constellation projects gained popularity, proposing a drastic increase in the number of satellites. One of the well-know mega-constellations is ONEWEB [6], illustrated in Fig. 1.5, where 882 spacecrafts, small and low-cost, are expected to provide global internet services to individual consumers in 2022. The communication satellites will operate in a circular LEO (1200 km), transmitting and receiving at Ku band for the user link and Ka-band for the feeder link. Each satellite provides 16 fixed Tx/Rx user beam generated by a passive antenna system. Each of these beams is highly elliptical and the 16 beams are arranged in a single row ($\pm 25°$ in the north-south direction) to create an almost square footprint on the Earth. An illustration of the beams from five ONEWEB satellites is given in Fig. 1.6, both within the same orbit plane (yellow, blue and turquoise beams) and between adjacent orbit planes (pink and green beams), to demonstrate how they overlap. The combination of the geographic coverage achievable from each satellite plus the number and proximity of the satellites in their orbits ensure the global Ku-band coverage. This unconventional beam shape and coverage was introduced as a way to reduce interference with GEO systems also operating at Ku-band.

As observed with these examples, this large number of satellites requires the development of low-cost multiple beam antennas for both space and ground segments.

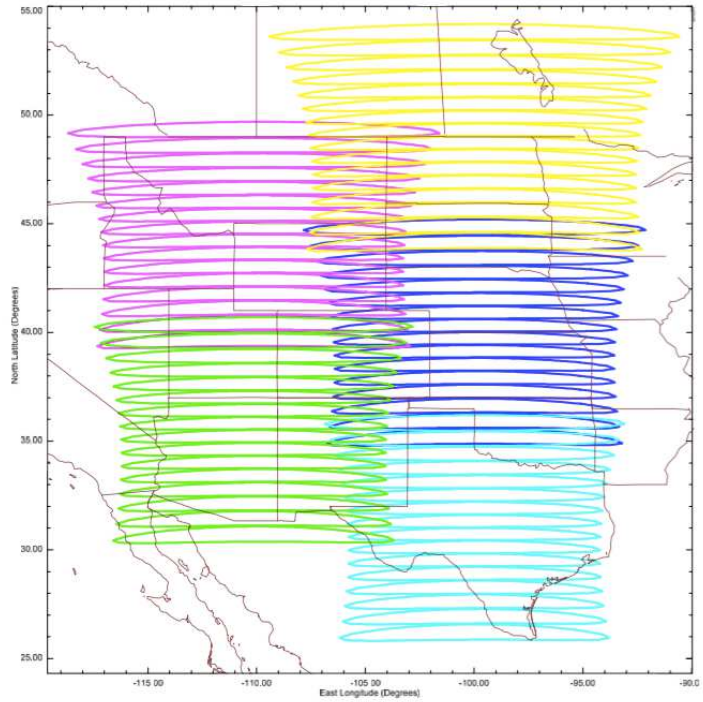

Figure 1.6: Illustration of ONEWEB Ku-band satellite beam coverage from five adjacent satellites [6].

Simpler mechanical designs operating over a wide frequency range or possibly over up and down-link bands a wide angular sector are required. Solutions with intermediate gain (20-30 dB), proposing regular or possibly shaped beams (as observed with the strongly elliptical beams proposed in the ONEWEB project [6]) are now of interest.

To provide steering capabilities, direct radiating array antennas are often designed, making use of complex beam forming networks (BFN), such as Blass ([7], [8]), Nolen ([9], [10], [11]) and Butler ([12], [13], [14]) matrices. These solutions based on interconnected elementary components provide high RF performance, but their complexity increases drastically with the number of beams and the array size. These solutions also tend to have limited frequency bandwidth due to grating lobes.

New research works have been initiated over the past few years on 2D lens based feed systems for space applications. In combination with a continuous line source, they can provide a large number of spot beams over a wide band operation, avoiding undesired effects such as propagation cut-off and grating lobes. A state of the art of the solutions existing in the literature is given in the next Section 1.2, describing their potential capabilities to cope with those new challenges.

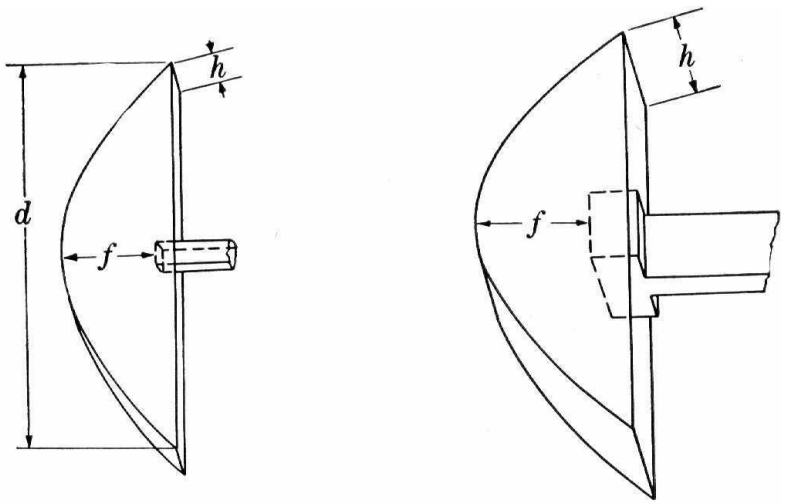

Figure 1.7: Pillbox and Cheese antenna [15].

1.2 State of the Art : 2D-lens like antennas

1.2.1 Pillbox antenna

The pillbox antenna is one of the well-known concepts working with a parallel-plate waveguide (PPW) with integrated vertical walls acting as mirrors. The vertical walls have usually a shaped profile to collimate the energy coming from the feed. A one dimensional radiating aperture is thus generated, producing a wide beam in one plane and a narrow beam in the orthogonal one. For this reason, the pillbox antenna is integrated in the fan beam antennas family. This system was first used for military surveillance during the second world war and the british version was called "Cheese antenna", as presented in [15]. In the parallel plate waveguide (PPW), a TEM mode is propagating, with an electric field vector normal to the conducting plates, and possibly a TE01 mode, in which the electric vector is parallel to the plates.

Different variant were referred to as pillbox antennas. This concept presents the advantage to be wide band with the use of a continuous radiating aperture, easy to design and low-cost. A multi-layer structure, shown in Fig. 1.8, was proposed later on by Rotman in [16], with the feeds located in one layer and a second layer containing the radiating aperture. This configuration avoids aperture blockage with the advantage to use multiple feeds without shadowing effects.

In transmission, the cylindrical wave coming from the open end of the waveguide propagates within the entrance layer, transferts to the exit layer through the parallel-plate bend where it is converted into a quasi plane wavefront, and then radiates into free space from the linear aperture. From the configuration presented in Fig. 1.8a, the beam may be scanned by moving the waveguide in a circle whose center

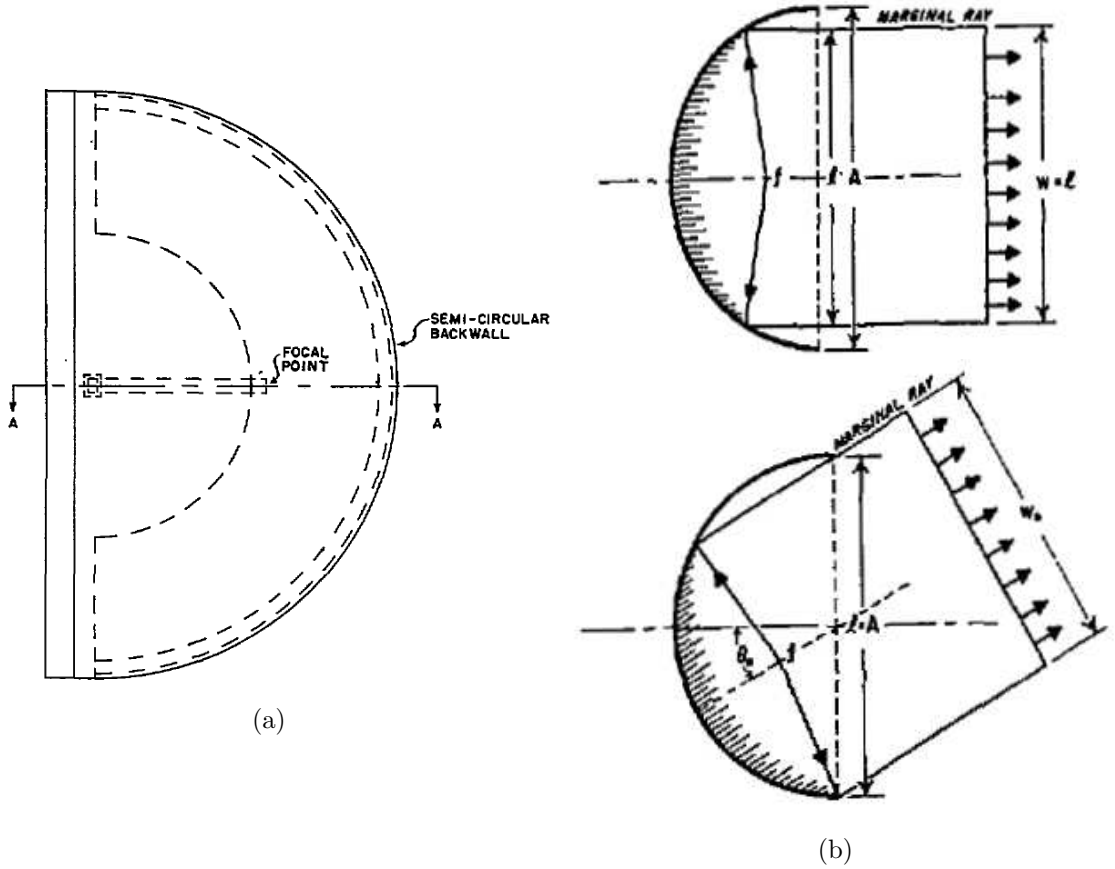

(a)

(b)

Figure 1.8: Pillbox antenna configuration proposed by Rotman in [16].

coincides with the center of curvature of the model. A direct relationship is obtained with the angular position of the feed when a TEM mode is considered.

This circularly symmetry design has the advantage to provide fairly stable beam shape over a wide scanning range, but results in spherical aberrations limiting the efficiency of the antenna. Shadowing and spill-over effects also exist when large pointing directions are considered (Fig. 1.8b). Spherical aberrations could be corrected using various means: dielectric or auxiliary lens moving with the feed, quasi-point source feeds or geodesic shapes, as further explained in [16].

Rotman also studied this double layers solution, considering a parabolic profile with one on-axis true focal point as shown in Fig. 1.9a. This design was limited by the phase aberrations errors, increasing strongly when scanning away from broadside. More recently, this configuration has been also reviewed by Holzmann [17] in 2003 with a single layer and an offset feeding technique, limiting however the number of feeds that can be accommodated (Fig. 1.9b).

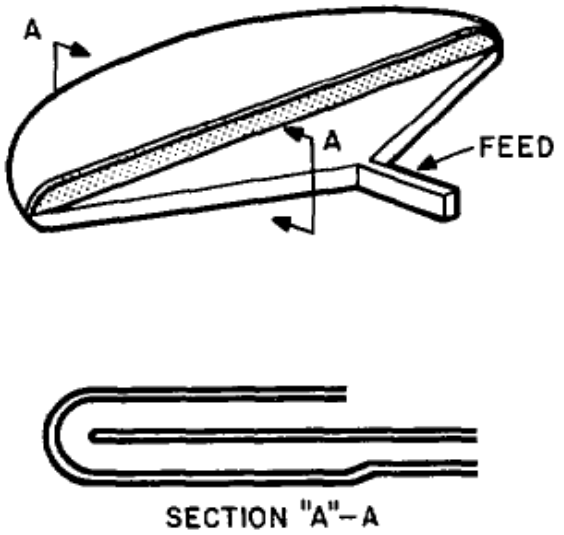

(a) [16]

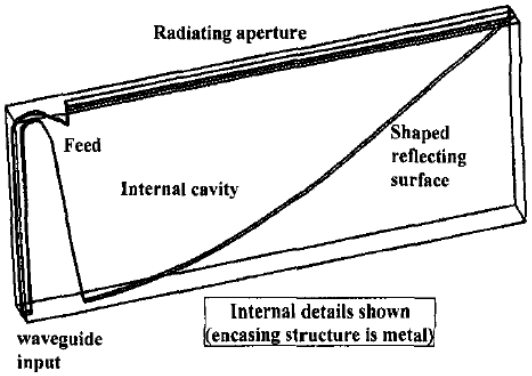

(b) [17]

Figure 1.9: Pillbox antenna configuration with a parabolic profile.

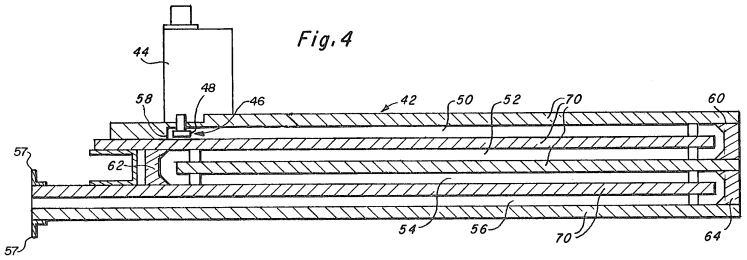

Figure 1.10: Cross section view of the multi-layer pillbox [18].

A multilayer pillbox antenna, with reflector profiles at each layer was introduced in [18], which permits to increase the equivalent focal length and thus reduce scan losses due to phase aberrations. The concept is presented in Fig. 1.10. The multiple number of reflectors provide multiple focal points and is a way to select a forward or backward propagation. The manufacturing of this concept is less attractive as several layers are considered.

Various solutions, based on this concept have been proposed , particularly working on the power transfer efficiency of the wave from one layer to another. The initial solution, presented in [16], consists in a bend bordering along the entire length of the shaped profile. This solution was relatively narrow band, working for long focal lengths. A bend transition was developed in [20] and consists on an array of holes in the common wall between layers located along the entire parabolic profile. The hole diameter was optimized to achieve wide band performances while maintaining relatively compact designs.

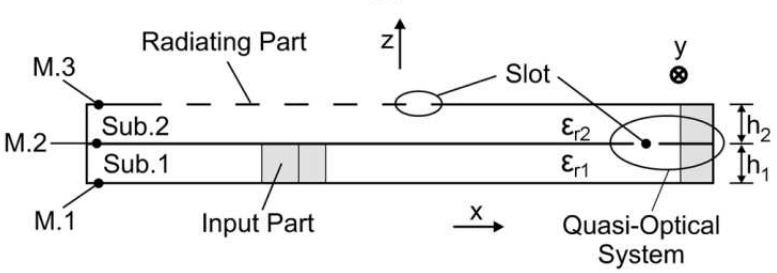

(a) 2D view in xz plane

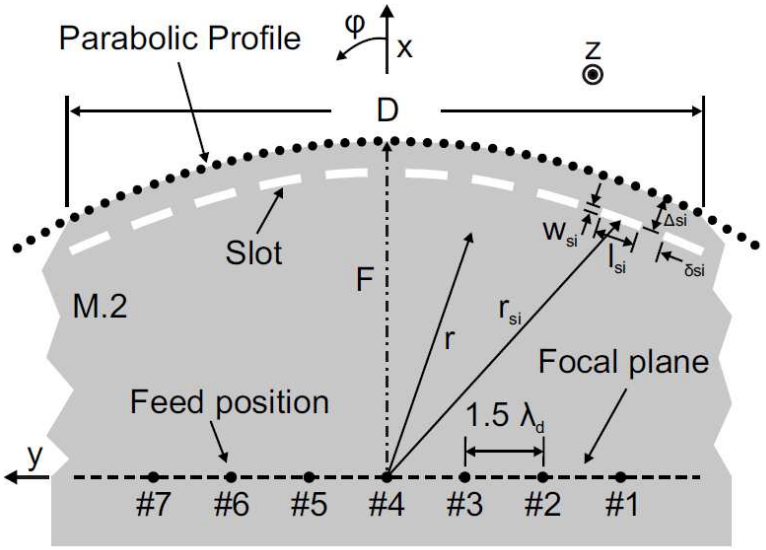

(b) Top view with the proposed improved pillbox transition with slots

Figure 1.11: Multibeam multilayer leaky-wave pillbox antenna [19].

Based on the substrate integrated waveguide technology (SIW), this approach has been reviewed and improved at IETR [19]. As shown in Fig. 1.11, the pillbox works as a beamformer and the transition between two layers is made by several optimized small slots providing up to 30% fractional frequency bandwidth over a large range of illumination angles (±50°). This beamformer solution has been used in several antenna configurations ([21], [22], [23] and [24]) especially for tracking/radar applications.

1.2.2 Bootlace lenses: Design considerations

Constrained lenses also referred to as bootlace lenses, first described by Gent [25], were introduced as a way to enhance the scanning performance of more conventional dielectric lenses. The lens is composed of inner lens array elements connected to their respective outer lens array elements through transmission lines of variable length. The lens is fed by elementary feeds or beam ports placed at

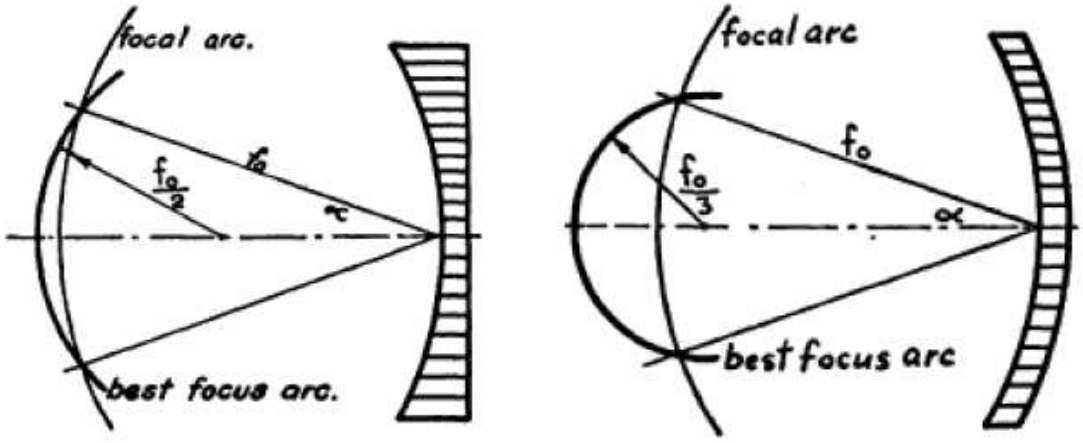

(a) Linear array

(b) Constant thickness

Figure 1.12: Two types of lenses studied by Ruze [26].

a suitable distance, linked to the focusing properties of the lens. The lens may be implemented in a two-dimensional or three-dimensional configuration. Here we focus on two-dimensional designs where the section between the beam ports and inner lens contour is constrained between two parallel plates, often referred to as parallel plate waveguide (PPW) section.

Those lenses introduce a higher number of freedom degrees, including the curvature of the focal arc, the shapes of inner and outer lens profiles and the different transmission line lengths. They propose multiple focal points and low phase aberrations over a wide scanning range.

Ruze introduced various designs of constrained metal plate lenses, as presented in [26]. The rays are guided by metal plates and different lenses with various inner and outer profiles have been derived and analyzed in terms of linear and high order phase errors. Two types of lenses studied are presented in Fig. 1.12. Different focusing techniques were investigated in order to derive the widest scanning beam capabilities.

Rotman and Turner introduced in [27] a two dimensional lens design, proposing three perfect focal points. The design cross section is presented in Fig. 1.13. Inner and outer lens contours are respectively defined by Σ_1 and Σ_2. The position of element ports are defined by the inner lens contour and are connected to radiating elements, defined along the outer lens contour, using TEM transmission lines of variable electrical path lengths W.

The three focal points are defined at angular positions ($-\alpha$, α and $0°$) with respect to $\overrightarrow{X}$-axis and are focal points for those three radiation angles. G is a first central axis focal point and the two others, F_1 and F_2, are symmetrically located

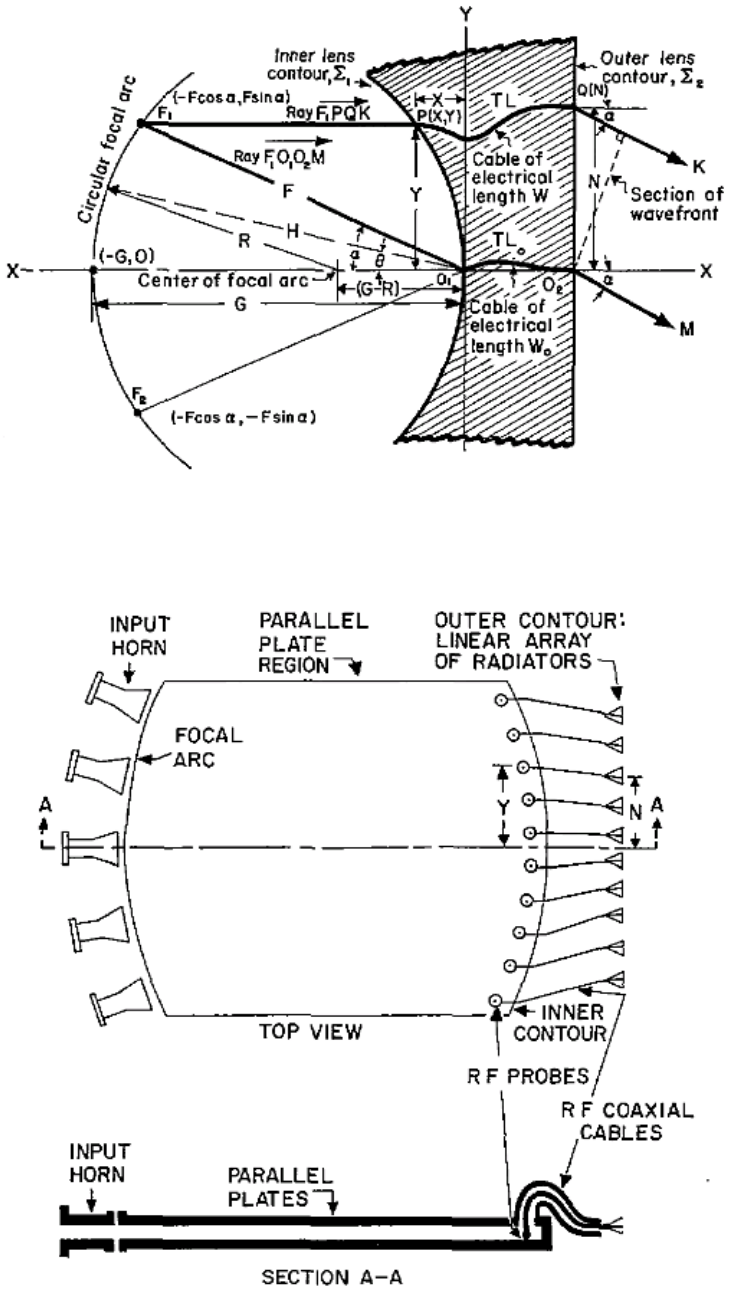

Figure 1.13: Rotman lens introduced by Rotman and Turner [27].

on either sides of the circular focal arc. For those three points, a perfect plane wave front is generated from the outer radiating array. For other beam ports located on the circular arc, phase aberrations appear and can alter the radiation pattern. The Rotman lens has four main parameters : The off-axis focal distance f (distance O_1F_1 or symmetrically O_1F_2), the on-axis distance G (distance O_1G), the focal angle α and the antenna array element spacing d.

Various modifications of the initial Rotman lens design have been proposed.

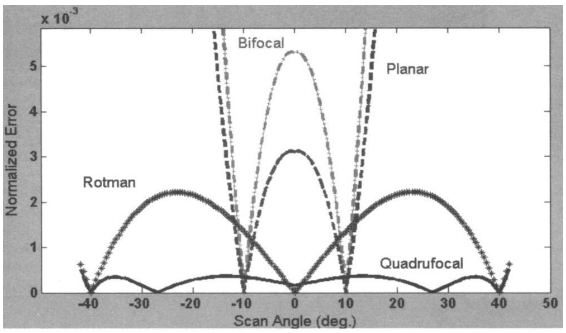

(a) [30]

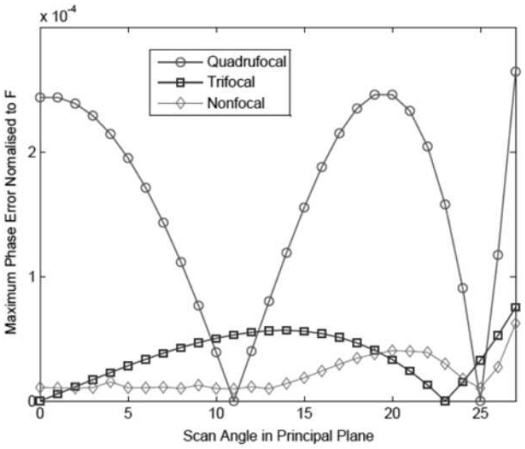

(b) [31]

Figure 1.14: Overview of several bootlace lenses including a scanning performances comparison.

Shelton [28] introduced a new design method to analyze more precisely the focusing properties/limitations of the concept, in relation with the lens parameters. Katagi [29] implemented a refocusing numerical method by changing the focal curve shape, introducing as an additional design parameter the ratio between the beam pointing angle and the angular position of the corresponding feed. The resulting lens can achieve smaller phase errors, especially for large arrays.

A paper [30] published in 2005 compared several designs (Fig. 1.14a), including design methods to proposed multiple focal points and analyzing the performances obtained in scanning. A non focal point method has been described in [31]. Instead of having zero path length errors only for selected focal points, it may be interesting to produce minimum average phase errors for all beam ports. A performances comparison is shown in Fig. 1.14b.

A more recent approach [32] describes a novel focal curve design method for two-dimensional Rotman lenses. The proposed design method offers some additional degrees of freedom in the design of such beamformers to extend significantly their angular scanning range, providing a solution to overcome the resulting focal arc and inner focal lens contour obstruction. Good scanning performances over a very wide angular range ($\pm 50°$) is demonstrated with phase-aberrations lower when compared to an equivalent standard Rotman lens.

1.2.3 Bootlace lenses: Technological implementation

The original Rotman lens first proposed was an air-filled microwave lens. The development of this concept has been initiated by the US Army, as presented in

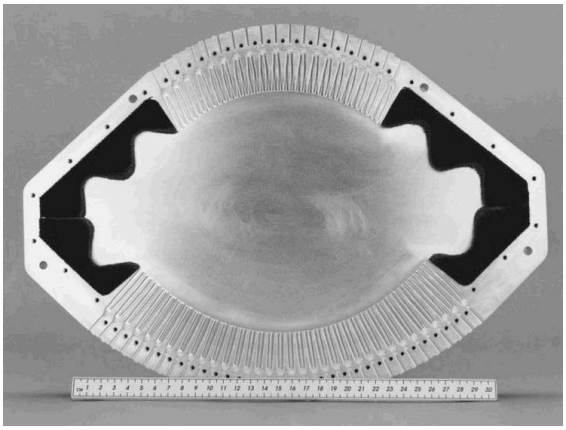

(a) Rotman lens working as a beamformer

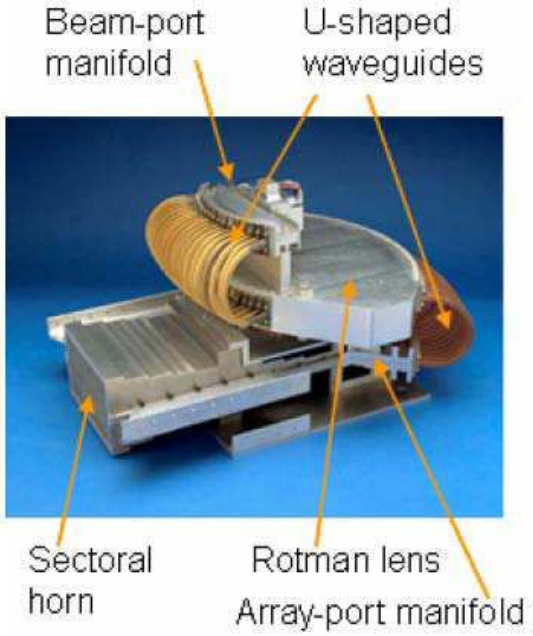

(b) Final antenna system

Figure 1.15: Rotman lens beamformer connected to radiating sectoral horns [33].

Fig. 1.15a, with an antenna operating between 33 and 37 GHz [34]. 32 active antenna element ports and 17 beam ports were used for the Rotman lens, defining a maximum scan angle at 22.2°. The losses estimated for this beamformer lens were below 2.3 dB. A final antenna system, making use of U-shaped waveguides through array ports connected to radiating sectoral horns was proposed [33], with a fine discretization of the array ports using coaxial cables. Thanks to this transmission lines technology, the configuration shown in Fig. 1.15b is wide band but leads to higher integration complexity. This Rotman lens antenna concept was improved with the integration of waveguide transmission lines, as proposed in [33] . Wave dispersion effects are consequently introduced and affect the true time delay of the Rotman concept with a beam squint of 4% over a frequency range of 35 to 40 GHz.

A Rotman lens at W-band has also been developed [35] for beam steering applications (Fig. 1.16a), completely realized in waveguide technology. A scanning range of ±30° is achieved, as shown in Fig. 1.16b, using 13 beam ports and 20 antenna elements. However, between 75 GHz and 80 GHz, the antenna pattern degrades based on the selected waveguide dimension. Wave dispersion effects appear and only for the design frequency, 94 GHz, the beam position is exactly the predicted one.

Alternative planar designs in printed technology have been presented to be low cost and more simpler to integrate. Many designs of Rotman lenses based on

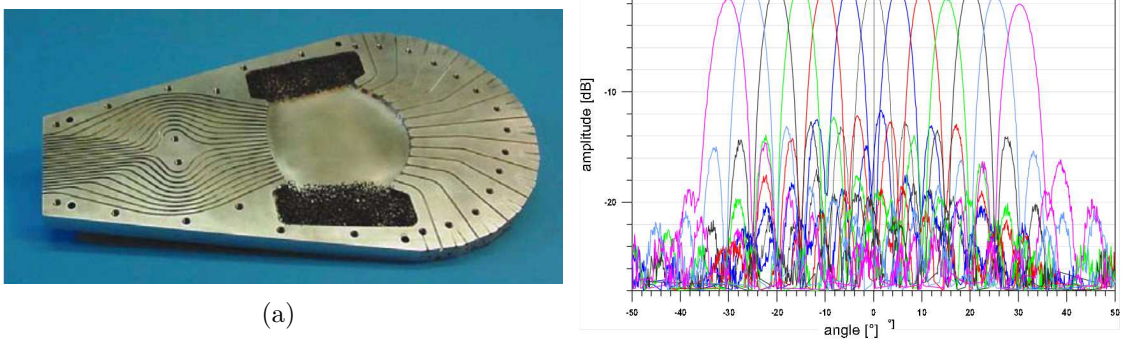

(a) (b)

Figure 1.16: Rotman lens beamformer at W-band [35].

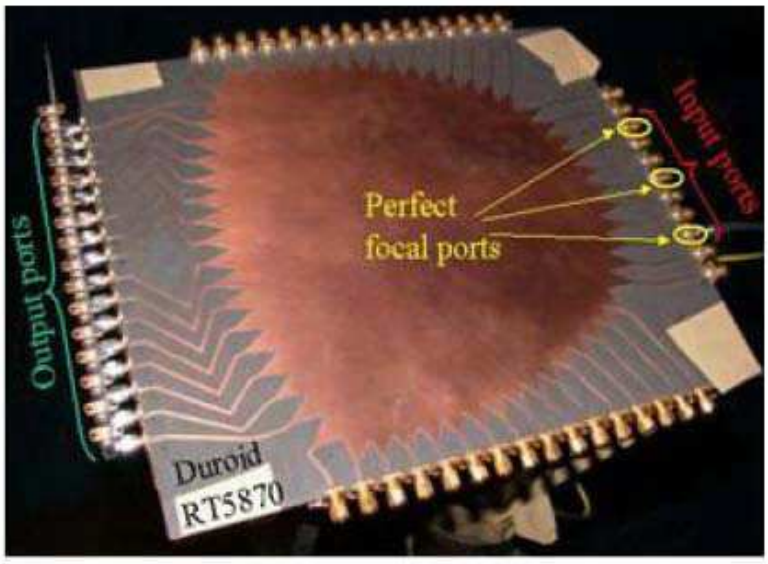

Figure 1.17: A Ku band microstrip Rotman lens [33].

printed circuit board (PCB) technology with feeds and delay lines using microstrip or stripline transmission lines are reported in the literature. A Ku-band microstrip lens, presented in Fig. 1.17 was designed and fabricated by the US army [36] with 7 different beam positions and a linear array of 16 patches which suffer from important losses of 9.5 dB at 17 GHz. More recent examples have been proposed using this technology ([37], [38]). The use of dielectric material enables more compact designs but at the cost of increased losses, including higher mismatch between the PPW section and the transmission lines with the scanning angle.

More recent examples include some solutions in substrate integrated waveguide (SIW). A significant improvement has been made with this solution. It emulates a waveguide propagation in a multilayer printed circuit board. The upper and lower

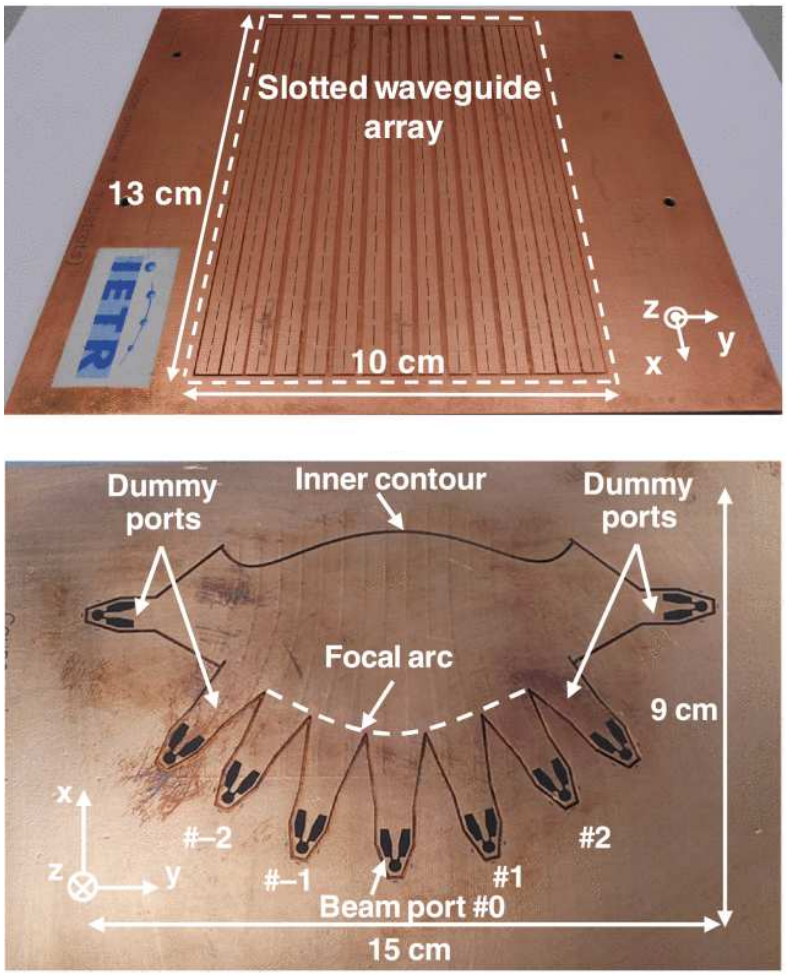

Figure 1.18: Multibeam SIW Slotted Waveguide Antenna System Fed by a Compact Dual-Layer Rotman Lens [39].

substrate metallization are used as the broad walls of the waveguide structure while the side walls are synthesized in the form of two rows of metallized via holes or grooves connecting the top and bottom metallic plates. The resulting structure is a waveguide that benefits from the advantages of printed technology, such as reduced manufacturing cost and higher integration.

A multiple beam Rotman lens in SIW technology has been reported [40] operating at Ku-band. The lens prototype includes 3 ports and 8 array elements. In the quasi-TEM PPW section, absorbing sidewalls are proposed in place of the more conventional dummy ports. Good performances in terms of insertion loss and side lobe level were measured. Based on this work, further investigations were made to reduce the losses, employing materials with higher thickness and lower tangent loss coefficient. A multiple beam antenna system fed by a compact Rotman lens has been developed at IETR and is presented in [39], using a multilayer substrate

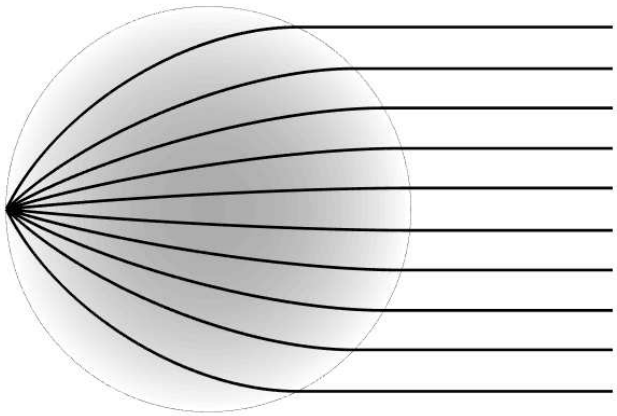

Figure 1.19: Luneberg lens principle.

integrated waveguide (SIW) technology . The final design prototyped is shown in Fig. 1.18. The lens is implemented in two layers using a new transition based on several star-shaped coupling slots and a SIW integrated reflector. The proposed Rotman lens leads to a reduction in lens footprint by a factor of two, as compared to single-layer implementations. The performance in compactness of the proposed antenna system makes it very attractive for multi-beam applications with stringent integration requirements. Nevertheless, wave dispersion effects exist, due to the use of waveguide transmission lines, limiting the available bandwidth. The multi-layers design approach also leads to a more complex manufacturing process requiring particular attention to alignment between layers.

1.2.4 Luneberg lenses

Luneberg lenses are quasi-optical beamformers with special characteristics enabling perfect focusing in any angular direction thanks to its intrinsic symmetries. Luneburg lenses are characterized by a refractive gradient index with spherical or rotational symmetry for respectively three-dimensional and two-dimensional implementations [41]. A spherical or cylindrical wave front, generated by a feed at any point of the surface of the lens, is transformed into a plane wave on the opposite side of the lens. The operation principle of the lens is illustrated in Fig. 1.19 using ray tracing.

Luneberg lenses allow beam scanning, beam steering and can be considered as very attractive for applications requiring very wide scanning range. A Luneberg lens can be design from the following refractive index law,

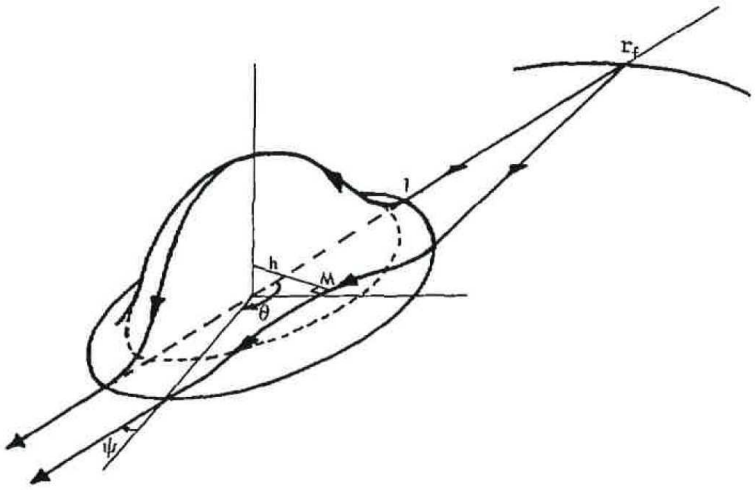

Figure 1.20: Geometry of the generalized Luneberg geodesic lens.

$$n(r) = \sqrt{2 - (r/R)^2}, \tag{1.1}$$

where r is the distance between a point of the lens of radius R and its center. The refractive index $n(r)$ is maximum at the center of the lens $n(0) = \sqrt{2}$ and minimum at its periphery $n(R) = 1$.

In theory, the focal arc consists of its entire periphery or circumference. Axial symmetry of the structure permits performances independent from the feed position and consequently no scanning losses. The field of view is only limited by the actual implementation of the radiating aperture and of the feeds when a multiple feed system is considered. The refractive index is equal to 1 at its periphery thus minimizing reflections due to material mismatch. In principle, the lens is frequency independent. Frequency dependence may come from the technological implementation of the feeding ports and/or radiating aperture.

Geodesic lenses are one class of two-dimensional Luneberg lenses with a homogeneous material. They are composed of a pair of non planar metal plates spaced by a constant distance with a spacing small enough that only a TEM mode can propagate. The shape of the non-planar metal plates is optimized to provide similar focusing performance as the non-homogeneous original design by Luneburg. In a way, this concept may be seen as an early implementation of transformation optics. The geometry of this type of lens is shown in Fig. 1.20. Several profiles of the plates such as Rinehart-Parker ([42], [43]), Tin Hat [44] have been introduced.

The refractive index in this case, is the one of the material, typically air ($n = 1$) and the ray path provides the phase delay. The rays path are adjusted by the curvature of the plates' profile.

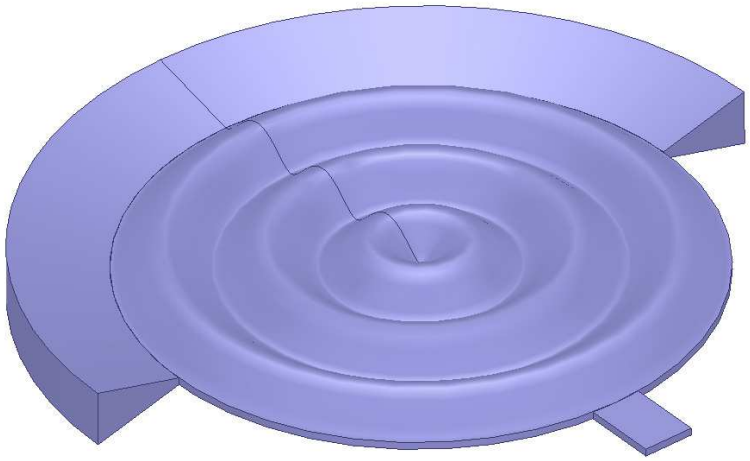

Figure 1.21: Water Drop Luneberg geodesic lens concept [45].

The advantages are the following: all metal structure without use of dielectric, wide frequency bandwidth properties, stack of lenses possibly proposed. The major drawback is the bulky and not planar configuration, due to the path length correction provided by the lens profile along the transversal direction, as shown in Fig. 1.20.

Recent efforts have been proposed in the frame of an ESA activity ([45], [46] and [47]), where the possibility to use plane symmetry, as suggested in [48], has been further investigated to reduce the height. The use of parallel curves has been studied to provide smooth profiles and ensure a propagation without mismatch at any angle of incidence. The main objective was to maintain the performance of the original Rinehart [42] geodesic lens while working as much as possible on the compactness along $\overrightarrow{Z}$-axis. The "water drop" lens concept obtained is shown in Fig. 1.21. Numerical results have been proposed at Ka-band without any further optimizations, confirming the potential of the concept. Excellent performances in terms of S-parameters and radiation patterns over a wide angular range ($\pm 60°$) are demonstrated while reducing strongly the height as compared to the reference geodesic lens.

As an alternative, all metal solutions have been recently developed ([49], [50]), synthesizing the graded refraction index by using the geometry of periodic pins or holes within a PPW section. The first idea of those design solutions was to avoid the use of dielectric material, where the losses increase with frequency. But solutions based on metasurfaces (modulated patch surfaces) have also been proposed to control locally the propagation constant or the refractive index within the parallel plate waveguide. Those solutions are described in [51], [52] and [53]

(a) Final prototype

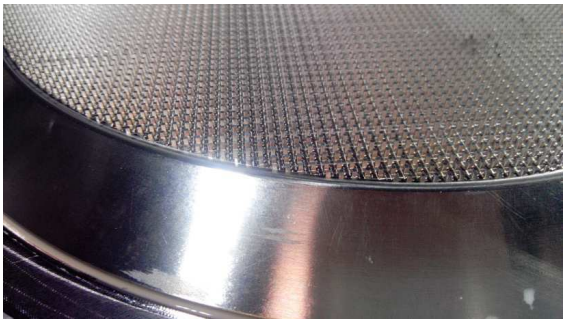

(b) Bottom plate: zoom on metal posts

Figure 1.22: Luneberg lens antenna at Ku-band based on variable parallel-plates spacing fakir bed of nails [54].

A recent PhD project, funded in part by Thales Alenia Space [55], [54] aimed to develop this concept for multibeam antenna architectures at Ku and Ka band. A wide scanning and frequency range Luneberg lens, shown in Fig. 1.22 has been developed. Although quite attractive, this design has been manufactured at Ku band with a classical milling approach. This process was already challenging but the difficulty increases drastically when the frequency increases, typically moving to Ka-band.

1.3 Continuous Parallel Plate Waveguide Lens beamformer

A new concept of continuous PPW beamformer has been introduced in [56]. This beamformer (Fig. 1.23) transforms the cylindrical wave launched by one of the primary feeds (sectoral horns in Fig. 1.23a) and propagating inside the PPW section, into a nearly plane wave radiated in free space by the radiating horn, and vice-versa. The primary feeds are vertically polarized (E-field along $\overrightarrow{Z}$-axis), and the beam radiated by this beamformer can be steered in H-plane depending on the feed position along the lens focal curve (indicated by the dotted line in Fig. 1.23a). The desired delay correction applied to ensure this wave transformation is provided by a PPW lens made of the transversal ridge and cavity (Figs. 1.23b and 1.23c) and whose inner and outer contours are labelled Σ_1 and Σ_2, respectively. The proposed lens has two focal points (F_1 and F_2, Fig. 1.23a) in its simplified

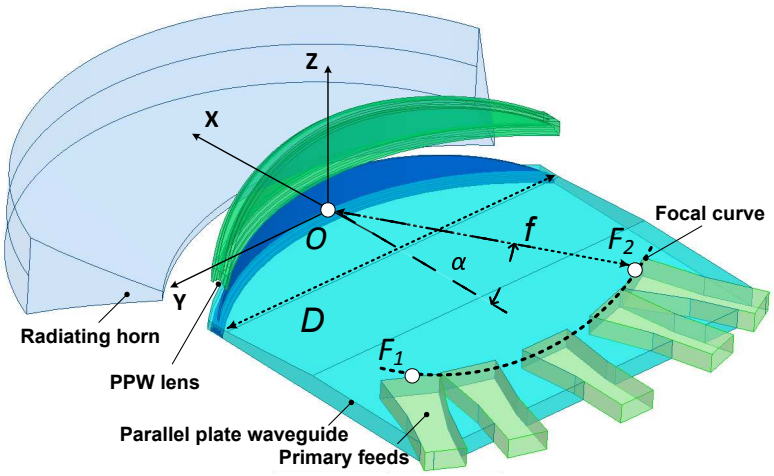

(a) 3D view

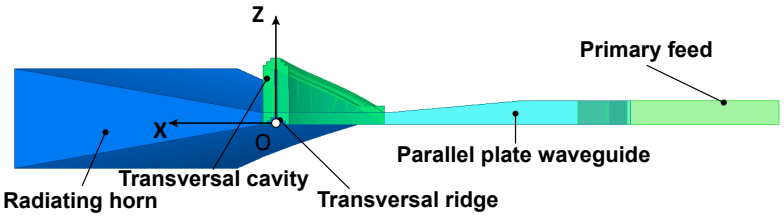

(b) Cross section view in $(O, \vec{X}, \vec{Z})$ cut plane

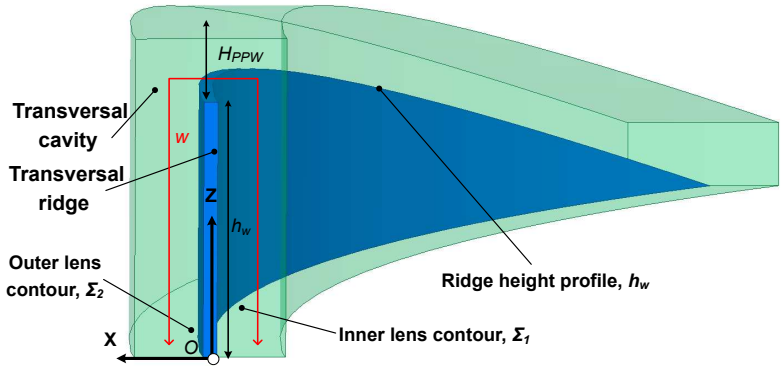

(c) Zoom on the transversal cavity (the red line highlights propagation path inside the transversal cavity)

Figure 1.23: Continuous PPW lens-like beamformer.

representation using a constrained lens formulation and the delay value is controlled by tuning the ridge height h_w (Fig. 1.23c).

This beamformer solution was first defined using a design approach similar to constrained lenses without the complexity and limitation in bandwidth resulting from the lens discretization. The original idea was to start from a Rotman lens design [27] but this was not found to approximate well the proposed structure. Indeed, in the case of the continuous parallel plate waveguide lens-like beamformer, the degrees

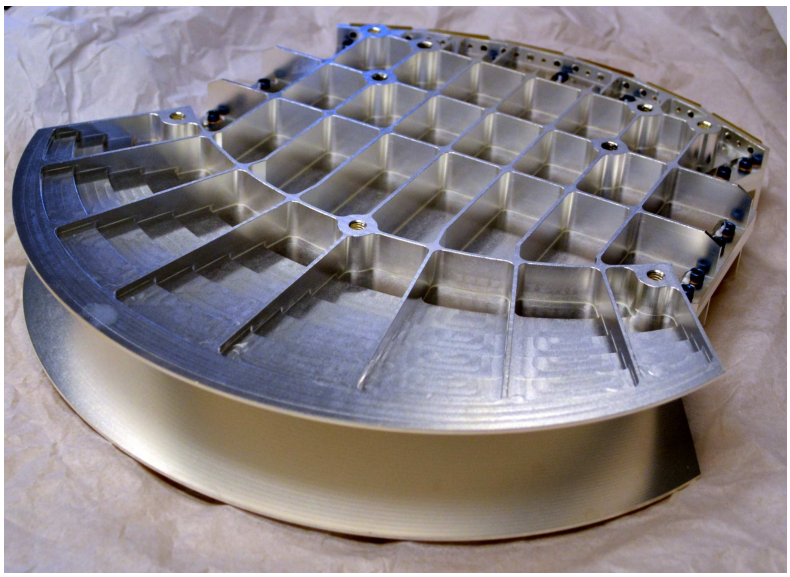

Figure 1.24: Manufactured continuous PPW beamformer [56].

of freedom are less as the shape of the inner and outer lens contours are constrained by the transversal ridge section (Fig. 1.23) and cannot be set independently.

A proof-of-concept, shown in Fig. 1.24, was optimized using full-wave modeling [56], and its performance has been experimentally validated at Ku-band. Its overall dimensions are the following: diameter $D = 200$ mm and focal distance $f = 144$ mm, including a radiating horn of length 100 mm. Large bandwidth properties ([10.7-14.5] GHz) have been demonstrated with S-parameters measurements presented in Fig. 1.25. Reflection (Fig. 1.25a) and Mutual Coupling (Fig. 1.25b) coefficients are measured below -21 and -22 dB respectively. The large scanning possibilities $[-30°, 30°]$ are demonstrated by the experimental characterization of the H-plane radiation patterns, which proved to be in very good agreement with simulation results (Fig. 1.26). Excellent comparisons are found down to levels typically 20 dB below the peak directivity. These results confirm that the full-wave model can be used as a benchmark to validate the development of this lens concept.

This solution is very simple from a mechanical point-of-view and is expected to lead to a low-cost design without compromising performance. Moreover, a full metal solution is compatible with high power applications . Nonetheless, the design procedure used in [56] relies on time consuming full-wave optimizations applicable only for small and medium size lenses. The performances of the final design may depend on the selected starting point. Such a procedure cannot be implemented for larger lenses because of the requested computational resources. Optimization of such beamformers requires fast and accurate analysis tools that also provide better insight on the lens operation principles, thus providing a more relevant starting point.

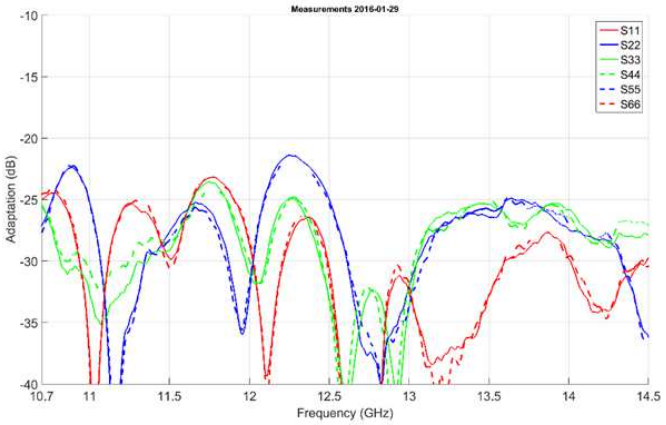

(a) Reflection coefficients

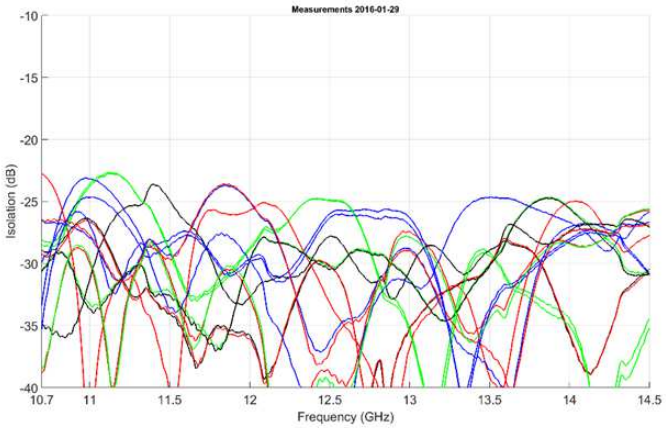

(b) Mutual Coupling coefficients

Figure 1.25: S-parameters measurements of the manufactured continuous PPW beamformer provided by Thales Alenia Space [56].

1.4 Thesis Goal and outline

This work was conducted in cooperation with the Antenna and Sub-Millimeter Wave Section of the European Space Agency, Noordwijk, The Netherlands and the Research&Technology Department of Thales Alenia Space, Toulouse, France in the frame of ESA's Networking/Partnering Initiative (NPI).

The main objective is to study the theoretical aspects of the proposed concept and develop an efficient tool to design and optimize it using a more adequate numerical method, overcoming the limitations of the time-consuming full-wave model optimization. Evolutions of the original concept were also identified and shall be covered by this design tool, such as the combination of multiple continuous lenses to enhance scanning performance or make it more compact.

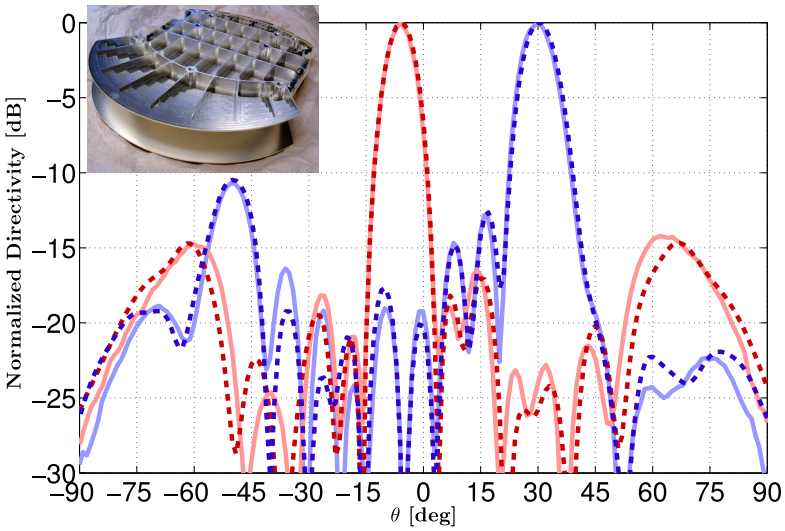

Figure 1.26: Simulated (dash line) versus measured (continuous line) radiation pattern of the manufactured PPW beamformer in H-plane at $f_0 = 10.7$ GHz, θ is the scanning angle in (O, $\overrightarrow{X}$, $\overrightarrow{Y}$) plane. Two beams pointing at 30° (blue curve) and −6° (red curve) (insert: manufactured lens prototype).

The proposed concept will have multiple applications in the space domain, ranging from GEO satellite multiple beam antennas down to low-profile ground terminals. Although this concept is mostly considered for communication applications, it may also find applications in Earth observation and science missions requiring multiple beam antennas.

The manuscript is organized as follows. In Chapter 2, an analytical model based on geometrical optics is proposed to design and analyze continuous parallel plate waveguide (PPW) lens-like antennas. A bifocal constrained lens model is first studied to propose a relevant starting point for the design. A refined model based on ray tracing is achieved by accounting the wave propagation inside the transversal cavity, demonstrating an excellent agreement of the full-wave based model while providing very low computational efforts ($\cong$ 1 or 2 seconds). In Chapter 3, phase and pattern optimization procedures, based on the numerical tool presented in Chapter 2, are proposed to design and analyze continuous parallel plate waveguide delay-lens multiple beam antennas. Two design evolutions, a thick delay lens with different inner and outer lens contours and a thin lens with polynomial profiles are proposed to improve the radiation performance. The potential of the proposed polynomial profiles is confirmed with path length errors very similar to those of simplified constrained lens models over a large scanning range ($[-30°, 30°]$). An experimental validation over the up-link Ka band ([27.5-31] GHz) is proposed in Chapter 4, validating the scanning performances proposed. Excellent radiation

performance are demonstrated over a wide scanning range, including low scanning loss and high radiation stability over the entire frequency range. High radiation efficiencies are confirmed with this full-metal solution, particularly suitable for space applications. Finally, reduction in size is investigated in Chapter 5. A second prototype targeting the same performances as the first one is proposed. A reduction of the transversal and longitudinal dimensions is obtained, while proposing similar radiation performances. A degradation of the S-parameters is observed but the levels obtained are still acceptable for most applications (reflection coefficients $<$ -17 dB, mutual coupling coefficients $<$ -18 dB). This prototype should be manufactured soon at IETR and measured.

2

Analytical Model to Study Continuous Parallel Plate Waveguide Lens-Like Multiple Beam Antennas

Contents

Abstract

An analytical model based on geometrical optics is proposed here to design and analyze continuous parallel plate waveguide (PPW) lens-like antennas.

By simplifying the propagation inside the transversal section, a bifocal constrained lens model is first defined in Subsection 2.1.1; it provides a relevant starting point to design the proposed beamformer.

A refined model based on ray tracing and with enhanced performance prediction is achieved by accounting for the wave propagation inside the transversal cavity. This is proposed in Subsection 2.1.2.

The radiation characteristics, computed and detailed in Section 2.2, are compared to full-wave simulation results. A performance analysis of the proposed tool is performed in Section 2.3. Finally, conclusions are drawn in Section 2.4. Unless otherwise stated, upper-case letters are used for physical dimensions while lower-case letters correspond to normalized dimensions. Also, most angles are oriented angles, counted positively when rotating anticlockwise with reference to $\overrightarrow{X}$-axis, unless otherwise specified.

2.1 Analytical model

2.1.1 Bifocal constrained lens model

Constrained lenses have gained interest over the years because they rely on very simple analytical formulas, providing a quick starting point for their design and optimization. For this reason, it was decided to first approximate the proposed continuous delay-lens with a simplified discrete lens model based on a constrained lens approach. The use of the transversal ridge, defined with ideal transmission lines of length W as shown in Fig. 2.1, constrains the shape of the inner (Σ_1) and outer (Σ_2) contours of the lens. This is the main difference when compared to a classical Rotman lens design [27] where these contours are considered as independent. Here we assume that the ridge is electrically thin, consequently the inner and outer lens contours are, in a first approximation, considered as collocated. Therefore the corresponding points P and Q on both sides of a given transmission line (Fig. 2.1) are collocated.

Using these approximations, the degrees of freedom are reduced compared to Rotman lenses [27]. The latter provides three degrees of freedom which are the relative positions of points P and Q along both the $\overrightarrow{X}$ and $\overrightarrow{Y}$ axes and the transmission line lengths W connecting them, thus leading to three perfect focal points. Due to the approximations defined above, one degree of freedom is lost, the relative position between points P and Q along $\overrightarrow{Y}$-axis. The bifocal constrained lens model first introduced in [57] is further detailed below.

The inner and outer lens contours, Σ_1 and Σ_2, are defined by the cartesian coordinates (X, Y) of points P and Q. θ_1 defines the angular position of any point source F on the focal curve as shown in Fig. 2.1, while θ_2 defines the pointing direction of the resulting beam. Here we assume $\theta_2 = \theta_1$. Using path

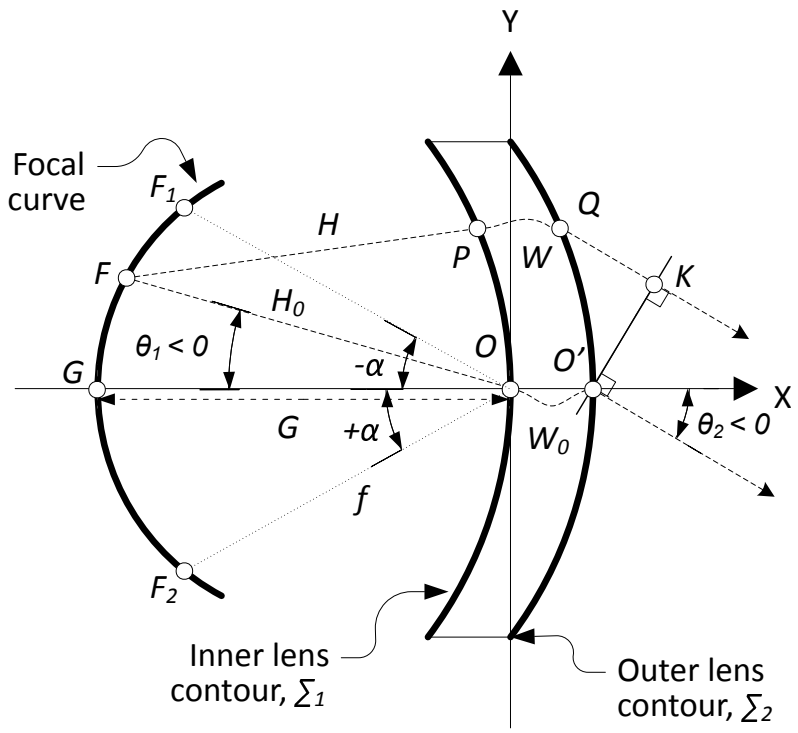

Figure 2.1: Two-dimensional bifocal constrained lens model [57]. For readability, Σ_1 and Σ_2 are distinct in this schematic representation but are effectively collocated in this simplified model.

length equality between a central path F_1OO' passing through the origin O and a general path F_1PQK coming from F_1 and by applying the same path length constraint for F_2, we obtain

$$F_1P + W + S = f + W_0, \tag{2.1}$$

and

$$F_2P + W + S = f + W_0, \tag{2.2}$$

where,

$$S = QK = -sin(atan(X/Y) + \theta_1)\sqrt{X^2 + Y^2}sign(Y). \tag{2.3}$$

In addition, by considering the geometry represented in Fig. 2.1, we can write

$$F_1P^2 = f^2 + X^2 + Y^2 + 2fXcos(\alpha) - 2fYsin(\alpha), \tag{2.4}$$

and

$$F_2P^2 = f^2 + X^2 + Y^2 + 2fXcos(\alpha) + 2fYsin(\alpha), \tag{2.5}$$

with $\theta_1 = -\alpha$ for F_1 and $\theta_1 = \alpha$ for F_2. Using the same notations as Rotman in his seminal paper [27], we introduce here a set of parameters normalized by the off-axis focal distance f,

$$x = X/f,\ y = Y/f,\ w = \tfrac{W-W_0}{f},\ h_0 = H_0/f,\ s = S/f$$

and,

$$a_0 = cos(\alpha),\ b_0 = sin(\alpha).$$

Using these notations, Eqns. (2.4) and (2.5) become

$$\frac{F_1P^2}{f^2} = 1 + x^2 + y^2 + 2xa_0 - 2yb_0, \tag{2.6}$$

$$\frac{F_2P^2}{f^2} = 1 + x^2 + y^2 + 2xa_0 + 2yb_0. \tag{2.7}$$

By combining (2.6) and (2.7) with the normalized forms of (2.1) and (2.3), we obtain

$$1 + x^2 + y^2 + 2xa_0 - 2yb_0 = (1 - w + xa_0 - yb_0)^2, \tag{2.8}$$

and

$$1 + x^2 + y^2 + 2xa_0 + 2yb_0 = (1 - w + xa_0 + yb_0)^2. \tag{2.9}$$

As both focal points F_1 and F_2 are located symmetrically about $\overrightarrow{X}$-axis, the lens contour defined by (x, y) is also symmetric. Thus, replacing y by $-y$ into (2.8) and comparing the changed and unchanged terms, we obtain one set of two equations

$$-2yb_0 = -2yb_0 + 2wyb_0 - 2yxb_0a_0, \tag{2.10}$$

and

$$1 + x^2 + y^2 + 2xa_0 = 1 - 2w + 2xa_0 + w^2 - 2wxa_0 + b_0^2y^2 + a_0^2x^2. \tag{2.11}$$

From Eqn. (2.10) we have

$$w = a_0x. \tag{2.12}$$

Then, using Eqns. (2.11) and (2.12)

$$x = a_0(\sqrt{1 - y^2} - 1), \tag{2.13}$$

or alternatively

$$(x/a_0 + 1)^2 + y^2 = 1. \tag{2.14}$$

The quadratic form (2.14) defines an ellipse with parameters A and B, considering a major axis oriented along $\overrightarrow{Y}$, as illustrated in Fig. 2.2,

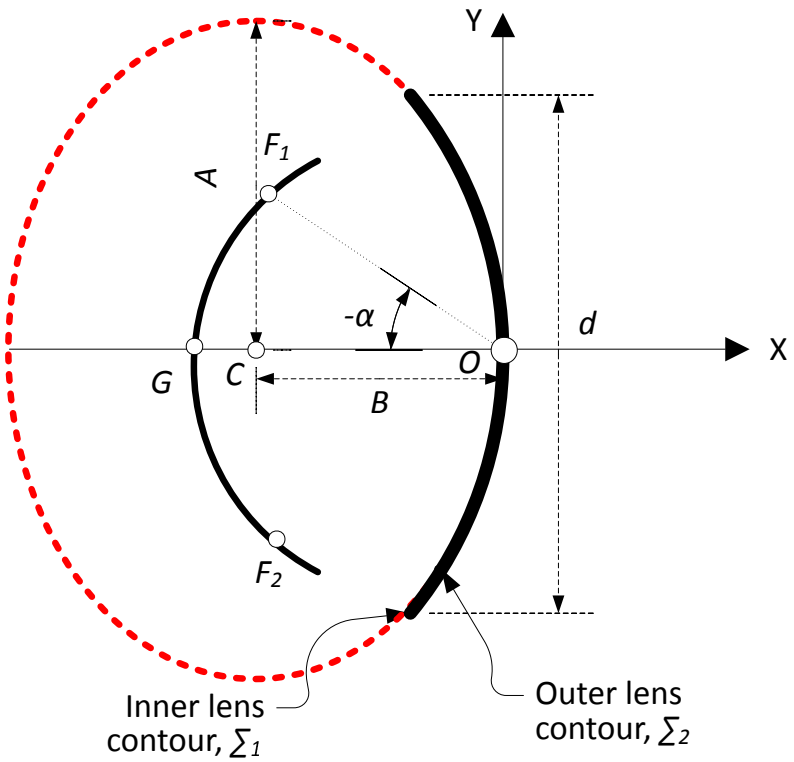

Figure 2.2: Elliptical shape (red dotted line) of the inner Σ_1 and outer Σ_2 lens contours.

$$A = 1,\ B = a_0.$$

Assuming P and Q collocated and the propagation in the cavity to be parallel to $\overrightarrow{Z}$-axis, the ridge height may be defined as a first approximation to be half of w, as shown in Fig. 1.23c. Being proportional to the lens contour, the resulting ridge height is also elliptical. The values are shifted with respect to the transmission line length on the lens edges $w[y = d/2]$, defining finally a positive and normalized by f ridge height h_w (Eqn. (2.15)), using Eqns. (2.12) and (2.13),

$$2h_w = w - w[y = d/2]. \tag{2.15}$$

The maximum normalized aperture of the lens is defined by $d_{max} = D_{max}/f = 2A$. In practice, proper illumination of the lens from any point on the focal curve between F_1 and F_2 will require the normalized lens aperture to be smaller than $2A$ (see Fig. 2.2). As in [27], the parameter $g = GO/f$ (Fig. 2.1) which defines the radius of a circular focal curve is used to minimize aberrations for the on-axis beam and for any beam radiated between $[-\alpha, \alpha]$. Therefore the focal curve is selected as a portion of a circle of radius R which passes through both focal points (F_1 and F_2) and point G on the center axis.

This two-dimensional bifocal constrained lens model, defined by simple analytical formulas is a relevant starting point to design easily the proposed continuous PPW lens. Starting from this model, a more precise evaluation of the beamformer performance requires a better characterization of the wave propagation inside the transversal cavity (Fig. 1.23), more representative of the continuous nature of the PPW ridge. To this end, a ray tracing ridge model is added to the bifocal constrained lens model. This specific part of the model is detailed in the following section.

2.1.2 Ray tracing model inside the transversal cavity

The proposed continuous lens model is represented in Fig. 2.3. Let us consider a ray k coming from F, tilted by an angle γ_k and impinging on the inner lens contour at P_k. Plane T_k is defined as the vertical plane tangent to the inner lens contour Σ_1 and passing through P_k. The corresponding local coordinate system is $(P_k, \overrightarrow{X_k}, \overrightarrow{Y_k})$. Axis $\overrightarrow{X_k}$ is orthogonal to T_k and is used to characterize the upward propagation of ray k in the transversal section. According to reflection law, the incident propagation angle ζ_k (Fig. 2.3) with respect to $\overrightarrow{X_k}$ is equal to the one propagating in the orthogonal plane T_k with respect to $\overrightarrow{Z_k}$ (Fig. 2.4).

A positive coordinate z along $\overrightarrow{Z}$-axis is defined as,

$$z = (-p_1 + \sqrt{(p_1)^2 - 4p_2p_0})/2p_2, \tag{2.16}$$

with,

$$\begin{gathered} p_0 = y_{P_k}^2 - (d/2)^2, \\ p_1 = 2y_{P_k}tan(\zeta_k) + (4/a_0^2)(\sqrt{1-(-d/2)^2}), \\ p_2 = 4/a_0^4 + tan(\zeta_k)^2. \end{gathered}$$

The propagation is then defined in the plane T_k using a change of the principal coordinate system, with (x, y, z) and (x', y', z') respectively the coordinates in $(O, \overrightarrow{X}, \overrightarrow{Y})$ and $(P_k, \overrightarrow{X_k}, \overrightarrow{Y_k})$, as defined in Eqn. (2.17),

$$\begin{cases} x' = (x - x_{P_k})cos(\delta_k) + (y - y_{P_k})sin(\delta_k) \\ y' = -(x - x_{P_k})sin(\delta_k) + (y - y_{P_k})cos(\delta_k) \\ z' = z - z_{P_k}, \end{cases} \tag{2.17}$$

with δ_k the angular coefficient associated to T_k at point P_k and calculated using the derivative of the inner lens contour (Σ_1).

We define the coordinates of R_k in $(P_k, \overrightarrow{X_k}, \overrightarrow{Y_k})$ using Eqn. (2.18),

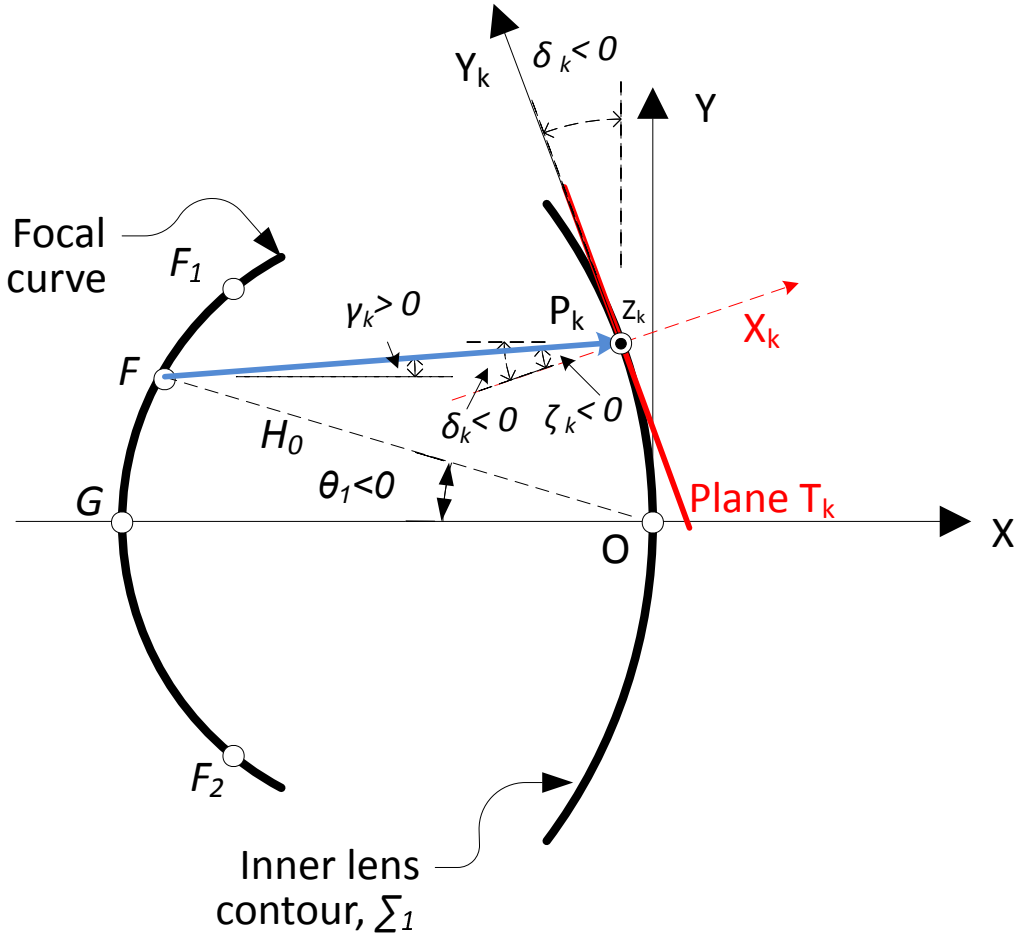

Figure 2.3: Continuous lens model to account for wave propagation inside the transversal cavity.

$$\begin{cases} x'_{R_k} = 0 \\ y'_{R_k} = z tan(\zeta_k) \\ z'_{R_k} = z. \end{cases} \tag{2.18}$$

The complete ray tracing procedure in the transversal cavity is presented in Fig. 2.4. The incoming ray k propagates inside the transversal section as illustrated in Fig. 2.4, by following path $P_k R_k Q_k$, where R_k is the intersection point with the ridge profile h_w. The incident angle of the incoming ray $R_k Q_k$ is labelled $\zeta_k + \epsilon_k$ with respect to the normal of the ridge profile $\overrightarrow{Z'_k}$ at R_k. ϵ_k is the angle between the local vector normal to the ridge profile $\overrightarrow{Z'_k}$ and $\overrightarrow{Z_k}$, derived from Eqn. (2.15),

$$\epsilon_k = atan(-\frac{1}{2} a_0^2 y_{R_k} / \sqrt{1 - y_{R_k}^2}). \tag{2.19}$$

The position of the outer lens point Q_k in $(P_k, \overrightarrow{X_k}, \overrightarrow{Y_k})$ is defined using the propagation angle $\rho_k = \zeta_k + 2\epsilon_k$ and following Eqn. (2.20),

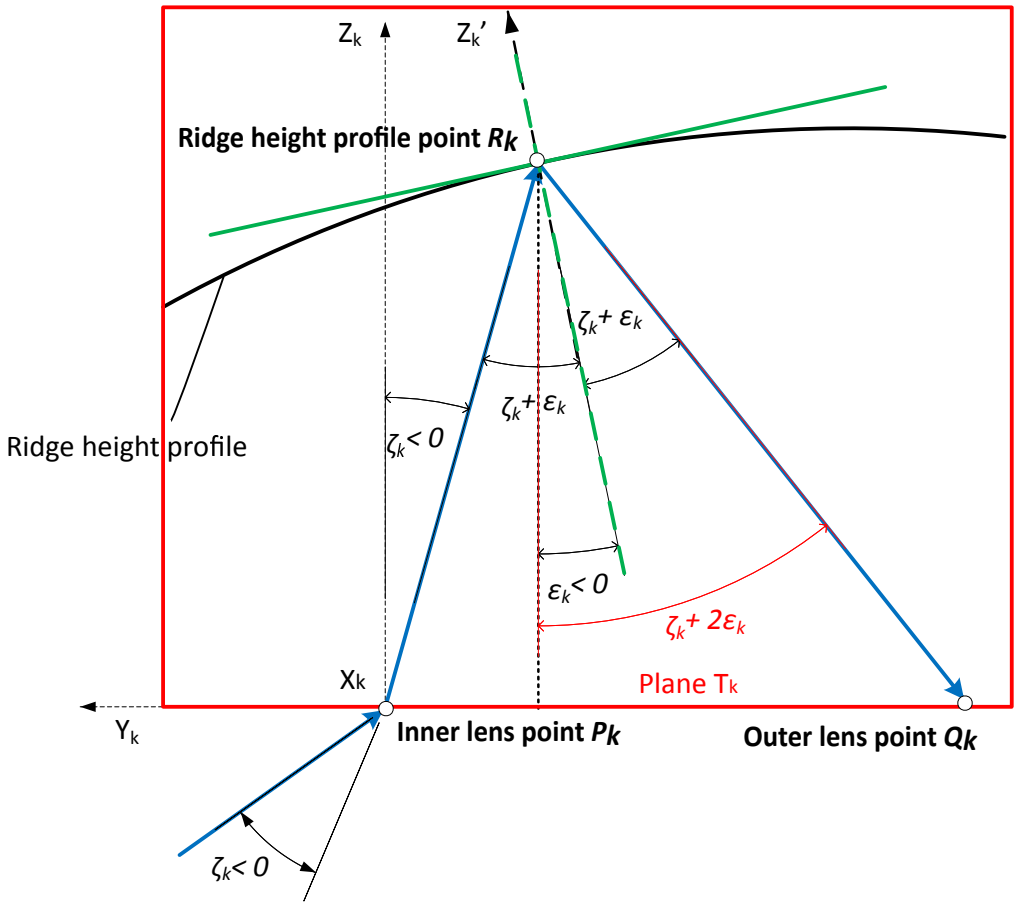

Figure 2.4: Ray tracing inside the transversal cavity.

$$\begin{cases} x'_{Q_k} = x'_{R_k} \\ y'_{Q_k} = y'_{R_k} + z'_{R_k} tan(\rho_k) \\ z'_{Q_k} = 0. \end{cases} \tag{2.20}$$

The final coordinates of Q_k in $(O, \overrightarrow{X}, \overrightarrow{Y})$ are calculated using Eqn. (2.21),

$$\begin{cases} x_{Q_k} = x'_{Q_k} cos(\delta_k) - y'_{Q_k} sin(\delta_k) + x_{P_k} \\ y_{Q_k} = x'_{Q_k} sin(\delta_k) + y'_{Q_k} cos(\delta_k) + y_{P_k} \\ z_{Q_k} = z'_{Q_k} = 0. \end{cases} \tag{2.21}$$

The position Q_k is first calculated on the plane T_k and then projected along $\overrightarrow{X}$-axis on the outer lens contour Σ_2. This approximation is valid for lens designs having contours and height profiles with sufficiently large radius of curvature when compared to the wavelength. Further details are given in Annex A, where for generality purposes, the propagation along the thickness of the ridge is also considered, using different inner (Σ_1) and outer (Σ_2) lens profiles. In this first approach, both shapes of inner and outer lens profiles are identical and the thickness

considered is low with respect to the wavelength, without noticeable impact on the RF performances analyzed here.

Several pairs of connected inner and outer lens contour points P_k and Q_k are plotted in Fig. 2.5 by considering two configurations: in the first case (Fig. 2.5a), wave propagation inside the transversal section is assumed parallel to $\overrightarrow{Z}$-axis, which corresponds to the bifocal constrained lens model approximation, where P_k and Q_k are collocated; the second case (Fig. 2.5b) corresponds to the ray tracing model inside the transversal cavity as defined in this section. This continuous model shows that the inner and outer lens points are closer for positive y values and quite distant for the negative ones. This leads to an asymmetric increase of the path length in the transversal cavity resulting in phase errors which deviate from the bifocal behavior of the simplified constrained lens model (Section 2.1.1).

In the next section, the constrained (Subsection 2.1.1) and continuous (Subsection 2.1.2) lens models are compared in terms of phase aberrations to equivalent GO models of alternative beamformer designs in order to confirm the scanning capabilities of the proposed concept.

2.1.3 Comparative analysis of phase aberrations

We analyze here the phase aberrations of the proposed PPW beamformer to characterize its scanning properties. These aberrations are defined as the difference in electrical path lengths between a central path passing through the origin and any other ray. The different electrical paths under consideration are coming from a source point on the focal curve which is defined by an angle θ_1 and a normalized distance $h_0 = H_0/f$ as shown in Fig. 2.1.

By referring to Fig. 2.1, the path length error Δ_l is thus given by

$$\Delta_l = \sqrt{(x + h_0 cos(\theta_1))^2 + (y + h_0 sin(\theta_1))^2} - h_0 + w + s, \tag{2.22}$$

with,

$$s = -sin(atan(x/y) + \theta_1)\sqrt{x^2 + y^2} sign(y).$$

Variation of the root mean square (RMS) values of Δ_l over the lens aperture have been computed for various values of the pointing angle θ_2 (or for different angular positions θ_1 of the point source F, but as defined previously $\theta_2 = \theta_1$) and different values of g in Fig. 2.6 and are compared to the performances of two other

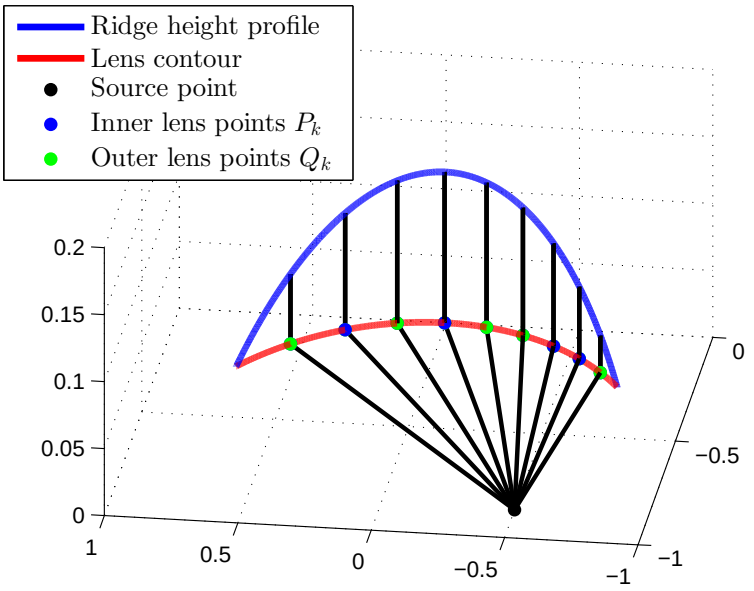

(a) Constrained lens model (Subsection 2.1.1)

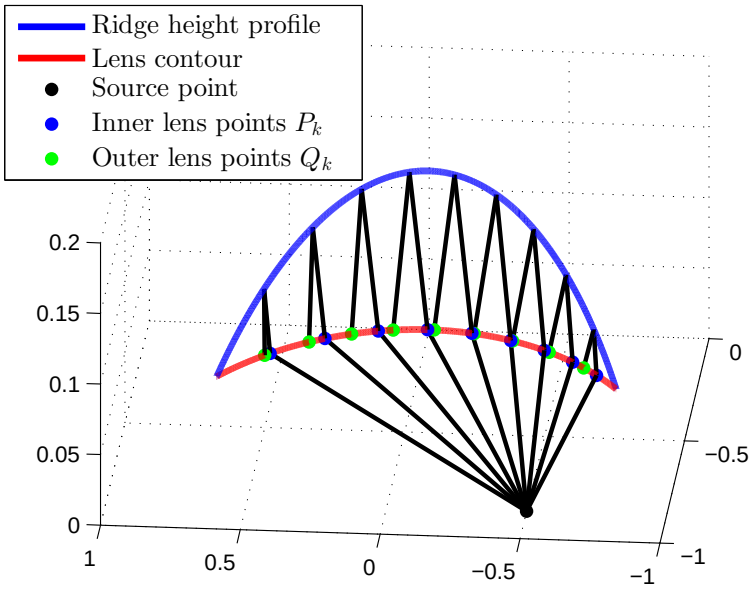

(b) Continuous lens model (Subsection 2.1.2)

Figure 2.5: Positions of the inner and outer lens points P_k and Q_k computed with the ray tracing model. Here with $\theta_1 = \alpha$ and $g = 1.25$. The lens parameters are $D = 10\lambda$, $\frac{f}{D} = 0.7$ and $\alpha = 30°$. Axis values are normalized to the focal distance f.

PPW beamformers, namely a Rotman lens [27] and a pillbox antenna [19]. The pillbox antenna is characterized by its parabolic reflector,

$$x = -y^2/4g, \tag{2.23}$$

whereas the Rotman lens contour is computed following the resolution presented

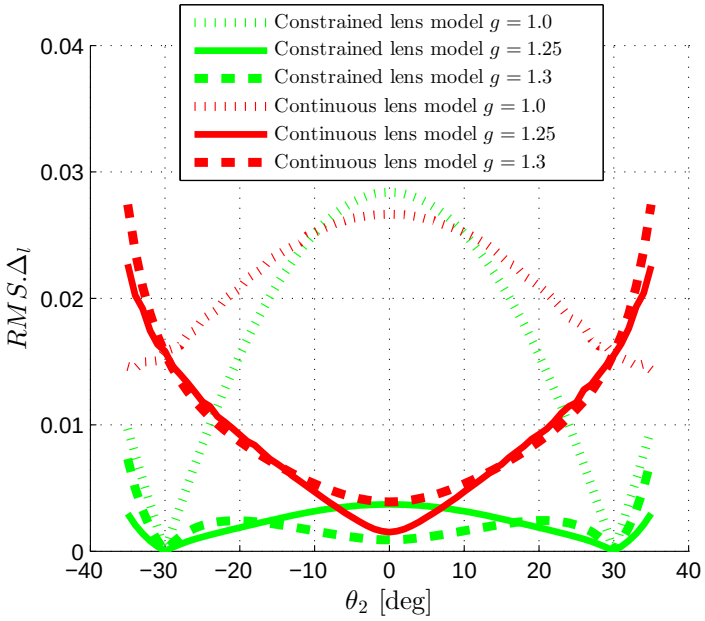

Figure 2.6: RMS value of the normalized path length error versus pointing angle θ_2 for the proposed lens models with $g = 1, 1.25$.

in [27] with $\eta = y$.

The three beamformers are built assuming $f = 0.7D$. $\alpha = 30°$ for our proposed beamformer models and the Rotman lens. As shown in Fig. 2.1, a circular focal curve is used in all cases as an additional parameter to further reduce the phase aberrations. As expected, the results given in Fig. 2.6 clearly demonstrate the bifocal behavior of the constrained lens model (Subsection 2.1.1) with no phase aberrations for $\theta_2 = \pm\alpha$. In addition, we can notice that the aberration levels depend on the value of g; in particular there is no value of g leading to a perfect on-axis focal point, but aberrations can be minimized by selecting a suitable value of g (e.g. $g = 1.3$ in Fig. 2.6) . The proposed continuous model (Subsection 2.1.2), shows an increase of the path length errors with θ_2; the bifocal behavior is lost, as expected from the conclusions given in Subsection 2.1.2. From the comparisons given in Fig. 2.7, the continuous model with $g = 1.25$ exhibits results very similar to a parabolic pillbox antenna. It is then anticipated that with a proper adjustment of the ridge profile and height, the bifocal behavior could be retrieved to some extent and the actual performance of an optimized continuous PPW lens beamformer should be between the performance of the two lens models discussed here. The objective of this chapter is to validate the numerical method developed for the concept, consequently optimized configurations and optimization processes using the models provided will be considered later.

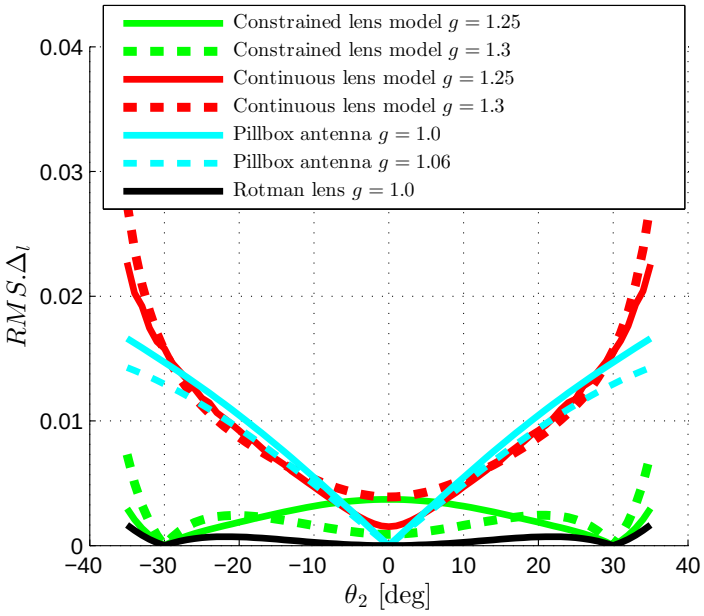

Figure 2.7: RMS value of the normalized path length error versus pointing angle θ_2 for different beamformer types and both models of the proposed PPW lens.

To better evaluate the impact of the path length errors on the antenna radiation pattern, we propose in the next section a GO model to compute the radiation patterns of the proposed lens and compare it to full-wave simulations.

2.2 Performance in radiation

2.2.1 Amplitude and phase distribution along the outer lens contour

To compute the far field radiated by the PPW lens, the continuous outer lens contour Σ_2 is represented by a finite summation of sources $Q_k(k = 1, ...n)$ [58] with phase and amplitude distributions governed by the beamformer geometry.

The coordinates of P_k along the inner lens contour are first defined by considering a cylindrical wave front originating from a given point source F on the focal curve. The inner lens contour Σ_1 is sampled regularly with a uniform angular distribution γ as shown in Fig. 2.8. The positions of both extreme points P_1 and P_n, given by $P_1(a_0(\sqrt{1-(-d/2)^2}-1), -d/2)$ and $P_n(a_0(\sqrt{1-(+d/2)^2}-1), +d/2)$ in $(O, \overrightarrow{X}, \overrightarrow{Y})$ coordinate system are used to calculate the angular values,

$$\gamma_1 = atan((y_{P_1} + b)/(x_{P_1} + a)), \tag{2.24}$$

and

$$\gamma_n = atan((y_{P_n} + b)/(x_{P_n} + a)), \tag{2.25}$$

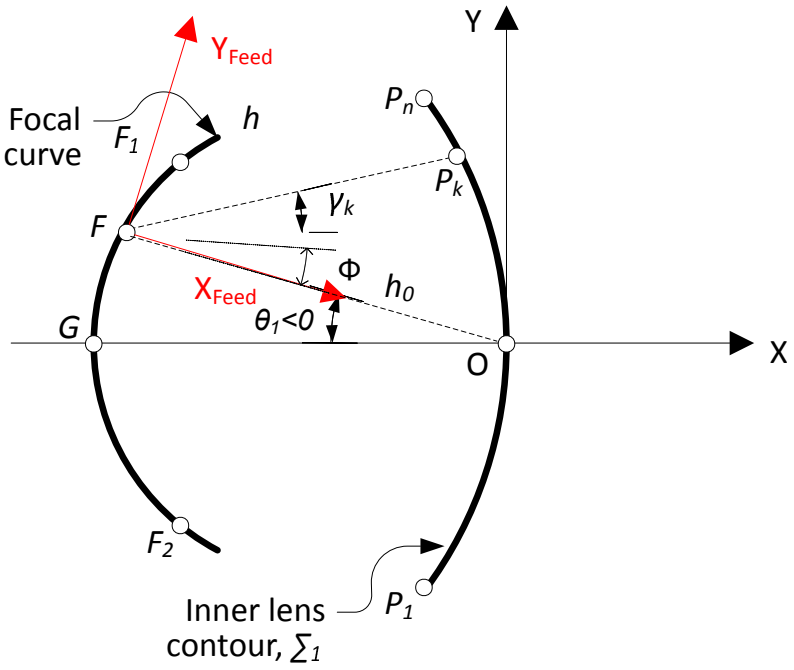

Figure 2.8: Discretization of the inner lens contour Σ_1.

where, $a = h_0 cos(\theta_1)$, $b = h_0 sin(\theta_1)$ (Fig. 2.1). Thus, for $1 \leq k \leq n$, γ_k is defined as follows,

$$\gamma_k = \gamma_1 + \frac{k-1}{n-1}(\gamma_n - \gamma_1). \tag{2.26}$$

The coordinates of P_k, defined in $(O, \overrightarrow{X}, \overrightarrow{Y})$ are the following

$$x_{P_k} = (-p_2 + \sqrt{(p_1)^2 - 4p_2p_0})/2p_2, \tag{2.27}$$

with

$$\begin{aligned} p_0 &= a^2 tan(\gamma_k)^2 - 2abtan(\gamma_k) + b^2, \\ p_1 &= 2/a_0 + 2atan(\gamma_k)^2 - 2btan(\gamma_k), \\ p_2 &= 1/a_0^2 + tan(\gamma_k)^2, \end{aligned}$$

and

$$y_{P_k} = \sqrt{-(x_{P_k}/a_0 + 1)^2 + 1)} sign(\gamma_k - \theta_1). \tag{2.28}$$

The coordinate x_{P_k} can be easily computed as the intersection between FP_k defined by γ_k and the elliptical inner contour of the lens. y_{P_k} is then defined using the quadratic form (2.14). The positions of the outer lens points Q_k are defined using either the constrained lens model (Subsection 2.1.1) or the continuous lens model (Subsection 2.1.2).

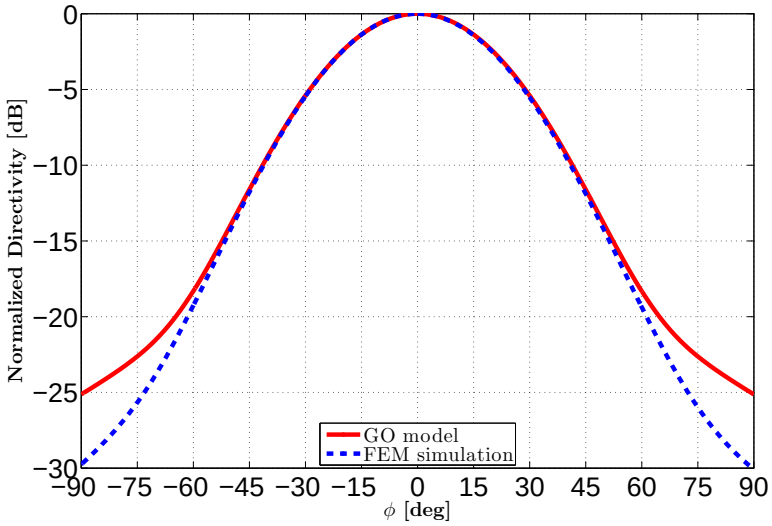

Figure 2.9: Normalized amplitude A of the cylindrical wave. ϕ is defined from $\overrightarrow{X_{Feed}}$ positive semi-axis.

To define the amplitude distribution on the outer lens contour Σ_2, we first assume that the beamformer is excited by a H-plane sectoral horn aperture whose width equals 1.5λ, where λ is the wavelength in vacuum at the operating frequency. The GO model is derived from [59] and successfully validated by comparison with FEM results in Fig. 2.9. Note that any other radiating aperture could be used without loss of generality. The primary feed orientation is defined using (F, $\overrightarrow{X_{Feed}}$, $\overrightarrow{Y_{Feed}}$), as shown in Fig. 2.8 . Here, the feed orientation is specified in order to point towards the center of the inner lens contour O, ensuring a suitable illumination of the lens and providing adequate edge taper.

As shown in Subsection 2.1.2, the outer point lens distribution Q_k differs from the inner point lens distribution P_k and thus has an impact on the near field distribution computed on Σ_2. The unknown amplitude distribution at points Q_k is computed by imposing power conservation in elementary ray tubes (RT), as described in [60]. In particular, when the RT cross-section decreases, the power density inside this RT increases, and vice-versa. The procedure implemented here is illustrated in Fig. 2.10. The infinitesimal elements dL_k, are equal to the distance between rays $k-1$ and $k+1$. With these notations, the amplitude associated to a given ray tube k is given by

$$A'_k = A_k \sqrt{dL_k / dL'_k}, \tag{2.29}$$

where dL_k and dL'_k, and A_k and A'_k are the RT widths and RT amplitudes for wave fronts WF and WF', respectively. In Eqn. (2.29), A_k is imposed by the primary feed illumination (Fig. 2.9).

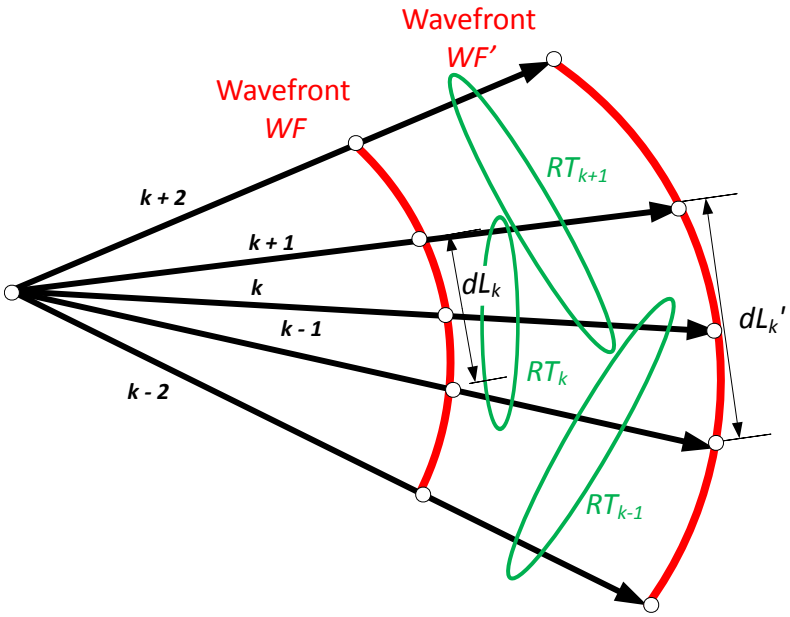

Figure 2.10: A ray tube between 2D wavefronts described by a ray tracing.

In addition, as dL_k is constant due to the regular distribution γ, we have

$$A'_k \propto A_k/\sqrt{dL'_k}, \tag{2.30}$$

with,

$$dL'_k = f\sqrt{(x_{Q_{k+1}} - x_{Q_{k-1}})^2 + (y_{Q_{k+1}} - y_{Q_{k-1}})^2}, \tag{2.31}$$

Finally, the phase distribution is easily derived using the path length $path_k = FP_kQ_k$

$$phase_k = path_k f k_0, \tag{2.32}$$

where f is the focal distance and k_0 the free space wave number.

2.2.2 Computation of the radiation patterns

The amplitude and phase distribution associated to Q_k have been defined previously (Eqns. (2.30) and (2.32)). With the elliptical shape of the lens contour and the theoretical approach developed in [61], we provide below the theoretical expression of the far field radiated by the continuous PPW lens. The locations of Q_k are defined by their polar coordinates (R_k, β_k), in reference to the center of the elliptical lens profile C, as shown in Fig. 2.11. The far field component is expressed by the summation

$$E \propto \sum_{k=1}^{n} P(\Psi_k) A'_k exp(-jphase_k) exp(jk_0 \Delta_{R_k} f) dL'_k, \tag{2.33}$$

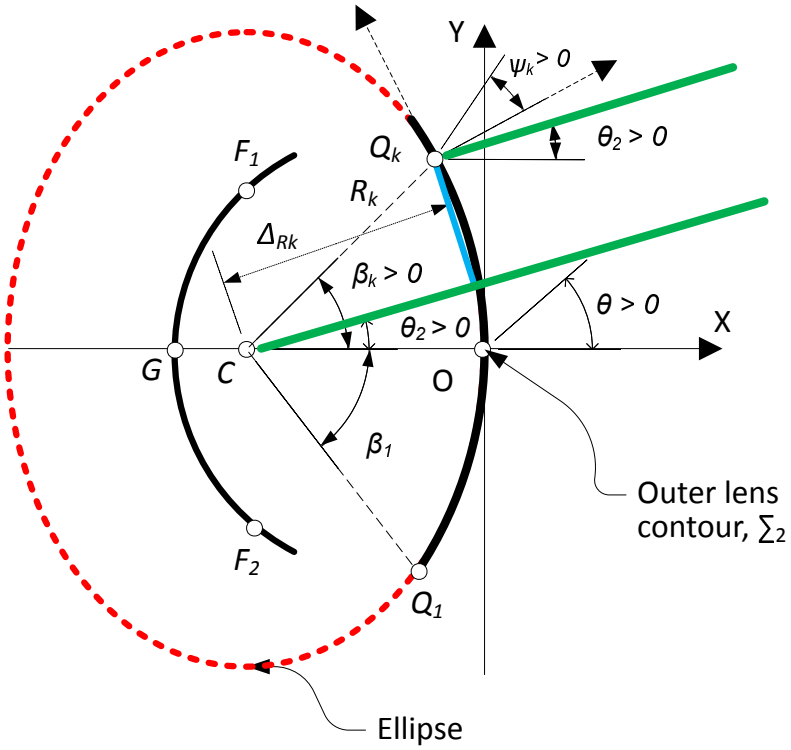

Figure 2.11: Elliptical array of point sources Q_k. The main beam direction is θ_2.

where A'_k, $phase_k$ and dL'_k are given respectively by Eqns. (2.30), (2.32) and (2.31). Δ_{R_k} is the electrical path length delay (normalized to the focal distance f) associated to Q_k for a beam pointing direction θ and is given by

$$\Delta_{R_k} = R_k cos(\theta - \beta_k) = \sqrt{(x_{Q_k} + a_0)^2 + y_{Q_k}^2} cos(\theta - \beta_k). \tag{2.34}$$

In Eqn. (2.33), $P(\Psi_k)$ is the elementary pattern radiated by Q_k with Ψ_k defined as follows

$$\Psi_k = \theta + \delta_k, \tag{2.35}$$

where

$$\delta_k = atan(-a_0 y_{Q_k} / \sqrt{1 - y_{Q_k}^2}).$$

We assume here that this pattern is nearly isotropic for $\Psi_k \in [-90°\ 90°]$ and that there is no backward radiation, as represented in Fig. 2.12.

These theoretical aspects are used to compare our numerical models with full-wave analysis, presented in the next section.

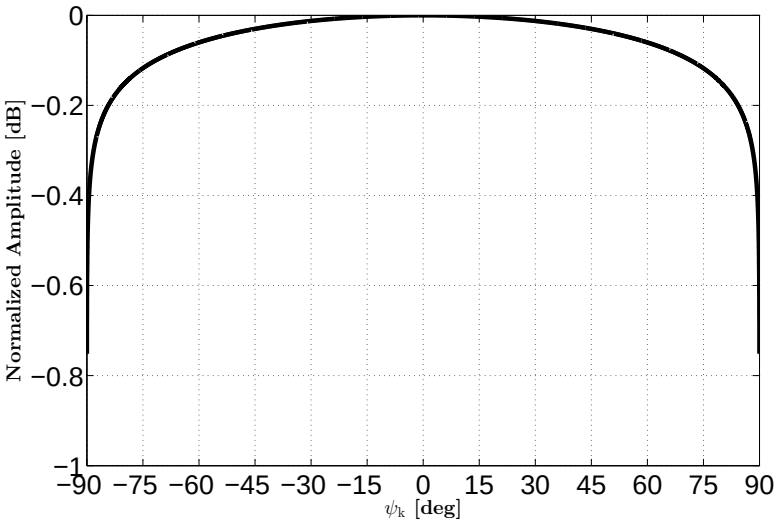

Figure 2.12: Cosine pattern radiated by each point source Q_k $(\cos(\psi_k)^{0.01})$.

Table 2.1: Design parameters of the lens-like PPW beamformer.

D	$\frac{f}{D}$	α [deg]	H_{PPW}
10λ	0.7	30	0.2λ

2.2.3 Numerical results and comparison with full-wave simulations

A specific continuous PPW beamformer, similar to the one described in [56] which demonstrated excellent agreement between measurements and the finite element method (FEM) [62], is selected here to assess the accuracy of the proposed analytical model. Its geometrical parameters are provided in Table 2.1.

For validation purposes, we consider two test configurations with two feed positions defined by $\theta_1 = 18°$ and $30°$. Each feed is identical and is an H-plane sectoral horn (aperture equal to 1.5λ); it radiation pattern is represented in Fig. 2.9. Subscripts GO and FEM are used to refer to the GO models and to the FEM model respectively. Fig. 2.13 represents the patterns observed with the first lens configuration where the feed is located at the focal point ($\theta_1 = \alpha$). The radiation patterns have been computed with the constrained lens model (Subsection 2.1.1), the continuous model (Subsection 2.1.2) and with HFSS [62].

These results confirm the collimating properties of the beamformer when using the elliptical profiles as derived from the simplified bifocal constrained lens model but also highlight some differences between the results computed with HFSS (blue curve in Fig. 2.13) and the constrained lens model (green curve in Fig. 2.13), namely a 2°-pointing error and a much higher side lobe level (SLL) for positive

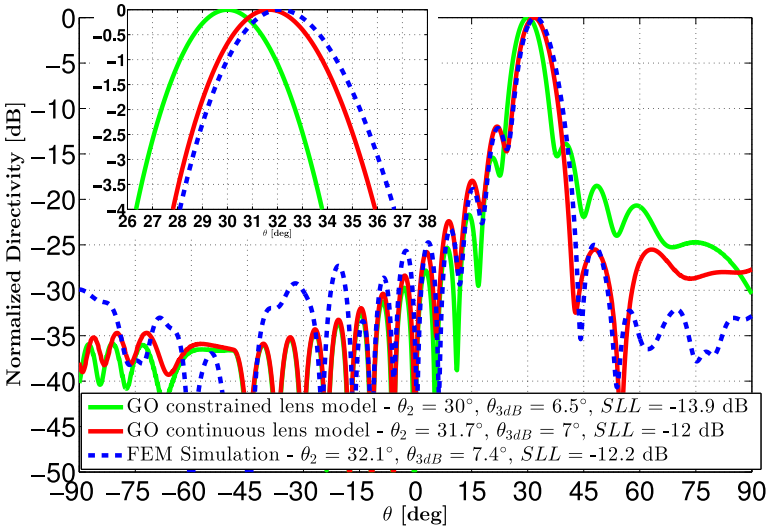

Figure 2.13: Radiation pattern of the PPW beamformer in H-plane for $\theta_1 = \alpha$. θ is the angle defined in Fig. 2.11.

elevation angles; a slight increase (+1°) of the half-power beamwidth HPBW (7°) is also observed with HFSS (7.4°) as compared to the constrained lens model. Fig. 2.13 also confirms the relevance and accuracy of the continuous model (red curve in Fig. 2.13) which is shown to be in excellent agreement with full-wave simulations. In particular, the main beam directions and HPBW computed with the continuous model and HFSS equal 31.7° and 7°, 32.1° and 7.4°, respectively. The first side lobes predicted by GO are also very accurate, down to levels 25 dB below the maximum. Larger discrepancies are observed for lower levels, which are obviously a consequence of the approximations made in the GO model and of the numerical accuracy in the FEM model. Yet, this is considered to be sufficient for the targeted multiple beam applications as interference is mainly driven by the first side lobes anyway and levels 25 to 30 dB below the maximum directivity may be neglected.

To further assess the relevance of the proposed numerical model, we compare in Figs. 2.14 and 2.15 the phase and amplitude distributions computed along the outer lens contour Σ_2. The values obtained with HFSS have been computed on a virtual line coinciding with Σ_2. The phase distribution corresponds to the phase variation between the phase center of the primary feed F and this specific calculation line. The values are based on a reference specified by the phase value at $Y_Q = 0$, defined modulo 360°,

$$\begin{cases} phase_{GO}(Y_Q = 0) \in [-180°180°], \\ phase_{FEM}(Y_Q = 0) \in [-180°180°]. \end{cases} \tag{2.36}$$

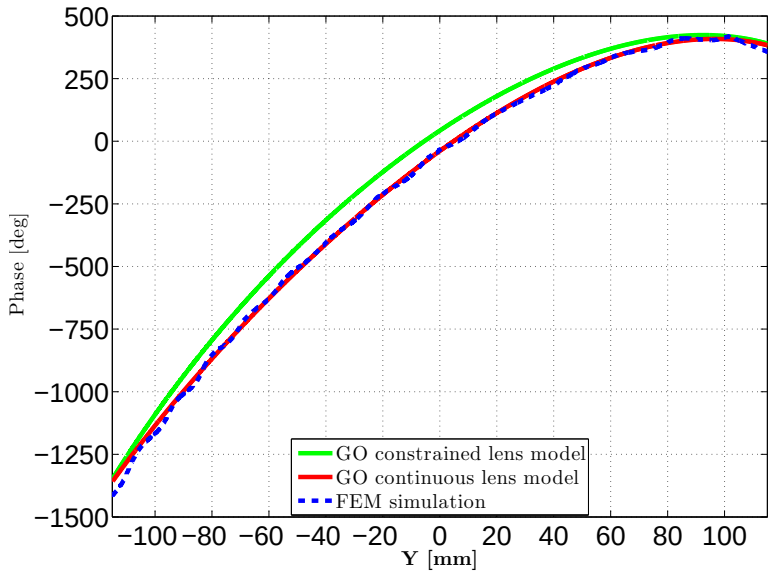

Figure 2.14: Phase distribution on the outer lens contour Σ_2 of the PPW beamformer in H-plane for $\theta_1 = \alpha$. Y defines the outer lens point positions along $\overrightarrow{Y}$-axis. λ defined at a frequency $f_0 = 12.6$ GHz.

The amplitude distribution (Fig. 2.15) is normalized to the total amount of energy contained along Σ_2. The normalized values are defined as follows

$$\begin{cases} NormA_{GO} = 20log(\frac{|A_{GO}/\sum A_{GO}|}{max(|A_{GO}/\sum A_{GO}|)}), \\ NormA_{FEM} = 20log(\frac{|A_{FEM}/\sum A_{FEM}|}{max(|A_{GO}/\sum A_{GO}|)}). \end{cases} \tag{2.37}$$

As anticipated from the far field patterns in Fig. 2.13, the amplitude and phase distributions computed with the continuous lens model are in much better agreement with HFSS than those computed with the constrained lens model. Comparing the two analytical models, phase values appear closer for extreme Y-values and more distant for central ones. This result is in line with the ray tracing representation provided in Fig. 2.5. In the continuous lens model, the propagation in the cavity is mainly driven by the incident angle at the inner lens contour when considering small to medium ridge heights. On the edges and particularly on the positive side of the $\overrightarrow{Y}$-axis for the considered focal point, this incidence angle is almost perpendicular to the inner lens contour resulting in a propagation in the cavity almost parallel to $\overrightarrow{Z}$-axis, which resembles the propagation assumption in the case of the constrained lens model. Hence the strong similarity of the two phase responses in that part of the Y interval. Concerning the amplitude distribution, strong ripples are present in the FEM results (blue curve in Fig. 2.15) which are

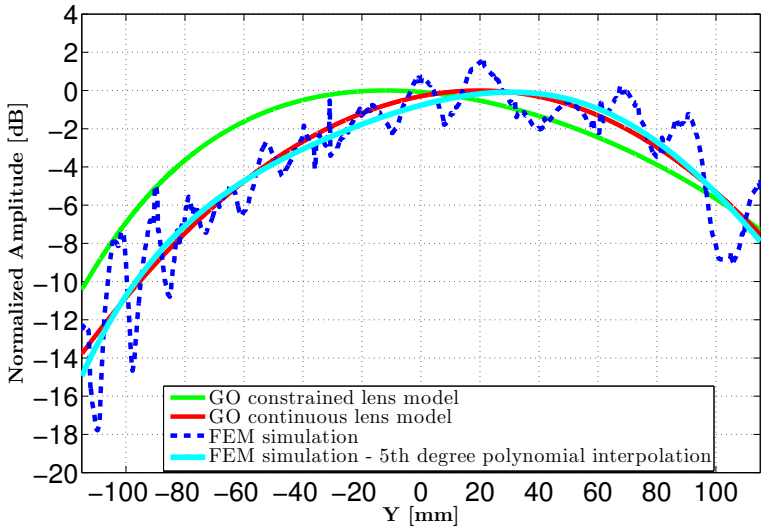

Figure 2.15: Amplitude distribution on the outer lens contour Σ_2 of the PPW beamformer in H-plane for $\theta_1 = \alpha$. Y defines the outer lens point positions along $\overrightarrow{Y}$-axis. λ defined at a frequency $f_0 = 12.6$ GHz.

the consequence of undesired reflections at the different bend transitions between PPW sections. As shown in Fig. 2.15 differences of 1.5 and 2 dB are observed respectively at $Y = 20$ and 70 mm, between the continuous model (red curve) and HFSS (blue curve). The profiles of the transitions are effectively optimized to minimize reflections, but performance varies with the angle of incidence resulting in some interference observed here. This may be slightly improved by designing a more sophisticated transition (e.g. by increasing the number of steps) but at the expense of higher mechanical complexity with significant impact on the hardware cost. In line with this aspect, FEM simulation results have been interpolated (turquoise curve) to approach the amplitude distribution we could expect with such ideal transitions, confirming the good prediction proposed by the GO model (red curve). Similar ripples are present in the phase response but are less visible due to the phase scale. Interestingly, those ripples, both in phase and amplitude, have limited impact on the relevant parts of the radiation patterns.

The numerical results obtained with the second configuration ($\theta_1 = 18°$) are provided in Figs. 2.17 and 2.16, for two values of g (1 and 1.25 respectively). In both cases, similar differences are observed between the constrained model and HFSS in terms of side lobe levels and main beam direction, whereas the continuous model provides very accurate results. When $g = 1.25$, the main beam directions and HPBW computed with the continuous model equal 19.1° and 6°, as compared to 19.3° and 6.1° with HFSS. The first side lobe level is equal to −14.9 dB (continuous

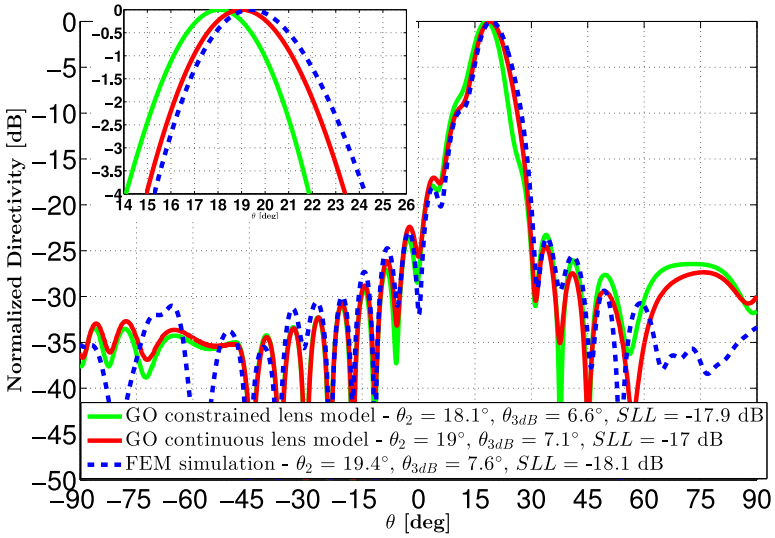

Figure 2.16: Radiation pattern of the PPW beamformer in H-plane for $\theta_1 = 18°$ and $g = 1.0$. θ is the angle defined in Fig. 2.11.

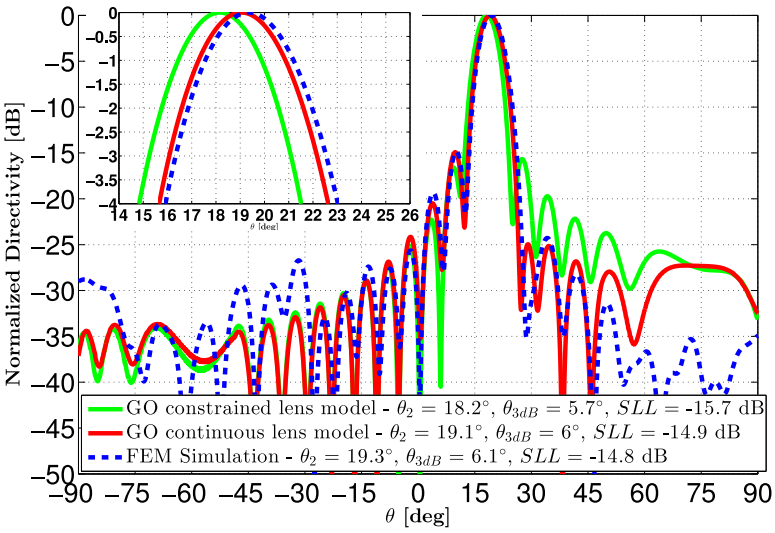

Figure 2.17: Radiation pattern of the PPW beamformer in H-plane for $\theta_1 = 18°$ and $g = 1.25$. θ is the angle defined in Fig. 2.11.

model) and -14.8 dB (FEM simulation). Note also that, even for the case $g = 1$ where the phase aberrations are higher, the shape of the main lobe and the first side lobe level are still defined accurately by the continuous model ($\theta_2 = 19°$, $\theta_{3dB} = 7.1°$, $SLL = -17$ dB) when compared to the FEM simulation ($\theta_2 = 19.4°$, $\theta_{3dB} = 7.6°$, $SLL = -18.1$ dB). The pattern degradations are less pronounced for smaller values of θ_1 because more centered feeds naturally lead to less asymmetries in amplitude and phase distributions.

Finally, it is important to mention that the proposed continuous lens model requires very low computational effort. The beamformer described here needs analysis times of about 2 seconds while the full-wave model requires about 4 minutes per frequency point using a workstation Intel Xeon 2.67 GHz, 64 Gb RAM.

2.3 Domain of validity of the GO design tool

The domain of validity of the proposed GO tool is investigated considering several parameters, used to design and optimize several continuous PPW lens-like beamformers with various RF characteristics.

This study is mainly dependent of the f/D value and the curvature of both elliptical inner lens (Σ_1) and ridge height (h_w) profiles. Using the bifocal lens model (Subsection 2.1.1) as a starting point, both equations were linked by a coefficient $a_0 = cos(\alpha)$, α defining the angular position of the focal points. Here, a more general approach is considered with two independent lens and ridge height profiles.

Following this idea, they are respectively defined using Eqns. 2.38 and 2.39 by

$$x = a_{in}(\sqrt{1-y^2} - 1), \tag{2.38}$$

and,

$$h_w = a_w(\sqrt{1-y^2} - \sqrt{1-(d/2)^2}), \tag{2.39}$$

where $d = D/f$, a_{in} and a_w are the elliptical coefficients of both elliptical profiles.

The angular position θ_1 is used to define the limits of acceptable angular positions of the feeds relatively to the inner lens contour (Σ_1). Each feed is identical and is an H-plane sectoral horn (aperture equal to 1.5λ), pointing towards the center of the inner lens contour ensuring a suitable illumination of the lens, as proposed in the previous sections. The lens diameter is maintained at $D = 10\lambda$ as well as the distance $h_0 = 1$. The values of θ_1 are limited by the f/D considering the limits defined by the diameter D following Eqn. (2.40),

$$\theta_1 < \arcsin(\frac{D}{2f}). \tag{2.40}$$

To define objectives and coherent comparisons between the different configurations leading to different pointing angles θ_2, HPBW θ_{3dB} and side lobe level SLL, two criterions have been chosen. The pointing angle error Δ_{θ_2} is limited to 10% of the 3 dB beamwidth θ_{3dB} considering a pointing angle precision as more important as this parameter decreases. The second one is the side lobe level

Table 2.2: Validity Domain of the proposed tool using $f/D = 0.51$

a_w \ a_{in}	< 0.7	< 0.5	< 0.3	< 0.1
< 0.3	$\theta_1 < 40°$	$\theta_1 < 40°$	$\theta_1 < 50°$	$\theta_1 < 50°$
< 0.2	$\theta_1 < 50°$	$\theta_1 < 50°$	$\theta_1 < 60°$	$\theta_1 < 60°$

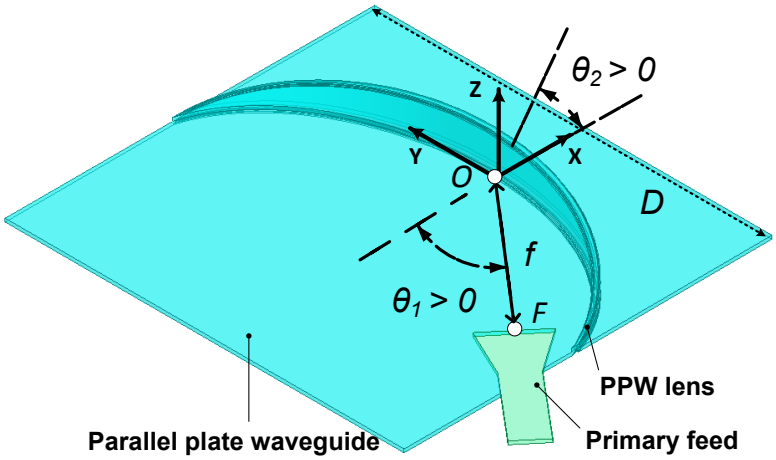

Figure 2.18: Continuous PPW lens-like beamformer defined by $f/D = 0.51$ with $a_{in} = 0.7$ and $a_w = 0.3$, for $\theta_1 = 40°$ and $h_0 = 1$.

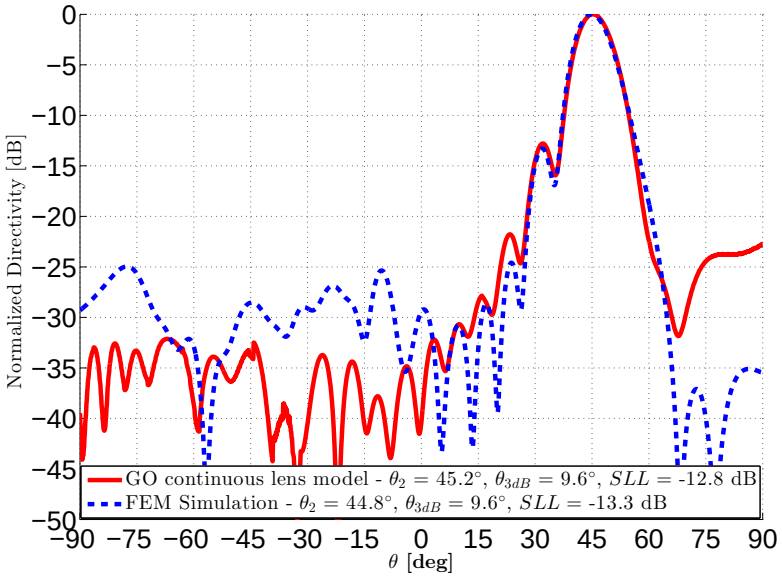

Figure 2.19: Radiation pattern of the PPW beamformer in H-plane using $f/D = 0.51$ with $a_{in} = 0.7$ and $a_w = 0.3$, for $\theta_1 = 40°$ and $h_0 = 1$. θ is the angle defined in Fig. 2.11.

difference Δ_{SLL} between the GO tool and the FEM simulation, evaluated on the first side lobes only and limited to 1.5 dB.

The performance of the tool is first proposed in Table. 2.2, considering the

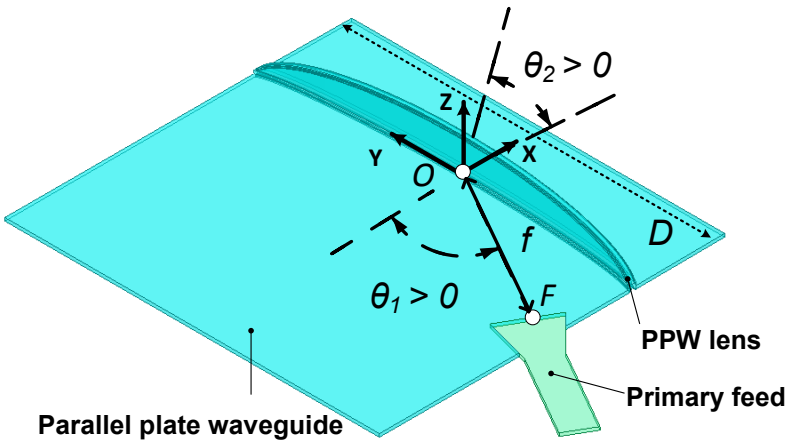

Figure 2.20: Continuous PPW lens-like beamformer defined by $f/D = 0.51$ with $a_{in} = 0.1$ and $a_w = 0.2$, for $\theta_1 = 60°$ and $h_0 = 1$.

Table 2.3: Performance of the proposed tool using $f/D = 0.7$

a_w \ a_{in}	< 0.9	< 0.7	< 0.5	< 0.3
< 0.7	$\theta_1 < 20°$	$\theta_1 < 30°$	$\theta_1 < 30°$	$\theta_1 < 40°$
< 0.5	$\theta_1 < 40°$	$\theta_1 < 40°$	$\theta_1 < 40°$	$\theta_1 < 40°$

worst case $f/D = 0.51$. A first configuration has been proposed in Fig. 2.18, demonstrating an important curvature of the inner lens contour (Σ_1). A large angular position of the feed is defined with $\theta_1 = 40°$. The H-plane radiation pattern radiated by the PPW beamformer is provided in Fig. 2.19, showing the prediction given by the numerical tool. Even in this critical configuration, a good comparison is observed. The main beam directions, HPBW and first side lobe level equal 45.2°, 9.6° and −12.8 dB with the continuous model and 44.8°, 9.6° and −13.3 dB considering the FEM simulation. Larger differences are observed at levels 25 dB below the maximum peak directivity, but with less impact for the applications considered in this thesis.

A second configuration is presented in Fig. 2.20 with a very low curvature of the inner lens contour (Σ_1) but increasing the angular feed position ($\theta_1 = 60°$). In this case, the prediction proposed is still in good agreement, especially for the side lobes predicted in the far out region ($\theta < -15°$).

The same study is conducted for $f/D = 0.7$ and the results are summarized in Table. 2.3. In this configuration, the curvature associated to the profiles are less pronounced, resulting in a lower impact on the ray tracing approach and consequently on a larger validity region of the parameters, as compared to the configuration where $f/D = 0.51$.

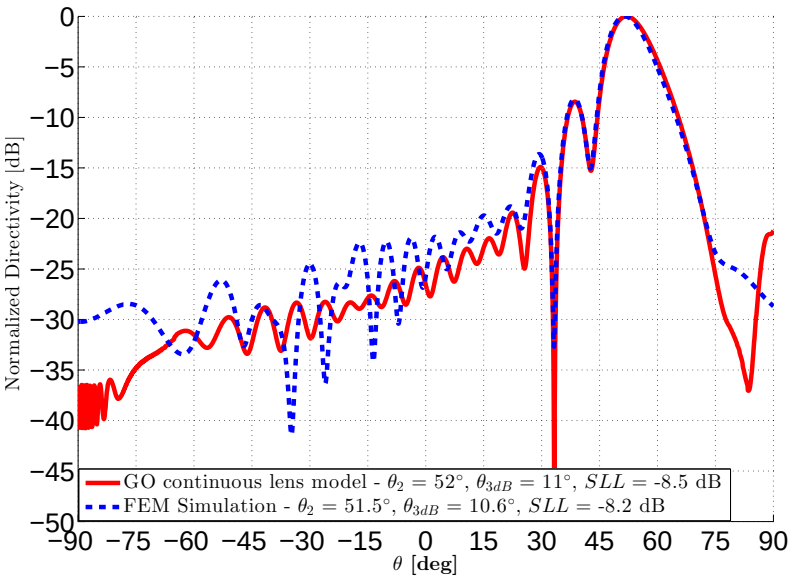

Figure 2.21: Radiation pattern of the PPW beamformer in H-plane using $f/D = 0.51$ with $a_{in} = 0.1$ and $a_w = 0.2$, for $\theta_1 = 60°$ and $h_0 = 1$. θ is the angle defined in Fig. 2.11.

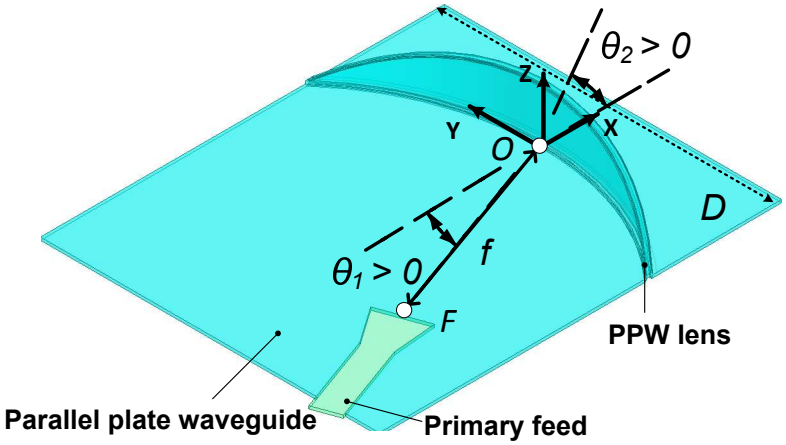

Figure 2.22: Continuous PPW lens-like beamformer defined by $f/D = 0.7$ with $a_{in} = 0.9$ and $a_w = 0.7$, for $\theta_1 = 40°$ and $h_0 = 1$.

An example of a PPW beamformer is proposed in Fig. 2.22, associated to the H-plane radiation pattern computed and shown in Fig. 2.23. This example demonstrates the capability of the tool to predict the behavior of configurations where a large HPBW region is obtained ($\theta_{3dB} = 31.8°$), corresponding to high phase aberration levels along the radiating aperture. In the same configuration but considering a feed at an angular position $\theta_1 = 30°$, we demonstrate the limits of the considered approximations, as shown in Fig. 2.24. This example demonstrates that some improvements are needed when the inner lens profile curvature or the ridge height increase significantly while moving the feed position to target large

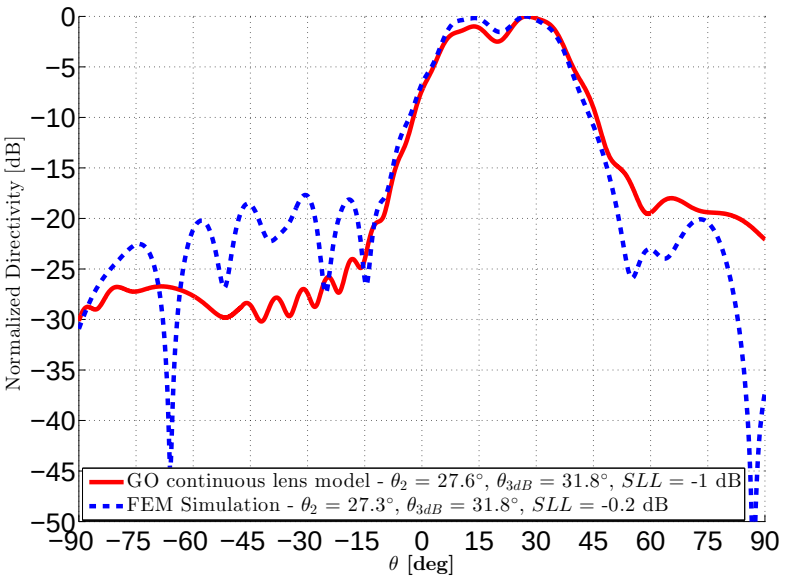

Figure 2.23: Radiation pattern of the PPW beamformer in H-plane using $f/D = 0.7$ with $a_{in} = 0.9$ and $a_w = 0.7$, for $\theta_1 = 20°$ and $h_0 = 1$. θ is the angle defined in Fig. 2.11.

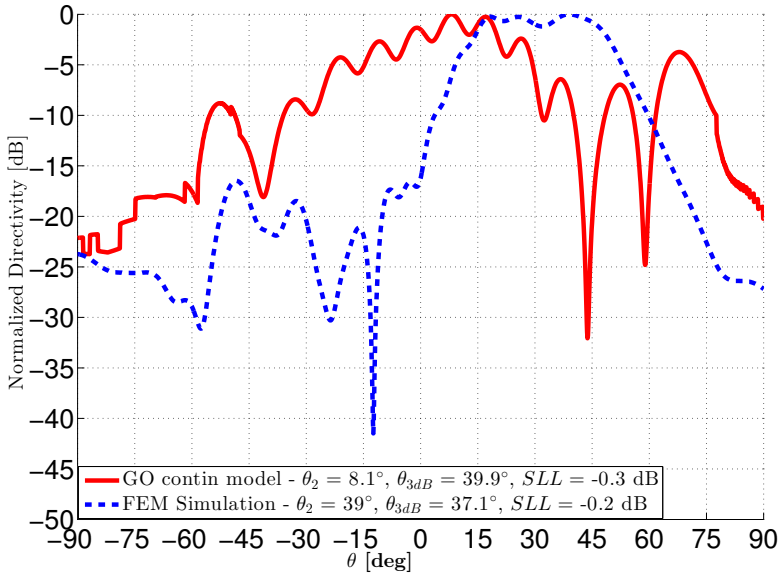

Figure 2.24: Radiation pattern of the PPW beamformer in H-plane using $f/D = 0.7$ with $a_{in} = 0.9$ and $a_w = 0.7$, for $\theta_1 = 30°$ and $h_0 = 1$. θ is the angle defined in Fig. 2.11.

scanning performances.

This investigation could be easily extended to larger f/D ratio since no real limitations exist due to lower curvature of the considered elliptical profiles.

This study is obviously not exhaustive, as a large number of parameters have to be taken into account to define a complete and precise validity domain. However,

we demonstrate here the good prediction given by the tool in various configurations, showing the possibility to combine it with optimization processes.

2.4 Conclusion

In this chapter, an accurate analytical model for the proposed continuous PPW lens-like beamformer has been defined using geometrical optics. It provides better insight for the analysis and understanding of phase aberrations. We have first shown that a bifocal constrained lens (which assumes that the inner and outer lens contours are collocated) leads to an acceptable but still approximate prediction of the lens radiation performance. This model has the advantage to provide an analytical model serving as starting point for further developments.

We have demonstrated that, by accounting for field propagation inside the transversal ridge section using a ray tracing model, we can improve significantly the accuracy of the analytical results that are in excellent agreement with full-wave simulation results. Furthermore, the model requires very low computational effort ($\cong$ 1 or 2 seconds).

A parametric study has demonstrated the wide range of validity of the tool making it suitable for optimization purposes, discussed in the following chapter.

3

Optimization and Design of Continuous Parallel Plate Waveguide Lens-Like Multiple Beam Antennas

Contents

Abstract

A combination of the proposed analysis tool (Chapter 2) with phase and pattern optimization procedures is proposed here.

The proposed analytical model, based on elliptical lens profiles and derived from the bifocal constrained lens model, demonstrates residual path length errors. A phase-only optimization method is proposed in Subsection 3.2.2 and shows the

potential of the concept, as a good compromise between the pillbox antenna and the Rotman lens in terms of scanning performance and mechanical simplicity. However, the radiation patterns presented all display a residual side lobe imbalance. A pattern based optimization method is presented in Subsection 3.2.3 showing the same results, which indicates that the side lobe imbalance is an inherent limitation of the elliptical lens design.

To overcome those limitations, additional degrees of freedom are added in Section 3.3, introducing the propagation along the thickness of the PPW lens with different inner and outer lens contours. Based on a pattern optimization procedure, the pattern shape is improved. However, some differences are observed in the prediction given by the proposed GO model when compared to full-wave analysis, indicating this solution is outside the domain of validity of the tool.

Shaped polynomial delay lens profiles are finally introduced in Section 3.4 to improve the radiation performances. Optimized configurations demonstrate a reduction of the path length error levels over a large scanning range, proposing performances close the ones obtained with simplified constrained lens models (Rotman lens, Bifocal lens). The associated radiation patterns demonstrate lower and more balanced first side lobe levels.

3.1 Choice of a global optimization algorithm

Various optimization algorithms have been used to solve electromagnetic problems and design antennas. In this section, we do not describe local optimization methods (e.g gradient methods [63], [64]), as we are interested in global optimization solutions for the problem considered. Global optimization algorithms are a branch of applied mathematics focusing on optimization which aims to find the best feasible solution of an objective function (cost function), which has generally multiple local optima, as shown in Fig. 3.1. The global optimization methods are able to determine the global optimum of the function in a given search space, according to a set of criteria, without "blocking" at local optima.

When the problems considered have a large number of variables, many local optima exist, which increases the complexity to find the global solution. To solve those problems, two classes of algorithm are defined. Deterministic methods are first considered when objective functions are continuous and derivable in the complete search space. In our case, there are no direct links between the solution domain and the cost function, making them not usable.

Alternatively, probabilistic methods also called stochastic methods are considered as pure random processes, exploring and targeting best feasible solutions. Those

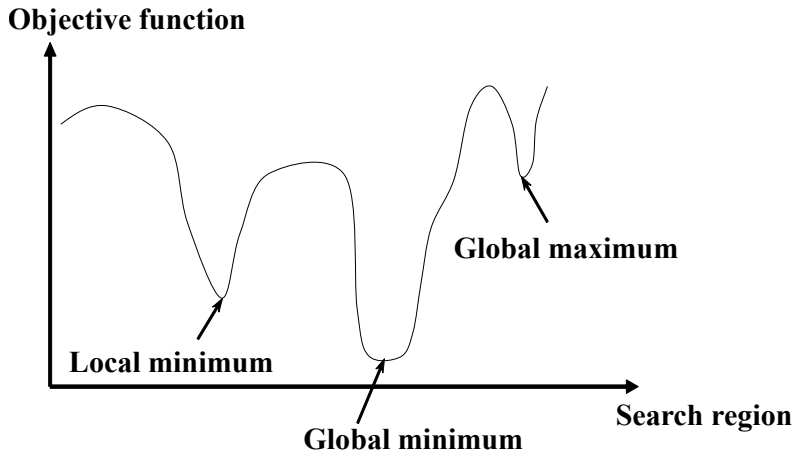

Figure 3.1: Global and local optimum of an objective function

methods are robust when a large number of parameters is considered. Among the categories of probabilistic methods, the most popular algorithms are :

- Simulate annealing (SA) [65], which is based on an analogy to annealing process used in the metallurgy and material science. Target of simulated annealing is to achieve a state of material at which global minimum of energy is found. The function to be minimized is defined as power or energy difference between geometries in the annealing process.
- Particle swarm optimization (PSO) [66], which emulates a form of swarm intelligence in which the behavior of social system of living animals is simulated, for example, a swarm of bees or a flock of birds looking for foods.
- Genetic algorithm (GA), which is inspired by the theory of evolution of Darwin describing natural evolution and selection, and modern genetic processes.

The genetic algorithm (GA), described in the next section, has been used in different antenna designs and electromagnetic problems ([67], [68]) and is considered suitable for our objectives in combination with the ray tracing numerical tool developed in Chapter 2.

3.1.1 Description of the genetic differential evolution (DE) algorithm

The differential evolution has been introduced in [69] as a genetic or metaheuristic algorithm to minimize possibly non linear and non diffentiable space functions. Providing different tests comparing with different global algorithm solutions proposed in the literature, Storn [69] demonstrated that this new method converges

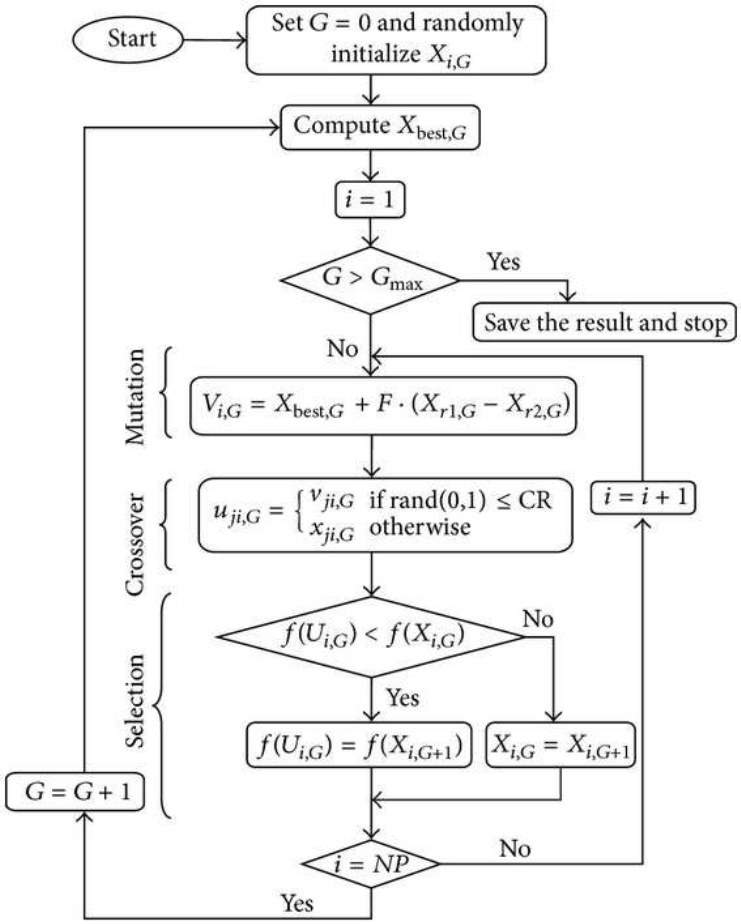

Figure 3.2: Flowchart of genetic algorithm.

faster and with more certainty. It can fulfill the following requirements, generally required by users for a practical minimization technique:

1. Ability to work with non-differentiable and non linear cost functions
2. Parallelizability to cope with computation intensive cost functions
3. Ease of use, i.e. few control variables to minimize the objective function.
4. Good convergence properties, i.e. consistent convergence to the global minimum in consecutive independent trials

Differential evolution (DE) is a parallel direct search method which makes use of NP (Number of Parameters) parameter vectors in a D-dimensional search space,

$$X_{i,G}, i = 1, 2, ..NP, \tag{3.1}$$

as a population for each generation G. NP does not change during the optimization process. The initial vector $X_{i,G}$ is chosen randomly and cover the entire parameter space.

For each target vector $X_{i,G}$, a mutant vector is generated as described by Eqn. (3.2),

$$V_{i,G+1} = X_{best,G} + F(X_{r_1,G} - X_{r_2,G}), \tag{3.2}$$

with random indexes r_1, $r_2 \in 1, 2..., NP$, integers, mutually different. The randomly chosen integers r_1, r_2 are also different from the running index i, consequently NP must be equal or greater than three. F is a real and constant factor $\in [0, 2]$ which control the amplification of the differential variation $(X_{r_1,G} - X_{r_2,G})$.

Then, to increase the diversity of the perturbed parameter vectors, cross-over is introduced. A trial vector is formed,

$$U_{i,G+1} = (U_{1i,G+1}, U_{2i,G+1}, .., U_{Di,G+1}) \tag{3.3}$$

where,

$$U_{ji,G+1} = \begin{cases} V_{ji,G+1} & \text{if}(randb_{[0,1)}(j) < CR) \\ X_{i,G} & \text{otherwise,} \end{cases}$$

$j \in 1, .., D$. Crossover factor CR (Crossover ratio) is constant in the range $[0, 1]$ and has to be defined by the user.

Finally, the operation of selection is performed with a comparison between the objective function (cost function) values at each trial vector $U_{i,G+1}$ and the previous target vector $X_{i,G}$. If vector $U_{i,G+1}$ yields a smaller cost function value than $X_{i,G}$, then $X_{i,G+1}$ is set to $U_{i,G+1}$; otherwise the value $X_{i,G}$ is retained.

The scheme presented here is not the only variant of DE which has proven to be useful. To classify the different variants, the notation $DE/x/y/z$ is introduced where, x is the vector to be mutated, as presented in Eqn. (3.2), which currently can be "rand" (randomly population vector) or "best" (best population vector). y is the number of differences vector used in the mutation operation. In the presented scheme, one difference vector has been chosen $X_{r_1,G} - X_{r_2,G}$. Finally, z corresponds to the cross-over scheme. The current variant is "bin" for binomial, corresponding to $randb(j)$, the j_{th} evaluation of a uniform random number generator with outcome $[0, 1]$.

3.2 Optimization procedures considering identical elliptical profiles

Starting from an ideal bifocal constrained lens design, as presented in Subsection 2.1.1, the complete analytical procedure (referred to as continuous lens model), taking into account the field propagation inside the transversal cavity (by the use of a ray tracing), has shown residual path length errors in line with full-wave simulation results which deviate from the ideal bifocal constrained lens model.

In this section, the objective is to combine the proposed analytical model, based on elliptical lens profiles, with an optimization procedure, performed by the differential evolution (DE) presented previously. The idea is to retrieve the bifocal behavior of the simplified model with a positive impact on the shape of the radiation patterns.

3.2.1 Optimization parameters

The design parameters are defined in Fig. 3.3. The lens diameter and the focal distance are set to $D = 10\lambda$ and $f = 0.7D$, as defined in Subsection 2.1.3, where λ is the wavelength in free space at the operating frequency. The focal points F_1 and F_2 are defined by their angular positions $\theta_1 = -\alpha = -30°$ and $\theta_1 = \alpha = 30°$. Both focal points and the lens are symmetrical with respect to $\overrightarrow{X}$-axis; as a consequence, only F_2 is considered in the optimization procedure. The feed orientation is specified in order to point towards O, ensuring a suitable illumination of the lens. The primary feed horn aperture is equal to 1.5λ, as in Subsection 2.1.3 for comparison purposes. The proposed procedure allows optimizing not only the profile of the inner lens contour (Σ_1), defined by

$$x = a_{in}(\sqrt{1-y^2} - 1), \tag{3.4}$$

but also the ridge height profile (h_w),

$$h_w = a_w(\sqrt{1-y^2} - \sqrt{1-(d/2)^2}), \tag{3.5}$$

where $d = D/f$, (x, y) denote the coordinates defining the inner lens contour (Σ_1) and h_w the height of the ridge profile, all normalized to the focal distance f. Both equations have been introduced in Section 2.3, in order to analyze the domain of validity of the proposed analytical tool.

As previously explained, these equations correspond to elliptical shapes as defined by the bifocal constrained lens model presented in Subsection 2.1.1, controlled by

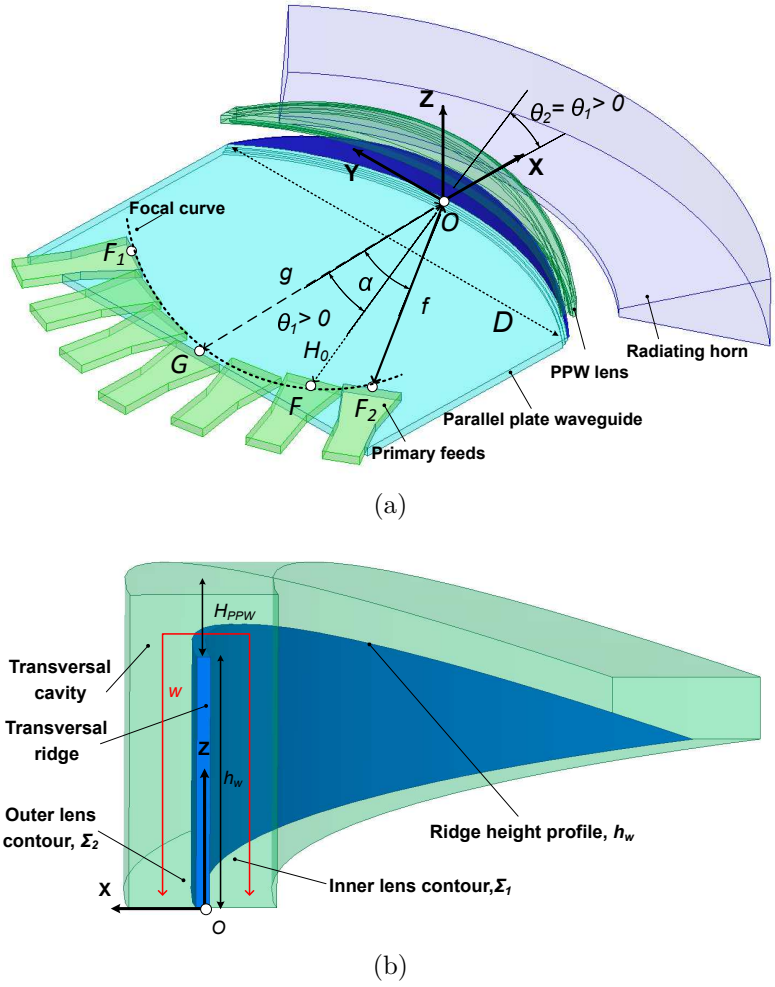

Figure 3.3: Continuous parallel plate waveguide (PPW) lens-like beamformer: (a) 3D view and (b) Cut view in $(O, \overrightarrow{X}, \overrightarrow{Z})$ plane of the PPW lens.

a_{in} and a_w which are here optimization parameters for the beam associated to F_2. As done by Rotman in his seminal paper [27], the parameter $g = GO/f$ is then used as an additional parameter to further reduce aberrations for any beam radiated in the angular range $[-\alpha, \alpha]$ by adjusting the curvature of the focal arc.

For the starting bifocal configuration, $a_{in} = a_0 = cos(\alpha) = 0.87$ and $a_w = 0.5a_0^2 = 0.37$ as shown in Subsection 2.1.3. During the optimization procedure, a_{in} and a_w are varying in the range $[0, 1]$ in order to maintain elliptical profiles with a major axis oriented along $\overrightarrow{Y}$-axis.

3.2.2 Phase-only optimization

The first approach aims at minimizing the path length errors Δ_l computed along the outer lens contour Σ_2,

$$\Delta_l = F_2PQ - F_2PQ[y_Q = 0]. \tag{3.6}$$

Eqn. (3.6) defines the difference in electrical path length between any ray coming from F_2 and a central ray chosen as a reference, passing through O on the outer lens contour Σ_2. The root mean square of the path length errors $RMS.\Delta_l$ is used as a cost function, as defined in the following Eqn. (3.7),

$$RMS.\Delta_l = \frac{1}{n}\sum_{i=1}^{n}\sqrt{\Delta_{l_i}^2}, \tag{3.7}$$

with n the number of outer lens points. The patterns radiated by the different geometrical optics (GO) lens models are provided in Fig. 3.4a. Starting from the bifocal constrained lens model (green curve), the continuous model (red curve) has demonstrated residual phase aberrations resulting in a pointing angle error of 1.7°, an increase of the half-power beamwidth θ_{3dB} and first side lobes imbalance. The optimized model (orange dotted line), with $a_{in} = 0.66$ and $a_w = 0.42$, reduces substantially the pointing angle error (0.1°) without improving significantly the side lobes imbalance ($SLL = -13.2$ dB). A good agreement with HFSS [62] is demonstrated in Fig. 3.4b therefore validating the analytical model presented in Chapter 2.

Based on this configuration, RMS values versus pointing angle are represented in Fig. 3.5 for the different lens models and different beamformer types defined with the same diameter D. The pillbox concept proposed by Rotman in [16], considering circular lens and focal curve profiles, is limited by spherical path length errors independent of the pointing direction. This is clearly shown here with a constant RMS value (blue curve) over the scanning range considered. The parabolic profile approach (turquoise curve) demonstrates one true focal point with phase aberrations increasing strongly with the scanning angle θ_2. The optimized continuous lens model is shown as a good compromise between the pillbox antenna [19] and the Rotman lens [27]. The ideal bifocal behavior (green curve) is not retrieved but a significant reduction of the phase aberration levels over the angular range $[-30°, 30°]$ is achieved.

Nevertheless, the pattern obtained with this optimized model (orange dotted line in Fig. 3.4a) still demonstrates first side lobes imbalance. Concluding on the limitations of such design with a phase-only approach is difficult. Indeed, we have already shown in the previous chapter, using the ray tracing approach, that the way the rays are distributed impacts the amplitude field distribution on Σ_2. A ray tube [60] approach was implemented to predict more accurately the field density on the aperture, as presented in Subsection 2.2.1. Additionally, it is interesting to

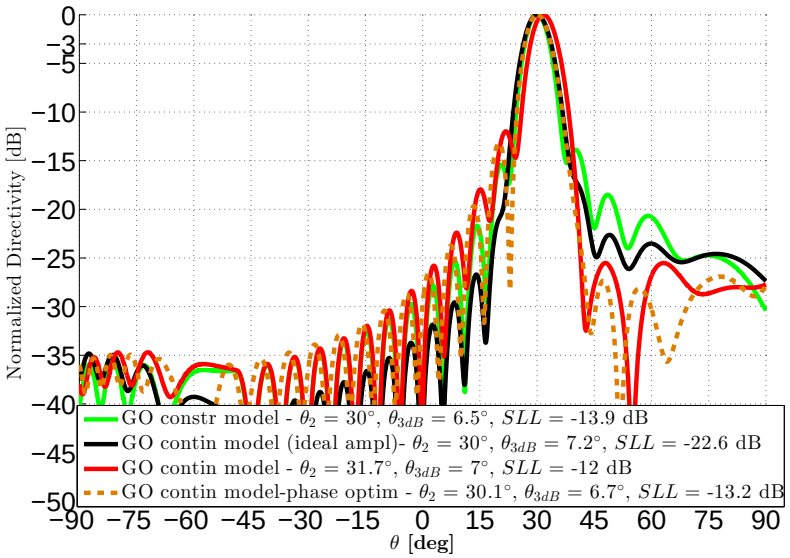

(a)

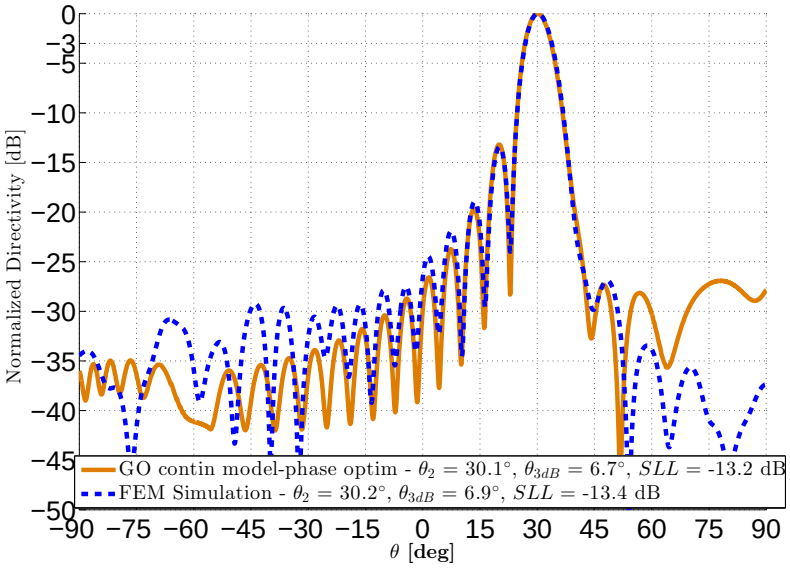

(b)

Figure 3.4: Radiation patterns of the PPW beamformer in H-plane for $\theta_1 = \alpha$, at the center frequency: (a) GO models, (b) GO continuous lens model – phase optimization (validation with HFSS).

notice that the ideal bifocal constrained lens patterns also display high first side lobes level (Fig. 3.4, green curve). This is found to be a consequence of the way the cylindrical wave, coming from F_2, is spread over the elliptical profile of the line source, as the amplitude distribution is defined by the primary feed aperture (1.5λ), with no phase aberrations for the pointing direction $\alpha = 30°$ (Fig. 3.5).

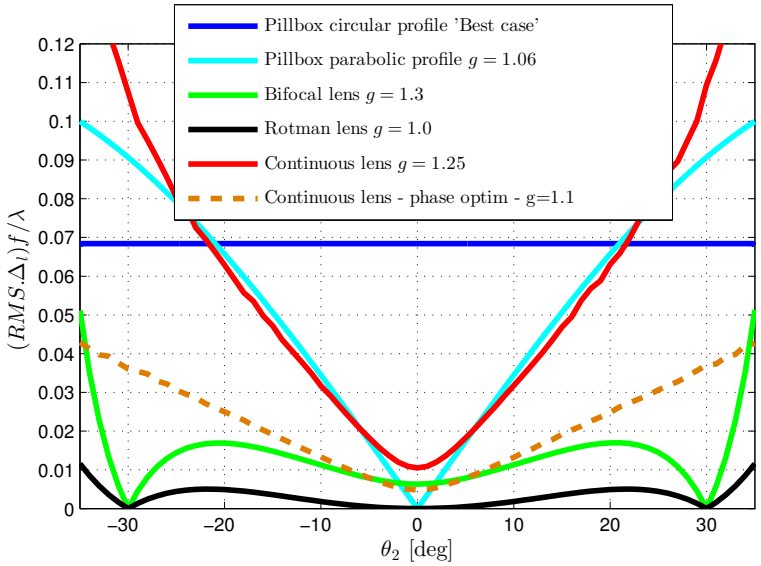

Figure 3.5: RMS value of the path length errors normalized to λ versus pointing angle θ_2 for different lens models and different beamformer types.

For further investigations, an alternative is considered in the next section where the optimization is performed on the pattern itself through a set of cost functions.

3.2.3 Pattern optimization

This second method is based on a pattern mask optimization as illustrated in Fig. 3.6. Lower bounds M_L are defined using a *sinc* function over the angular region limited to the half-power beamwidth θ_{3dB}.

Over the side lobe (SL) regions $\theta < \theta_{target} - \theta_{1N}$ and $\theta > \theta_{target} + \theta_{1N}$, where $\theta_{1N} = \arcsin(\theta_{3dB}/50.76)$ (calculated with respect to the *sinc* function), upper bounds M_U are defined to achieve a targeted side lobe level. The cost function is thus calculated if $M_U < P_{GO}(\theta)$ or $P_{GO}(\theta) < M_L$,

$$\boldsymbol{C}_f = \int_{\theta_{target}-\theta_{3_{dB}}/2}^{\theta_{target}+\theta_{3_{dB}}/2} (P_{GO}(\theta) - M_L)^2 d_\theta + max(P_{GO}(\theta) - M_U)_{[SL_{regions}]} \tag{3.8}$$

where P_{GO} corresponds to the GO numerical tool calculated pattern in H-plane. In this section, $\theta_{target} = 30°$ and the 3 dB beamwidth is $\theta_{3dB} = 6.5°$, as the one defined by the ideal bifocal constrained lens model (green curve in Fig. 3.4a). A desired side lobe level $SLL_{target} = -18$ dB is chosen.

The optimized GO model (brown dotted line) in Fig. 3.7a, with $a_{in} = 0.62$ and $a_w = 0.40$, is very close to the targeted mask in terms of pointing angle (error of 0.3°)

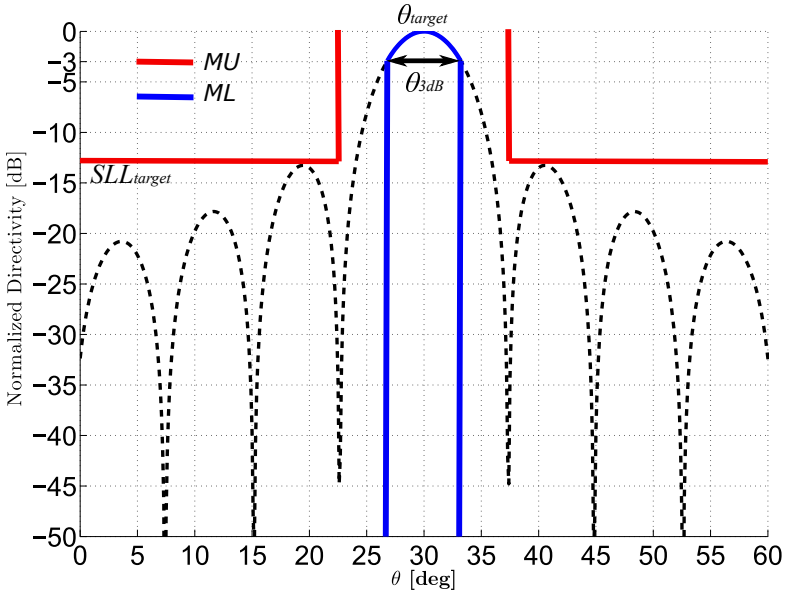

Figure 3.6: Definition of the power mask for pattern optimization.

but still demonstrates a first side lobes imbalance. A difference of approximately 5 dB with respect to the targeted SLL is observed. A good agreement between the analytical model and the full-wave analysis results with HFSS is demonstrated in Fig. 3.7b, particularly in the critical parts of the normalized pattern where the power is higher than 25 to 30 dB below the peak. It is important to add that the optimization results are not dependent on the relative weight between the SLL and the 3 dB beamwidth constraints. This has been validated by considering an extreme case where no constraint is applied on the 3 dB beamwidth, the pattern has been optimized based on a SLL constraint only. Even in this case, no improvement on the SLL is observed and the first side lobe imbalance remains.

Optimization results for a different lens configuration with $f = 0.55D$ are presented in Fig. 3.8. This even more compact configuration is still compatible with the developed analytical model as demonstrated by the good agreement with HFSS [62] in Fig. 3.8b. The initial design (red curve in Fig. 3.8a) deviates more from the ideal bifocal lens pattern, thus providing a more challenging test case for the two optimization procedures compared in Chapter 2. Interestingly, the conclusion is unchanged and both procedures provide very similar patterns.

The phase only approach has demonstrated the potential of the concept, showing a good compromise between the pillbox antenna and the Rotman lens in terms of scanning performance. When comparing this method with a pattern based optimization, very similar designs are obtained. The radiation patterns presented here all display a residual side lobe imbalance, demonstrating the actual limitations

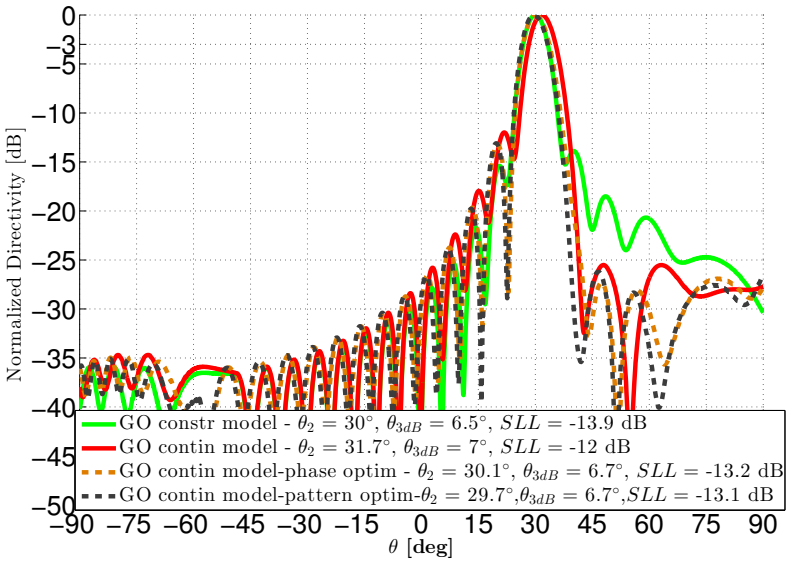

(a)

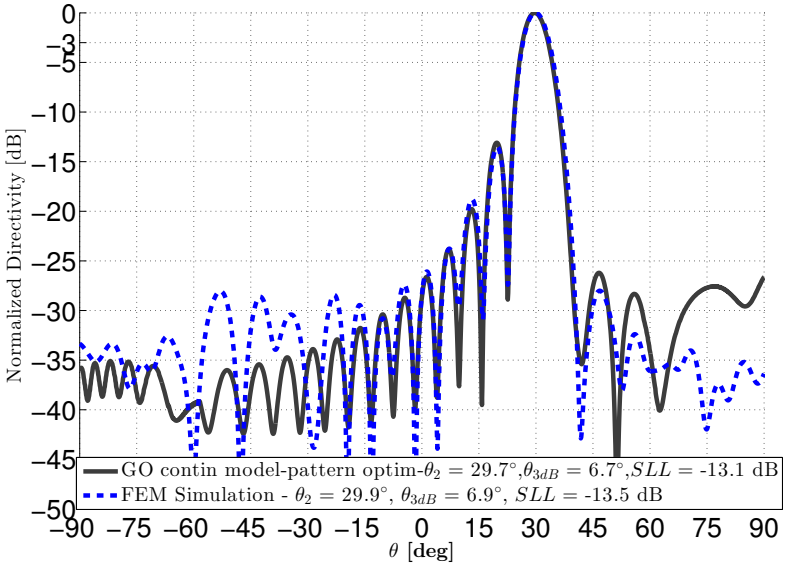

(b)

Figure 3.7: Radiation patterns of the PPW beamformer in H-plane for $\theta_1 = \alpha$, at the center frequency: (a) GO models, (b) GO continuous lens model – pattern optimization (validation with HFSS).

of the proposed configuration. Using two different elliptical curves for the lens contour and height profile is not sufficient to overcome this limitation.

There is a need to increase the control on both phase and amplitude distributions on the outer lens contour (Σ_2) and consequently increase the control on the pattern.

Additional design parameters are required to enable a side lobe level reduction.

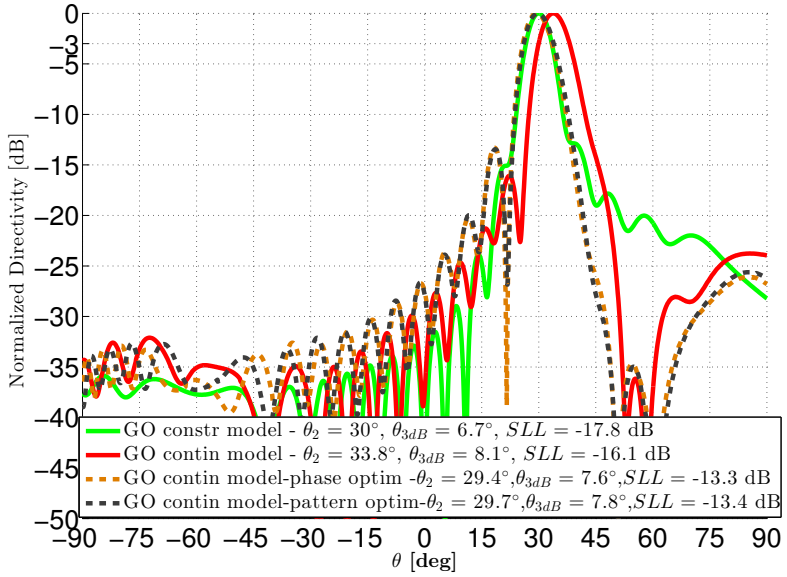

(a)

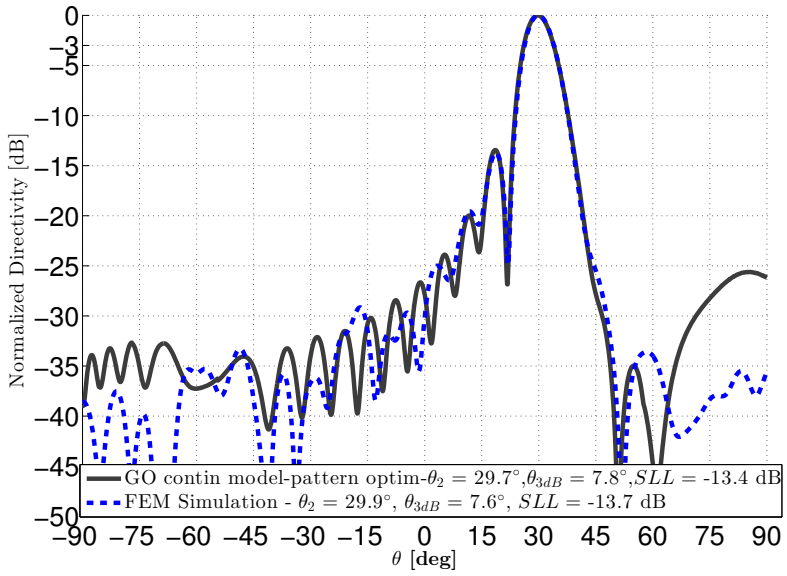

(b)

Figure 3.8: Radiation patterns of the PPW beamformer in H-plane for $\theta_1 = \alpha$ using $f = 0.55D$, at the center frequency: (a) GO models, (b) GO continuous lens model – pattern optimization (validation with HFSS).

Following this conclusion, two design evolutions are proposed and evaluated in the next sections.

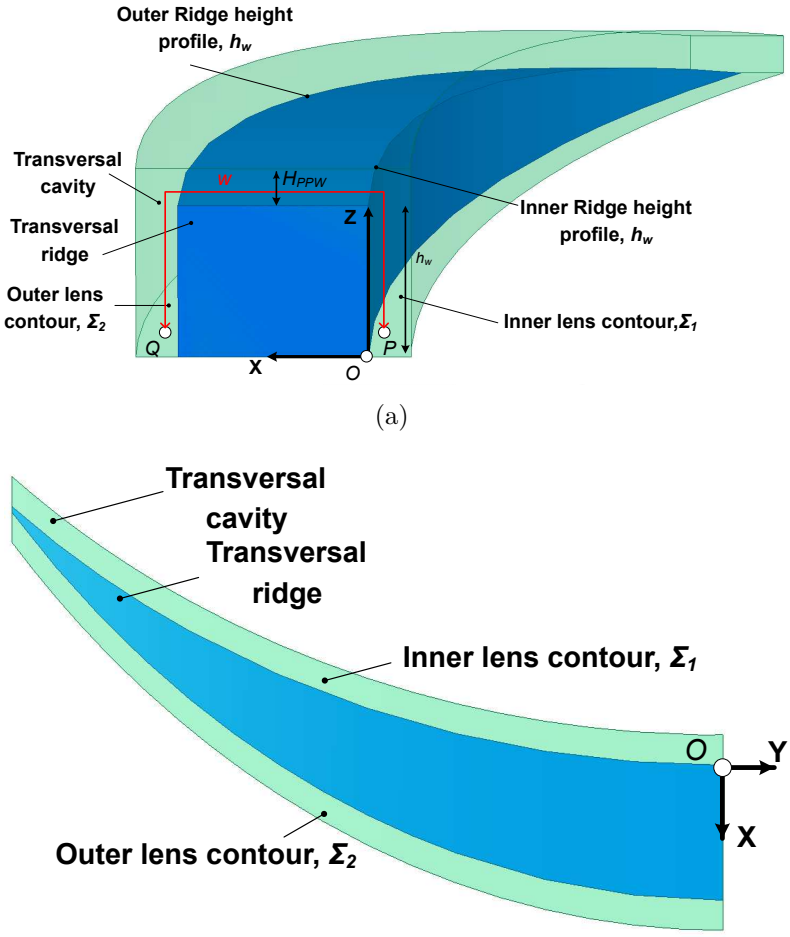

Figure 3.9: PPW lens considering independent inner (Σ_1) and outer (Σ_2) lens contours: (a) 3D view and (b) top view in xOy plane.

3.3 Additional degree of freedom considering independent elliptical inner and outer lens contour

3.3.1 Design update and pattern optimization procedure

To overcome the limitations observed in the previous section, the first approach considered is the use of independent inner (Σ_1) and outer (Σ_2) lens contours, as shown in Fig. 3.9. Consequently the propagation in the thickness of the PPW lens is used as an additional degree of freedom to enhance the lens performances.

The lens profile is now described by the following equations,

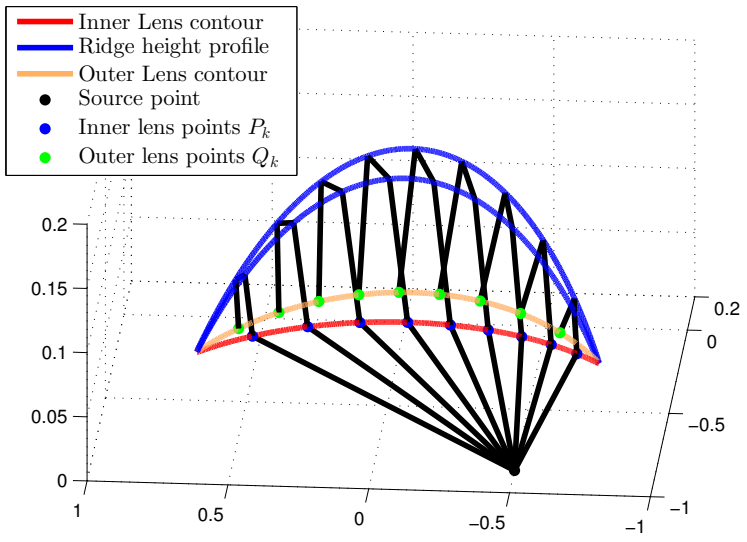

Figure 3.10: Positions of the inner and outer lens points P_k and Q_k computed with the ray tracing model, considering independent inner and outer lens profiles. Here with $\theta_1 = \alpha$. The lens parameters are $D = 10\lambda$, $\frac{f}{D} = 0.7$ and $\alpha = 30°$. Axis values are normalized to the focal distance f.

$$x = a_{in}(\sqrt{1 - y^2} - 1), \tag{3.9}$$

$$u = a_{out}(\sqrt{1 - y^2} - \Delta_{out}), \tag{3.10}$$

(x, y), (u, y) describing respectively the coordinates of the inner (Σ_1) and outer (Σ_2) lens contours. a_{in} and a_{out} are the main parameters of both elliptical profiles. Δ_{out} defines the outer lens (Σ_2) translation along $\overrightarrow{X}$-axis and is defined to achieve a minimum thickness of the ridge, as shown in Fig. 3.9b.

The ridge height profile (h_w) is always described by,

$$h_w = a_w(\sqrt{1 - y^2} - \sqrt{1 - (d/2)^2}) \tag{3.11}$$

where $d = D/f$, h_w the height of the ridge profile, normalized to the focal distance f. Considering, two independent inner and outer lens profiles, the ridge height is also defined by its inner and outer profiles as shown in Fig. 3.9a.

The ray tracing performed here is based on the description given in Chapter 2 and further details are given in Annex A, taking into account this additional ray tracing along the thickness of the ridge, with different inner (Σ_1) and outer (Σ_2) lens profiles. A similar approximation is made on the top part of the ridge, with a ray propagation assumed to be in a plane locally tangent to the ridge at

the point of incidence. Several pairs of connected inner and outer lens contour points P_k and Q_k are plotted in Fig. 3.10.

A pattern based optimization is conducted in this section based on this independent inner (Σ_1) and outer (Σ_2) lens profiles approach. The optimization parameters are the coefficients a_{in}, a_{out}, a_w which describe the three elliptical profiles considered in Eqn. (3.9), Eqn. (3.10) and Eqn. (3.11).

During the optimization procedure, a_{in} and a_w are varying in the range $[0, 1]$ in order to maintain elliptical profiles with a major axis oriented along $\overrightarrow{Y}$-axis, as presented in Section 3.2. a_{out} is defined to be higher than a_{in} and is varying in the range $[0, 2]$, as a first approach.

In this section, the antenna pattern mask is similar to the one described in Subsection 3.2.3. The parameters are the same as in the first approach with identical inner and outer lens profiles, $\theta_{target} = 30°$ and the 3 dB beamwidth is $\theta_{3dB} = 6.5°$, as the one defined by the ideal bifocal constrained lens model (green curve in Fig. 3.4a). A desired side lobe level $SLL_{target} = -18$ dB is chosen.

The optimized GO model obtained, defined by $a_{in} = 0.72$, $a_{out} = 1.29$, $a_w = 0.37$, is shown in Fig. 3.11a. A SLL reduction is observed (2.3 dB) when compared to the optimized GO model with identical inner and outer lens contours (brown dotted curve), reducing the residual side lobe imbalance.

The comparison proposed with HFSS in Fig. 3.11b demonstrates differences in the prediction proposed by the GO model. In this case, the SLL predicted by the GO model (-15.4 dB) is higher than the one obtained with the FEM simulation (-18.6 dB). A difference of 0.5° is also observed between the 3 dB beamwidth θ_{3dB} computed by both methods. The FEM performance obtained is better than the ones predicted by the GO model and those results demonstrate possible benefits in using the propagation along the thickness of the PPW lens.

To explain more precisely the performance improvement, mainly in terms of SLL, the path length errors normalized to the focal distance f, are provided in Fig. 3.12a along the outer lens contour (Σ_2) for both optimized GO models (with and without independent inner (Σ_1) and outer (Σ_2) lens contour). With the first model (brown curve), the side lobe imbalance observed in Fig. 3.11a is explained by the asymmetrical distribution of the phase aberrations, principally observed for Y values between $[-60, 60]$ mm. When the propagation along the ridge thickness is considered (green curve), phase aberrations still exist but this asymmetrical distribution is reduced in the same considered Y interval.

Moreover, the propagation along the thickness of the ridge impacts the amplitude distribution on the outer lens contour (Fig. 3.12b), where the amplitude tapering

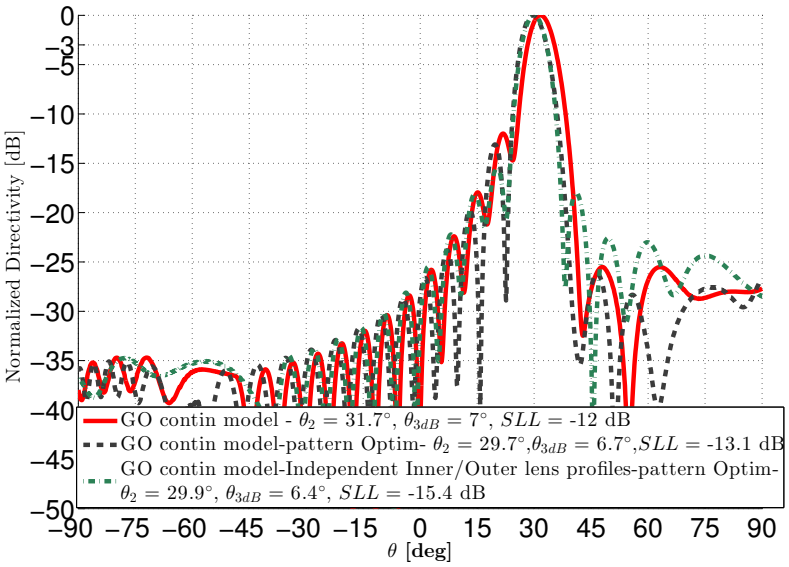

(a)

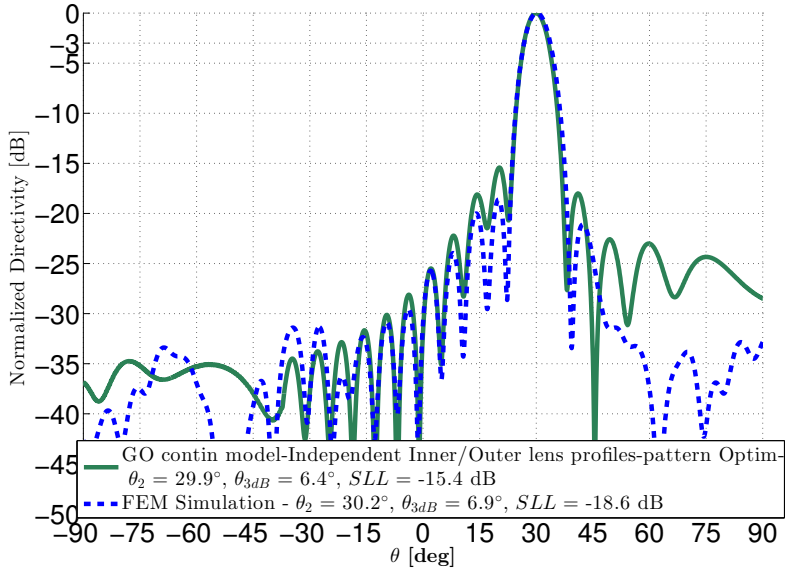

(b)

Figure 3.11: Radiation patterns of the PPW beamformer in H-plane for $\theta_1 = \alpha$, at the center frequency: (a) GO models, (b) GO continuous lens model with independent inner and outer lens profiles – pattern optimization (validation with HFSS).

is higher when independent inner and outer lens contours are considered (-12.5 dB as compared to -10 dB with identical inner and outer lens profiles at $Y = 100$ mm). The amplitude distribution given by the GO model is validated by the comparison provided with the FEM simulation in Fig. 3.13b. Strong ripples appear in the FEM results which are as well the consequence of undesired reflections at

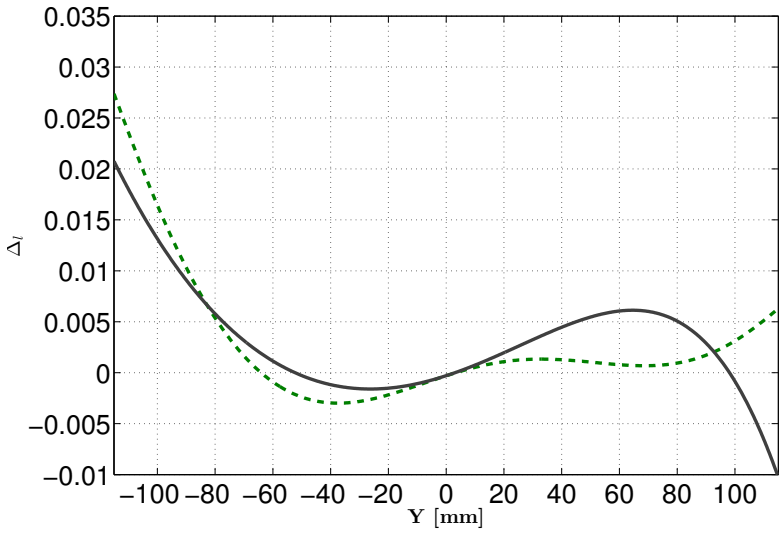

(a) Phase aberrations

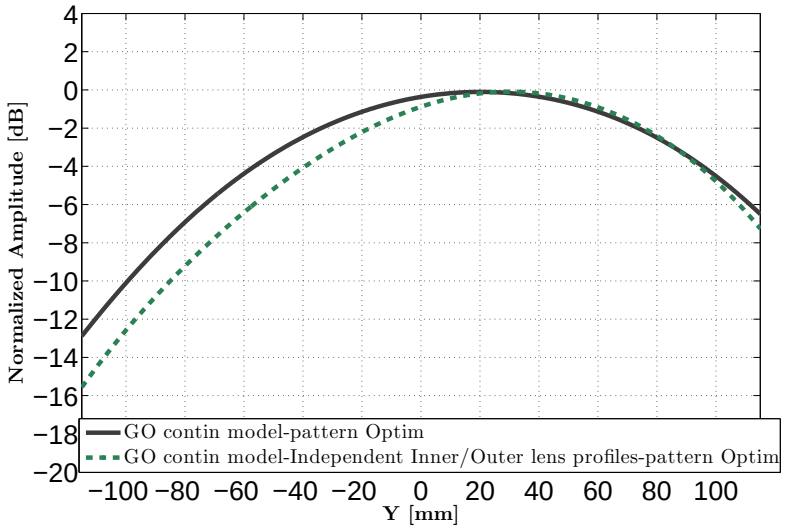

(b) Amplitude distributions

Figure 3.12: Amplitude and phase aberrations distributions along the outer lens contour Σ_2 of the PPW beamformer in H-plane for $\theta_1 = \alpha$. Y defines the outer lens point positions along $\overrightarrow{Y}$-axis. Both GO models are considered after pattern optimization

the different bend transitions between PPW sections, as presented in Subsection 2.2.3. For the considered optimized model, the phase distribution computed with the GO model along the outer lens contour is compared to the one obtained with the FEM implementation in Fig. 3.13a. This comparison demonstrates differences for extreme positive Y values (60° at $Y = 80$ mm), which characterize the limits of the ray tracing approximations.

For comparison purposes, two other pointing directions are considered, where

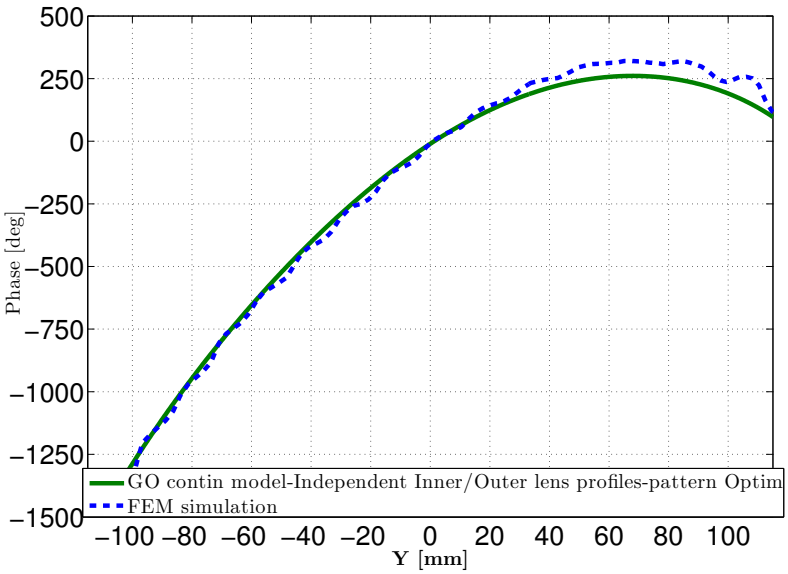

(a) Phase distribution

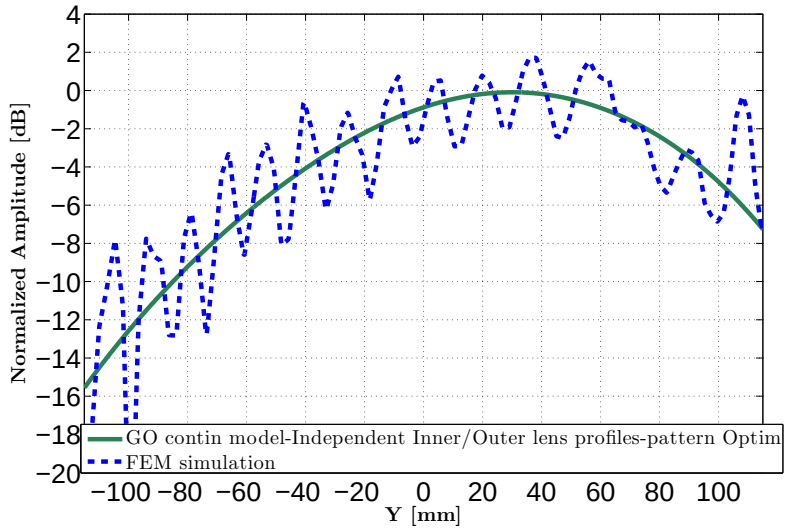

(b) Amplitude distribution

Figure 3.13: Amplitude and phase distributions on the outer lens contour Σ_2 of the PPW beamformer in H-plane for $\theta_1 = \alpha$ for the GO continuous lens model with independent inner and outer lens profiles – pattern optimization (validation with HFSS). Y defines the outer lens point positions along $\overrightarrow{Y}$-axis.

$\theta_1 = 15$ and $0°$. A value $g = 1.1$ has been considered as an optimized value to define the position of those feeds in the focal arc. The H-plane radiation patterns are presented respectively in Fig. 3.14a and 3.14b. As shown in those figures, the differences observed between the GO numerical tool (green curve) and the FEM simulation (blue dash curve) decrease when lower scanning angles are considered.

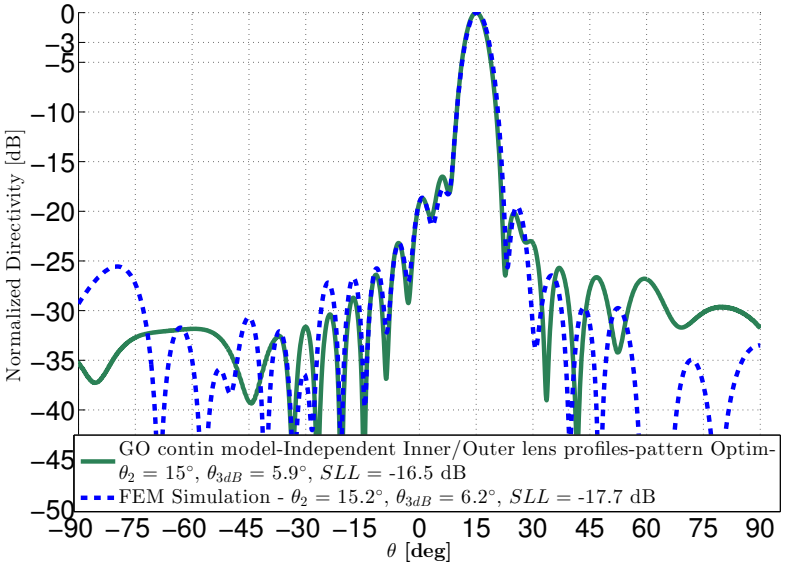

(a)

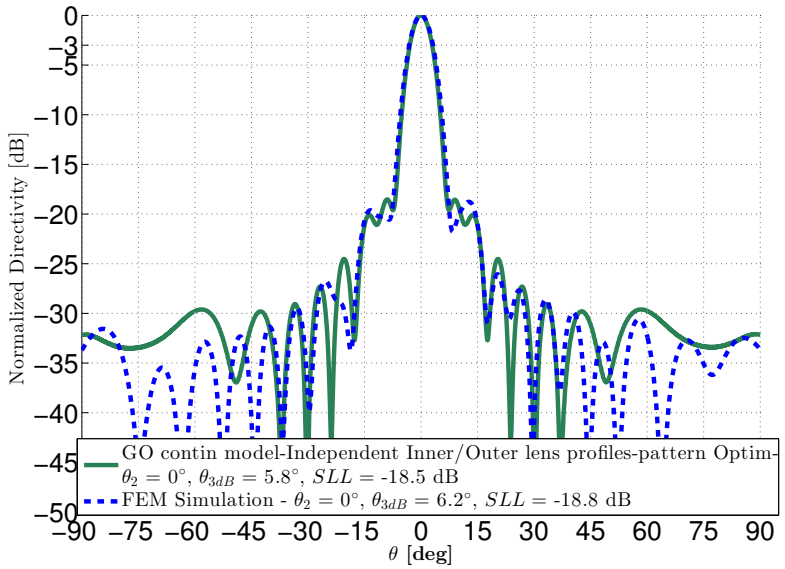

(b)

Figure 3.14: Radiation pattern of the PPW beamformer in H-plane for two values of θ_1 and $g = 1.1$ at the center frequency: (a) $\theta_1 = 20°$, (b) $\theta_1 = 0°$.

For the beam associated to $\theta_1 = 0°$ the prediction proposed is in very good agreement with HFSS [62]. The SLL obtained using the FEM method are below -18 dB, as demonstrated when $\theta_1 = 30°$ (Fig. 3.11b).

Here, the differences observed between the GO model and the FEM simulation are the main limitations of this approach, as the objective is to propose an analytical

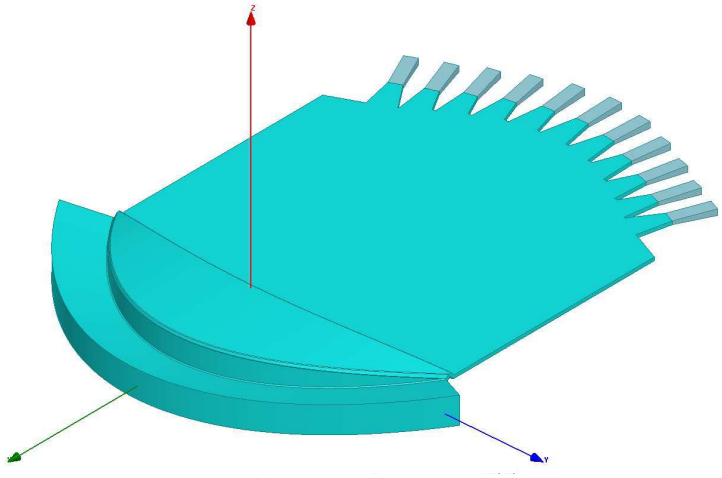

(a) Initial design in vacuum

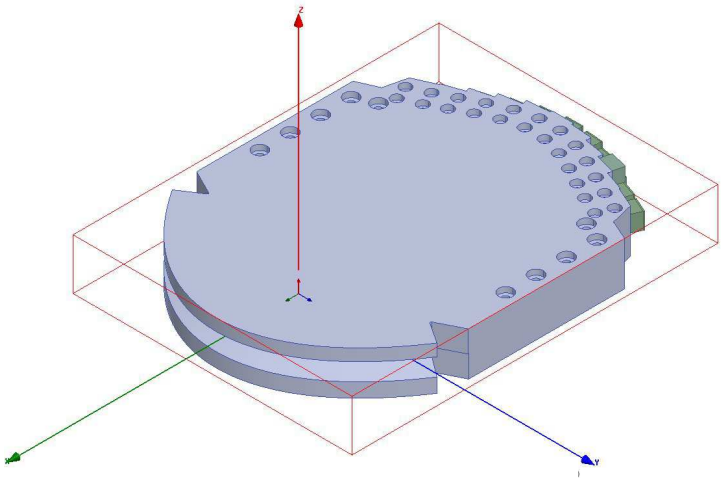

(b) Final design

Figure 3.15: Continuous parallel plate waveguide (PPW) lens-like beamformer design at Ka band (up-link), considered by Thales Alenia Space in the frame of the RAFQO project.

tool able to predict accurately the behavior of several continuous PPW lenses to enable global optimization. In this case, the FEM results appear to be better than predicted with the GO tool, but for other configurations they may be worst. It is then impossible to guarantee a global optimum with such deviations. Moreover, this increases the size of the complete antenna configuration (as the ridge thickness is increased along $\overrightarrow{X}$-axis, as shown in Fig. 3.3a).

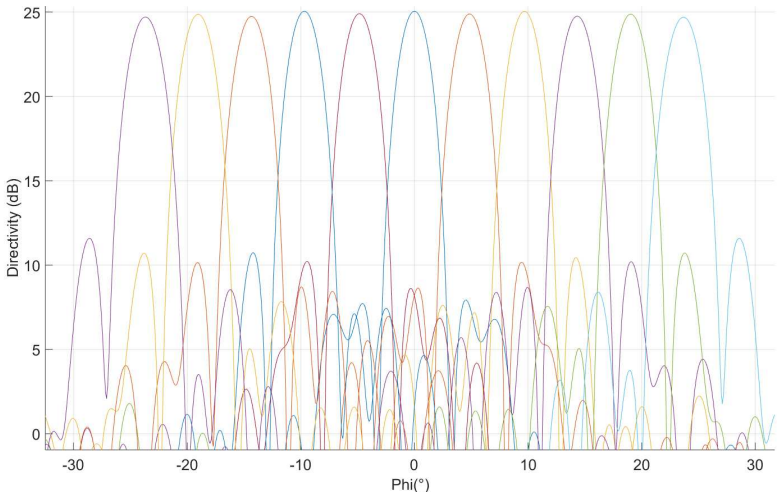

Figure 3.16: Simulated H-plane radiation patterns of the final PPW beamformer design at the frequency $f_0 = 30$ GHz, , provided by Thales Alenia Space.

3.3.2 RAFQO (Active array of quasi optical beamformers) project

This section will describe the possibility to consider innovative ways of manufacturing, namely the injection molding and why the additional degree of freedom brought by the inner and outer lens contour control is of interest for such a manufacturing process.

Injection molding is capable of producing thousands to millions of pieces with a controlled cost thanks to a repetitive and fast process. However this technique has some constraints:

- Need of clearance angle to be able to take the piece out of the mold without damaging it
- Minimum ratio between the height and width of an injected piece

This last constraint is problematic when considering a thin ridge with identical profiles. The first approach, shown in Fig. 3.3, will be difficult to inject easily. The proposed ridge thickness (Fig. 3.9) is an enabler, as with such configuration the ratio between the height and width can be controlled and adapted to the process.

One example is proposed in the frame of the RAFQO ANR project [70], involving Thales Alenia Space, Thales Communications & Security, IETR and MIP [71]. One of the objectives was to develop low-cost quasi-optical beamformers, making use of the plastic injection molding technology.

The variable ridge thickness approach was selected and the GO numerical tool (presented in Chapter 2, more precisely described in Annex A) was succesffully

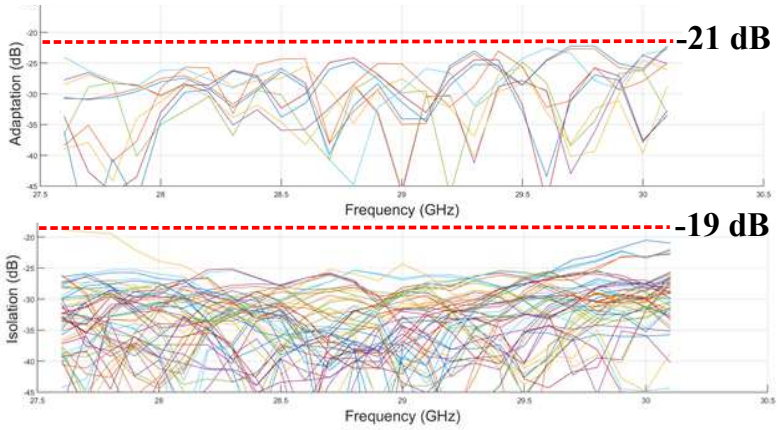

Figure 3.17: Simulated S-parameter coefficients of the final PPW beamformer design over the up-link Ka band, for the final design before manufacturing. Those results have been provided by Thales Alenia Space.

used to design a QOBF working over the up-link Ka band and generating 11 beams over a large angular range ($[-25°,\ 25°]$).

As observed in Fig. 3.16, the radiation patterns computed with the final FEM simulation demonstrate good performances (HPBW, SLL, scan loss) over the considered scanning range. The final S-parameters have been plotted over the frequency band, as shown in Fig. 3.17. Excellent performances with reflection and mutual coupling coefficients respectively below -21 and -19 dB are demonstrated.

The manufacturing process will include the realization of two plastic blocs and a metallization process. Manufacturing and measurements are planned in the frame of this RAFQO project to demonstrate the possibility to use a low-cost manufacturing technology (injection molding) and validate the good RF performances.

3.4 Polynomial shaped delay lens profiles

An alternative design evolution is to introduce shaped polynomial delay lens profiles (inner lens contour (Σ_1) and ridge height profile (h_w)) to increase the control on both phase and amplitude distributions along the outer lens contour (Σ_2) and improve the radiation performances. Additional parameters are considered here, where polynomial equations shape the different lens profiles. With this approach, the inner lens contour (Σ_1) and the ridge height profile (h_w) are now defined respectively by,

$$x = \sum_{k=0}^{n} p_k y^k, \tag{3.12}$$

$$h_w = \sum_{k=1}^{n} q_k y^k - min(\sum_{k=1}^{n} q_k y^k), \tag{3.13}$$

where x, y and h_w are the coordinates along the different reference system axis, all normalized to the focal distance f. p_k and q_k are the k^{th} degree coefficients, where $1 < k < n$, n defining the maximum degree. Assuming a symmetric lens design with with respect to $\overrightarrow{X}$-axis, only even order coefficients are considered.

The numerical tool presented in Chapter 2 was based on elliptical profiles. Some improvements of the model were needed to analyze those polynomial profiles but the general method remains the same assuming the ray propagation in the ridge locally approximated by tangent planes. An updated version is presented in Annex B, where a general approach is chosen, performing the ray tracing with independent inner (Σ_1) and outer (Σ_2) lens profiles. Here, both lens contours are identical, as in Section 3.2. The outer lens contour (Σ_2) is simply defined as a translation of the inner contour (Σ_1) along $\overrightarrow{X}$-axis. In this theoretical approach, the translation value is small in terms of λ, without real impact on the radiation performance analyzed here.

3.4.1 Phase-only optimization

For comparison purposes, the configuration set in Sections 3.2 and 3.3 is maintained. The lens diameter $D = 10\lambda$ and the focal distance $f = 0.7D$, where λ is the wavelength in freespace at the operating frequency. Two focal points F_1 and F_2 are defined by their angular positions $\theta_1 = -\alpha = -30°$ and $\theta_1 = \alpha = 30°$ to define beams pointing at $\theta_2 = \theta_1$, as previously shown in Fig. 3.3a. Using the lens symmetry, only F_2 is considered during the optimization processes. The feed points towards O ensuring a suitable illumination of the lens.

The polynomial coefficients p_k and q_k are optimization parameters for the beam associated to F_2. As presented in Section 3.2, a differential evolution (DE) metaheuristic algorithm ([68], [69]) is used to perform the optimization procedure. Once the lens profiles are optimized for the feed located at F_2, the parameter $g = GO/f$ is used as an additional tuning parameter to enhance performance for any beam radiated in the scanning range $[-\alpha, \alpha]$. This approach is similar to the one used on previous designs derived from the simplified bifocal constrained lens model (Chapter 2).

A phase-only optimization is first conducted with $f = 0.7D$. As described in Subsection 3.2.2, where only elliptical profiles were considered, the objective is to minimize the path length errors Δ_l, defined in Eqn. (3.6), computed along the outer lens contour (Σ_2). The root mean square of the path length error $RMS.\Delta_l$ (Eqn. (3.7)) serves as a cost function.

Here, starting with $n = 4$ (pink dash curve) a substantial reduction of the phase aberrations is observed for the beam associated to F_2 ($\theta_1 = \alpha = 30°$), when

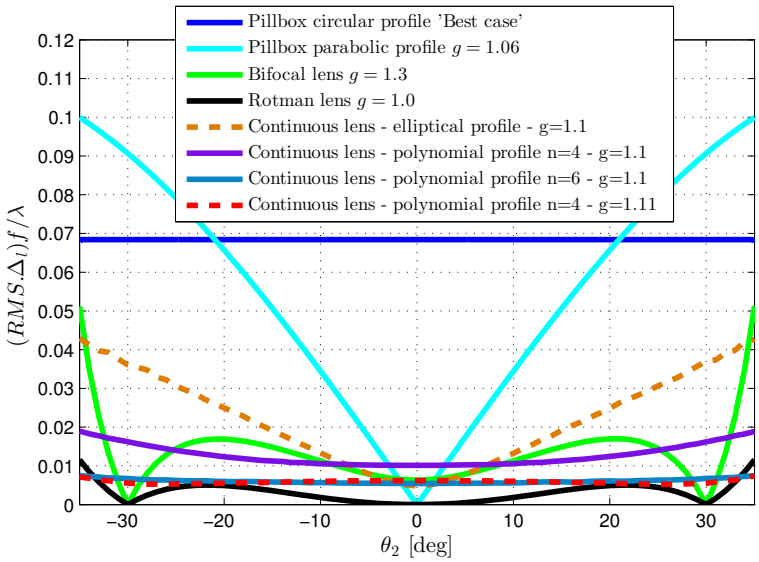

Figure 3.18: RMS value of the path length errors normalized to λ versus pointing angle θ_2 for different lens models and different beamformer types

compared to the previous optimized elliptical profiles (orange curve) (Subsection 3.2.2). Increasing the polynomial degree with $n = 6$ or 10 the phase aberrations may be further reduced for $\theta_2 = \alpha$, with some convergence observed which does not allow for a true focal point (RMS = 0) as in the case of the Rotman lens (black curve) and bifocal constrained lens (green curve). Using $g = GO/f$ as an additional parameter for all the configurations, suitable values have been defined to minimize the maximum RMS level over the entire scanning range $[-\alpha, \alpha]$. The results obtained for $n = 6$ or 10 are almost identical, thus indicating that there is no benefit in increasing further the order of the polynomial functions.

Shapes of the inner lens contour (Σ_1) and the ridge height profile are compared in Fig. 3.19 for the various delay-lens configurations analyzed. The differences observed between optimized polynomial and elliptical models (Fig. 3.19a) are not significant but could not be achieved using the first approach considered in Section 3.2.

The patterns radiated by the different GO models are plotted in Fig. 3.20a. Delay lenses with optimized elliptical profiles have a residual side lobe imbalance ($SLL = -13.2$ dB). Optimized polynomial profiles demonstrate lower and more balanced first side lobe levels ($\cong -18$ dB). Interestingly, the radiation patterns are very similar for the three polynomial cases considered, indicating that the further reduction of phase aberrations observed with $n = 6, 10$ has limited benefit on the first side lobes. A comparison is proposed with HFSS [62] in Fig. 3.20b for the lens model with $n = 10$. The FEM model analyzed is composed of a PPW section closed by PML boundaries and excited by a single primary feed at the focal point, the

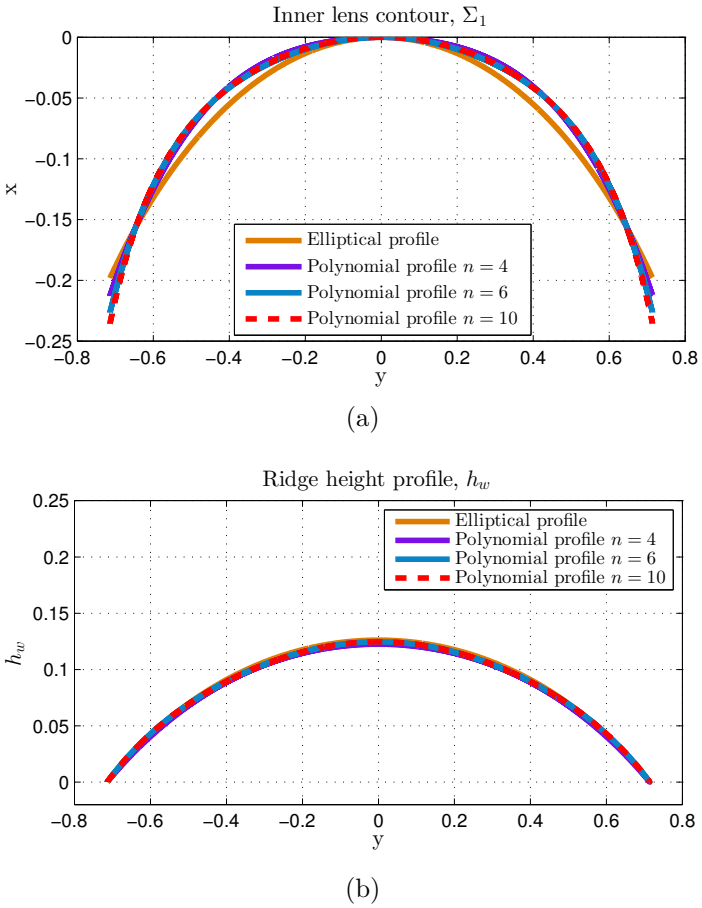

Figure 3.19: Comparison between elliptical and polynomial shapes of the PPW lens-like beamformer after phase optimization : (a) inner lens contour, (b) ridge height profile. The coordinates are normalized to the focal distance.

objective is to be as close as possible to the GO numerical model assumptions as described in this paper. A good agreement is demonstrated, including the pointing direction, the half power beamwidth θ_{3dB} and the first side lobes levels SLL down to levels of about 25 to 30 dB below the peak directivity.

3.4.2 Pattern optimization

As mentioned in the previous sections, the amplitude distribution over (Σ_2) and consequently the SLL may be impacted by the distribution of rays. For this reason, a pattern-based optimization is also investigated. The same constraints as in Subsection 3.2.3 for a similar configuration ($f = 0.7D$) are implemented: $\theta_{target} = 30°$, $\theta_{3dB} = 6.5°$ and $SLL < -18$ dB, those values being derived from the ideal bifocal constrained lens model (Chapter 2). Several optimizations are repeated to target a SLL as low as possible.

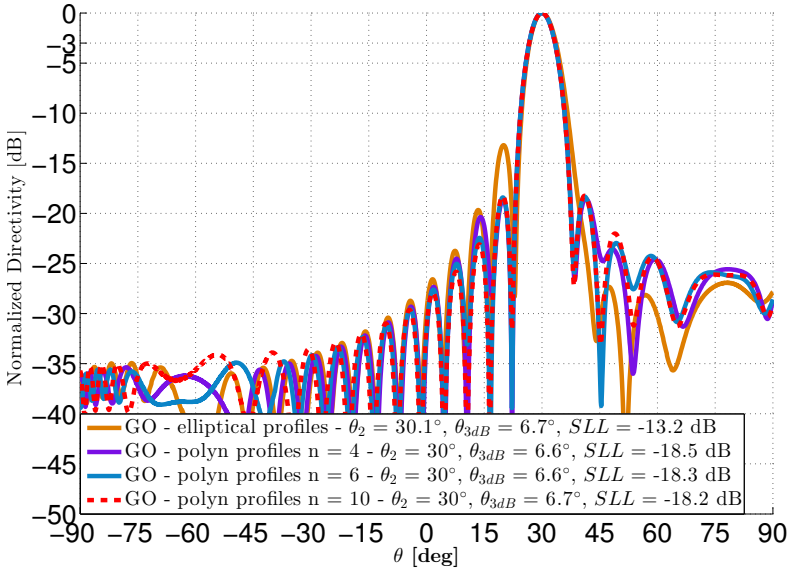

(a)

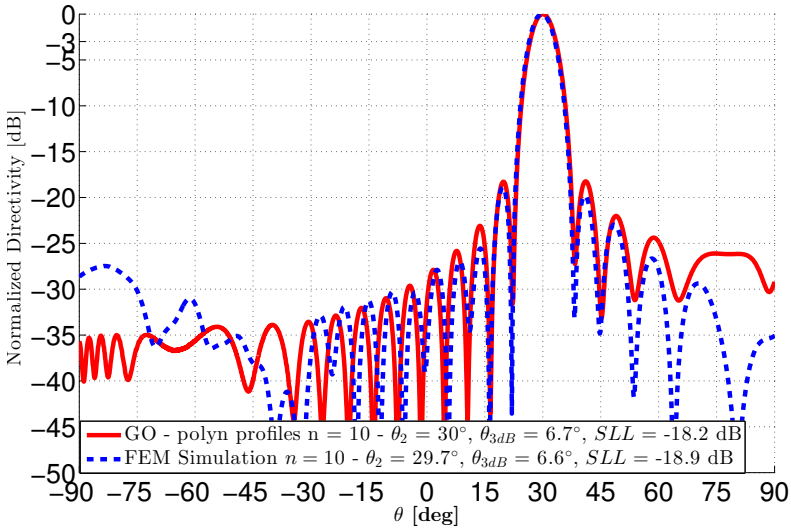

(b)

Figure 3.20: Radiation patterns of the PPW beamformer in H-plane for $\theta_1 = \alpha$, at the center frequency: (a) GO models, (b) GO continuous lens model – phase optimization (validation with HFSS) only considering $n = 10$. The polynomial profiles coefficients are the following : $p = [-0.999, -0.597, 0.0618, -0211, -0.223, 0]$ and $q = [-0.178, -0.031, -0.001, -0.029, -0.210, 0]$.

The optimized patterns are plotted in Fig. 3.21a and as observed, the results are very similar to those obtained with the phase-only optimization procedure (Fig. 3.20a) for all values of n. A good agreement between HFSS [62] and the GO tool is maintained using this optimization method, as shown in Fig. 3.21b. A marginal

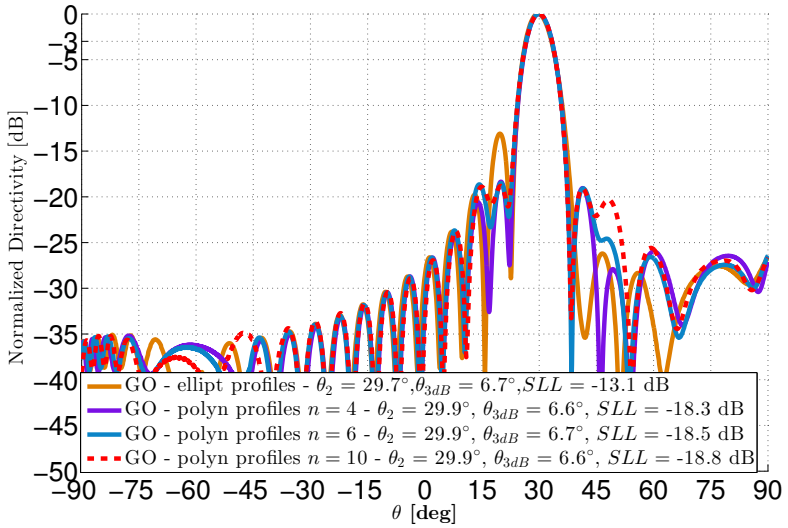

(a)

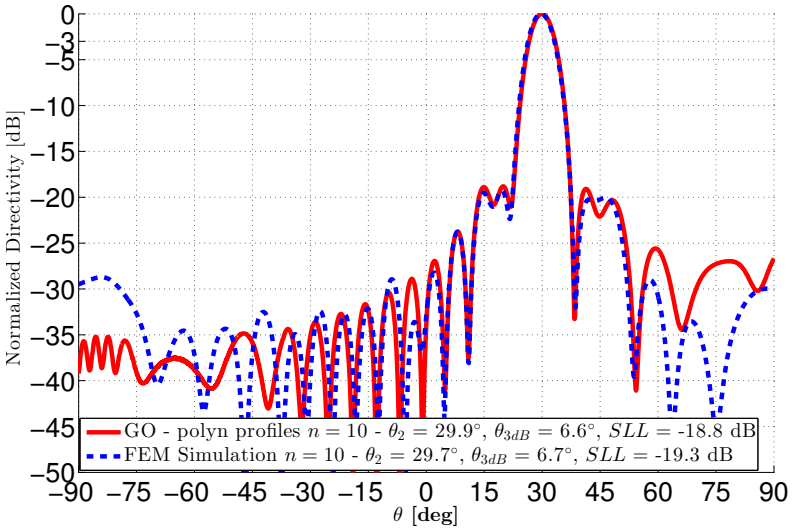

(b)

Figure 3.21: Radiation patterns of the PPW beamformer in H-plane for $\theta_1 = \alpha$, at the center frequency: (a) GO models, (b) GO continuous lens model – pattern optimization (validation with HFSS) only considering $n = 10$. The polynomial profiles coefficients are the following : $p = [-0.912, 0.378, -0.980, 0.186, -0.269, 0]$ and $q = [-0.129, -0.206, 0.024, 0.103, -0.243, 0]$.

improvement on the SLL is observed (ranging from 0.5 to 1 dB depending on the numerical results compared), indicating that SLL imbalance is mostly driven by phase aberrations. The numerical results presented in this section clearly indicate the potential of the polynomial-shaped delay lens over the previously investigated elliptical-based lens designs.

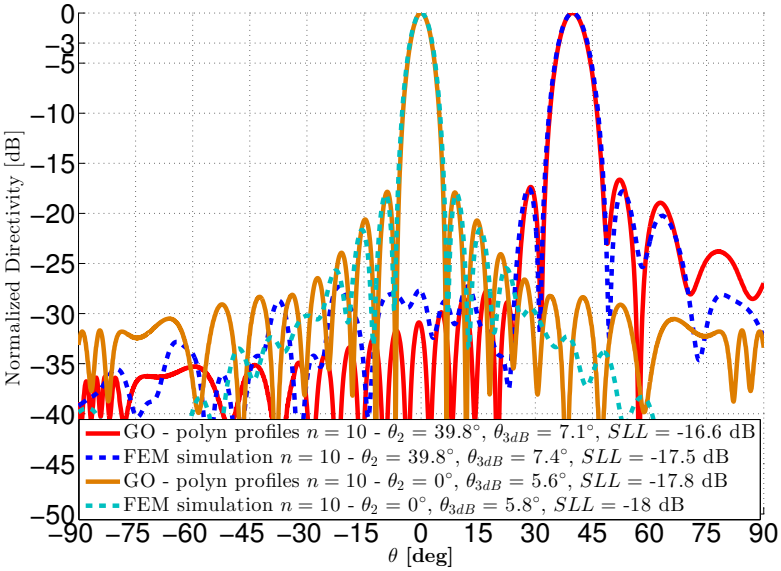

Figure 3.22: Radiation patterns of the PPW beamformer in H-plane for $\theta_1 = 40°$ and $\theta_1 = 0°$ with $g = 1.2$. A pattern optimization, validated with HFSS, has been performed considering $n = 10$. The optimized polynomial profiles coefficients are the following : $p = [-0.3187, -0.9369, -0.6576, 0.2634, -0.2593, 0]$ and $q = [0.4165, 0.2469, -0.3112, 0.0238, -0.1961, 0]$.

As an additional example, a pattern optimization was performed for a similar configuration ($f = 0.7D$), with $\theta_1 = \alpha = 40°$. The same constraints as in the previous optimization are implemented: $\theta_{target} = 40°$, $\theta_{3dB} = 6.5°$ and $SLL < -18$ dB. The beam associated to the central angular position $\theta_1 = 0°$, with an optimum focal arc ($g = 1.2$) is also plotted. As observed, excellent radiation properties in scanning are also demonstrated in this case, confirmed by an excellent agreement with HFSS [62].

3.5 Conclusion

Phase and pattern optimization procedures have been introduced in this chapter, to design continuous parallel plate waveguide delay-lens multiple beam antennas. Based on elliptical profiles, starting from a bifocal constrained lens approach, the proposed configurations all demonstrate a residual side lobe imbalance. This results in some interferences when multiple beam applications are targeted.

Two design evolutions, a thick delay lens with different inner and outer lens contours and a thin lens with polynomial profiles, were introduced to increase the control on both phase and amplitude distributions on the outer lens contour (Σ_2). The thick lens designs proved to be outside the domain of validity of the

developed GO tool, but the solution remains of interest in combination with alternative manufacturing techniques. The numerical results of the lens shaped with polynomials confirm the potential of the proposed profiles with path length errors very similar to those of simplified constrained lens models over a large scanning range ($[-30°, 30°]$). The corresponding radiated patterns present reduced and more balanced side lobe levels, when compared to the previously introduced solution using elliptical contour and profile for the delay-lens shape.

To validate those proposed developments and the scanning performances demonstrated, an experimental validation is proposed in Chapter 4.

4

Shaped Continuous Parallel Plate Waveguide Lens-Like Multiple Beam Antenna at Ka-band

Contents

Abstract

An experimental validation of the scanning performance demonstrated in the previous Chapter 3, using polynomial shaped delay lens profiles, is proposed here.

The manufacturing and test of a prototype designed to operate over the up-link Ka band ([27.5-31] GHz) is performed.

The proposed design is shown in Section 4.1. Eleven beams are radiated over a wide angular range ([$-31.5°$, $31.5°$]). The numerical results, presented in Section 4.2, demonstrate excellent radiation performances over the considered scanning range. In Section 4.3, a manufactured and measured prototype confirms the predicted performances, including low scanning loss and high radiation stability over the entire frequency range. High radiation efficiencies are demonstrated with this fully metallic design, particularly suitable for space applications.

4.1 Modeling and design

The delay-lens prototype discussed in this chapter has been designed to work over the entire up-link Ka-band ([27.5-31 GHz]) allocated to satellite communications. The lens diameter and the focal distance are respectively equal to $D = 20\lambda$ and $f = 0.7D$, where $\lambda = 10.9$ mm, the wavelength in free space at the lowest frequency of the operating band. The complete design is shown in Fig. 4.1.

The PPW cavity height is equal to $H_{PPW} = 2$ mm, such that only the fundamental TEM mode can propagate within the frequency band considered. The outer lens contour (Σ_2) is defined as a translation of 2 mm of the inner lens contour (Σ_1) along $\overrightarrow{X}$-axis. The radiating horn is defined along the local normal vector of the outer lens contour (Σ_2) with a length of 30 mm and a final height equal to 20 mm.

Eleven feeds are distributed on a circular focal curve (Fig. 4.1c) with angular positions θ_1 ranging from $-28.5°$ to $31.5°$ with an angular step of $6°$. The feed dimensions are equal to a_{WG}=7.556 mm and a_{FEED}=14 mm. This configuration provides patterns with a beamwidth $\theta_{3dB} = 3°$ while targeting minimum SLL, which requires an adequate edge taper and hence a minimum feed aperture. Consequently, this lens alone does not provide the adequate cross-over level between adjacent beams (typically lower than 3 dB below the peak directivity). An antenna system made of two superimposed lenses is defined. The two considered lenses are identical and a $180°$ rotation around an axis R_L is operated between both, as shown in Fig. 4.2a. 22 equally spaced beams are radiated, achieving the desired cross-over level. The feeds distributions of both lenses are provided in Fig. 4.2b, explaining clearly the way to provide the $3°$ spacing between the 22 beams. This approach is similar to the one proposed in [72], where a 2D stack of Rotman lenses is presented to provide triangular beam lattices. On the first 1D stack, the Rotman lens geometry considers feeds rotated around a central axis by an amount of the beam spacing

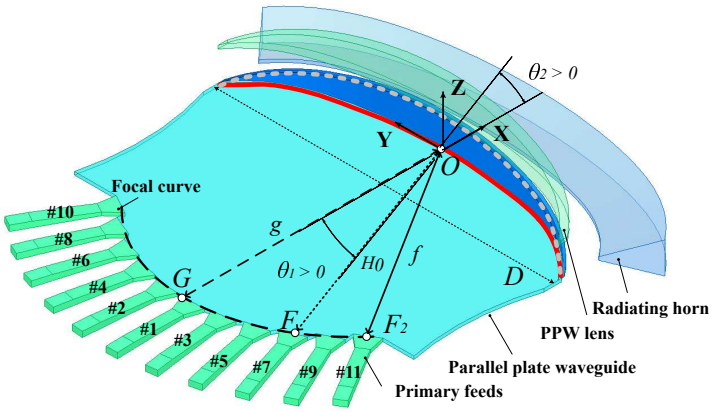

(a) 3D view

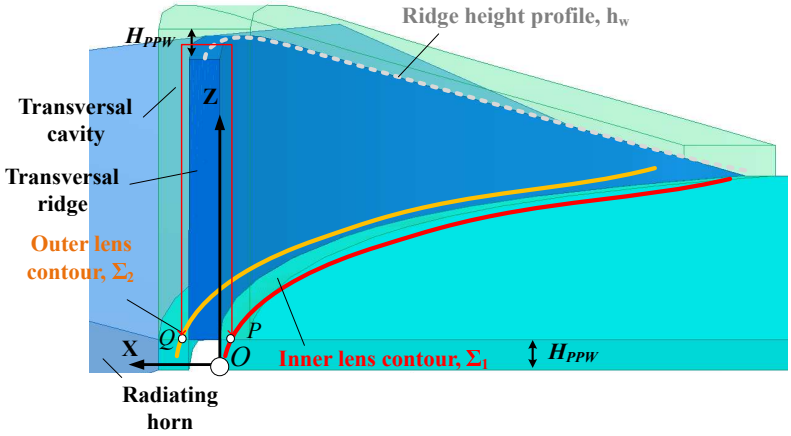

(b) Cut view in $(O, \overrightarrow{X}, \overrightarrow{Z})$ plane of the PPW lens

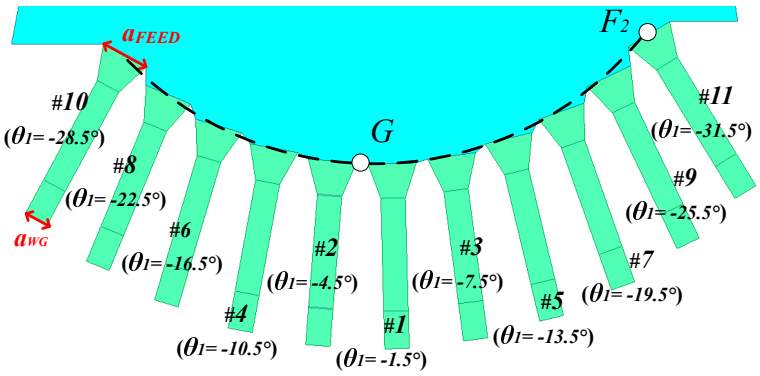

(c) Top view of the feeds system

Figure 4.1: Continuous parallel plate waveguide (PPW) lens-like beamformer at Ka-band.

divided by 4. Between two superimposed lenses, a 180° rotation is then operated to achieve a desired beam spacing divided by 2. Applying this method to the concept proposed here, the continuous lens (Fig. 4.1a) defines a beam spacing of 6° and the rotation of the feeds with respect to the central $\overrightarrow{X}$-axis along the

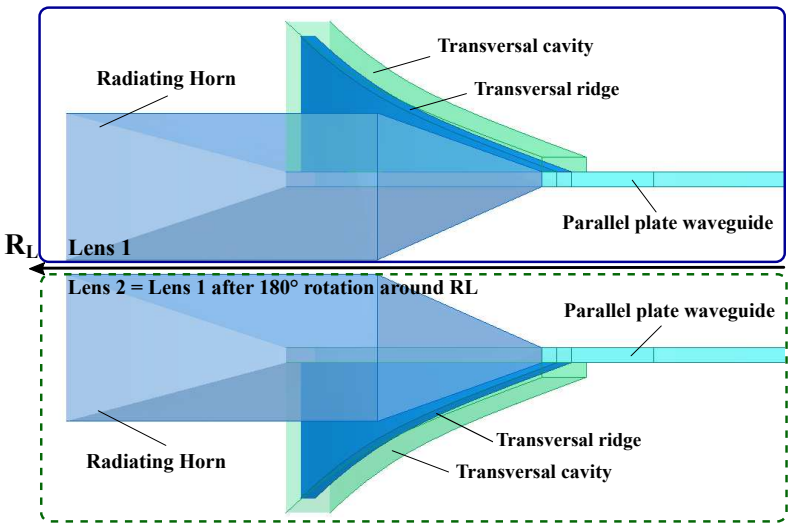

(a)

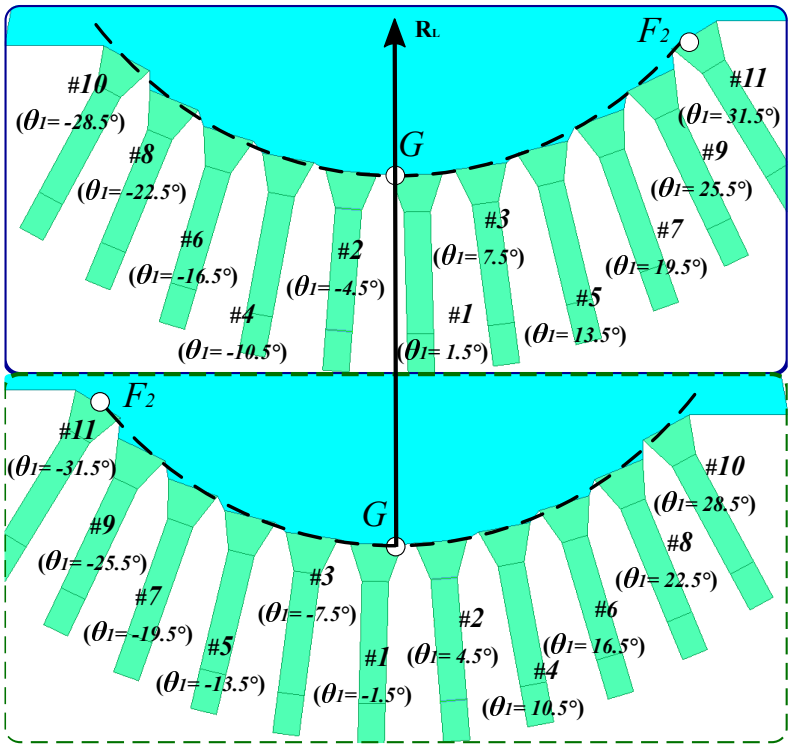

(b)

Figure 4.2: Antenna system to provide a complete coverage of 22 beams with a desired 3 dB cross-over level. (a) Final configuration with two superimposed lenses, lens 2 is identical to lens 1, defined with a 180° rotation around R_L (b) 180° rotation of the feed distribution obtained between lens 1 and lens 2.

focal arc equals $6/4 = 1.5°$ (Fig. 4.1c). The 180° rotation between two lenses finally provides the 22 beams spaced of 3°.

A pattern based optimization, as presented in the previous chapter (Subsection

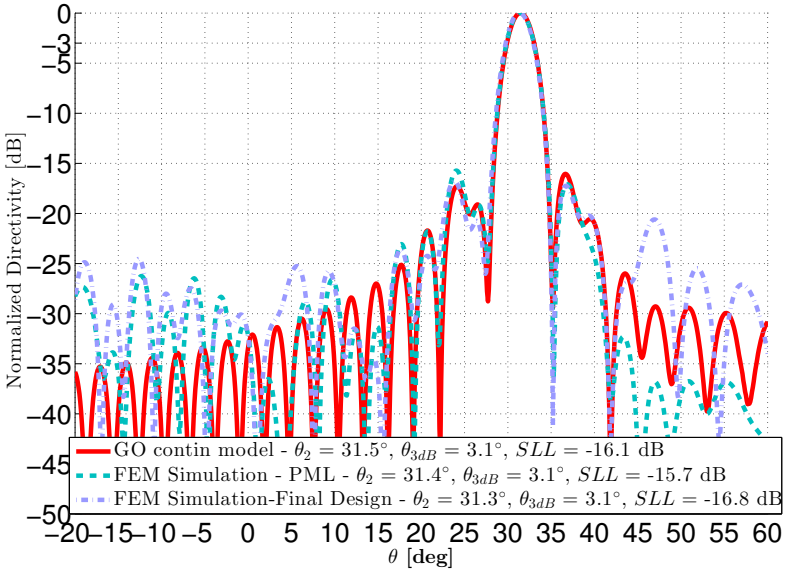

Figure 4.3: H-plane normalized radiation patterns of the PPW beamformer at $f_0 = 30$ GHz for feed #11 defined by an angular position $\theta_1 = 31.5°$ computed with the GO continuous model (red curve), the FEM analysis considering PML boundaries (ideal design) and the final design.

3.4.2), is used to achieve the desired performance at the frequency $f_0 = 30$ GHz for the extreme beam pointing at $\theta_2 = \theta_1 = 31.5°$. The polynomial coefficients resulting from the optimization process are the following: p =[-0.217,-0.747,-0.165,-0.090,-0.246,0] and q =[-0.527,-0.048,0.038,0.061,-0.237,0]. Then g is tuned to achieve the best results over the scanning range under consideration, leading to $g = 1.1$.

4.2 Numerical results

The H-plane radiation patterns obtained with the GO model for the extreme feed #11 ($\theta_1 = 31.5°$) are first compared to the corresponding FEM model results in Fig. 4.3 for two cases, the ideal one considering PML boundaries on the edges, thus neglecting reflection effects, and the one with PEC boundaries as in the final design prototyped. The choice to use metallic sidewalls in the prototype leads to a simpler design and assembly (no absorbing material or dummy ports required) but slightly degrades side lobes away from the main lobe. This first comparison demonstrates the accuracy of the GO model by the agreement with the ideal FEM simulation [62]. The main beam direction and the HPBW computed with the GO and FEM models are respectively equal to 31.5°, 3.1° and 31.4°, 3.1°. The first side lobe level is equal to -16.1 and -15.7 dB for the two models respectively. The other side lobes predicted are also accurate, down to levels of about 25 dB below the peak

directivity. When the final FEM model of the as-built beamformer is considered, a good prediction is maintained for the main beam and the first side lobes. Some higher side lobes are observed far away from the main lobe region ($[-90°, -60°]$), explained by the reflection effects due to the metallic side walls. Those effects remain quite low, limited to power levels 20 dB below the maximum directivity.

For the beams presented in Fig. 4.4a and 4.4b, the prediction given by the GO model is still in accordance with the FEM simulations. Note that in both cases, the embedded primary pattern of the feed is implemented in the GO model. Indeed, some marginal blockage effects appear due to the on-axis focal distance $g > 1$ combined with the fact that all feeds are pointing towards the center of the lens O (Fig. 4.1a). This results in some asymmetry in the primary feed patterns affecting the final radiation patterns. In the design described here, the primary pattern of feed #7 ($\theta_1 = 19.5°$) is impacted by #9, defined at $\theta_1 = 25.5°$. The central feed #1 ($\theta_1 = 1.5°$) is less impacted by this effect but is as well considered in the complete feeding system environment, as some coupling with the adjacent feeds also marginally impacts its primary pattern.

For the feed defined at $\theta_1 = 19.5°$ (Fig. 4.4a), the main beam direction and HPBW are respectively equal to 19.4°, 2.9° for the continuous model and 19.5°, 2.9° for the ideal FEM simulation. The first side lobe levels are well predicted by the continuous model ($SLL = -17.6$ dB) as compared to -17.5 dB (ideal FEM simulation). When $\theta_1 = 1.5°$ (Fig. 4.4b), the pattern provided by the GO model ($\theta_2 = 1.5°$, $\theta_{3dB} = 2.6°$ and $SLL = -17$ dB) is still validated by the ideal FEM simulation ($\theta_2 = 1.5°$, $\theta_{3dB} = 2.6°$ and $SLL = -17.7$ dB). In both cases, the FEM model with PEC boundaries shows some far out lobe level degradation without major impact on the validation proposed here. Hence, this supports the manufacturing of the simpler prototype with metallic walls on the edges of the PPW section.

For comparison purposes, all the feeds have been considered in Fig. 4.5 and 4.6 at the frequency $f_0 = 30$ GHz, with the GO model, the FEM analysis considering PML boundaries (ideal design) and the final as-built design. In all cases, the prediction described previously for feeds #11 (Fig. 4.3), #7 and #1 (Fig. 4.4) is confirmed. The far out lobe level degradation is still observed with the final FEM simulation (PEC boundaries) but always with levels limited to 20 dB below the maximum peak of directivity.

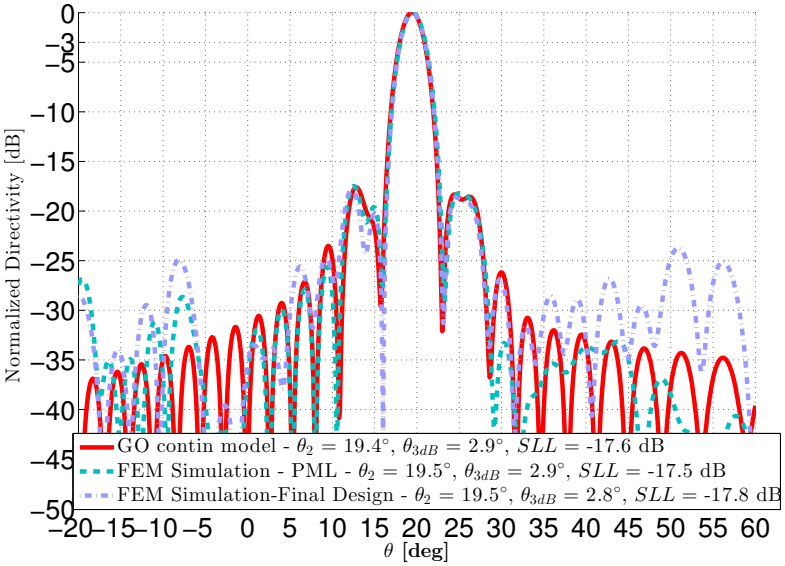

(a) $\theta_1 = 19.5°$

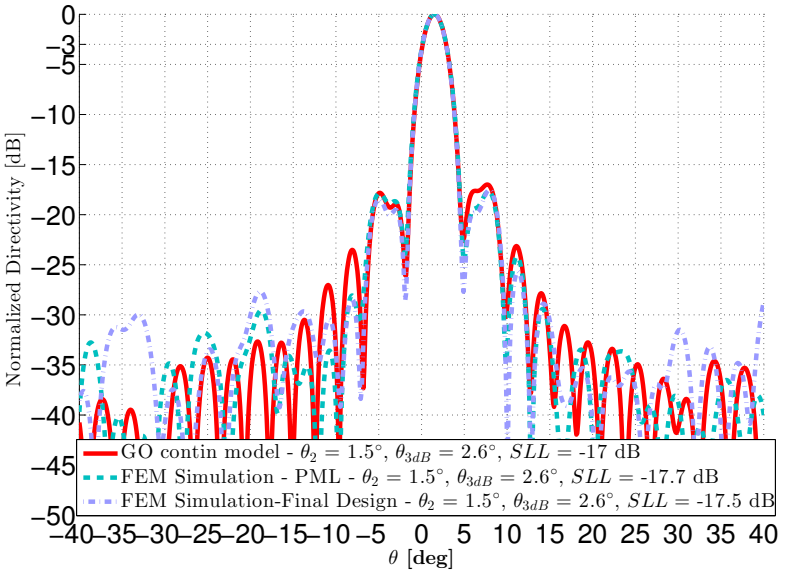

(b) $\theta_1 = 1.5°$

Figure 4.4: H-plane normalized radiation patterns of the PPW beamformer at $f_0 = 30$ GHz for feeds #7 and #1, defined by their angular positions θ_1, computed with the GO continuous model (red curve), the FEM analysis considering PML boundaries (ideal design) and the final design

4.3 Experimental validation

4.3.1 Antenna manufacturing

The antenna design described in the previous section has been manufactured in bare aluminum. A picture of one plate inside the milling machine is shown in

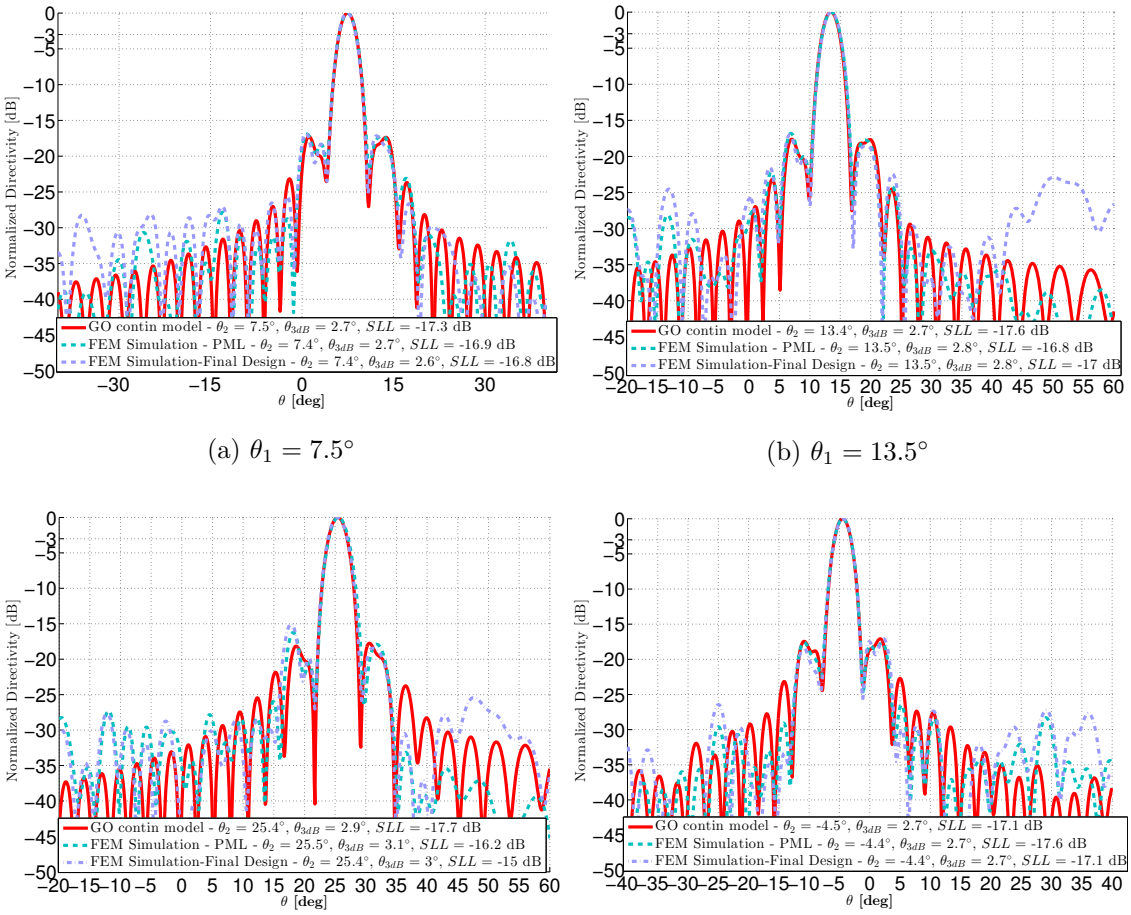

(a) $\theta_1 = 7.5°$ (b) $\theta_1 = 13.5°$

(c) $\theta_1 = 25.5°$ (d) $\theta_1 = -4.5°$

Figure 4.5: H-plane normalized radiation patterns of the PPW beamformer at $f_0 = 30$ GHz for feeds #3, #5, #9 and #2, defined by their angular positions θ_1, computed with the GO continuous model (red curve), the FEM analysis considering PML boundaries (ideal design) and the final design.

Fig. 4.7. As a 180° rotation is operated from the same lens geometry to obtain the final antenna system (Fig. 4.2a), only one lens can be manufactured and measured in this experimental validation.

The two blocks, corresponding to the top and bottom part of the antenna, comprise for one the transversal cavity and for the other the transversal ridge, as defined in Fig. 4.1. The transversal ridge part (or transversal blade) is presented in Fig. 4.8a, where we can recognize both inner lens (Σ_1) and ridge height (h_w) profiles. The two blocks are assembled by means of screws, as shown in Fig. 4.8b.

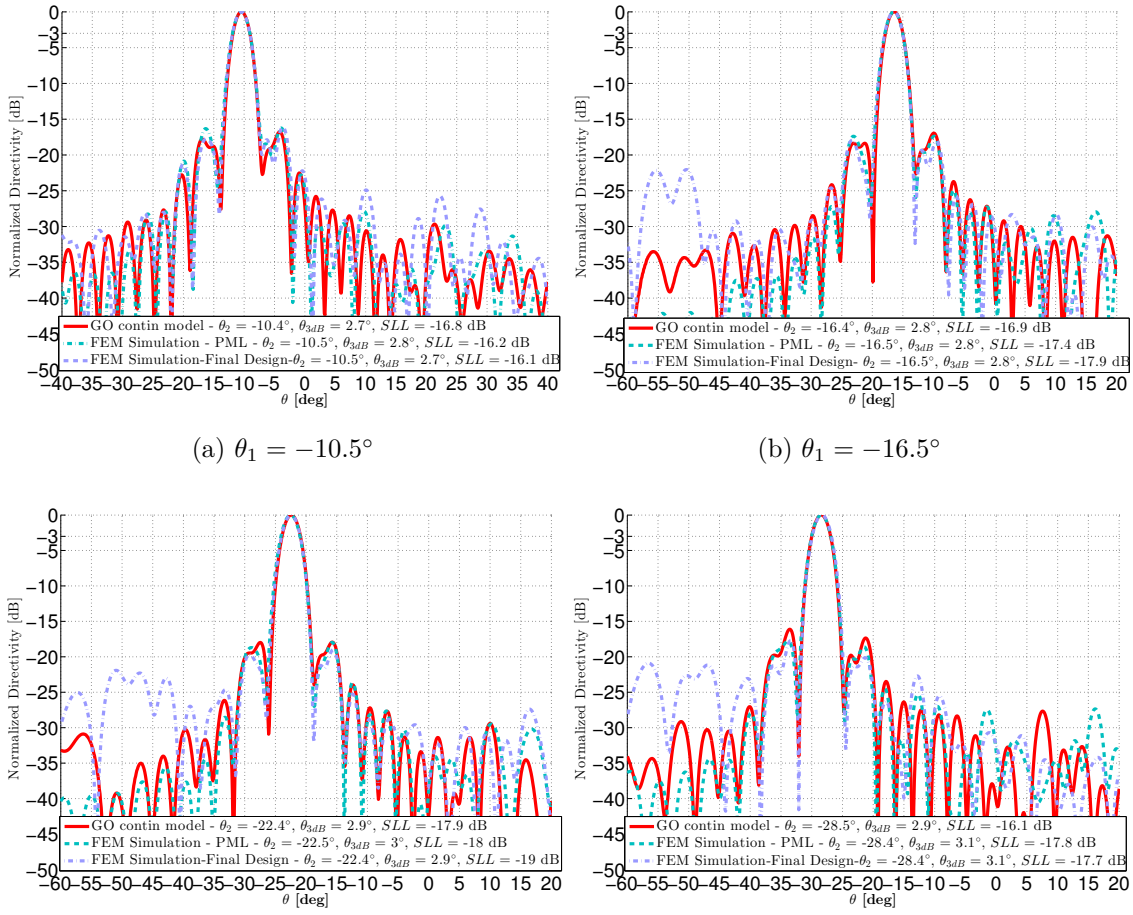

(a) $\theta_1 = -10.5°$ (b) $\theta_1 = -16.5°$

(c) $\theta_1 = -22.5°$ (d) $\theta_1 = -28.5°$

Figure 4.6: H-plane normalized radiation patterns of the PPW beamformer at $f_0 = 30$ GHz for feeds #4, #6, #8 and #10 defined by their angular positions θ_1 computed with the GO continuous model (red curve), the FEM analysis considering PML boundaries (ideal design) and the final design.

4.3.2 Far-field measurement

The prototype has been measured using the millimeter wave far-field compact antenna test range (CATR) available at IETR. A picture of the measurement chamber is given in Fig. 4.9.

A first measurement campaign is considered for all the feeds (11 for this prototype), to measure the different H-plane radiation patterns. They will be used to validate the GO model and the comparisons performed in Section 4.2.

Then a second measurement campaign is done over a full sphere for directivity and gain characterization. This second measurement is performed only for #11, #7, #1, #2, #6 and #10, due to the time needed to perform them.

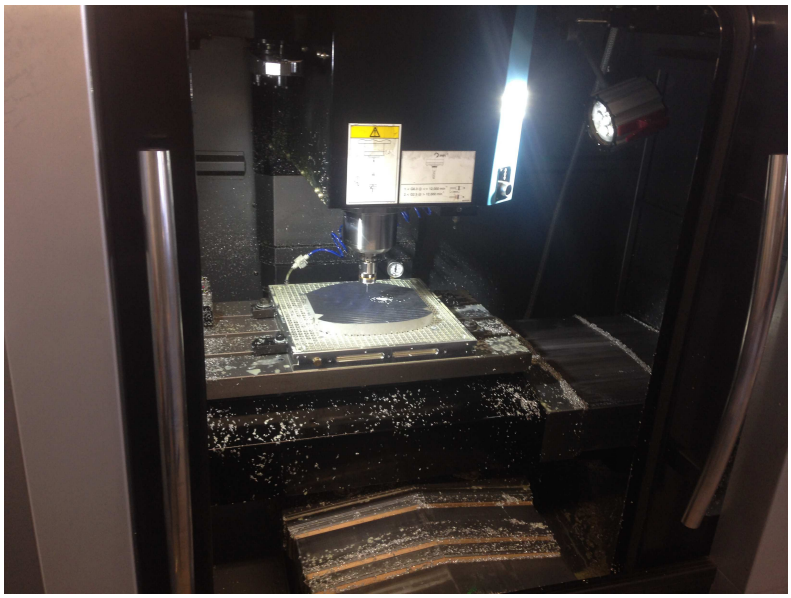

Figure 4.7: Manufacturing of the prototype inside the milling machine (IETR).

4.3.2.1 H-plane radiation patterns: Validation with the measurements

Comparisons between the final FEM simulation results and the measurements are reported in Fig. 4.10, for feed #11. An excellent agreement is obtained along the scanning range reported and for power levels down to 30 dB below the peak directivity. The agreement is maintained over the entire scanning range [−90° 90°] acquired during the measurement. The main beam directions equal 31.3° and 31.2° respectively for the FEM simulation and the measurement. The HPBW θ_{3dB} obtained are identical while the SLL are equal to -16.8 and -16.4 dB respectively, indicating excellent agreement.

The comparisons are performed in Fig. 4.11a and 4.11b for feeds #7 and #1. For feed #7, the pointing angle, HPBW and SLL equal 19.5°, 2.8°, -17.8 dB and 19.4°, 2.8°, -17.1 dB respectively for the FEM simulation and the measurement. For the central feed #1 (Fig. 4.11b), the excellent agreement observed between simulation and measurement is further confirmed.

For comparison purposes, feeds #3, #5, #9 and #2 are also reported in Fig. 4.12 at the central frequency $f_0 = 30$ GHz. For all cases, the agreement described previously for feeds #11 (Fig. 4.10), #7 and #1 (Fig. 4.11) is confirmed.

The reconstructed coverage with the 22 measured beams is shown in Fig. 4.13. The patterns obtained at $f_0 = 30$ GHz with the considered lens (continuous blue line) have been combined with the ones obtained after the 180° lens rotation around axis R_L, as shown in Fig. 4.2a). As observed a 3 dB cross-over level is obtained while maintaining low side lobe levels over the entire scanning range ([−31.5°, 31.5°]).

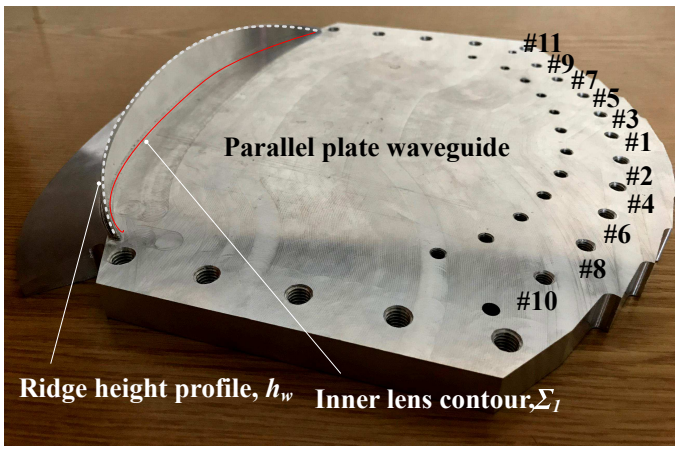

(a)

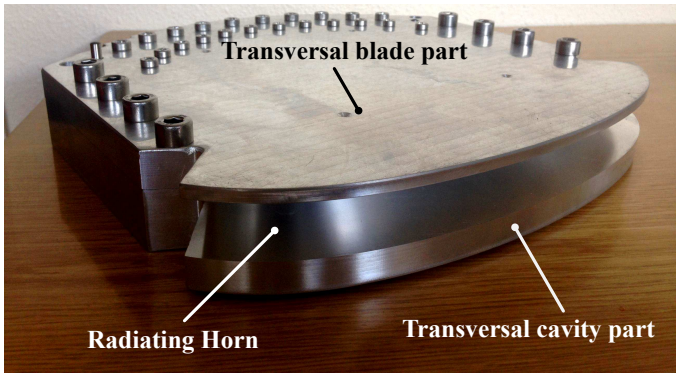

(b)

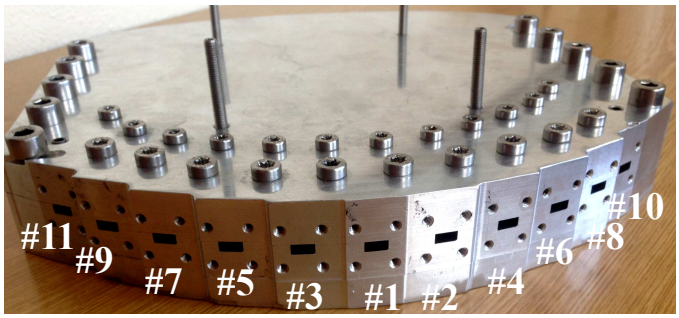

(c)

Figure 4.8: Prototype of the continuous PPW lens-like beamformer at Ka-band. (a) lower part of the PPW beamformer with the transversal ridge, (b) full assembled beamformer and (c) feeds distribution

4.3.2.2 Performance over the frequency band

The H-plane radiation pattern of feed #11 is plotted over the range [27.5-31] GHz, in Fig. 4.14, to demonstrate the stability of the design in frequency (pointing angle, SLL). Some higher side lobe levels are observed far away from the main lobe region ($[-90°, -60°]$) and are due to the metallic side walls, as discussed

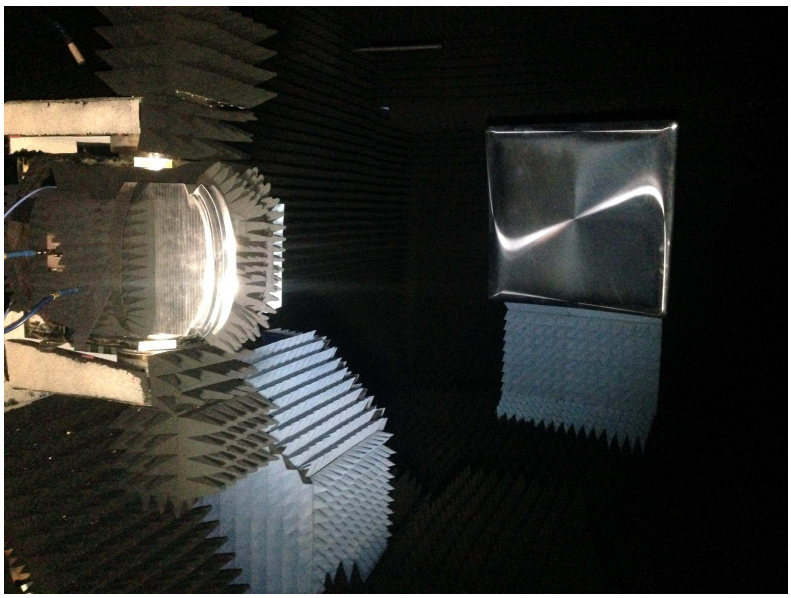

Figure 4.9: Measurement setup in the compact antenna test range (CATR) facility of IETR

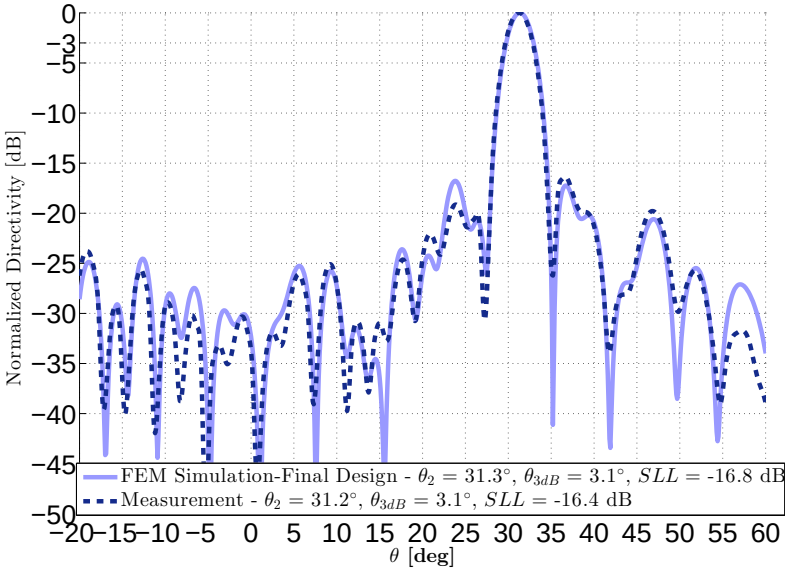

Figure 4.10: H-plane normalized radiation patterns of the final PPW beamformer design at $f_0 = 30$ GHz for feed #11, defined by an angular position $\theta_1 = 31.5°$, computed with the FEM simulation (continuous line) and after measurement (dash line).

previously. Their levels remain quite low, with power levels around -20 dB below the maximum peak of directivity.

The HPBW and the side lobe levels are plotted in Fig. 4.15 over the entire up-link Ka frequency band. At $f_0 = 30$ GHz, the difference in terms of measured HPBW is about 0.1° between feeds #11 and #7 and 0.4° between feeds #11 and #1.

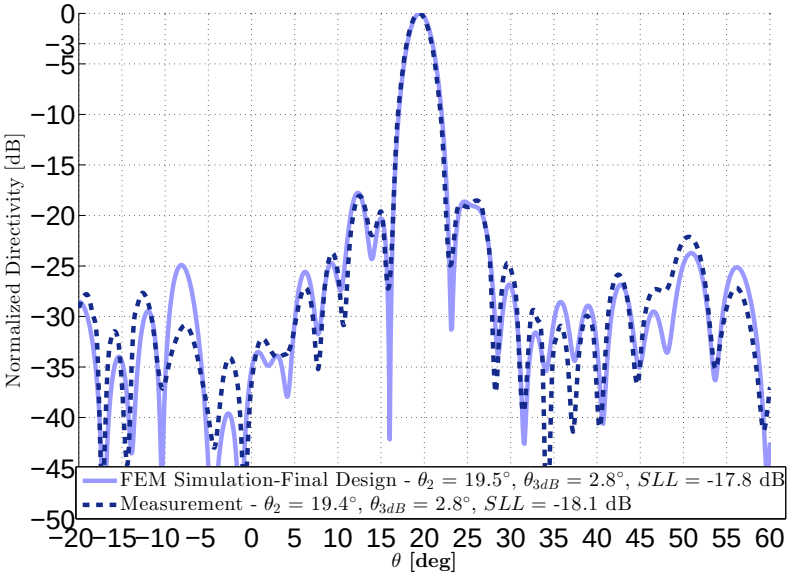

(a) $\theta_1 = 19.5°$

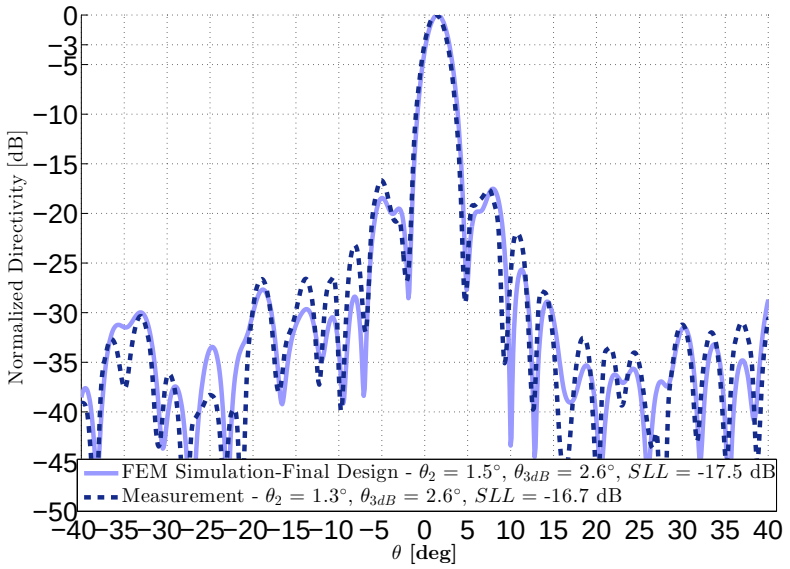

(b) $\theta_1 = 1.5°$

Figure 4.11: H-plane normalized radiation patterns of the final PPW beamformer design at $f_0 = 30$ GHz for feeds #7 and #1 defined by their angular positions (a) $\theta_1 = 19.5°$ and (b) $\theta_1 = 1.5°$, computed with the FEM simulation (continuous line) and after measurement (dash line).

The evolution over the entire frequency range is limited to 0.3° for the three feeds considered here. For feeds #11 and #1, the measured HPBW equals respectively 3.4°, 3.1° at $f = 27.5$ GHz and 3.1°, 2.7° at $f = 31$ GHz. The SLL plotted in Fig. 4.15 further demonstrate the scanning or phase aberrations properties of this

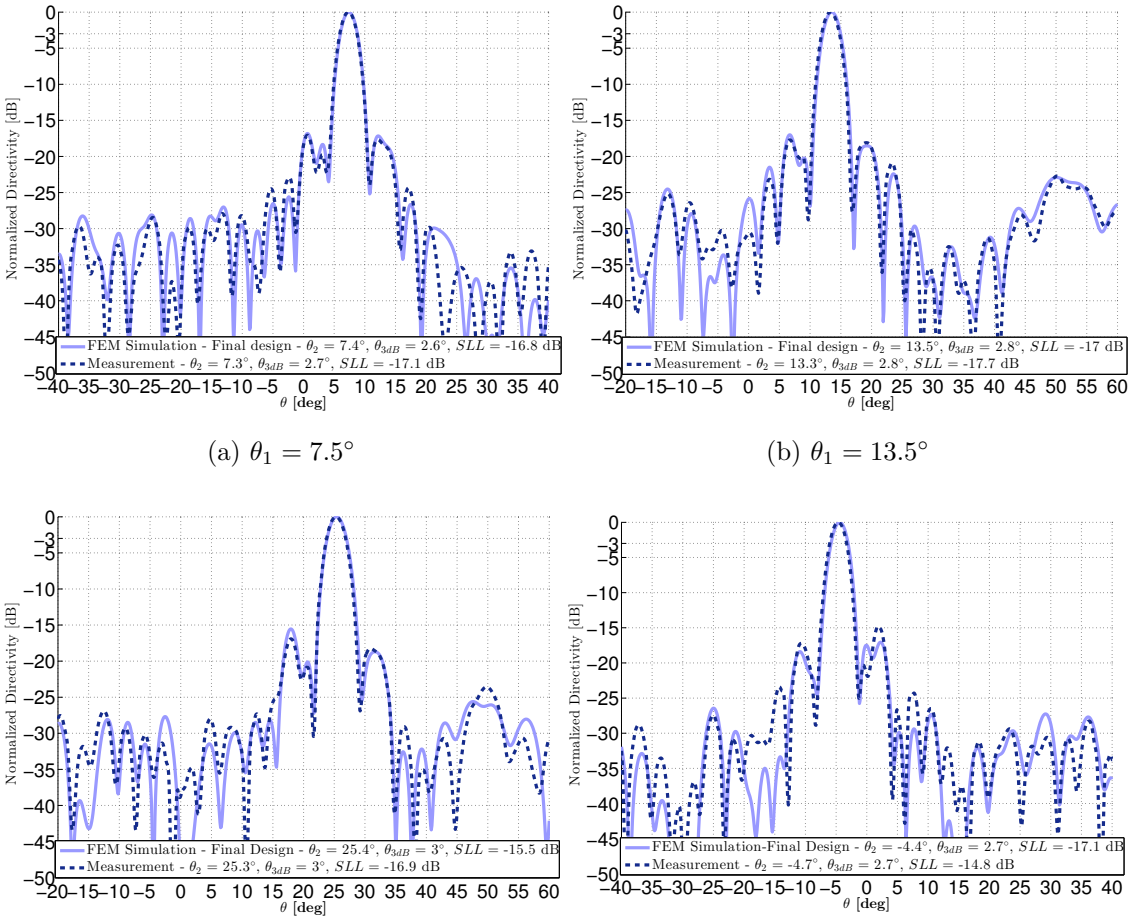

(a) $\theta_1 = 7.5°$ (b) $\theta_1 = 13.5°$

(c) $\theta_1 = 25.5°$ (d) $\theta_1 = -4.5°$

Figure 4.12: H-plane normalized radiation patterns of the final PPW beamformer design at $f_0 = 30$ GHz for feeds #3, #5, #9 and #2 defined by their angular positions θ_1, computed with the FEM simulation (continuous line) and after measurement (dash line).

concept, since no large degradations are visible between feeds #11 ($\theta_1 = 31.5°$) and #1 ($\theta_1 = 1.5°$) over the entire frequency range. Some larger values are observed at some frequency points, especially for feeds #11 (blue curve) and #1 (orange curve), limited to -15 dB with respect to the maximum peak of directivity.

4.3.2.3 Directivity and realized gain

The measured realized gain values are compared to the directivity computed with the FEM simulation in Fig. 4.16 for the extreme ($\theta_1 = 31.5°$) and central ($\theta_1 = 1.5°$) feeds.

Simulated and measured scanning losses have been computed from the interpolated values (Fig. 4.16) of feeds #11 ($\theta_1 = 31.5°$) and #7 ($\theta_1 = 19.5°$), with respect to the central feed #1 ($\theta_1 = 1.5°$). Those results are shown in Fig. 4.17.

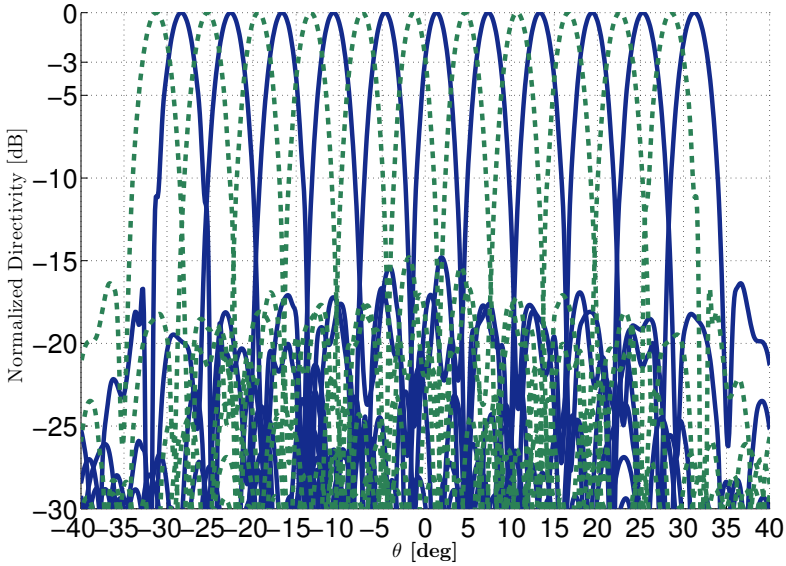

Figure 4.13: Measured H-plane normalized radiation patterns of the final PPW beamformer design at $f_0 = 30$ GHz for all the feeds (continuous line) and for the same beamforer considering the 180° rotation around R_L (dash line).

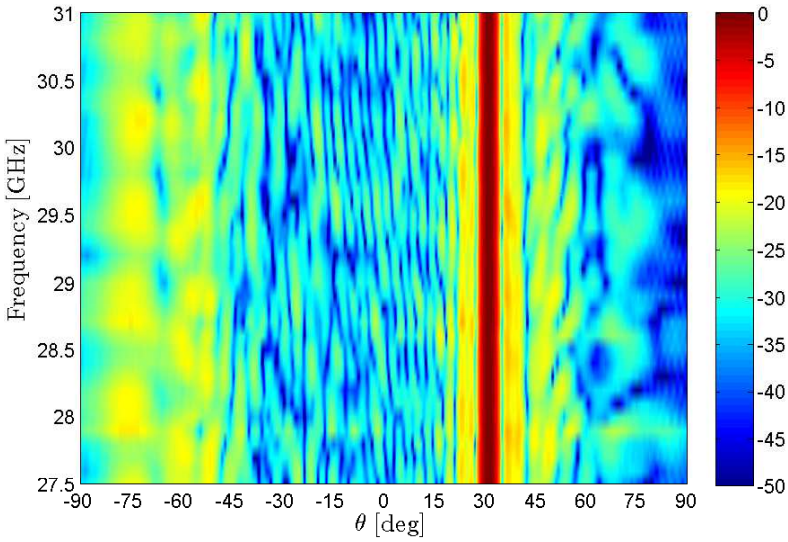

Figure 4.14: Measured H-plane normalized radiation patterns of the final PPW beamformer design over the entire frequency band ([27.5-31] GHz) for feed #11, defined by an angular position $\theta_1 = 31.5°$.

Low scanning losses were expected at the frequency $f_0 = 30$ GHz, where the interpolated directivities equal 26 and 25.35 dB respectively for feeds #1 and #11. This correspond to a simulated scan loss of 0.65 dB, as shown in Fig. 4.17. The simulated scan loss obtained for feed #7 at this frequency equals 0.31 dB.

The measured interpolated realized gain values at $f_0 = 30$ GHz equal 25.8 dB for

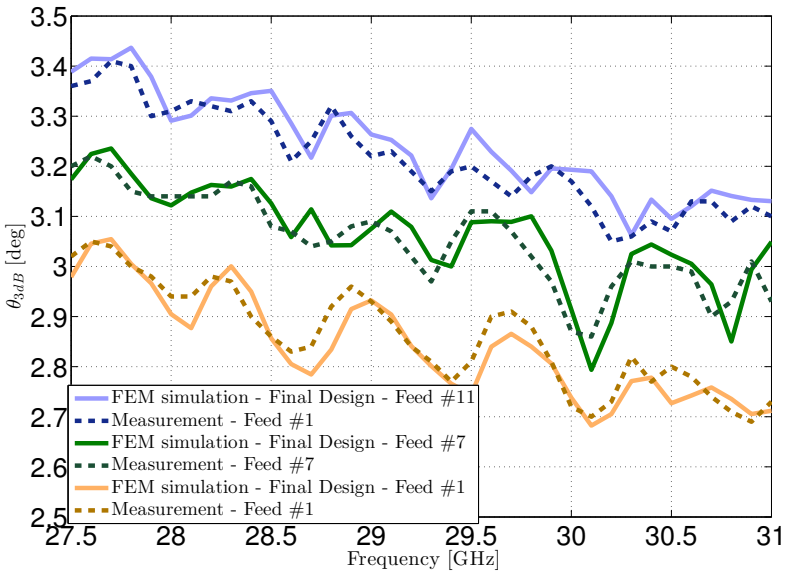

(a) HPBW θ_{3dB}

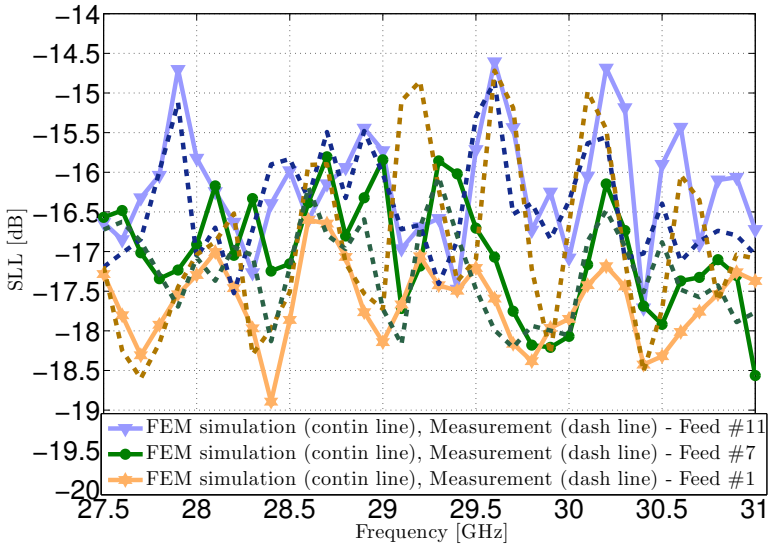

(b) Side lobe level SLL

Figure 4.15: HPBW θ_{3dB} and side lobe levels SLL in H-plane of the final PPW beamformer design over the entire frequency band ([27.5-31] GHz) for feeds #11 ($\theta_1 = 31.5°$, #7 ($\theta_1 = 19.5°$) and #1 ($\theta_1 = 1.5°$).

feed #1, corresponding to a radiation efficiency $\eta = 95.5$ %, and 25.2 dB ($\eta = 98$ %) for feed #11. In Fig. 4.17 the gain drop observed equals 0.55 dB for feed #11 and 0.23 dB for feed #7. Those results confirm the scanning losses computed with the simulated directivity values. The efficiency obtained for the reference central feed #1 is slightly lower than those ones, explaining the better scan losses computed.

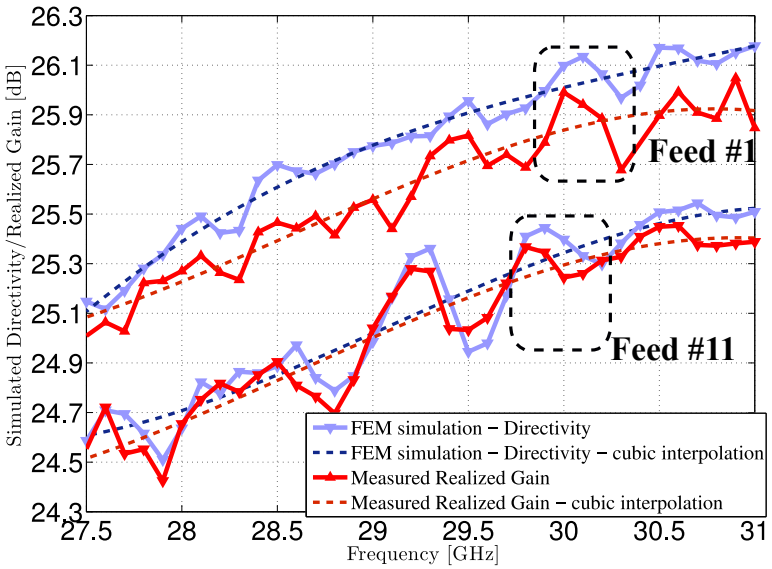

Figure 4.16: Measured realized gain (red curve) and simulated directivity (blue curve) of the PPW beamformer for feeds #1 ($\theta_1 = 1.5°$) and #11 ($\theta_1 = 31.5°$) over the entire up-link Ka frequency band ([27.5-31] GHz).

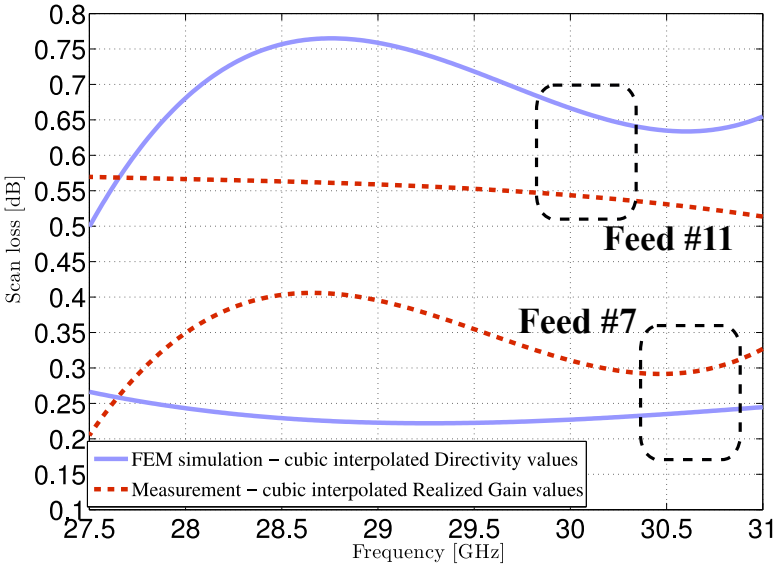

Figure 4.17: Measured realized gain (red curve) and simulated directivity (blue curve) scan losses, with respect to the central feed #1 ($\theta_1 = 1.5°$), of the PPW beamformer for feeds #7 ($\theta_1 = 19.5°$) and #11 ($\theta_1 = 31.5°$) over the entire up-link Ka frequency band ([27.5-31] GHz).

Note that those scan losses are quite stable within the overall frequency band.

This difference observed for the central feed #1 will be further analyzed using the S-parameters measurements, as mutual coupling and matching can affect the

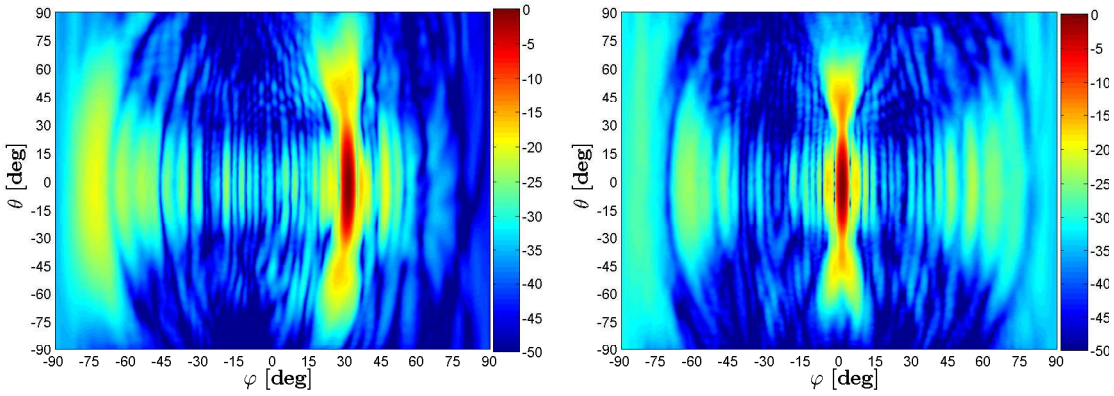

(a) (b)

Figure 4.18: Measured Co-polarization 3D normalized radiation patterns of the final PPW beamformer design at $f_0 = 30$ GHz for feeds #11 (a) and #1 (b), defined by their angular positions $\theta_1 = 31.5°$, $\theta_1 = 1.5°$.

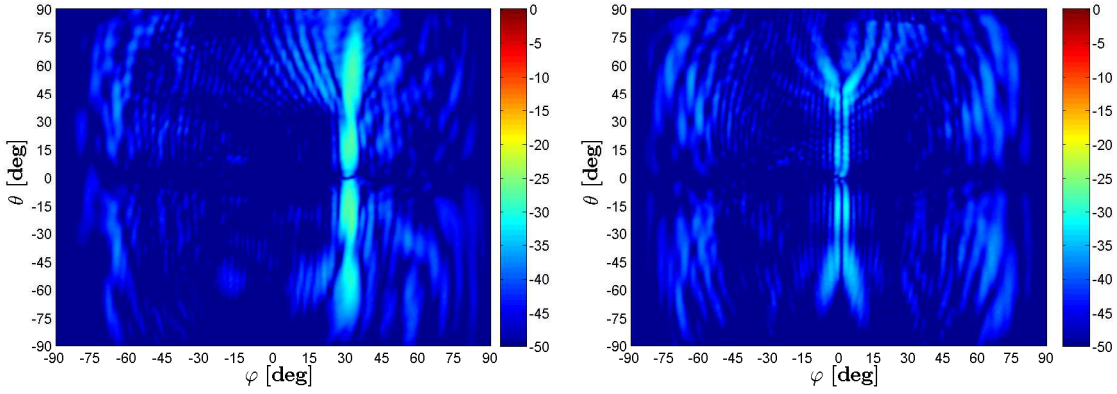

(a) (b)

Figure 4.19: Measured Cross-polarization 3D normalized radiation patterns of the final PPW beamformer design at $f_0 = 30$ GHz for feeds #11 (a) and #1 (b), defined by their angular positions $\theta_1 = 31.5°$, $\theta_1 = 1.5°$.

losses associated to the different feeds.

4.3.2.4 3D radiation patterns

The radiation patterns in spherical coordinates are presented in Fig. 4.18 and 4.19, respectively for the co- (field polarized along $\overrightarrow{Z}$-axis) and cross-polarization, for feeds #11 (a) and #1 (b) defined by their angular positions $\theta_1 = 31.5°$, $\theta_1 = 1.5°$. In these specific figures, the conventional spherical coordinates are used with reference to the cartesian coordinate system $(O,\overrightarrow{X},\overrightarrow{Y},\overrightarrow{Z})$ (Fig. 4.1a). The angle θ now describes the radiation pattern in E-plane, for a given pointing direction in H-plane φ.

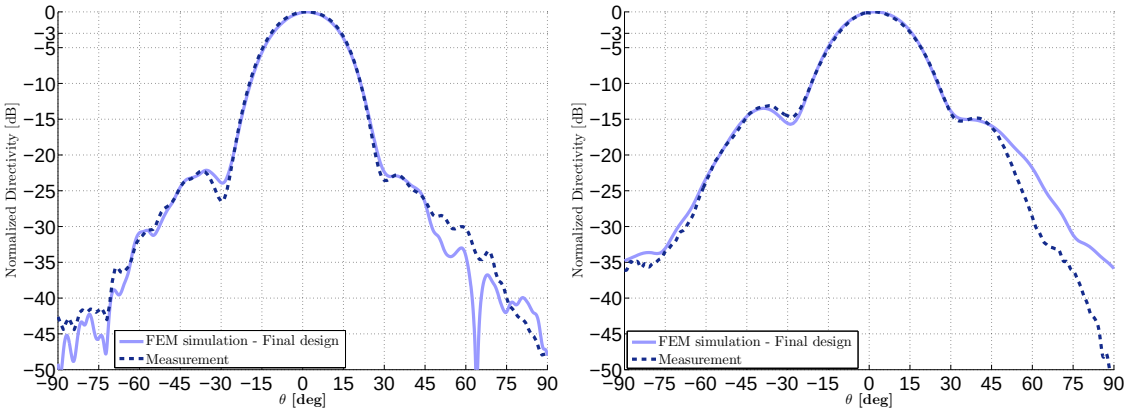

(a) (b)

Figure 4.20: Measured E-plane normalized radiation patterns of the final PPW beamformer design at $f_0 = 30$ GHz for feeds #11 (a) and #1 (b), defined by their angular positions $\theta_1 = 31.5°$, $\theta_1 = 1.5°$.

The expected fan beam shape is observed in Fig. 4.18. A large HPBW ($\cong 25°$) is obtained for both feeds #11 (a) and #1 (b) along E-plane. For the extreme beam in Fig. 4.18a, higher side lobe levels are observed far away from the main lobe region ($[-90°, -60°]$) due to the metallic side walls, previously discussed. The power levels observed are around -20 dB with respect to the maximum peak of directivity. The cross polar levels obtained are plotted in Fig. 4.19. The maximum value obtained equal -24.7 dB and -30.4 dB below the maximum peak of the co-polar component, respectively for feed #11 and #1.

The E-plane patterns are plotted in Fig. 4.20 for both feeds. Interestingly the SLL obtained for feed #11 ($SLL = -22$ dB) is lower than the one measured for feed #1 ($SLL = -13$ dB). This effect is probably explained by the behavior of the final radiating horn, affected by the projection of the beam with the scanning angle θ_2. This aspect also appears in Fig. 4.18 where for feed #11, as compared to the central feed #1, a curvature of the iso-power levels is observed around the main beam region. This needs to be further analyzed, including the way to define the final radiating horn design, with respect to the outer lens contour (Σ_2) as this may be of importance for some applications.

4.3.3 S-parameters measurements

The S-parameters have been measured at IETR, using a vector network analyzer capable of operating from 10 MHz to 67 GHz. The measurement setup is shown in Fig. 4.21. The complete S-matrix associated to the 11 feeds has been acquired during

Figure 4.21: Setup for the measurements of the S-parameters

those measurements. As observed, only two coaxial to waveguide transitions are connected while the other ports are let opened. As a first approach, this simplifies the process since no matched transitions are connected to the other ports. It was verified in simulation that such an approach had a limited impact on the S-parameters.

4.3.3.1 Reflection coefficients

The reflection coefficients associated to feeds with positive (#1, #3, #5, #7, #9 and #11) and negative (#2, #4, #6, #8 and #10) angular positions θ_1 are respectively presented in Fig. 4.22 and .4.23. The measured input reflection coefficients are better than -19 dB. The worst case is observed for the central feed #1, as the major part of the reflected energy is coming back towards the feed. All the other feeds measured reflection coefficients are below -20 dB over the entire frequency band ([27.5-31] GHz), as observed in both Fig. 4.22a and 4.23a. The differences shown in the comparisons provided with the simulated results (Fig. 4.22b and 4.23b) are likely explained by the manufacturing precision, as they are further noticed for the highest frequencies of the considered band of operation.

4.3.3.2 Mutual coupling coefficients

The mutual coupling coefficients associated to feeds #1, #7 and #11 are respectively presented in Fig. 4.24, 4.25 and 4.26. The maximum measured levels obtained are lower than -22 dB for those three feeds. The maximum levels obtained for feed #1 ($\theta_1 = 1.5°$) are observed for feed #2 (Fig. 4.24a), corresponding to the closest angular position ($\theta_1 = -4.5°$). About feed #7 ($\theta_1 = 19.5°$) in (Fig. 4.25a), the specular reflections explain the higher levels observed with feed #6 ($\theta_1 = -16.5°$) as those feeds are quasi symmetric with respect to $\overrightarrow{X}$-axis (Fig. 4.1c). Those specular

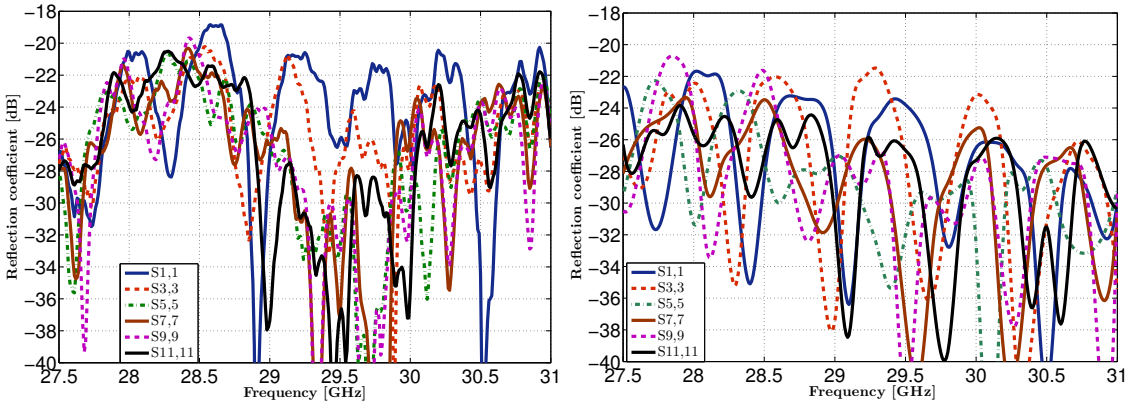

(a) (b)

Figure 4.22: Reflection coefficients of the PPW beamformer over the entire Ka up-link frequency band ([27.5-31] GHz) for feeds #1, #3, #5, #7, #9 and #11. (a) Measurements and (b) FEM simulation.

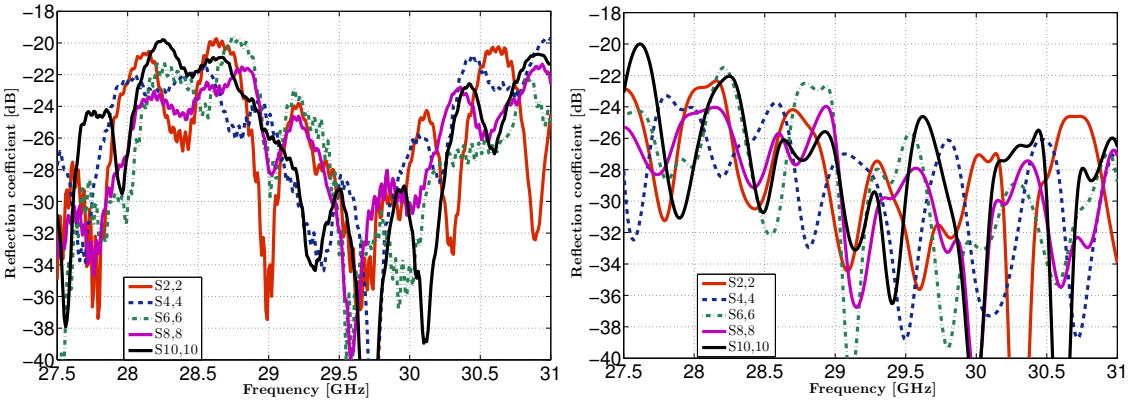

(a) (b)

Figure 4.23: Reflection coefficients of the PPW beamformer over the entire Ka up-link frequency band ([27.5-31] GHz) for feeds #2, #4, #6, #8 and #10. (a) Measurements and (b) FEM simulation.

effects are also observed for the extreme feed #11 (Fig. 4.26a) as the highest levels are obtained with feeds #10 ($\theta_1 = -28.5°$) and #8 ($\theta_1 = -22.5°$), especially for the lowest frequencies ($[27.5 - 28]$ GHz). Those effects described with those measurement results were also observed with the FEM simulation, as closer levels are presented in the comparisons provided in Fig. 4.24b, 4.25b and 4.25c respectively for feeds #11, #7 and #1. Higher reflection and mutual coupling coefficients are observed for the central feed #1, as compared to the extreme feed #11. This explains the difference of efficiency computed using the comparisons provided in Fig. 4.16 between the simulated directivity and the measured realized gain.

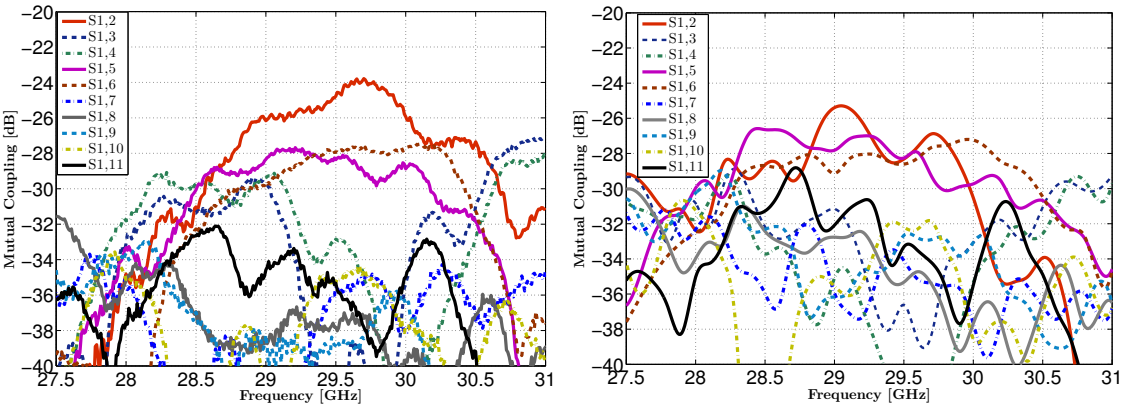

(a) (b)

Figure 4.24: Mutual coupling of the PPW beamformer over the entire Ka up-link frequency band ([27.5-31] GHz) for the central feed #1. (a) Measurements and (b) FEM simulation.

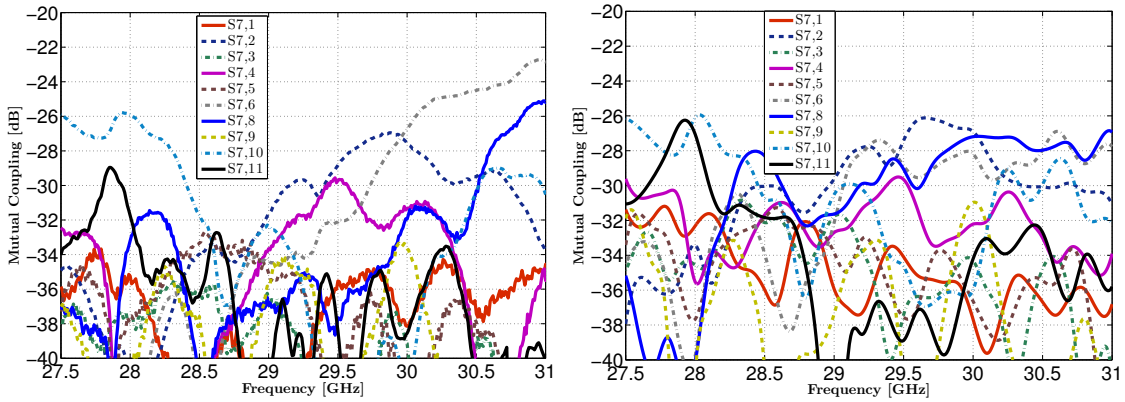

(a) (b)

Figure 4.25: Mutual coupling of the PPW beamformer over the entire Ka up-link frequency band ([27.5-31] GHz) for feed #7. (a) Measurements and (b) FEM simulation.

4.4 Conclusion

An experimental validation has been proposed over the up-link Ka-band ([27.5-31] GHz), confirming the properties in scanning offered by the concept. Excellent beam performance (HPBW, SLL) were demonstrated over a wide angular range ([−31.5°, 31.5°]), including low scanning loss and high radiation stability within the overall frequency band. High radiation efficiencies are obtained with this fully metallic design, particularly suitable for space applications. The mechanical simplicity offered by the concept is also quite attractive to propose low-cost multi-beam satellite platforms. With the specific antenna system considered in this chapter,

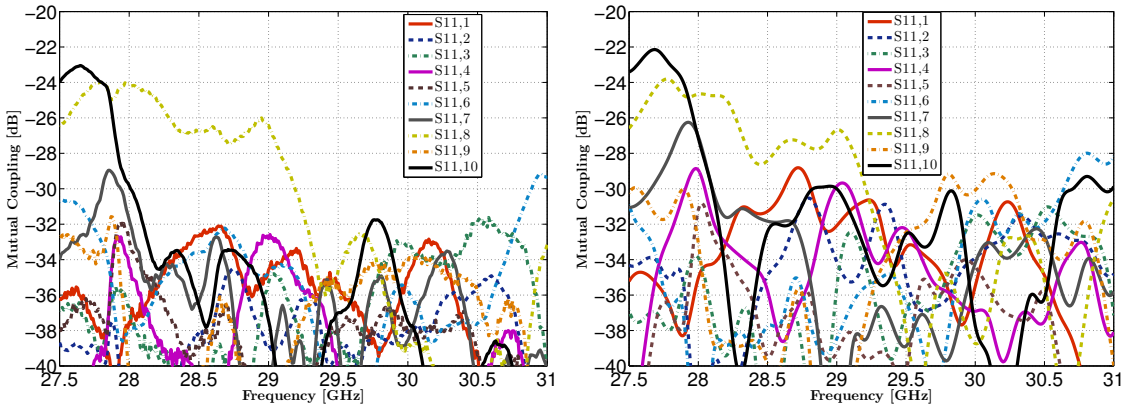

(a) (b)

Figure 4.26: Mutual coupling of the PPW beamformer over the entire Ka up-link frequency band ([27.5-31] GHz) for feed #11. (a) Measurements and (b) FEM simulation.

the height of the ridge was not an issue. For some applications, there is an interest in stacking more beamformers, possibly with a smaller spacing between them. In such a case, there is a need to reduce the height of the ridge while maintaining the good performance of the beamformer. Those aspects are discussed in Chapter 5

5

Compact Shaped Continuous Parallel Plate Waveguide Lens-Like Multiple Beam Antenna at Ka-band

Contents

Abstract

Size reduction is targeted in this chapter. This study is particularly suitable to fulfill strong integration requirements or propose a 2D array using a stack of continuous PPW lenses. The scanning properties in the orthogonal plane will be limited by the distance between the center of each radiating aperture due to grating lobes. The transversal cavity introduced by the concept is the main limitation for the reduction of the beamformer height, and the works conducted demonstrate the possibility with the considered numerical tool (Chapter 2) to reduce the transverse dimension while maintaining high RF performances.

A design working over the same up-link Ka-band ([27.5-31] GHz) and targeting the same RF performance is proposed. The design is presented in Section 5.1. The diameter is identical to the one proposed in the previous Chapter 4, eleven beams are radiated over the same wide angular range ([−31.5°, 31.5°]).

The transversal compactness is first targeted in Section 5.2 using 4 optimized ridges and cavities working as delay lenses, defined between the feeds and the radiating aperture in order to reduce the total height. A reduction factor of 2.7 of the transversal height is obtained. Then the longitudinal compactness is targeted in Section 5.3, using two straight transversal ridges and cavities.

The final design performance is described in Section 5.4. The radiation properties are analyzed, demonstrating similar performances (Directivity, HPBW, SLL), as compared to the final design presented in Chapter 4. Reflection and mutual coupling coefficients are respectively below -17 dB and -18 dB over the entire frequency range. This second prototype should be fabricated soon at IETR and measured.

5.1 Modeling and Design

The lens diameter and the focal distance are respectively equal to $D = 20\lambda$ and $f = 0.7D$, where $\lambda = 10.9$ mm, the wavelength in free space at the lowest frequency of the operating band. The PPW cavity height is equal to $H_{PPW} = 2$ mm, as only the fundamental TEM mode can propagate within the frequency band considered.

5.2 Compactness along the transversal direction

The first objective is to work on the reduction of the beamformer height, limited as shown in Chapter 4, by the transversal section working as a delay lens. The design considered here is shown in Fig. 5.1a. The goal is to possibly distribute the transverse height obtained in Chapter 4 over several and separate ridges and cavities having all a lower height. To this end four transversal sections are considered while trying to maintain the same performance as the previous continuous lens proposed (Chapter 4). This number of ridges was selected as a trade-off between height reduction and the accuracy of the GO tool.

Each lens is defined by two profiles (inner (Σ_1) and ridge height (h_w) profiles), as shown in Fig. 5.1b. Each outer lens contour (Σ_2) is then defined as a translation of 2 mm from its relative inner lens profile (Σ_1) along $\overrightarrow{X}$-axis. The reference system $(O,\overrightarrow{X},\overrightarrow{Y},\overrightarrow{Z})$ is associated to the final lens and is used to define the focal distance f and the angular positions θ_1 of the eleven feeds considered along a circular focal curve (Fig. 5.1c). The radiating horn is defined along the local normal vector of

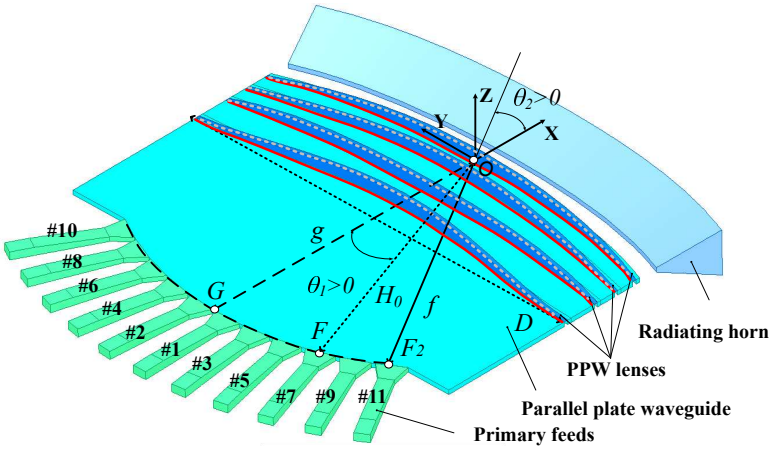

(a) 3D view

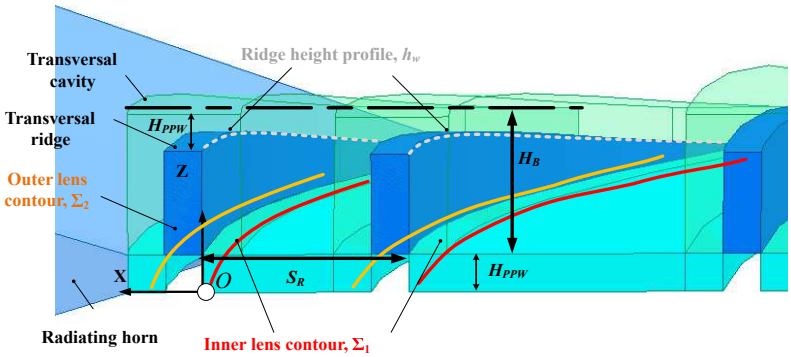

(b) Cut view in $(O, \vec{X}, \vec{Z})$ plane of the PPW lens

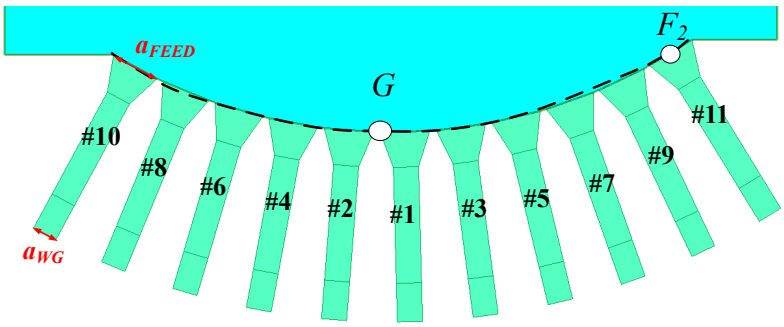

(c) Top view of the feeds system

Figure 5.1: Continuous parallel plate waveguide (PPW) beamformer at Ka-band including multiple ridge working as delay lenses.

the final outer lens contour (Σ_2) with a length of 30 mm and an aperture height equals of 20 mm, to be comparable to the design proposed previously (Chapter 4).

The feeds are identical to the ones of the previous continuous lens design at Ka band, with angular positions θ_1 ranging from $-28.5°$ to $31.5°$ and an angular step of $6°$ (Fig. 5.1c). The feed dimensions are equal to a_{WG}=7.556 mm and a_{FEED}=14 mm. This configuration provides patterns with a beamwidth $\theta_{3dB} = 3°$ while targeting a

minimum SLL, which requires an adequate edge taper and hence a minimum feed aperture. Using an antenna system with two superimposed lenses, operating a 180° rotation between both, as proposed in Fig. 4.2 for the prototyped continuous lens, 22 equally spaced beams are radiated, achieving the desired cross-over level.

A pattern based optimization, as presented in the previous Chapter 3 (Subsection 3.4.2), is used to achieve the desired performance at the frequency $f_0 = 30$ GHz for the extreme feed defined at an angular position $\theta_1 = 31.5°$, and the central one ($\theta_1 = 1.5°$), imposing the on-axis focal distance equal to $g = 1$ (Fig. 5.1c). A minimum HPBW θ_{3dB} is targeted while minimizing as much as possible the side lobe level SLL. In this case and as we target similar performances as the previous continuous lens design, the HPBW values targeted equal 3° and 2.6°, respectively for feed #11 and #1. Those values were obtained with the GO numerical model for both feeds, resulting from the optimization performed for the design presented in the previous Chapter 4 (Fig. 4.3 and 4.4).

The use of $g = 1$ avoids any blockage effects between the different feeds, observed when $g > 1$, and enables a reduction of the beamformer size along $\overrightarrow{X}$-axis. As compared to the previous configuration with $g = 1.1$, a reduction of 10% of the focal distance f is achieved. The multiple optimized lenses profiles introduce additional degrees of freedom to target this focal curve definition despite the sub-optimal phase aberrations (Fig. 5.1c).

During the optimization process, each lens is translated along $\overrightarrow{X}$-axis of a distance value S_R from the reference system $(O,\overrightarrow{X},\overrightarrow{Y},\overrightarrow{Z})$, as shown in Fig. 5.1b. A minimum distance equals of $\lambda = 10.9$ mm, the wavelength in free space at the lowest frequency of the operating band, is assigned between the successive inner lens profiles (Σ_1). This is chosen in order to avoid strong reflection effects between the different bend transitions but also to respect the accommodation constraints of the four transversal cavities considered.

Several optimization processes are repeated minimizing progressively and as much as possible the beamformer height H_B, while maintaining the desired pattern performances. This parameter is defined, as shown in Fig. 5.1b, by the distance computed along $\overrightarrow{Z}$-axis between the upper plate of the parallel plate section and the maximum height of the transversal cavities.

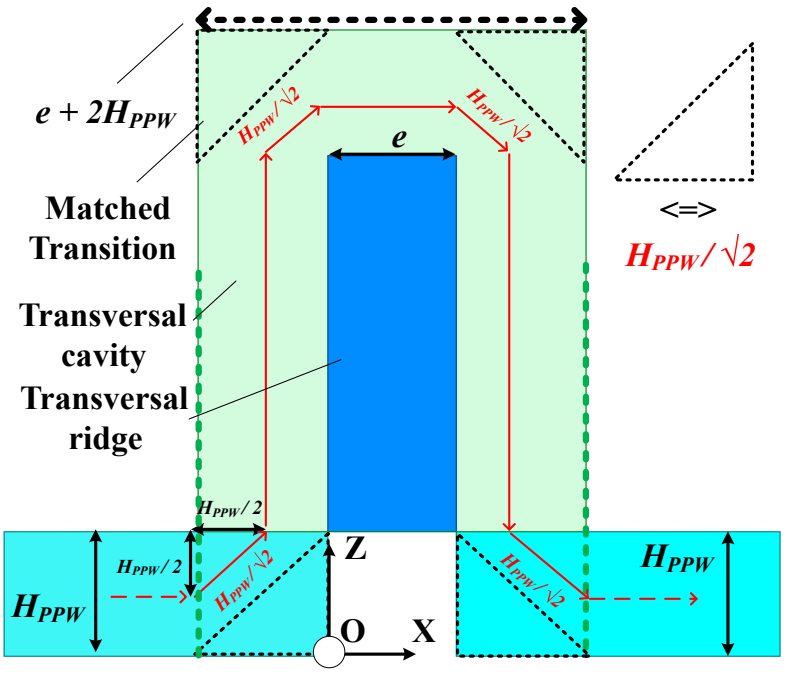

(a) Geometry of the PPW section including four E-plane 90° bend transitions.

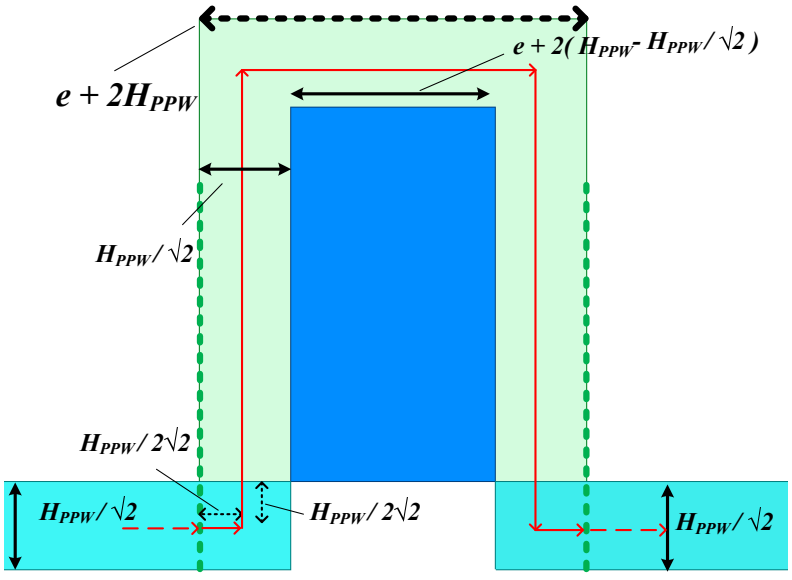

(b) Electrically equivalent PPW section considered for the ray tracing

Figure 5.2: Analysis tool update taking into account the phase behavior of the PPW section working as a delay lens

5.2.1 Analysis tool update

When only one transversal section is introduced (Chapter 4), working as a delay lens, the parallel plate section height H_{PPW} and the behavior of the considered matched transitions could be neglected without a major impact on the accuracy

of the predicted patterns. Here, as multiple PPW lenses are considered, the combination of all the approximations results in significant deviations, translating mostly in beam pointing error.

A cut view in $(O,\overrightarrow{X},\overrightarrow{Z})$ plane shows the four E-plane 90° bend transitions connecting the PPW sections and the delay lens (Fig. 5.2a). Various types of transitions can be considered, including square steps or right bends with different phase behaviors. Analyzing several configurations considering a TEM mode with a broadside incidence, the path length associated to each transition is close to $H_{PPW}/\sqrt{2}$. This length corresponds geometrically to the distance between the middle of both longitudinal and transversal sections (Fig. 5.2a). To simplify the process, this value is thus added in the proposed analysis tool. This approach still remains an approximation, as performance also varies with the angle of incidence, but avoid the use of the combination with an FEM implementation while enhancing the prediction accuracy.

To maintain the same approach as in the previous model with rays propagating either in the $(O,\overrightarrow{X},\overrightarrow{Y})$ or in the $(O,\overrightarrow{Y},\overrightarrow{Z})$ plane, an electrically equivalent PPW section of height $H_{PPW}/\sqrt{2}$ is defined, as shown in Fig. 5.2b. The ray tracing considered inside this section (red line) enables the electrical path length of each E-plane transition ($H_{PPW}/\sqrt{2}$). An equivalent thickness of the transversal ridge, equals of $e+2(H_{PPW}-H_{PPW}/\sqrt{(2)})$, is considered to define the same longitudinal dimension for the PPW transverse section geometry (Fig. 5.2a) and the considered equivalent model (Fig. 5.2b) (here the distance $e+2H_{PPW}$ is constant between the green dotted lines).

Consequently, the ray tracing procedure presented in Annex B can be easily updated. The position of both inner (Σ_1) and outer (Σ_2) lens contours but also the ridge height profile (h_w) are translated along their respective $\overrightarrow{X}$ and $\overrightarrow{Z}$-axis, as performed considering,

$$\begin{cases} x_u = x - (H_{PPW} - H_{PPW}/\sqrt{(2)})/f - (H_{PPW}/2\sqrt{2})/f, \\ h_{w_u} = h_w + (H_{PPW}/\sqrt{2})/f, \\ u_u = u + (H_{PPW} - H_{PPW}/\sqrt{(2)})/f + (H_{PPW}/2\sqrt{2})/f. \end{cases} \tag{5.1}$$

x_u, u_u and h_{w_u}, are respectively the coordinates of the inner (Σ_1), outer (Σ_2) and ridge height (h_w) profiles, considered for the ray tracing procedure.

5.2.2 H-plane radiation patterns and performance of the proposed analytical tool

The optimization processes are based on 4^{th} order polynomial coefficients. As demonstrated in Chapter 3, Subsection 3.4.1, where polynomial based lens profiles were introduced, the pattern performance is almost identical for a 4, 6 or 10^{th} polynomial coefficient order. As four inner lens (Σ_1) and ridge height (h_w) profiles are considered, we reduce the number of optimization variables and consequently the computation time of the optimization processes by selecting 4^{th} order polynomial profiles.

The final design obtained is characterized by two matrices, defining both inner (Σ_1) and ridge height (h_w) polynomial profiles for each transversal cavity. The last matrix lines correspond to the profiles obtained for the PPW lens next to the radiating horn. The matrices are defined respectively by,

$$p = \begin{bmatrix} 0 & 0 & 0 & 0.319 & -0.327 & 0 \\ 0 & 0 & 0 & 0.045 & -0.098 & 0 \\ 0 & 0 & 0 & 0.039 & -0.226 & 0 \\ 0 & 0 & 0 & -0.136 & -0.136 & 0 \end{bmatrix}, \tag{5.2}$$

and,

$$q = \begin{bmatrix} 0 & 0 & 0 & 0.028 & -0.084 & 0 \\ 0 & 0 & 0 & -0.115 & -0.010 & 0 \\ 0 & 0 & 0 & 0.051 & -0.094 & 0 \\ 0 & 0 & 0 & 0.070 & -0.106 & 0 \end{bmatrix}. \tag{5.3}$$

The final beamformer height obtained equals $H_B = 7.5$ mm, as compared to 20.5 mm for the design presented in Chapter 4, which corresponds to a reduction factor of 2.7. Interestingly, the on-axis path lengths are quite similar for both designs. For the lens with four ridges, the total added path length is around 60 mm, while for the lens with one ridge, the corresponding length is about 40 mm, to which must be added about 15 mm due to the longer on-axis distance ($g = 1.1$).

The H-plane radiation pattern obtained with the proposed GO model and the corresponding ideal FEM simulation are first compared in Fig. 5.3a for the extreme feed #11 ($\theta_1 = 31.5°$). This ideal design considers PML boundaries on the edges, thus neglecting reflection effects. The main beam direction and the HPBW computed with the GO and FEM simulation are respectively equal to 31.4°, 3.1° and 31.4°, 3.2°. The first side lobe level equals -17 and -15.9 dB, respectively for both models.

For the central feed #1, the same comparison is provided in Fig. 5.4a. Based on those main parameters, a good prediction is as well demonstrated. However, there was a need to quantify the accuracy of the predications obtained with the GO model

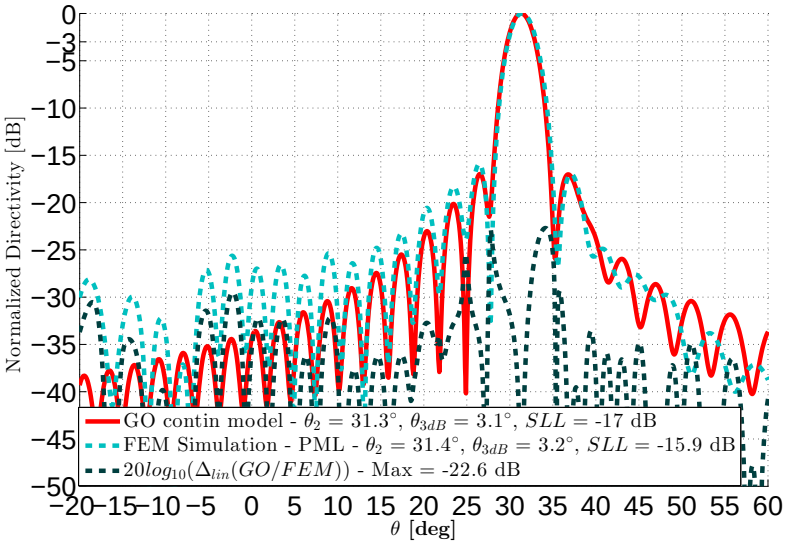

(a) Compact continuous lens at Ka-band

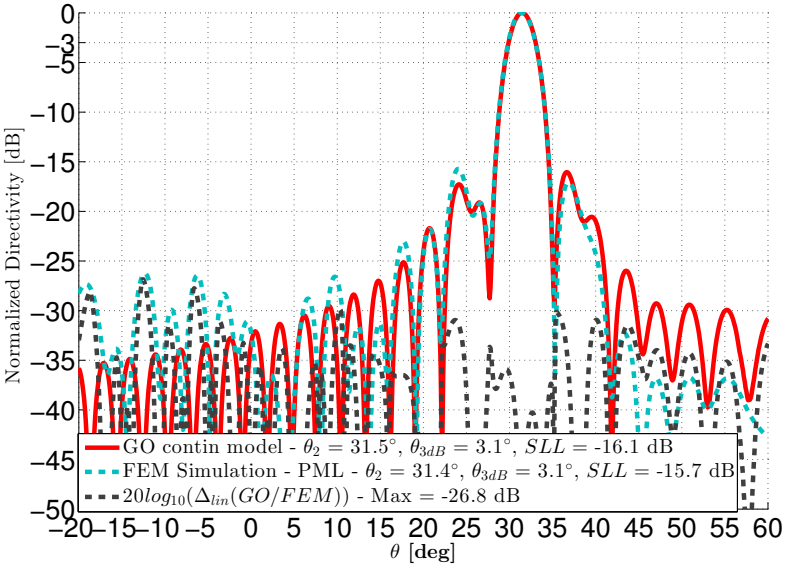

(b) Single-ridge continuous lens at Ka-band

Figure 5.3: H-plane normalized radiation patterns of the PPW beamformer at $f_0 = 30$ GHz for the extreme feed #11, defined by an angular position $\theta_1 = 31.5°$, computed with the GO model (red curve) and the FEM analysis considering PML boundaries (ideal design).

as deviations started to become more significant when compared to the full-wave results, although remaining within the domain of validity derived in the case of the single ridge. Consequently, we compute the linear amplitude difference Δ_{lin} between the patterns obtained using both methods (GO and FEM models). This comparison strategy has been proposed in [73], in order to perform a comparison between

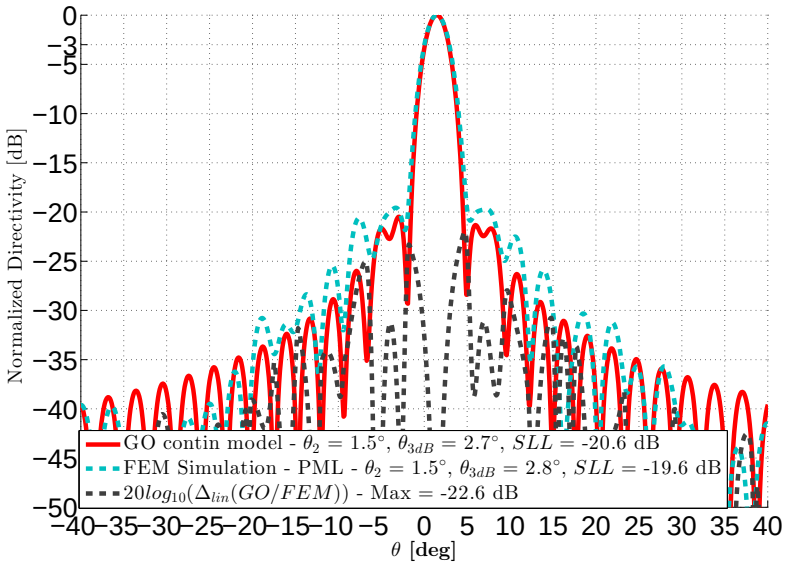

(a) Compact continuous lens at Ka-band

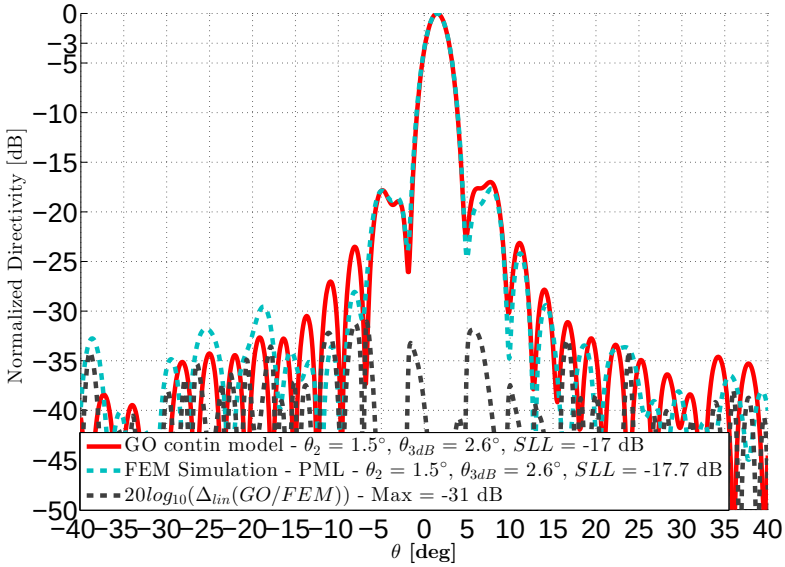

(b) Single-ridge continuous lens at Ka-band

Figure 5.4: H-plane normalized radiation patterns of the PPW beamformer at $f_0 = 30$ GHz for the central feed #1, defined by an angular position $\theta_1 = 1.5°$, computed with the GO continuous model (red curve) and the FEM analysis considering PML boundaries (ideal design).

radiation patterns measured using different facilities. This linear difference has the advantage to keep the information of the absolute levels, i.e. a 1 dB difference close to the peak of directivity between patterns will appear as a larger error when compared to the same difference at lower levels, such as in the side lobes. This

information is more meaningful for the targeted applications. This difference is represented in Fig. 5.3a, using a logarithmic scale, evaluating the prediction in dB for the different angular positions θ, where the patterns are computed.

This linear difference calculation has been performed for this compact lens design (Fig. 5.3a) and the continuous lens design presented in Chapter 4 (Fig. 5.3b). In both cases, an ideal simulation is performed with PML boundaries on the lens edges. As observed, the maximum level of amplitude difference equals -22.6 dB for the considered lens. The prediction given is mainly degraded around the main beam region, as with the previous concept and in the same angular range, the difference of amplitude levels obtained were below -30 dB. The same comparison is provided in Fig. 5.4 for the central feed #1, showing also higher differences. With the ray tracing approximations presented in Chapter 2, this degradation was expected in this configuration. However, the amplitude differences obtained are low, typically below -20 dB, and the tool still proposes an acceptable prediction. Increasing further the number of ridges was found to result in significantly higher linear differences and was thus discarded.

Comparing the performances between the two configurations, for the extreme feed #11, the patterns obtained are almost identical. The main beam direction computed with the FEM simulation for both lenses is identical (31.4°) while the HPBW equals 3.2°, as compared to 3.1° for the previous continuous lens. The first side lobe level is equal to -15.9 and -15.7 dB, respectively for both lenses. The main differences appear for the central feed #1, where the side lobe level SLL obtained with the FEM implementation equal -19.6 and -17.7 dB, respectively for the configuration proposed here and the one in Chapter 4. Consequently, the main beam region is widen, demonstrating a HPBW of 2.8°, as compared to 2.6° previously. This effect is mainly dependent on the amplitude distribution obtained along the final outer lens contour (Σ_2) and can affect the maximum directivity. This aspect will be further analyzed in Subsection 5.3.2.

5.3 Compactness along the longitudinal direction

The compactness along the transversal direction has been addressed successfully in the previous section, proposing a design with four transversal lenses, as shown in Fig. 5.1a. The idea was then to work on the reduction of the longitudinal beamformer dimension, here along $\overrightarrow{X}$-axis. Using the design previously optimized, we introduce two straight transversal ridges and cavities, folding up the longitudinal PPW section. Those straight ridges have less impact on the overall GO model

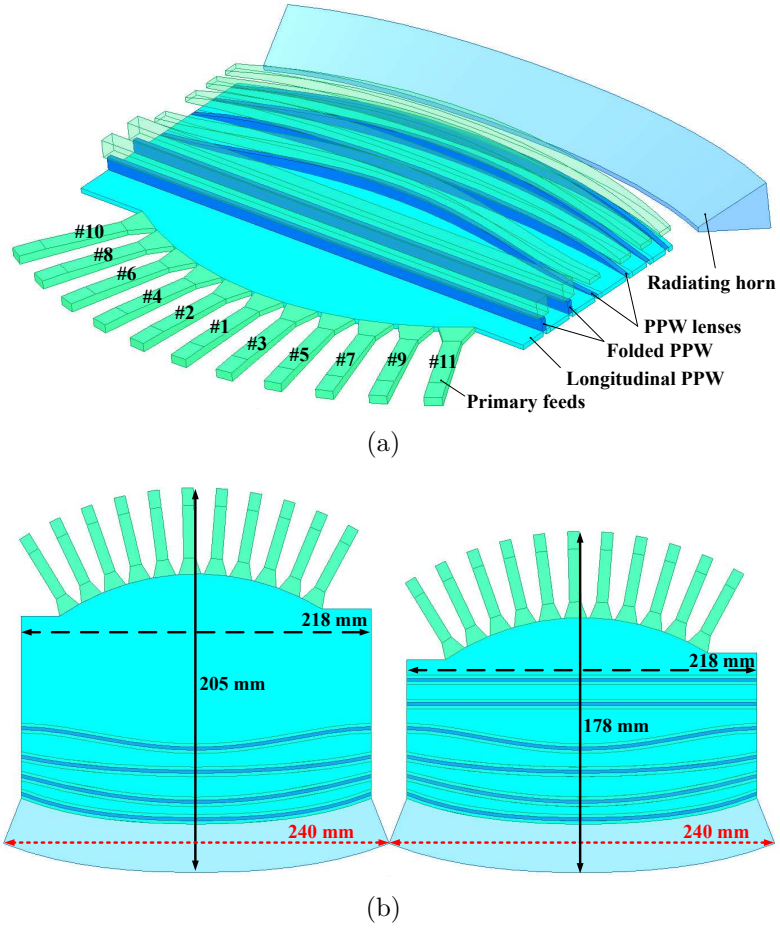

Figure 5.5: Continuous parallel plate waveguide (PPW) beamformer at Ka-band including 4 ridges working as delay lenses and two straight ridges to achieve a more compact design along the longitudinal direction, (a) 3D view and (b) Comparisons before and after the longitudinal dimension reduction.

accuracy. The two transversal cavities are defined with the maximum beamformer height $H_B = 7.5$ mm, obtained from the previous optimized configuration. Their positions and the distance between both have been optimized to avoid reflection effects and maintain pattern performances close to the ones proposed in the previous section. The distance between the first transversal section and the closest feed #11 has been maintained larger than λ, the wavelength at the lowest frequency of operation. The 3D view of the design considered here is shown in Fig. 5.5a, where we can see both transversal sections considered to reduce the longitudinal dimension. In Fig. 5.5b, the designs obtained before and after $\overrightarrow{X}$-axis length reduction are compared. As observed, a size reduction of 27 mm is performed, which is more than 10% starting from 205 mm.

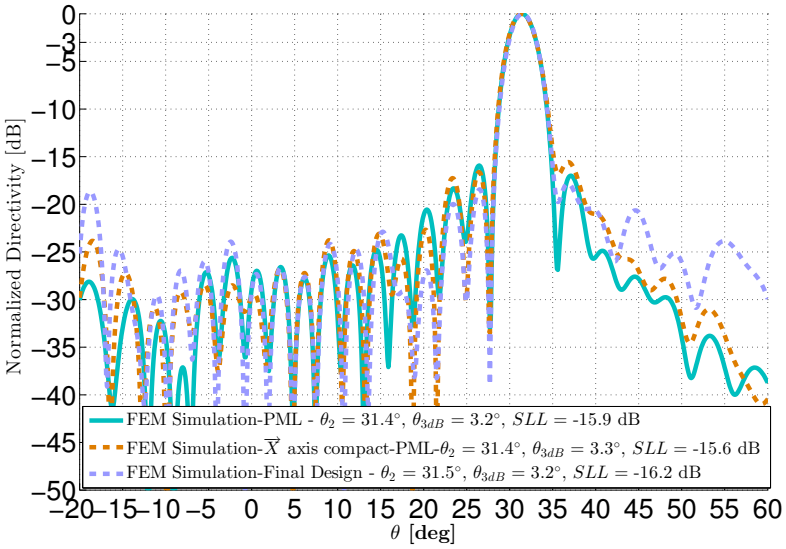

(a) $\theta_1 = 31.5°$

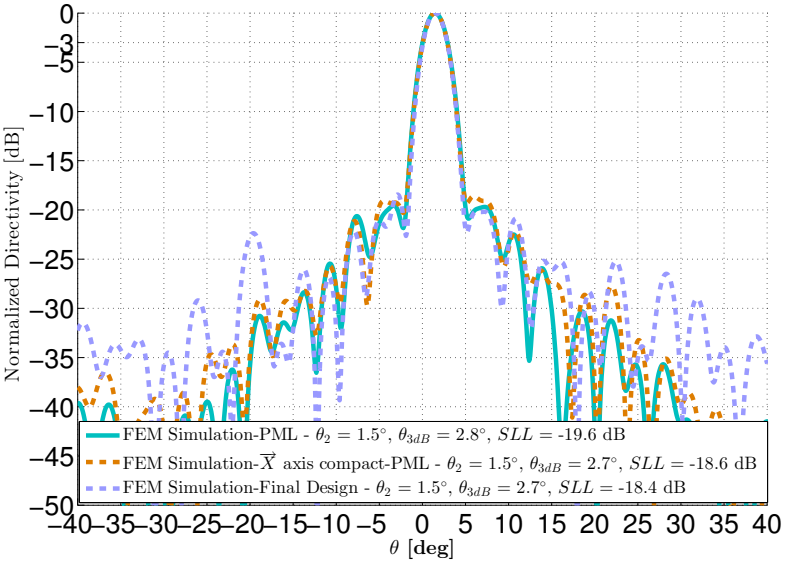

(b) $\theta_1 = 1.5°$

Figure 5.6: H-plane normalized radiation patterns of the PPW beamformer at $f_0 = 30$ GHz for feed #11 and #1 defined by their angular positions θ_1 computed with the FEM analysis considering PML boundaries (ideal design), with and without longitudinal length reduction, and the final design.

5.3.1 H-plane radiation patterns

The H-plane patterns radiated by the full-wave designs, with (Fig. 5.5a) and without (Fig. 5.1) longitudinal length reduction, are compared. An ideal design, considering PML boundaries to avoid reflection effects, is first considered. The

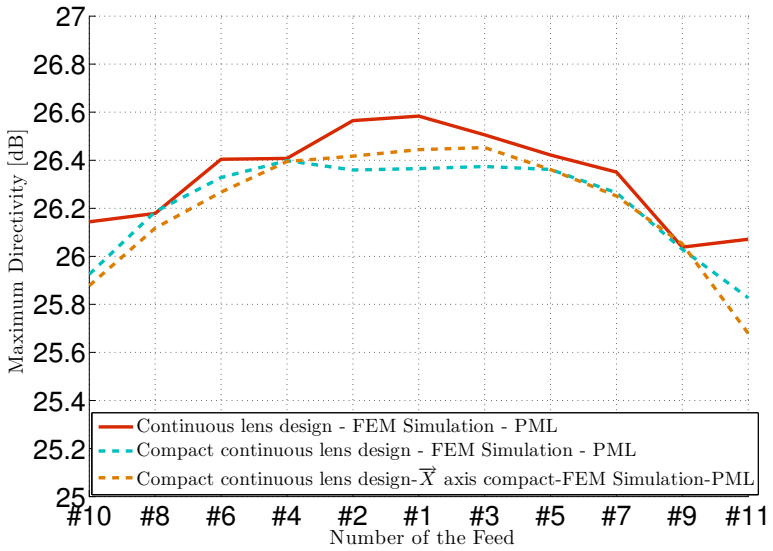

Figure 5.7: Maximum Directivity at $f_0 = 30$ GHz for all the feeds, defined by their angular positions θ_1, computed with the FEM analysis considering PML boundaries (ideal design), for the considered lens and for comparison purposes with the lens defined in Chapter 4.

patterns obtained for the extreme feed #11 in both cases, with (orange dotted line) and without (turquoise line) longitudinal length reduction, are presented in Fig. 5.6a. As observed, the pointing direction is preserved (31.4°) while the HPBW θ_{3dB} is almost identical, 3.3° as compared to 3.2°. A slight degradation is observed for the first side lobe level ($\cong$ 1 dB), explained by the bend transitions added with the two straight transversal sections. This difference is acceptable in this case and will be further analyzed in the final design, where PEC boundaries are considered. For the central feed #1 (Fig. 5.6b), the performances are very close, without large differences observed.

5.3.2 Directivity, HPBW and Side lobe level

The maximum directivity, HPBW θ_{3dB} and side lobe level SLL have been computed with the FEM analysis for the considered lens design at the frequency $f_0 = 30$ GHz, with and without longitudinal length reduction, and for comparison purposes with the continuous lens proposed in Chapter 4. The FEM simulations have been considered with PML boundaries, avoiding reflection effects in this analysis.

The first comparison is made for the central feeds (#1, #2 and #3), where the maximum directivity obtained is reduced of approximately 0.2 dB for both cases (with and without longitudinal length reduction). As shown in the previous Subsection (Fig. 5.4) for the central feed #1, this is in line with an amplitude edge

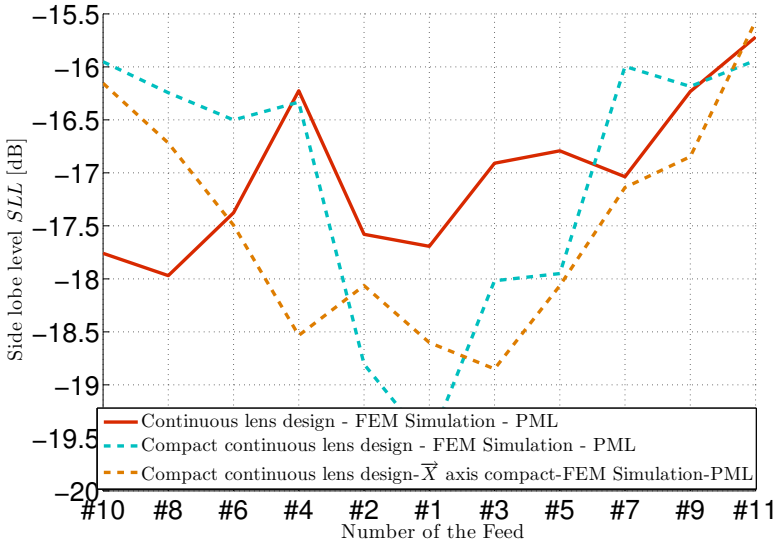

(a) Side lobe level SLL

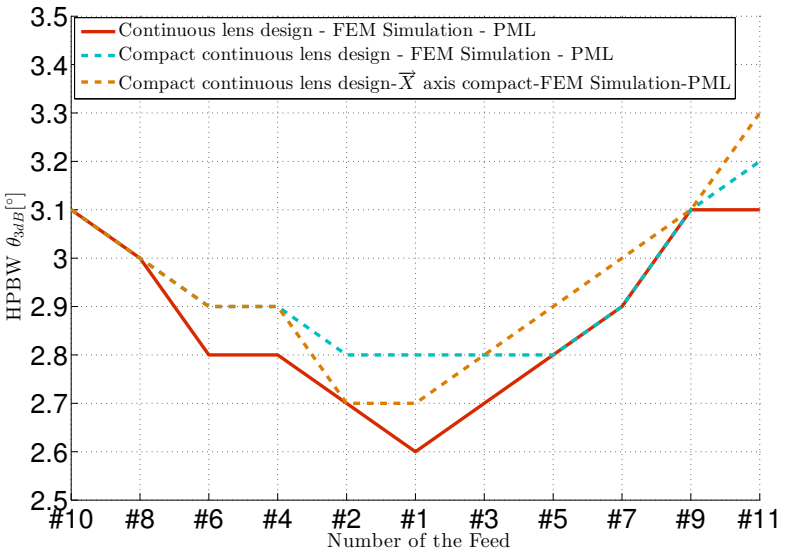

(b) HPBW θ_{3dB}

Figure 5.8: HPBW θ_{3dB} and Side lobe level SLL at $f_0 = 30$ GHz for all the feeds, defined by their angular positions θ_1, computed with the FEM analysis considering PML boundaries (ideal design), for the considered lens and for comparison purposes with the lens defined in Chapter 4.

taper effect, as the side lobe level SLL is reduced while the HPBW is widen. This is respectively observed for those three central feeds in Fig. 5.8a and 5.8b.

The maximum directivity obtained for the extreme feeds #10 and #11 is reduced of about 0.2 dB for both cases (with and without longitudinal length reduction), as compared to the first approach (red curve). This effect is explained by the

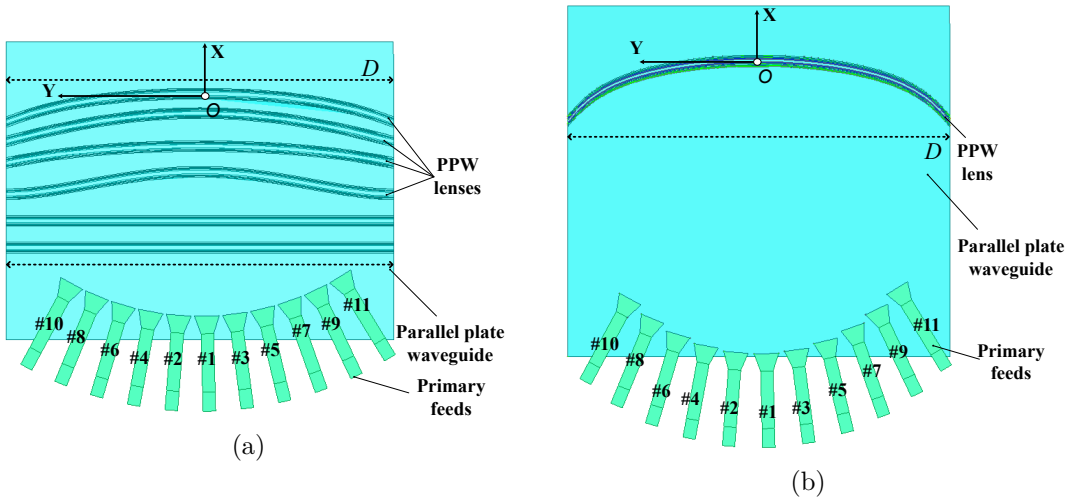

Figure 5.9: Ideal continuous lens design with output PML boundaries. (a) Multiple lenses design considered here and (b) Single lens design defined in Chapter 4.

curvature of the final optimized outer lens profile (Σ_2), lower as compared to the one optimized in Chapter 4. Indeed, the shape of the final outer lens profile is constrained by the beamformer height reduction. Several studies have been considered to restrict the profile curvature while trying to maintain the same pattern requirements. However, no satisfactory solutions have been found as the beamformer height constraint needs to be reduced in order to obtain resulting configurations with the desired performances.

The HPBW θ_{3dB}, higher for feed #11 as observed in Fig. 5.8b , is also explained by the scanning performances, slightly reduced in this proposed configuration. The side lobe level (SLL) performances proposed are similar (Fig. 5.8a). Some differences are observed with (orange dotted line) and without (blue dotted line) longitudinal length reduction, explained by the reflections effects, further noticed in the compact configuration where bend transitions have been added.

5.3.3 S-parameters analysis

5.3.3.1 Output PML boundaries

An analysis of the S-parameters is given in this section. As compared to the previous Chapter 4, the number of bend transitions is multiplied by the number of transversal cavities considered.

An ideal design with PML boundaries on the edges is analyzed, avoiding the reflection effects. Moreover, a final PPW section closed by PML boundaries is connected to the lens output, as shown in Fig. 5.9, removing the radiating horn impact in a first step.

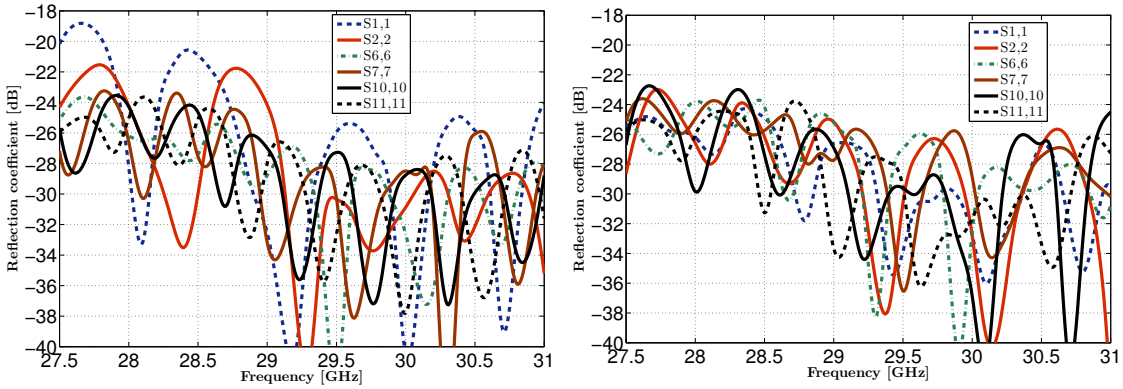

(a) (b)

Figure 5.10: Reflection coefficients of the PPW beamformer over the entire Ka up-link frequency band ([27.5-31] GHz) obtained with the ideal FEM simulation and output PML boundaries. (a) Multiple lenses design considered here and (b) Single lens design defined in Chapter 4.

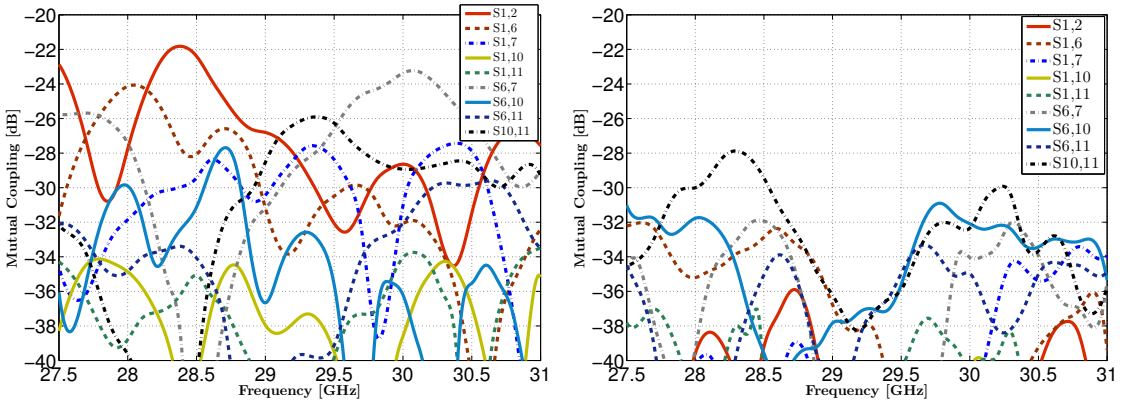

(a) (b)

Figure 5.11: Mutual Coupling coefficients of the PPW beamformer over the entire Ka up-link frequency band ([27.5-31] GHz) obtained with the ideal FEM simulation and output PML boundaries. (a) Multiple lenses design considered here and (b) Single lens design defined in Chapter 4.

The reflection coefficients obtained in this configuration are compared in Fig. 5.10 with the continuous lens design presented in Chapter 4. As observed, the central feeds #1 and #2, are mainly affected by the reflections, principally for the lowest frequencies of the operating band. The maximum level observed in Fig. 5.10a equals -19 dB for feed #1.

The same comparison is performed for the computed mutual coupling coefficients in Fig. 5.11. For brevity and clarity purposes, only feeds #1, #2, #6, #7, #10 and #11 are analyzed. As clearly demonstrated, the coupling is higher in the

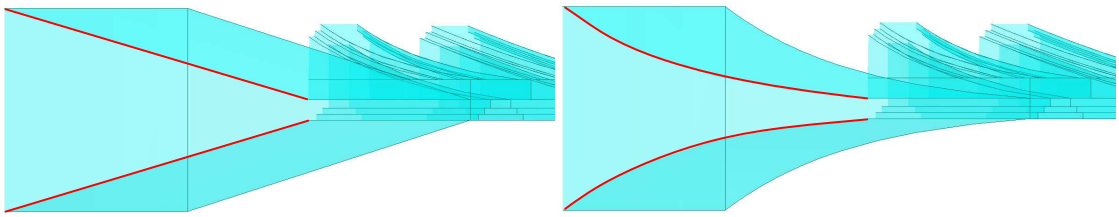

(a) (b)

Figure 5.12: Final horn design connected to the lens design. (a) Straight profile horn, (b) Vivaldi profile horn.

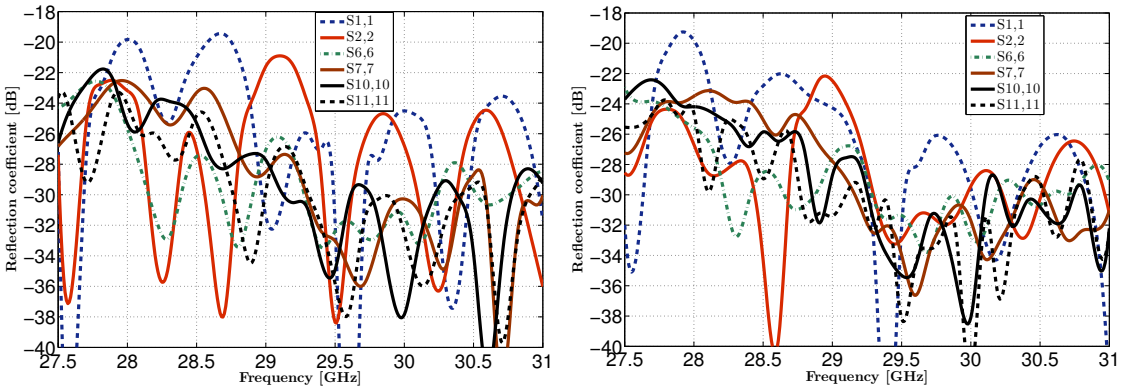

(a) (b)

Figure 5.13: Reflection coefficients of the PPW beamformer over the entire frequency band ([27.5-31] GHz) obtained with the ideal FEM simulation and an output horn. Multiple lenses design connected to: (a) a straight profile horn and (b) a Vivaldi profile horn.

proposed configuration. The highest levels observed correspond to coefficients S12, S67 and S1011, showing higher specular reflections, as the feeds considered are quasi-symmetric with respect to $\overrightarrow{X}$-axis.

The S-parameters degradation due to the multiple bend transitions is limited in both configurations. This confirms the possibility to reduce the dimensions of the beamformer while proposing high RF performances.

5.3.3.2 Output Radiating Horn

As presented previously in Section 5.2, a radiating horn is connected to the lens output and is defined along the local normal vector of the final outer lens profile (Σ_2) with a length of 30 mm and an aperture height equals of 20 mm. Its impact on the S-parameters performances is analyzed here.

As observed in Fig. 5.12a, the outer lens profile is connected to the final radiating aperture, using a straight line profile. This first approach was also used

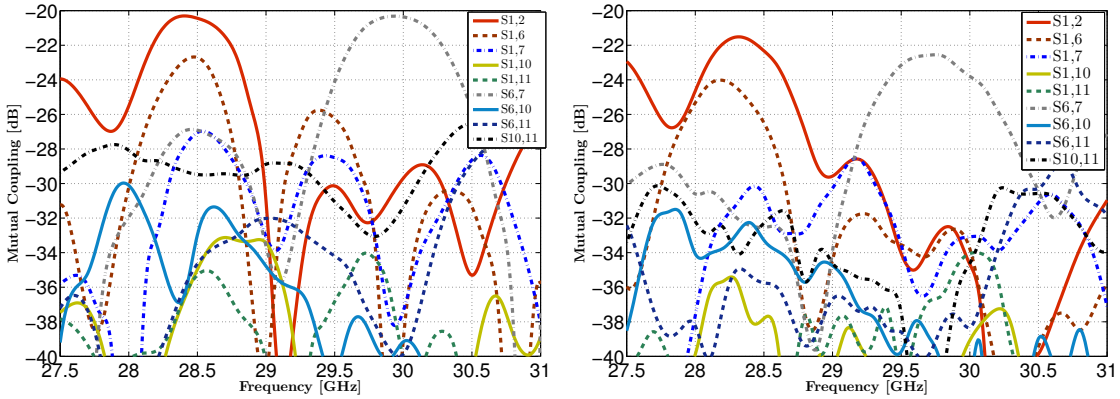

Figure 5.14: Mutual Coupling of the PPW beamformer over the entire frequency band ([27.5-31] GHz) obtained with the ideal FEM simulation and an output horn. Multiple lenses design connected to: (a) a straight profile horn and (b) a Vivaldi profile horn.

to design the radiating horn of the first manufactured prototype (Chapter 4). The reflection and mutual coupling coefficients associated are plotted respectively in Fig. 5.13a and Fig. 5.14a. Comparing those results with the performances obtained with output PML boundaries, the reflection coefficients are maintained below -19 dB while some degradation appear for the mutual coupling coefficients. S12 and S67 coefficients show maximum values close to -20 dB, as compared to -22 dB in the previous case (Fig. 5.11).

This introduce some interests to further optimize the horn profile transition. As an example, a Vivaldi profile is considered between the outer lens contour and the radiating aperture, using Eqn. (5.4).

$$H(l) = H_{min} + e^{\ln\left((H_{max}-H_{min})/L_{taper}\right)l}, \tag{5.4}$$

with $H(l)$ the height of the profile, calculated along the local normal vector of the outer lens point considered. H_{min} and H_{max} are the minimum and maximum heights defined, respectively equal to 2 and 20 mm. The tapering distance L_{taper} equals 30 mm.

The performance is improved, particularly for the mutual coupling performance and further work both on the horn profile and delay-lens transitions is expected to improve S-parameters in the case of multiple ridge configurations. As we want to propose a comparison with the design prototyped and measured (Chapter 4), we maintained the original straight horn profile. The final design radiation and S-parameters performances are presented and analyzed in the next section.

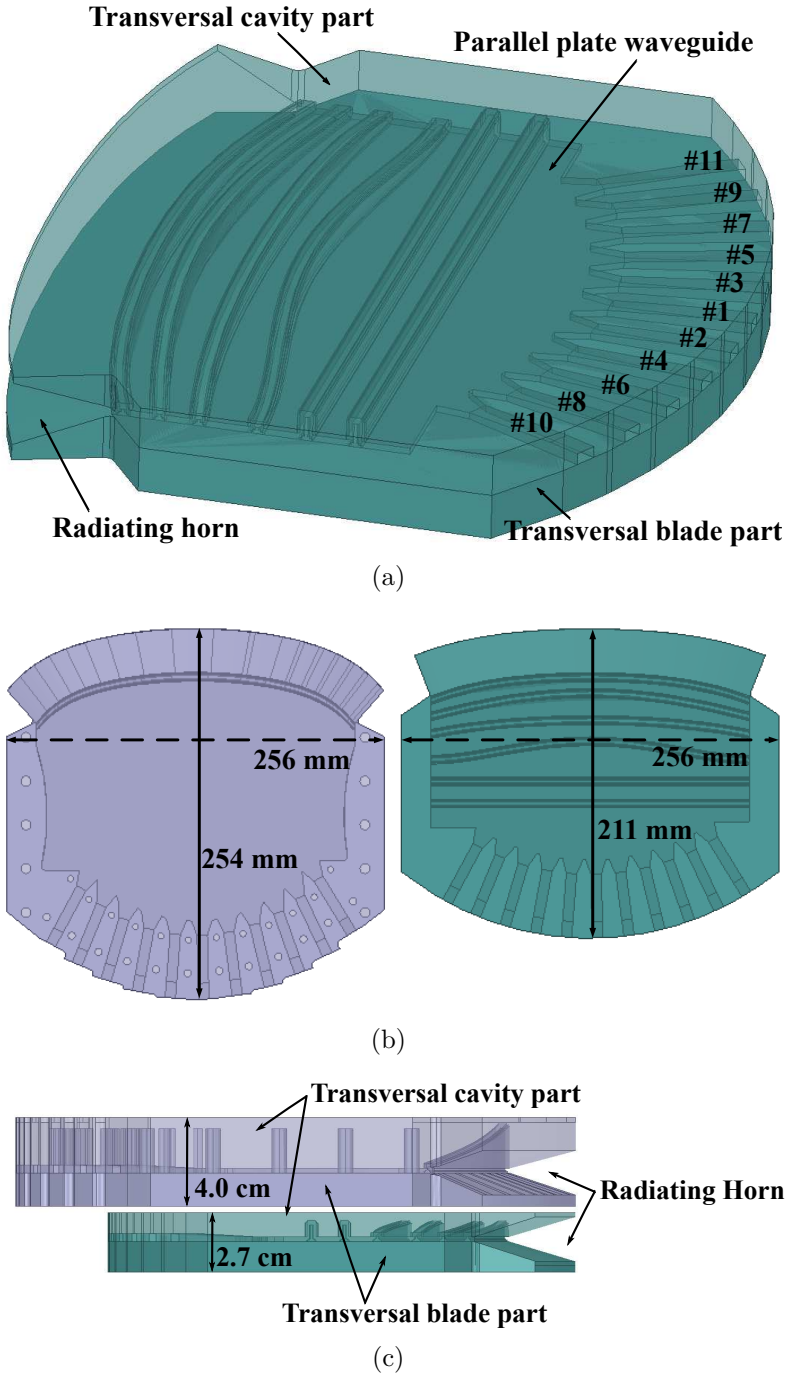

Figure 5.15: Final second continuous lens design before prototyping. (a) 3D view, (b) longitudinal and (c) transversal compactness comparisons with the continuous lens design prototyped in Chapter 4.

5.4 Final design performances and comparisons with the breadboard

The final as-built design considers metallic sidewalls in order to propose a simpler design and assembly process, and avoid the use of absorbing materials like in the

previous prototype. The final design is shown in Fig. 5.15a, where we can recognize both transversal blade and cavity parts. Comparisons with the design presented in Chapter 4 are provided in Fig. 5.15b and 5.15c.

The first comparison provided in Fig. 5.15b demonstrates the longitudinal compactness obtained. The final dimension along $\overrightarrow{X}$-axis equals 211 mm, as compared to 254 mm for the continuous lens prototyped which is a 17% reduction. The transversal dimensions ($\overrightarrow{Z}$-axis) are compared in Fig. 5.15c, where the final heights equal 4 and 2.7 cm (32.5% reduction). As observed, the reduction of the transversal section is limited by the horn aperture (20 mm), chosen identical to the prototyped design for comparisons purposes. The transversal blade part is as well defined by a minimum metal thickness, limiting the final size along $\overrightarrow{Z}$-axis.

5.4.1 H-plane radiation patterns

The final H-plane radiation patterns obtained are presented in Fig. 5.6a and 5.6b, respectively for the extreme #11 ($\theta_1 = 31.5°$) and the central ($\theta_1 = 1.5°$) feeds. As observed in Chapter 4 for the design prototyped, the final design with PEC boundaries shows radiation pattern performances similar to the simplified design, where PML boundaries are considered. Some far out lobe level degradations are observed without major consequences on the performances targeted.

The H-plane patterns associated to feeds #3, #5, #7, #9 are plotted in Fig. 5.16. The three cases proposed for feeds #11 and #1 (Fig. 5.6) are also considered, with an ideal case considering PML boundaries with (orange dotted curve) and without (green curve) longitudinal length reduction, and then for the final design (PEC boundaries). The patterns associated to feeds #2, #4, #6, #8, #10 are not shown for brevity purposes.

As previously observed, some far out lobe level degradation are present in the final configuration, but always with levels around 20 dB below the maximum peak of directivity.

The reconstructed coverage with the 22 final simulated beams is shown in Fig. 4.13. The patterns obtained at $f_0 = 30$ GHz with the considered lens (continuous blue line) have been combined with the ones obtained after the 180° lens rotation between both, as shown in Fig. 4.2a for the design prototyped in Chapter 4. As observed a -3 dB cross-over level is obtained while maintaining low side lobe levels over the entire scanning range ($[-31.5°, 31.5°]$).

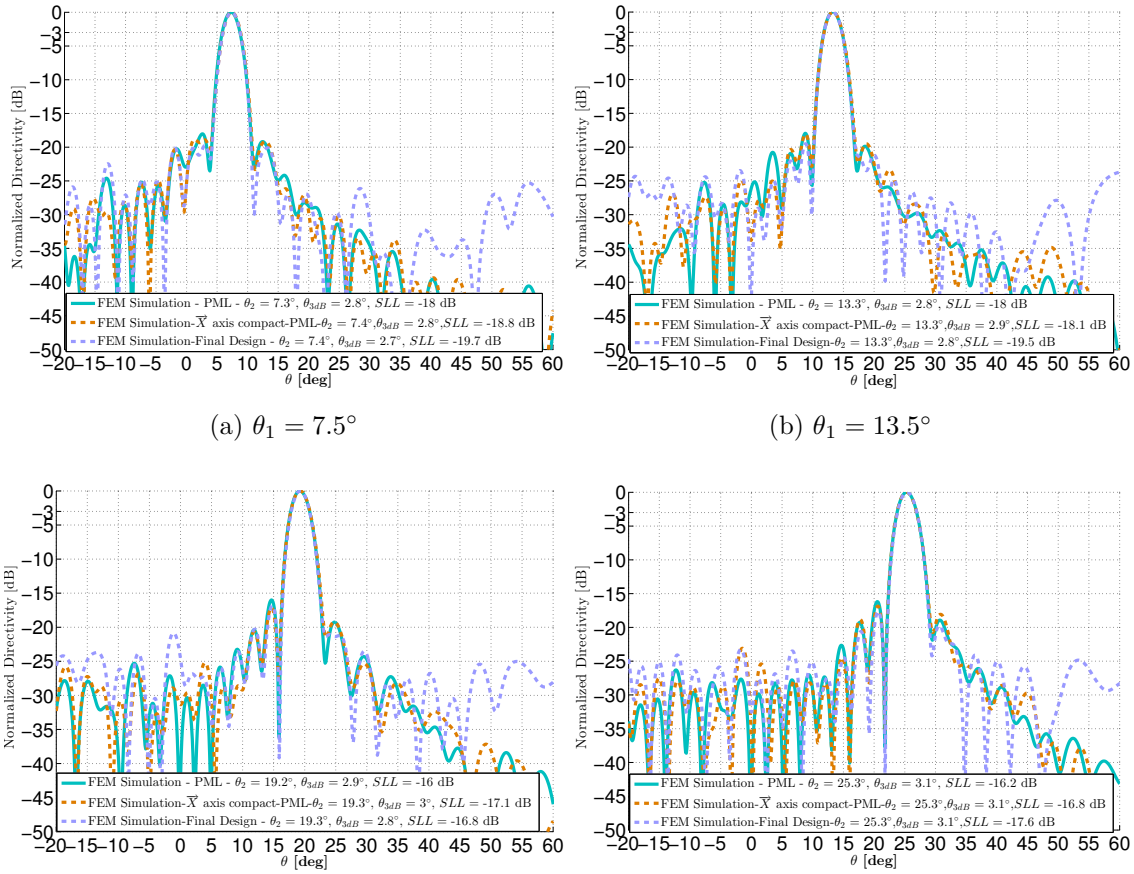

(a) $\theta_1 = 7.5°$ (b) $\theta_1 = 13.5°$

(c) $\theta_1 = 19.5°$ (d) $\theta_1 = 25.5°$

Figure 5.16: H-plane normalized radiation patterns of the final PPW beamformer design at $f_0 = 30$ GHz for feeds #3, #5, #7 and #9 defined by their angular positions θ_1, computed with the FEM analysis considering PML boundaries (ideal design), with and without compactness along the longitudinal direction, and the final design.

5.4.2 Simulated Directivity over the frequency band

The directivities computed with the final FEM model have been plotted in Fig. 5.18 for the extreme ($\theta_1 = 31.5°$) and central ($\theta_1 = 1.5°$) feeds. A comparison is performed with the directivity obtained in simulation with the design prototyped in Chapter 4.

In Fig. 5.18a, a first comparison is provided, considering ideal designs with PML boundaries on the edges, avoiding the reflection effects. As previously discussed in Subsection 5.3.2 and particularly using Fig. 5.7, the maximum directivity obtained for the central feed #1 is lower for the compact lens ($\cong -0.2$ dB). This is confirmed over the entire frequency band. The scan loss obtained in this ideal case is higher for the compact lens ($\cong 0.9$ dB), as for the extreme feed #11 the directivity is reduced of about 0.4 dB as compared to the single lens case.

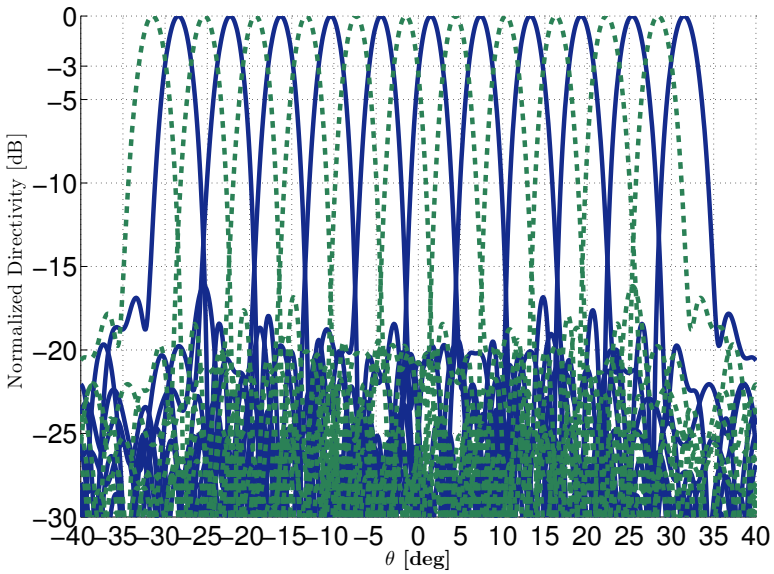

Figure 5.17: Simulated H-plane normalized radiation patterns of the final PPW beamformer design at $f_0 = 30$ GHz for all the feeds (continuous line) and for the same beamformer considering the 180° rotation.

The final design is considered in Fig. 5.18b, with PEC boundaries and the two assembled metal blocs shown in Fig. 5.15. For the central feed #1 the final maximum directivity obtained with the compact lens is higher of approximately 0.2 dB as a difference with the single lens case over the entire frequency range. For the extreme feed #11 the directivities computed have now similar levels. The degradation due to the metallic side walls is difficult to control and a compromise needs to be found between the S-parameters and radiation performances.

With the design proposed in Chapter 4, the edges were shaped to limit the far out lobe pattern and S-parameters degradation, as shown in Fig. 5.15b. In this first case, the maximum directivity was more affected as compared to the design studied here, where this optimization was not possible due to the multiple delay lenses introduced. This aspect will be as well discussed in Subsection 5.4.4 with the final S-parameters performance.

5.4.3 HPBW and Side lobe level over the frequency band

The HPBW θ_{3dB} of the H-plane radiation patterns are computed using the final FEM simulation and plotted in Fig. 5.19, over the entire frequency range ([27.5-31] GHz) for feed #11, #7 and #1. For comparison purposes, the values obtained are compared to the ones simulated for the design prototyped, presented in Chapter 4.

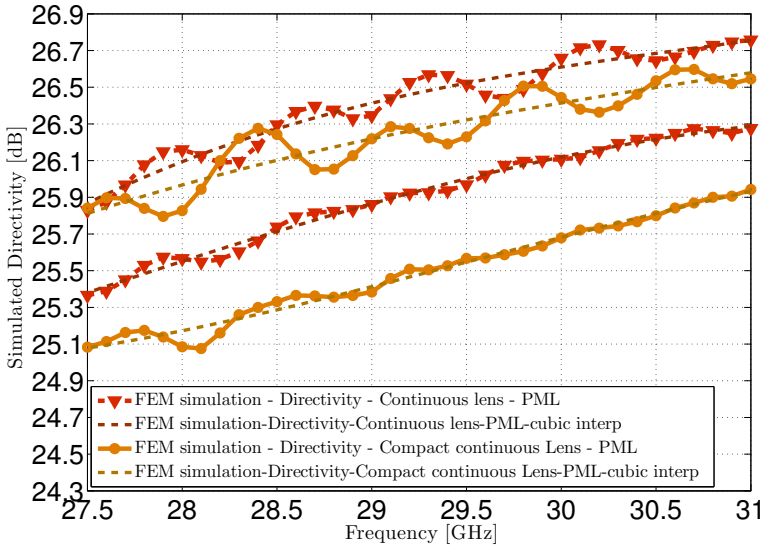

(a)

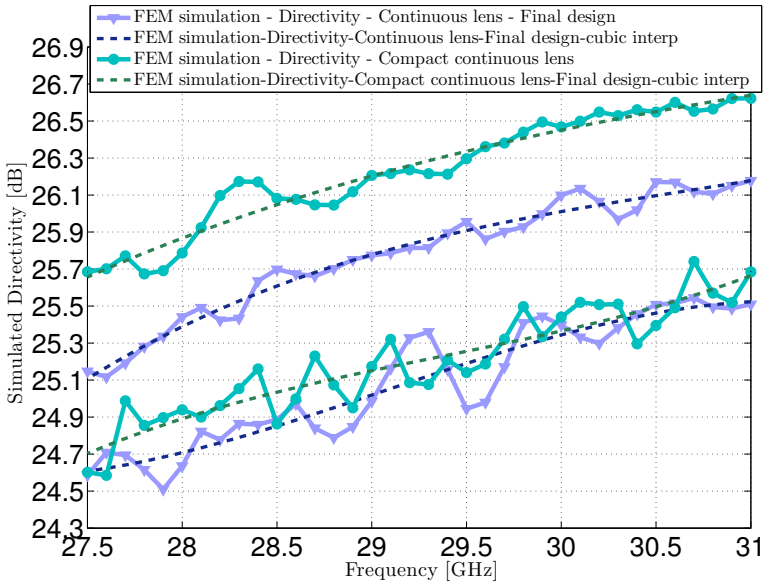

(b)

Figure 5.18: Simulated directivity (blue curve) of the PPW beamformer for feeds #1 ($\theta_1 = 1.5°$) and #11 ($\theta_1 = 31.5°$) over the entire frequency band ([27.5-31] GHz).

As observed, the distributions obtained for both lenses are very close, the conclusions discussed in Subsection 5.3.2 are confirmed over the complete frequency range. For the extreme feed #11, the beamwidth obtained is slightly increased, which is explained by the scan loss. For the central feed #1, the levels are slightly higher, as the amplitude distribution is affected by the wave front propagation inside the parallel plate section. This is in line with the side lobe level computed and

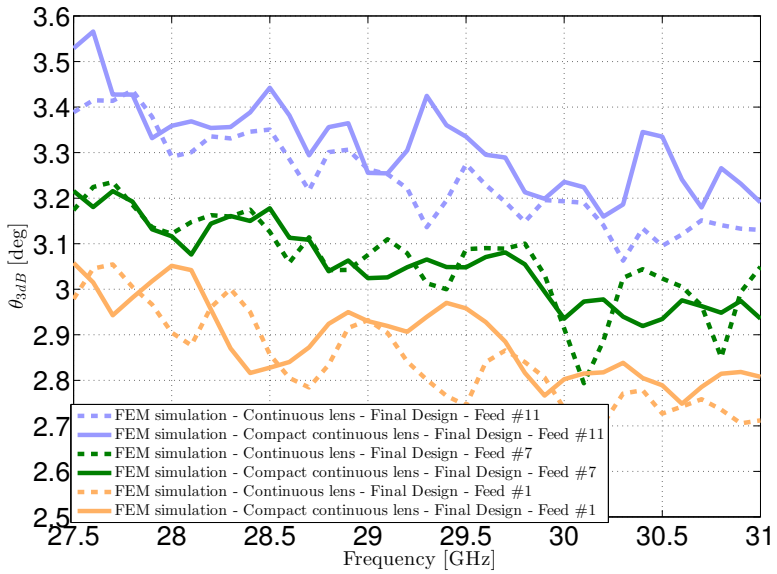

Figure 5.19: HPBW θ_{3dB} in H-plane computed with the final FEM simulation over the entire frequency band ([27.5-31] GHz), for feeds #11 ($\theta_1 = 31.5°$), #7 ($\theta_1 = 19.5°$) and #1 ($\theta_1 = 1.5°$).

represented in Fig. 5.20a. As a difference with the first lens (Fig. 5.20b), where the SLL were almost identical for all the feeds, a larger difference is observed between the central feed #1 ($\cong -19$ dB) and feeds #7, #11 ($\cong -16$ dB). For those feeds, the performances are close to the ones obtained with the first lens. At some frequency points, higher levels are observed, explained by the reflection effects. Those levels are limited, proving the stability of the performances over the frequency band.

5.4.4 S-parameters

The S-parameters simulated with the FEM model associated to the final prototype, prepared for the manufacturing process, are presented in this section. They are compared to the ones simulated for the last design measured and presented in Chapter 4.

5.4.4.1 Reflection coefficients

The reflection coefficients associated to feeds with positive (#1, #3, #5, #7, #9 and #11) and negative (#2, #4, #6, #8 and #10) angular positions θ_1 are respectively presented in Fig. 5.21 and 5.22.

As observed, the degradation is mainly observed for the central feeds (#1, #3 in Fig. 5.21a and #2, #4 in Fig. 5.22b). As described in Subsection 5.3.3, they are mainly affected by the reflections added by the multiple bend transitions, especially for the lowest frequencies of the band of operation. The

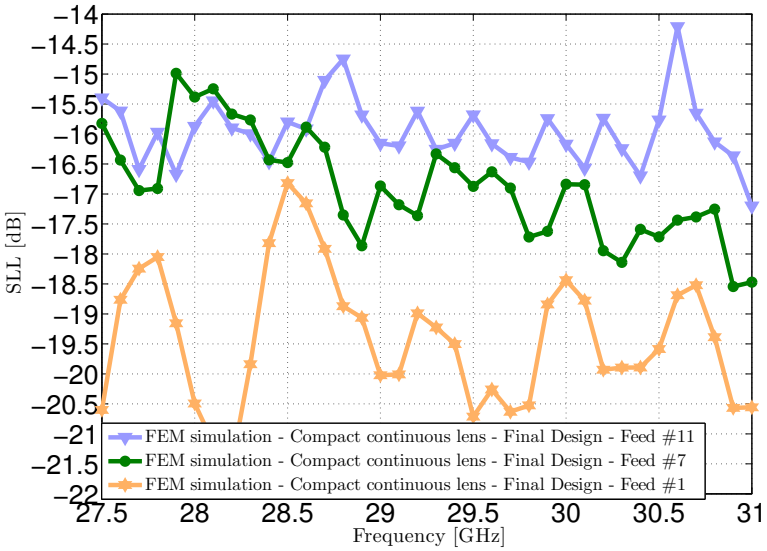

(a)

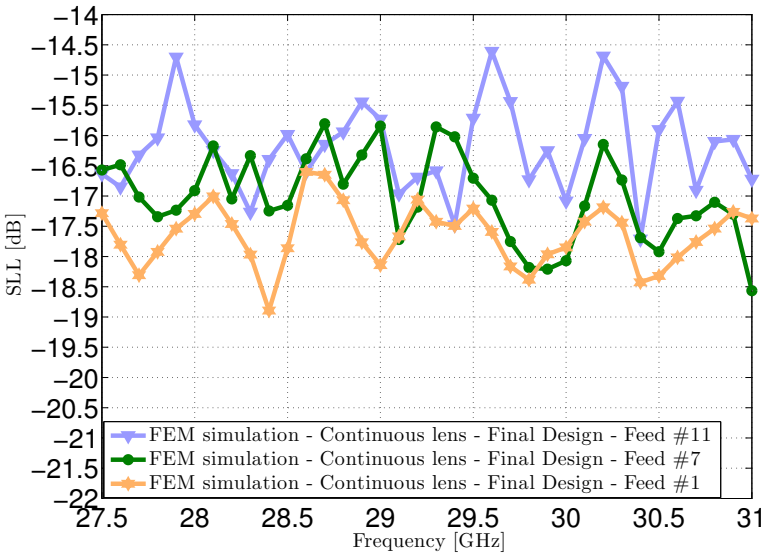

(b)

Figure 5.20: Side lobe levels SLL in H-plane computed with the final FEM simulation over the entire frequency band ([27.5-31] GHz), #11 ($\theta_1 = 31.5°$), #7 ($\theta_1 = 19.5°$) and #1 ($\theta_1 = 1.5°$). (a) Compact and (b) First continuous lens.

levels obtained are maintained below -17 dB. As a comparison with the ideal case simulation results, presented in Fig. 5.13, a degradation of the maximum level of around 2 dB is observed for feeds #1 and #2. Those results are still acceptable since no large degradations are observed over the bandwidth to compromise the performances targeted.

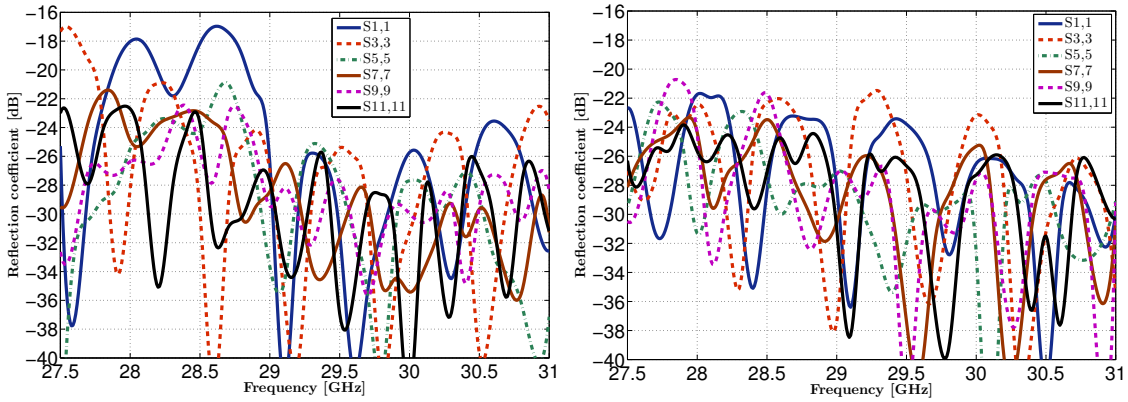

(a) (b)

Figure 5.21: Reflection coefficients of the PPW beamformer over the entire frequency band ([27.5-31] GHz) for feeds #1, #3, #5, #7, #9 and #11, obtained with the final FEM simulation. (a) Multiple lenses design considered here and (b) Single lens design defined in Chapter 4.

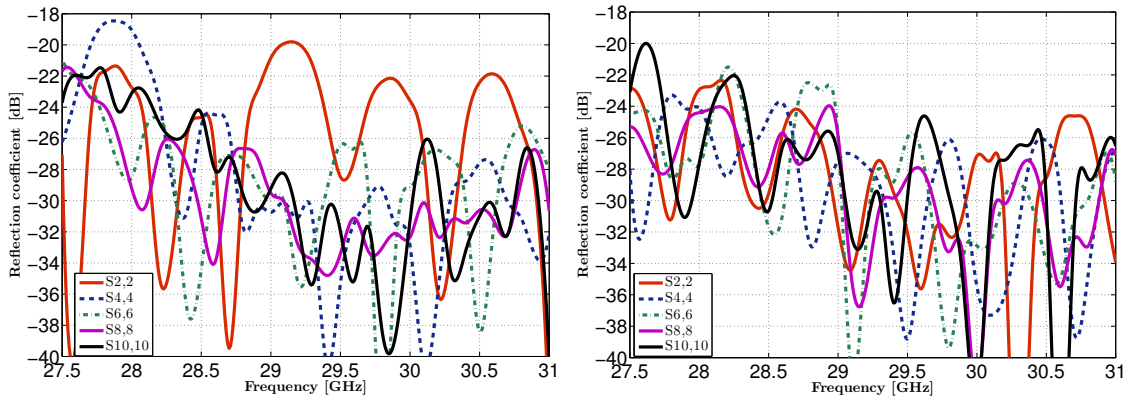

(a) (b)

Figure 5.22: Reflection coefficients of the PPW beamformer over the entire frequency band ([27.5-31] GHz) for feeds #2, #4, #6, #8 and #10, obtained with the final FEM simulation. (a) Multiple lenses design considered here and (b) Single lens design defined in Chapter 4.

5.4.4.2 Mutual coupling coefficients

The mutual coupling coefficients associated to feeds #1, #7 and #11 are respectively presented in Fig. 5.23, 5.24 and 5.25.

The maximum levels are observed for the coefficients S12, S76 and S78, associated to an increase of the specular reflections. This in line with the analysis given in Subsection 5.3.3 where the ideal design was considered. As compared to Fig. 5.14, the degradation of the maximum level of coefficients S12, S76 equals 2 dB. The

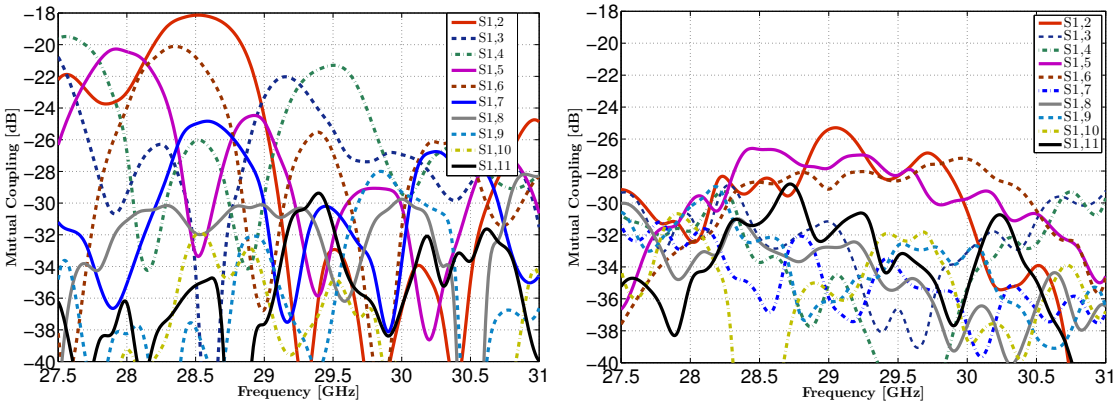

(a) (b)

Figure 5.23: Mutual coupling of the PPW beamformer over the entire frequency band ([27.5-31] GHz) obtained with the final FEM simulation for feed #1. (a) Multiple lenses design considered here and (b) Single lens design defined in Chapter 4.

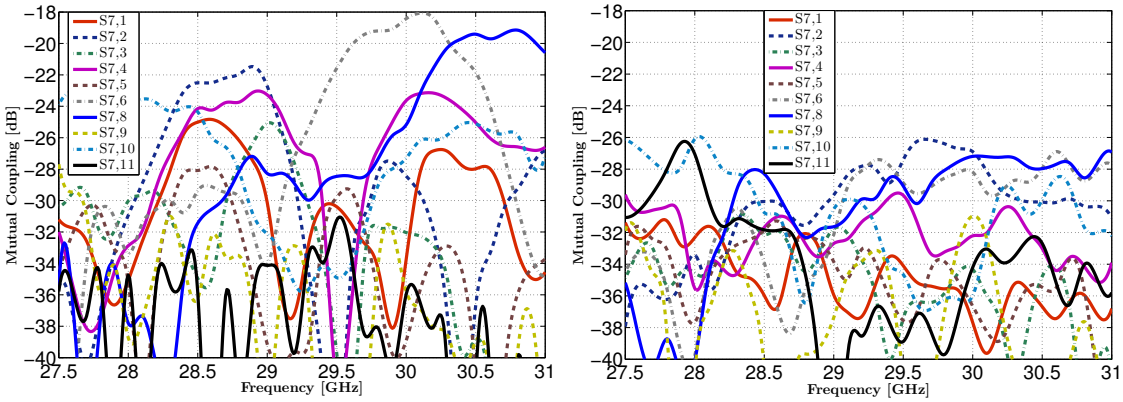

(a) (b)

Figure 5.24: Mutual coupling of the PPW beamformer over the entire frequency band ([27.5-31] GHz) obtained with the final FEM simulation for feed #7. (a) Multiple lenses design considered here and (b) Single lens design defined in Chapter 4.

maximum levels are lower than -18 dB.

Unlike with the maximum directivity computed, the S-parameters degradation is more pronounced between the ideal and the final design. However, those results are still acceptable since no large degradations are observed over the bandwidth which could compromise the performance of the targeted missions. As mentioned previously in Subsection 5.3.3, an optimization of the horn profile transition could be added to further improve them.

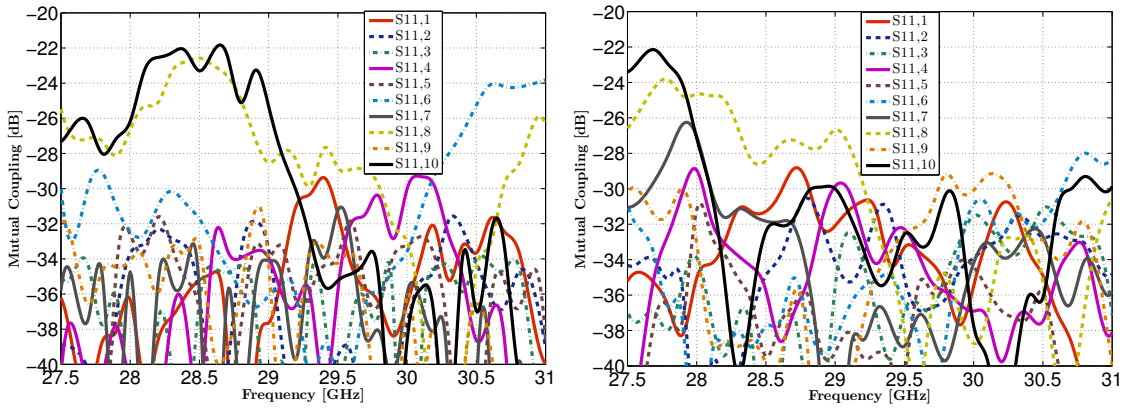

Figure 5.25: Mutual coupling of the PPW beamformer over the entire frequency band ([27.5-31] GHz) obtained with the final FEM simulation for feed #11. (a) Multiple lenses design considered here and (b) Single lens design defined in Chapter 4.

5.5 Conclusion

Size reduction has been targeted here. Based on the prototype measured over the up-link Ka-band ([27.5-31] GHz), a second design targeting the same performances has been proposed, while reducing the transversal and longitudinal dimensions. The radiation performances demonstrate similar performances (Directivity, HPBW, SLL). The S-parameters degradation is limited, without compromising this approach. Reflection and mutual coupling coefficients are respectively computed below -17 and -18 dB. This design should be prototyped at IETR using two blocs of aluminum and a classical milling. The measurements aim to validate those latest developments. Further size reduction by increasing the number of ridges would require to update the modelling approach to maintain acceptable accuracy of the performance predictions.

6
General conclusions

The thesis has dealt with the development of continuous parallel plate waveguide lenses for future low cost and high performances multiple beam antennas. This solution transforms the cylindrical wave launched by one of the primary feeds and propagating inside the PPW section, into a nearly plane wave radiated in free space by the radiating horn, and vice-versa.

This beamformer is defined using a design approach similar to constrained lenses without the complexity and limitation in bandwidth resulting from the lens discretization. The desired delay correction applied to ensure this wave transformation is provided by a PPW lens made of a transversal ridge and cavity. This solution is very simple from a mechanical point-of-view and is expected to lead to a low-cost design without compromising performance. Moreover, this full metal solution is compatible with high power applications. The design has been illustrated and precisely described in Chapter 1.

A proof of concept was provided at Ku-band, in order to demonstrate scanning capabilities over a large bandwidth. This first approach was optimized using a complex and time consuming full-wave approach, justifying the need to develop fast and accurate tools that provide better insight on the lens operation principles and are more suitable to study configurations with larger dimensions. This aspect was addressed in Chapter 2. An analytical model based on geometrical optics has been proposed for the design and analysis. As the design approach was originally based on a constrained lens model, a bifocal model has been studied, simplifying first the propagation inside the transversal cavity with ideal transmission line lengths. This approach provides a relevant starting point for the concept. A refined

model based on ray tracing led to a final version of the tool by accounting for the wave propagation inside the transversal cavity. An excellent prediction of the full-wave simulation results has been demonstrated with a reasonably large validity domain. Furthermore, the model requires very low computational effort, around 1 or 2 seconds, as compared to 4 or 5 minutes with the classical FEM implementation. The main achievement obtained through this numerical tool has been the ability to characterize a large amount of continuous PPW lenses in a short time, opening the way for the combination with optimization processes to target specific and various requirements.

Optimizations based on phase and pattern procedures was proposed in Chapter 3. First based on elliptical lens profiles, starting from the bifocal constrained lens model, the proposed analytical model demonstrates residual path length errors. All the radiation patterns presented display a residual side lobe imbalance, which results in some interferences when multiple beam applications are targeted. Two design evolutions, a thick delay lens with different inner and outer lens contours and a thin lens with polynomial profiles, were introduced to increase the control on both phase and amplitude distributions on the outer lens contour (Σ_2). The thick lens designs proved to be outside the domain of validity of the developed GO tool, but the solution remains of interest in combination with alternative manufacturing techniques. Shaped polynomial delay lens profiles were finally introduced. The numerical results of the lens shaped with polynomials confirm the potential of the proposed profiles with path length errors very similar to those of simplified constrained lens models over a large scanning range ($[-30°, 30°]$). The corresponding radiated patterns present reduced and more balanced side lobe levels, when compared to the previously introduced solution using elliptical contour and profile for the delay-lens shape.

An experimental validation of the scanning performance has been reported in Chapter 4. A design working over the up-link Ka band ([27.5-31] GHz) and proposing eleven beams over a wide angular range ($[-28.5°, 31.5°]$) with an angular step of 6° has been studied. The configuration proposed provides patterns with a beamwidth of 3° while targeting a minimum side lobe level. Consequently, the idea was to consider a final configuration made of two identical superimposed lenses, with a 180° rotation between them. Excellent beam performances (HPBW, SLL) have been obtained with the final FEM simulation, confirming the results obtained in the previous Chapter 3. A manufactured and measured prototype confirms the predicted performances, including low scanning loss and high radiation stability over the complete frequency band of operation. High radiation efficiencies are

obtained with this fully metallic design, particularly suitable for space applications. The mechanical simplicity offered by the concept has been proved again with this prototype, possibly enabling low-cost multi-beam satellite platforms.

In Chapter 5, size reduction was investigated. This was performed in order to fulfill integration requirements or propose a 2D array of stacked continuous PPW lenses. Indeed, the transversal cavity introduced by the concept is the main limitation for the reduction of the beamformer height. A design working over the same up-link Ka-band ([27.5-31] GHz) and targeting the same performances is proposed. Compactness along the transversal direction is first considered with 4 optimized ridges and cavities working as delay lenses, in order to reduce the finale height. A reduction factor of 2.7 of the transversal cavities height is obtained. Then two straight transversal ridges and cavities are added to reduce the longitudinal dimension. Analyzing the radiation properties, similar performances (Directivity, HPBW and SLL) are obtained in simulation, as compared to the first design presented in Chapter 4. The S-parameters demonstrate a degradation, explained by the several bend transitions. However the levels are still acceptable without compromising the performances targeted, as with the final FEM simulation, reflection and mutual coupling coefficients are respectively below -17 dB and -18 dB over the entire frequency range. This second prototype is planned to be fabricated soon at IETR and measured.

Future developments

LEO/MEO missions require low or medium antenna gains over a wide field of view, making use of direct radiating arrays. For GEO satcom applications, the scanning range is limited ($\pm 8°$) but the combination between a reflector geometry is needed to provide higher gains.

A recent activity between ESA and Thales Alenia Space proposes the combination between a stack of line sources (typically continuous PPW lenses) and a doubly curved reflector configuration [74]. The proposed hybrid array fed reflector antenna converts fan beams into pencil beams targeting the gain requirements. The coverage is created by selecting the desired horn along each lens feeding system, enabling more flexibility as compared to a classical SFPB multiple beam reflector antennas (Chapter 1).

Thus, a future work would be to combine the proposed GO numerical tool, presented in Chapter 2, with the TICRA GRASP [75] software currently used to study reflector configurations. The idea would be first to optimize the PPW lens for a fixed doubly curved reflector and then propose a combined optimization process.

This requires further developments in order to create adequate inputs/outputs between the developed numerical tool and GRASP.

The mechanical simplicity offered by the concept opens the way to alternative manufacturing techniques (3D printing or plastic injection), to further reduce the cost. This has been previously introduced in Chapter 3 (Subsection 3.3.2), where the RAFQO ANR project [70] was presented, making use of the developments performed in this thesis. Thales Alenia Space, in the frame of future projects, will continue investigating those potentially low-cost fabrication techniques in combination with the continuous delay-lens concept, including prototyping and measurements.

Appendices

A

Ray tracing model considering elliptical profiles

The lens profile is described by the following equations,

$$x = a_{in}(\sqrt{1-y^2} - 1), \tag{A.1}$$

$$u = a_{out}(\sqrt{1-y^2} - \Delta_{out}), \tag{A.2}$$

(x, y), (u, y) describing respectively the coordinates of the inner (Σ_1) and outer (Σ_2) lens contours. a_{in} and a_{out} are the main parameters of both elliptical profiles. Δ_{out} defines the outer lens (Σ_2) translation along $\overrightarrow{X}$-axis and is defined to achieve a minimum thickness of the ridge, as shown in Fig. A.1b.

The ridge height profile (h_w) is described by,

$$h_w = a_w(\sqrt{1-y^2} - \sqrt{1-(d/2)^2}) \tag{A.3}$$

where $d = D/f$, h_w the height of the ridge profile, normalized to the focal distance f. Considering, two independent inner and outer lens profiles, the ridge height is also defined by its inner and outer profiles as shown in Fig. A.1a.

A.1 Propagation inside the transversal cavity, along the inner lens contour

The ray tracing model considered in this section is represented in Fig. A.2. We consider a ray k coming from F, tilted by an angle γ_k and impinging on the inner

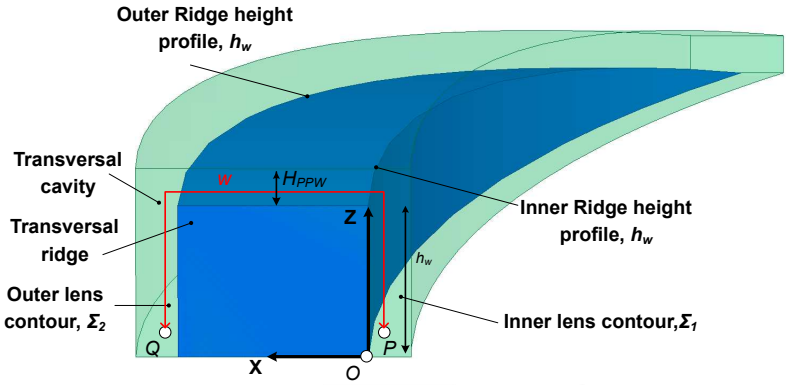

(a)

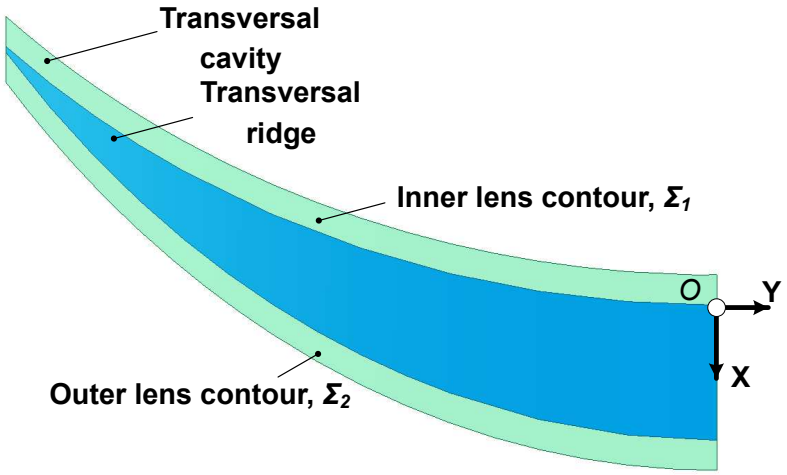

(b)

Figure A.1: PPW lens considering independent inner (Σ_1) and outer (Σ_2) lens contours: (a) 3D view and (b) top view in xOy plane.

lens contour at P_k. Plane T_k is defined as the vertical plane tangent to the inner lens contour (Σ_1) and passing through P_k. The corresponding local coordinate system is $(P_k, \overrightarrow{X_k}, \overrightarrow{Y_k})$. Axis $\overrightarrow{X_k}$ is orthogonal to T_k and is used to characterize the upward propagation of ray k in the transversal section. According to reflection law, the incident propagation angle ζ_k (Fig. A.2) with respect to $\overrightarrow{X_k}$ is equal to the one propagating in the orthogonal plane T_k with respect to $\overrightarrow{Z_k}$.

The propagation inside the transversal cavity, associated to the inner lens contour Σ_1 is always performed in the way presented in Subsection 2.1.2 (Chapter 2). This part is remind here and shown in Fig. A.3a, defining the inner ridge profile point R_{ink}.

The coordinates of R_{ink} are defined as the intersection between $P_k R_{ink}$ and the ridge height elliptical profile h_w, defined in Eqn. (A.3).

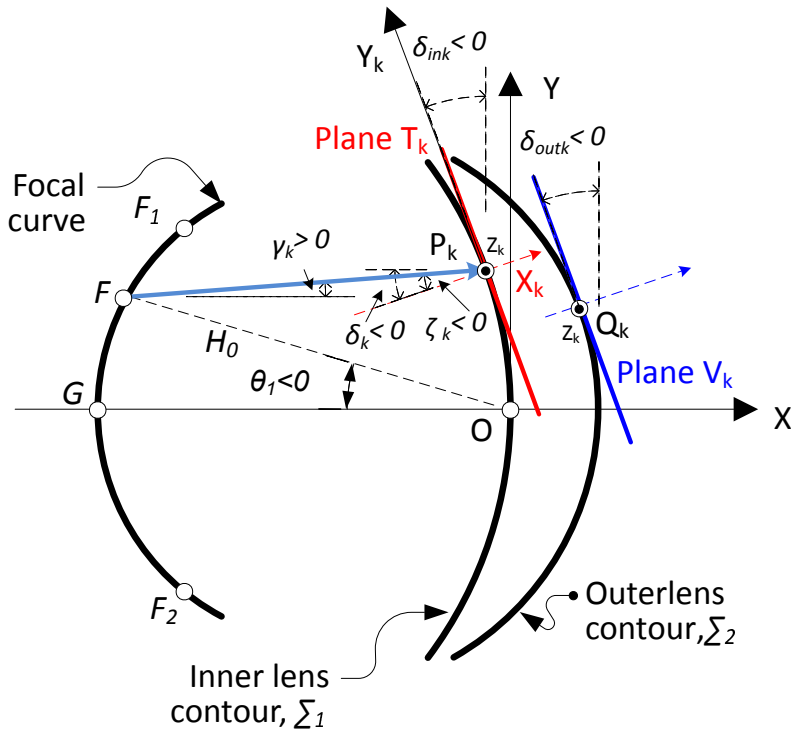

Figure A.2: Continuous lens model to account for wave propagation inside the transversal cavity, considering the PPW lens thickness

A positive coordinate z along $\overrightarrow{Z}$-axis is defined as,

$$z = (-p_1 + \sqrt{(p_1)^2 - 4p_2p_0})/2p_2, \tag{A.4}$$

with,

$$\begin{gathered} p_0 = y_{P_k}^2 - (d/2)^2, \\ p_1 = 2y_{P_k}tan(\zeta_k) + (2/a_w)(\sqrt{1-(-d/2)^2}), \\ p_2 = 1/a_w^2 + tan(\zeta_k)^2. \end{gathered}$$

The propagation is then defined in the plane T_k using a change of the principal coordinate system, with (x, y, z) and (x', y', z') respectively the coordinates in $(O, \overrightarrow{X}, \overrightarrow{Y}, \overrightarrow{Z})$ and $(P_k, \overrightarrow{X_k}, \overrightarrow{Y_k}, \overrightarrow{Z_k})$, as defined in Eqn. (A.5),

$$\begin{cases} x' = (x - x_{P_k})cos(\delta_{ink}) + (y - y_{P_k})sin(\delta_{ink}) \\ y' = -(x - x_{P_k})sin(\delta_{ink}) + (y - y_{P_k})cos(\delta_{ink}) \\ z' = z - z_{P_k}, \end{cases} \tag{A.5}$$

with δ_{ink} the angular coefficient associated to T_k at point P_k and calculated using the derivative of the inner lens contour (Σ_1) (Eqn. (A.1)). We define the coordinates of R_{ink} in $(P_k, \overrightarrow{X_k}, \overrightarrow{Y_k}, \overrightarrow{Z_k})$ using Eqn. (A.6),

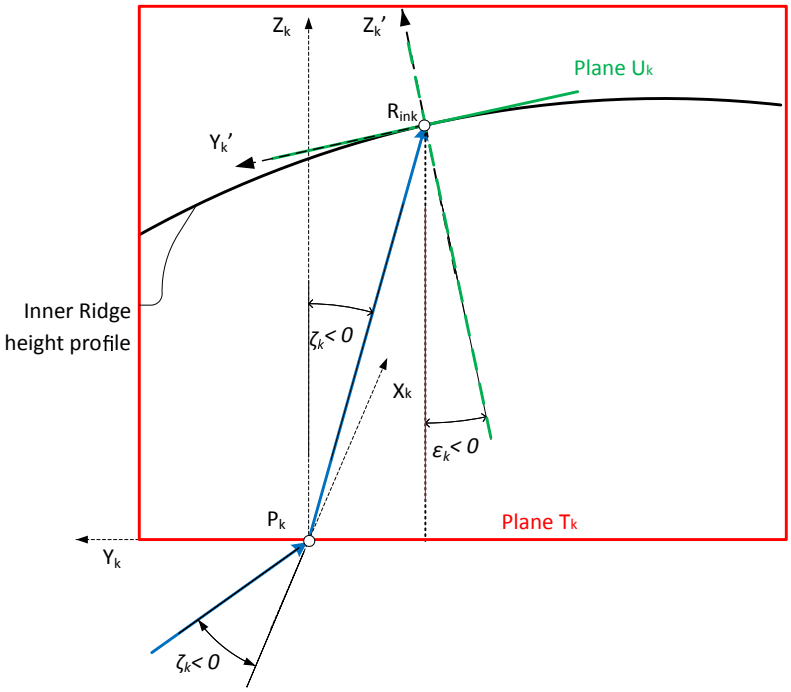

(a)

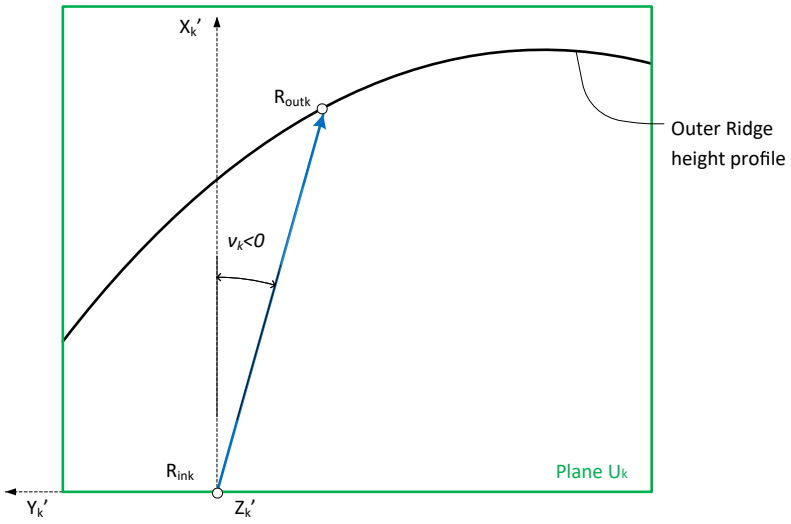

(b)

Figure A.3: Ray Tracing to account for wave propagation inside the transversal cavity: (a) Inner lens contour and (b) Thickness of the PPW lens.

$$\begin{cases} x'_{R_{ink}} = 0 \\ y'_{R_{ink}} = ztan(\zeta_k) \\ z'_{R_{ink}} = z. \end{cases} \tag{A.6}$$

The final coordinates of R_{ink} in $(O, \overrightarrow{X}, \overrightarrow{Y})$ are calculated using Eqn. (A.7),

$$\begin{cases} x_{R_{ink}} = x'_{R_{ink}} cos(\delta_{ink}) - y'_{R_{ink}} sin(\delta_{ink}) + x_{P_k} \\ y_{R_{ink}} = x'_{R_{ink}} sin(\delta_{ink}) + y'_{R_{ink}} cos(\delta_{ink}) + y_{P_k} \\ z_{R_{ink}} = z'_{R_{ink}} \end{cases} \tag{A.7}$$

A.2 Propagation along the thickness of the PPW lens

Let now consider the propagation along the thickness of the PPW lens. As shown in Fig. A.3b, we have a ray k coming from R_{ink}, tilted by an angle $\nu_k = \zeta_k - \delta_{ink} + \epsilon_k$ and impinging on the outer ridge height profile at R_{outk}. δ_{ink} and ϵ_k are respectively the angular coefficients associated to the inner lens contour (Σ_1) and the ridge height profile (h_w) at R_{ink}. Plane U_k is defined as the plane tangent to the ridge height profile h_w and passing through R_{ink}. The corresponding local coordinate system is $(R_{ink}, \overrightarrow{X'_k}, \overrightarrow{Y'_k}, \overrightarrow{Z'_k})$.

The coordinates of R_{outk} are first defined as the intersection between $R_{ink}R_{outk}$ and the outer ridge height profile.

A positive coordinate x along $\overrightarrow{X}$-axis is defined as,

$$x = (-p_1 + \sqrt{(p_1)^2 - 4p_2p_0})/2p_2, \tag{A.8}$$

with,

$$\begin{gathered} p_0 = x^2_{R_{ink}} tan(\nu_k) - 2x_{R_{ink}} y_{R_{ink}} tan(\nu_k) + y^2_{R_{ink}} - 1 + \Delta^2_{out}, \\ p_1 = -2x_{R_{ink}} tan(\nu_k)^2 + 2y_{R_{ink}} tan(\nu_k) + (2/a_{out})\Delta_{out}, \\ p_2 = 1/a^2_{out} + tan(\nu_k)^2. \end{gathered}$$

The propagation is then defined in the plane U_k using a change of the principal coordinate system, with (x, y, z) and (x', y', z') respectively the coordinates in $(O, \overrightarrow{X}, \overrightarrow{Y}, \overrightarrow{Z})$ and $(R_{ink}, \overrightarrow{X'_k}, \overrightarrow{Y'_k}, \overrightarrow{Z'_k})$, as defined in Eqn. (A.9),

$$\begin{cases} x' = x - x_{R_{ink}} \\ y' = -(z - z_{R_{ink}}) sin(\epsilon_k) + (y - y_{R_{ink}}) cos(\epsilon_k) \\ z' = (z - z_{R_{ink}}) cos(\epsilon_k) + (y - y_{R_{ink}}) sin(\epsilon_k). \end{cases} \tag{A.9}$$

We define the coordinates of R_{outk} in $(R_{ink}, \overrightarrow{X'_k}, \overrightarrow{Y'_k}, \overrightarrow{Z'_k})$ using Eqn. (A.10),

$$\begin{cases} x'_{R_{outk}} = x - x_{R_{ink}} \\ y'_{R_{outk}} = x'_{R_{outk}} tan(\nu_k) \\ z'_{R_{outk}} = 0. \end{cases} \tag{A.10}$$

The final coordinates of R_{outk} in $(O, \overrightarrow{X}, \overrightarrow{Y}, \overrightarrow{Z})$ are calculated using Eqn. (A.11),

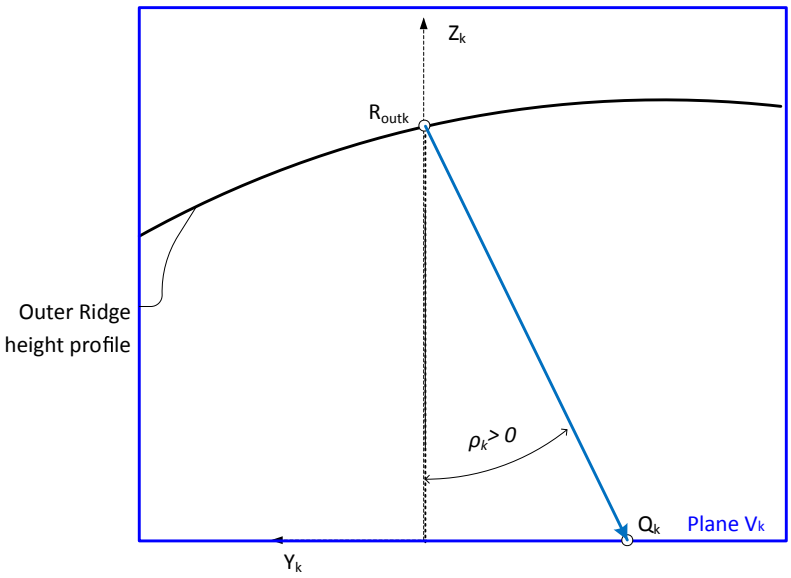

Figure A.4: Ray Tracing to account for wave propagation inside the transversal cavity : Outer lens contour

$$\begin{cases} x_{R_{outk}} = x'_{R_{outk}} + x_{R_{ink}} \\ y_{R_{outk}} = z'_{R_{outk}} sin(\epsilon_k) + y'_{R_{outk}} cos(\epsilon_k) + y_{R_{ink}} \\ z_{R_{outk}} = z'_{R_{outk}} cos(\epsilon_k) - y'_{R_{outk}} sin(\epsilon_k) + z_{R_{ink}}. \end{cases} \tag{A.11}$$

A.3 Propagation inside the transversal cavity, along the outer lens contour

The final coordinates of Q_k are finally calculated, using the same approach as for the propagation associated to the inner lens contour (Σ_1). Plane V_k is defined as the vertical plane tangent to the outer lens contour (Σ_2) and passing through R_{outk}, as shown in Fig. A.2. As shown in Fig. A.4, the coordinates of Q_k are defined as the intersection between $R_{outk}Q_k$, tilted by an angle $\rho_k = \nu_k + \delta_{outk} + \epsilon_k$ and the outer lens contour (Σ_2). δ_{outk} and ϵ_k are respectively the angular coefficients associated to the outer lens contour (Σ_2) and the ridge height profile (h_w) at R_{outk}.

The propagation in the plane V_k using a change of the principal coordinate system, with (x, y, z) and (x', y', z') respectively the coordinates in $(O, \overrightarrow{X}, \overrightarrow{Y}\overrightarrow{Z})$ and $(R_{outk}, \overrightarrow{X_k}, \overrightarrow{Y_k}, \overrightarrow{Z_k})$, as defined in Eqn. (A.12),

$$\begin{cases} x' = (x - x_{R_{outk}})cos(\delta_{outk}) + (y - y_{R_{outk}})sin(\delta_{outk}) \\ y' = -(x - x_{R_{outk}})sin(\delta_{outk}) + (y - y_{R_{outk}})cos(\delta_{outk}) \\ z' = z - z_{R_{outk}}, \end{cases} \tag{A.12}$$

with δ_{outk} the angular coefficient associated to V_k at point R_{outk} and calculated using the derivative of the inner lens contour (Σ_2).

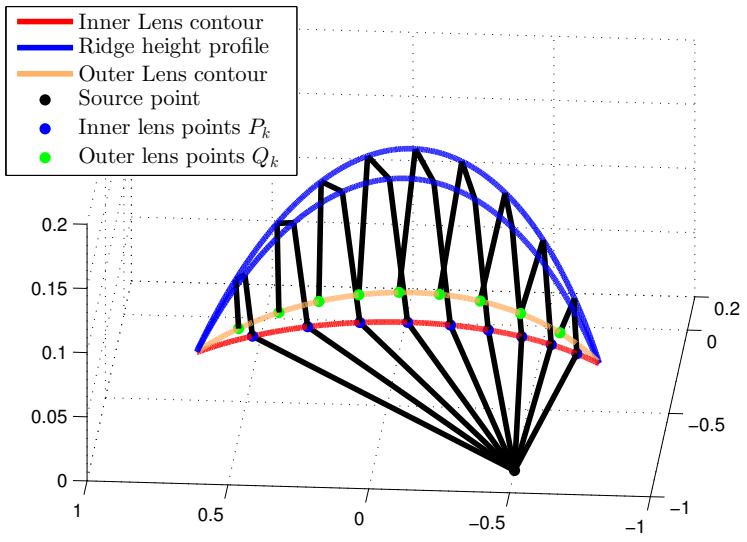

Figure A.5: Positions of the inner and outer lens points P_k and Q_k computed with the ray tracing model, considering independent inner and outer lens profiles. Here with $\theta_1 = \alpha$. The lens parameters are $D = 10\lambda$, $\frac{f}{D} = 0.7$ and $\alpha = 30°$. Axis values are normalized to the focal distance f.

The positions of the outer lens points Q_k in $(R_{outk}, \overrightarrow{X_k}, \overrightarrow{Y_k}, \overrightarrow{Z_k})$ are defined using the following Eqn. (A.13),

$$\begin{cases} x'_{Q_k} = 0 \\ y'_{Q_k} = z_{R_{outk}} tan(\rho_k) \\ z'_{Q_k} = -z_{R_{outk}}. \end{cases} \tag{A.13}$$

The final coordinates of Q_k in $(O, \overrightarrow{X}, \overrightarrow{Y}\overrightarrow{Z})$ are calculated using Eqn. (A.14),

$$\begin{cases} x_{Q_k} = x'_{Q_k} cos(\delta_{outk}) - y'_{Q_k} sin(\delta_{outk}) + x_{R_{outk}} \\ y_{Q_k} = x'_{Q_k} sin(\delta_{outk}) + y'_{Q_k} cos(\delta_{outk}) + y_{R_{outk}} \\ z_{Q_k} = z'_{Q_k} + z_{R_{outk}} = 0. \end{cases} \tag{A.14}$$

The different points positions P_k, R_{outk} and Q_k are first calculated on the tangent plane considered (T_k, S_k and V_k) and then respectively projected along $\overrightarrow{Z}$-axis for (P_k, Q_k) and $\overrightarrow{X}$-axis (R_{outk}). This approximation introduces some limitations, in line with the validity domain of the proposed model. When the curvature of the different profiles increases significantly, improvements have to be considered. An example of ray tracing, including the propagation along the ridge thickness, performed in this section, is shown in Fig. A.5.

B

Ray tracing model considering polynomial profiles

Contents

The ray tracing procedure presented in Annex. A was based on elliptical profiles. An updated version is introduced here, considering polynomial profiles.

Inner (Σ_1) and outer (Σ_2) lens profiles are now described respectively by,

$$x = \sum_{l=0}^{n} p_l y^l, \tag{B.1}$$

and,

$$u = \sum_{l=0}^{n} p'_l y^l. \tag{B.2}$$

The ridge height profile (h_w) is now defined by,

$$h_w = \sum_{l=1}^{n} q_l y^l - min(\sum_{l=1}^{n} q_l y^l). \tag{B.3}$$

(x, u), y and h_w are the coordinates along the different reference system axis, all normalized to the focal distance f. p_l, p'_l and q_l are the l^{th} degree coefficients,

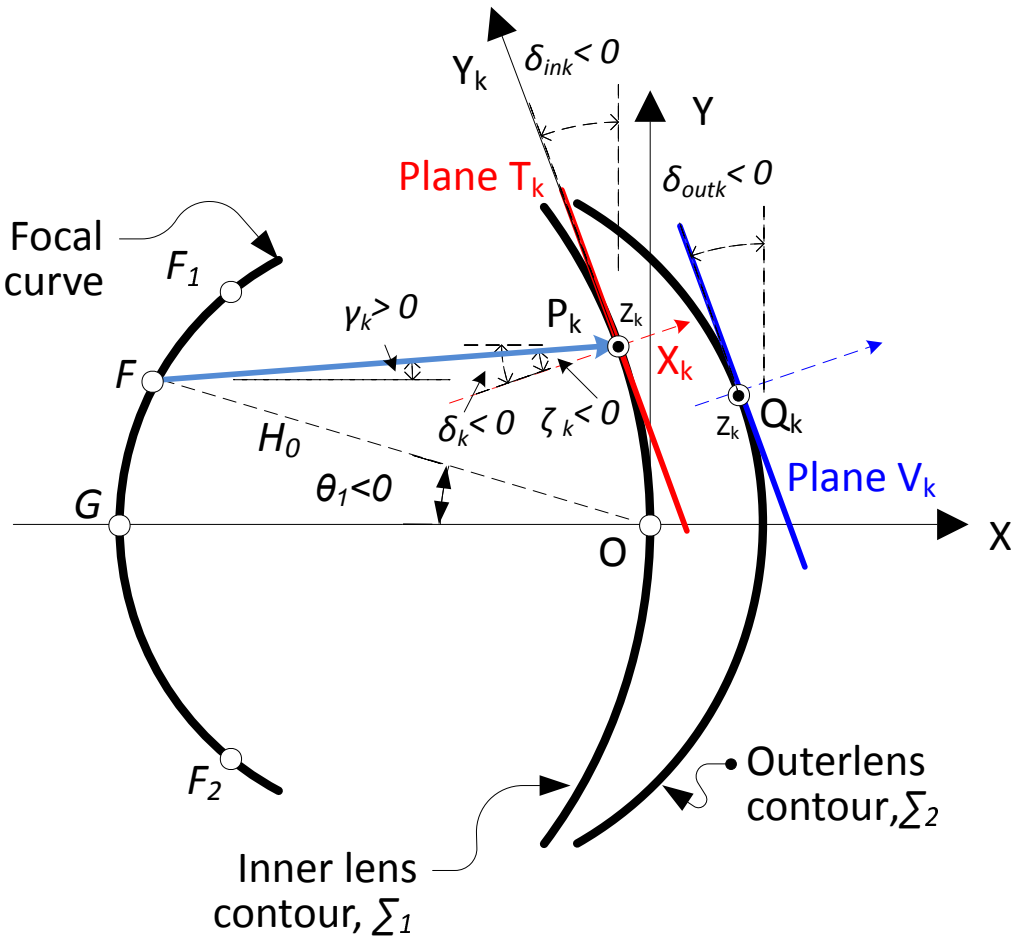

Figure B.1: Continuous lens model to account for wave propagation inside the transversal cavity.

where $1 < l < n$, n defining the maximum degree. Using the lens symmetry with respect to $\overrightarrow{Y}$-axis, only even order coefficients are considered.

B.1 Propagation inside the parallel plate section

The coordinates of P_k, defined in $(O, \overrightarrow{X}, \overrightarrow{Y})$ are first calculated using the following equations. P_k is defined as the intersection between a ray k coming from a point source $F(a = h_0 cos(\theta_1), b = h_0 sin(\theta_1))$, and the inner lens contour (Eqn. (B.1)), as shown in Fig. B.1.

The coordinate y_{P_k} along $\overrightarrow{Y}$-axis is defined as a solution of

$$\sum_{l=0}^{n} t_l y_{P_k}^l = 0, \tag{B.4}$$

with

$$t_l = tan(\gamma_k)p_l \text{ for } 2 < l < n$$
$$t_1 = -1$$
$$t_0 = tan(\gamma_k)p_0 + atan(\gamma_k) - b.$$

The coordinate along $\overrightarrow{X}$-axis x_{P_k} is defined by,

$$x_{P_k} = (y_{P_k} + b)/tan(\gamma_k) - a. \tag{B.5}$$

B.2 Propagation inside the transversal cavity, along the inner lens contour

Plane T_k is then defined as the vertical plane tangent to the inner lens contour Σ_1 and passing through P_k. The corresponding local coordinate system is $(P_k, \overrightarrow{X_k}, \overrightarrow{Y_k})$. Axis $\overrightarrow{X_k}$ is orthogonal to T_k and is used to characterize the upward propagation of ray k in the transversal section. According to reflection law, the incident propagation angle ζ_k (Fig. B.1) with respect to $\overrightarrow{X_k}$ is equal to the one propagating in the orthogonal plane T_k with respect to $\overrightarrow{Z_k}$ (Fig. B.2a).

The coordinates of R_{ink} are defined as the intersection between P_kR_{ink} and the ridge height profile h_w, defined in Eqn. (B.3).

A positive coordinate y along $\overrightarrow{Y}$-axis is first defined as a solution of the following equation,

$$\sum_{l=0}^{n} t_l y^l = 0, \tag{B.6}$$

with,

$$t_0 = -tan(\zeta_k)min(\sum_{l=1}^{n} q_l y^l) - z_{P_k}tan(\zeta_k) + y_{P_k},$$
$$t_1 = -1,$$
$$t_l = tan(\zeta_k)q_l \text{ for } 2 < l < n.$$

The propagation is then defined in the plane T_k using a change of the principal coordinate system, with (x, y, z) and (x', y', z') respectively the coordinates in $(O, \overrightarrow{X}, \overrightarrow{Y}, \overrightarrow{Z})$ and $(P_k, \overrightarrow{X_k}, \overrightarrow{Y_k}, \overrightarrow{Z_k})$, as defined in Eqn. (B.7),

$$\begin{cases} x' = (x - x_{P_k})cos(\delta_{ink}) + (y - y_{P_k})sin(\delta_{ink}) \\ y' = -(x - x_{P_k})sin(\delta_{ink}) + (y - y_{P_k})cos(\delta_{ink}) \\ z' = z - z_{P_k}, \end{cases} \tag{B.7}$$

with δ_{ink} the angular coefficient associated to T_k at point P_k and calculated using the derivative of the inner lens contour (Σ_1), defined in Eqn. (B.1).

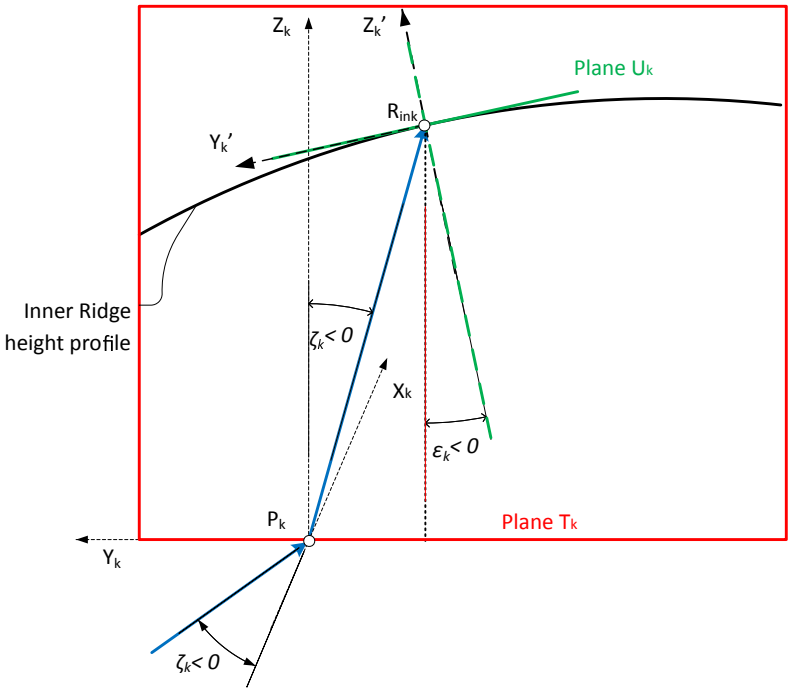

(a)

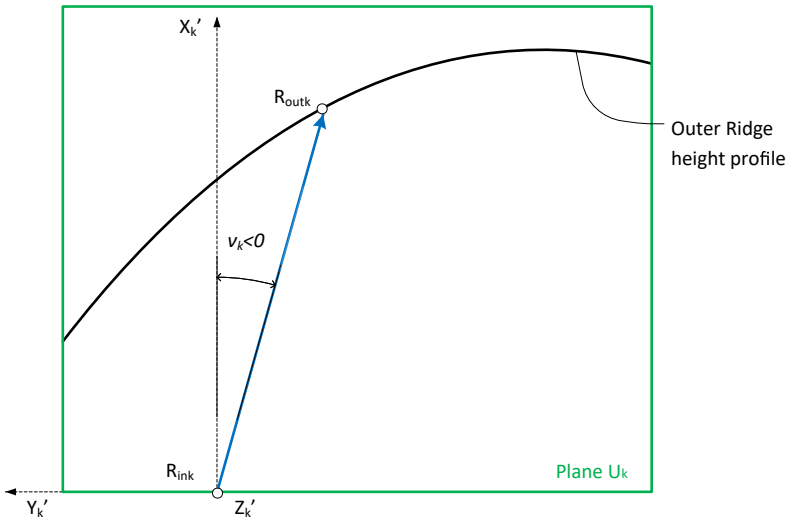

(b)

Figure B.2: Ray Tracing to account for wave propagation inside the transversal cavity: (a) Inner lens contour and (b) Thickness of the PPW lens.

We define the coordinates of R_{ink} in $(P_k, \overrightarrow{X_k}, \overrightarrow{Y_k}, \overrightarrow{Z_k})$ using Eqn. (B.8),

$$\begin{cases} x'_{R_{ink}} = 0 \\ y'_{R_{ink}} = y - y_{P_k} \\ z'_{R_{ink}} = y'_{R_{ink}}/tan(\zeta_k). \end{cases} \tag{B.8}$$

The final coordinates of R_{ink} in $(O, \overrightarrow{X}, \overrightarrow{Y}, \overrightarrow{Z})$ are calculated using Eqn. (B.9),

$$\begin{cases} x_{R_{ink}} = x'_{R_{ink}} cos(\delta_{ink}) - y'_{R_{ink}} sin(\delta_k) + x_{P_k} \\ y_{R_{ink}} = x'_{R_{ink}} sin(\delta_{ink}) + y'_{R_{ink}} cos(\delta_k) + y_{P_k} \\ z_{R_{ink}} = z'_{R_{ink}} + z_{P_k} \end{cases} \tag{B.9}$$

B.3 Propagation along the thickness of the PPW lens

Let now consider the propagation along the thickness of the PPW lens. As shown in Fig. B.2b, we have a ray k coming from R_{ink}, tilted by an angle $\nu_k = \zeta_k - \delta_{ink} + \epsilon_k$ and impinging on the outer ridge height profile at R_{outk}. δ_{ink} and ϵ_k are respectively the angular coefficients associated to the inner lens contour (Σ_1) and the ridge height profile (h_w) at R_{ink}. Plane U_k is defined as the plane tangent to the ridge height profile h_w and passing through R_{ink}. The corresponding local coordinate system is $(R_{ink}, \overrightarrow{X'_k}, \overrightarrow{Y'_k}, \overrightarrow{Z'_k})$.

The coordinates of R_{outk} are defined as the intersection between $R_{ink}R_{outk}$ and the outer ridge height profile.

A positive coordinate y along $\overrightarrow{Y}$-axis is defined as a solution of the following equation,

$$\sum_{l=0}^{n} t_l y^l = 0, \tag{B.10}$$

with,

$$\begin{gathered} t_0 = tan(\zeta_k) p'_0 - x_{P_k} tan(\nu_k) + y_{P_k}, \\ t_1 = -1, \\ t_l = tan(\nu_k) p'_l \text{ for } 2 < l < n. \end{gathered}$$

The propagation is then defined in the plane U_k using a change of the principal coordinate system, with (x, y, z) and (x', y', z') respectively the coordinates in $(O, \overrightarrow{X}, \overrightarrow{Y}, \overrightarrow{Z})$ and $(R_{ink}, \overrightarrow{X'_k}, \overrightarrow{Y'_k}, \overrightarrow{Z'_k})$, as defined in Eqn. (B.11),

$$\begin{cases} x' = x - x_{R_{ink}} \\ y' = -(z - z_{R_{ink}}) sin(\epsilon_k) + (y - y_{R_{ink}}) cos(\epsilon_k) \\ z' = (z - z_{R_{ink}}) cos(\epsilon_k) + (y - y_{R_{ink}}) sin(\epsilon_k). \end{cases} \tag{B.11}$$

We define the coordinates of R_{outk} in $(R_{ink}, \overrightarrow{X'_k}, \overrightarrow{Y'_k}, \overrightarrow{Z'_k})$ using Eqn. (B.12),

$$\begin{cases} y'_{R_{outk}} = y - y_{R_{ink}} \\ x'_{R_{outk}} = y'_{R_{outk}} ./ tand(\nu_k) \\ z'_{R_{outk}} = 0. \end{cases} \tag{B.12}$$

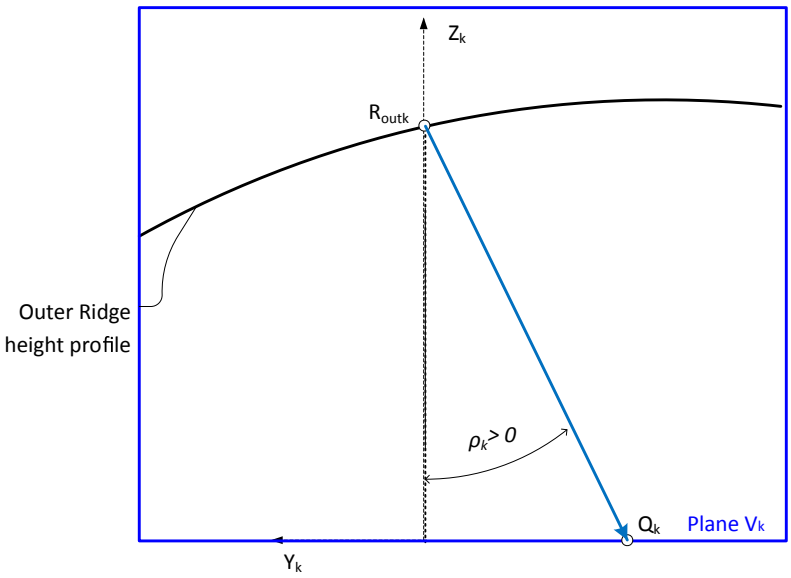

Figure B.3: Ray Tracing to account for wave propagation inside the transversal cavity : Outer lens contour

The final coordinates of R_{outk} in $(O, \overrightarrow{X}, \overrightarrow{Y}, \overrightarrow{Z})$ are calculated using Eqn. (B.13),

$$\begin{cases} x_{R_{outk}} = x'_{R_{outk}} + x_{R_{ink}} \\ y_{R_{outk}} = z'_{R_{outk}} sin(\epsilon_k) + y'_{R_{outk}} cos(\epsilon_k) + y_{R_{ink}} \\ z_{R_{outk}} = z'_{R_{outk}} cos(\epsilon_k) - y'_{R_{outk}} sin(\epsilon_k) + z_{R_{ink}}. \end{cases} \tag{B.13}$$

B.4 Propagation inside the transversal cavity, along the outer lens contour

The final coordinates of Q_k are finally calculated, using the same approach as for the propagation associated to the inner lens contour (Σ_1). Plane V_k is defined as the vertical plane tangent to the outer lens contour (Σ_2) and passing through R_{outk}, as shown in Fig. B.1. As shown in Fig. B.3, the coordinates of Q_k are defined as the intersection between $R_{outk}Q_k$, tilted by an angle $\rho_k = \nu_k + \delta_{outk} + \epsilon_k$ and the outer lens contour (Σ_2). δ_{outk} and ϵ_k are respectively the angular coefficients associated to the outer lens contour (Σ_2) and the ridge height profile (h_w) at R_{outk}.

The propagation in the plane V_k using a change of the principal coordinate system, with (x, y, z) and (x', y', z') respectively the coordinates in $(O, \overrightarrow{X}, \overrightarrow{Y}, \overrightarrow{Z})$ and $(R_{outk}, \overrightarrow{X_k}, \overrightarrow{Y_k}, \overrightarrow{Z_k})$, as defined in Eqn. (B.14),

$$\begin{cases} x' = (x - x_{R_{outk}})cos(\delta_{outk}) + (y - y_{R_{outk}})sin(\delta_{outk}) \\ y' = -(x - x_{R_{outk}})sin(\delta_{outk}) + (y - y_{R_{outk}})cos(\delta_{outk}) \\ z' = z - z_{R_{outk}}, \end{cases} \tag{B.14}$$

with δ_{outk} the angular coefficient associated to V_k at point R_{outk} and calculated using the derivative of the inner lens contour (Σ_2).

The positions of the outer lens points Q_k in $(R_{outk}, \overrightarrow{X_k}, \overrightarrow{Y_k}, \overrightarrow{Z_k})$ are defined using the following Eqn. (B.15),

$$\begin{cases} x'_{Q_k} = 0 \\ y'_{Q_k} = z_{R_{outk}} tan(\rho_k) \\ z'_{Q_k} = -z_{R_{outk}}. \end{cases} \tag{B.15}$$

The final coordinates of Q_k in $(O, \overrightarrow{X}, \overrightarrow{Y}, \overrightarrow{Z})$ are calculated using Eqn. (B.16),

$$\begin{cases} x_{Q_k} = x'_{Q_k} cos(\delta_{outk}) - y'_{Q_k} sin(\delta_{outk}) + x_{R_{outk}} \\ y_{Q_k} = x'_{Q_k} sin(\delta_{outk}) + y'_{Q_k} cos(\delta_{outk}) + y_{R_{outk}} \\ z_{Q_k} = z'_{Q_k} + z_{R_{outk}} = 0. \end{cases} \tag{B.16}$$

The different points positions P_k, R_{outk} and Q_k are first calculated on the tangent plane considered (T_k, S_k and V_k) and then respectively projected along $\overrightarrow{Z}$-axis for (P_k, Q_k) and $\overrightarrow{X}$-axis (R_{outk}). This approximation introduces some limitations, in line with the validity domain of the proposed model. When the curvature of the different profiles increases significantly, improvements have to be considered.

References

[1] "A concentration of constellations at Thales Alenia Space," https://www.thalesgroup.com/en/worldwide/space/news/concentration-constellations-thales-alenia-space, accessed: 2018-09-04.

[2] P. Lepeltier, P. Bosshard, J. Maurel, C. Labourdette, G. Navarre, and J. David, "Recent achievements and future trends for multiple beam telecommunication antennas," *Int. Symp. on Antenna Tech. Applied Electromagnetics*, pp. 1–6, Jun. 2012.

[3] P. Bosshard, J. Lafond, F. Dubos, P. Lepeltier, E. Vourch, F. Delepaux, C. Labourdette, L. Martin, G. Navarre, and C. Feat, "Thales Alenia Space HTS/V-HTS multiple beam antennas sub-systems on the right track," *The 10th European Conference on Antennas and Propagation (EuCAP)*, pp. 1–5, Apr. 2016.

[4] J. C. Lafond, E. Vourch, F. Delepaux, P. Lepeltier, P. Bosshard, F. Dubos, C. Feat, C. Labourdette, G. Navarre, and J. M. Bassaler, "Thales Alenia Space multiple beam antennas for telecommunication satellites," *The 8th European Conference on Antennas and Propagation (EuCAP)*, pp. 186–190, April 2014.

[5] "Iridium NEXT: a constellation of 66 operational satellites that will make history," https://www.thalesgroup.com/en/worldwide/space/press-release/iridium-next-constellation-66-operational-satellites-will-make, accessed: 2018-07-25.

[6] R. J. Barnett, "ONEWEB NON-GEOSTATIONARY SATELLITE SYSTEM, ATTACHMENT A: Technical information to supplement schedule S," Telecomm Strategies LLP, Tech. Rep., 2016.

[7] P. Chen, W. Hong, Z. Kuai, and J. Xu, "A double layer substrate integrated waveguide Blass matrix for beamforming applications," *IEEE Microwave Wireless Compon. Lett.*, vol. 19, no. 6, pp. 374–376, Jun. 2009.

[8] J. Blass, "Multidirectional antenna - a new approach to stacked beams," *IRE Int. Conv. Rec.*, vol. 8, pp. 48–50, Mar. 1960.

[9] J. Nolen, "Synthesis of multiple beam networks for arbitrary illuminations," Ph.D. dissertation, Bendix Corporation, Radio Division, Baltimore, 1965.

[10] N. Fonseca, "Printed S-band 4 × 4 Nolen matrix for multiple beam antenna applications," *IEEE Trans. Antennas Propag.*, vol. 57, no. 6, pp. 1673–1678, Jun. 2009.

[11] T. Djerafi, N. Fonseca, and K. Wu, "Broadband substrate integrated waveguide 4x4 Nolen matrix based on coupler delay compensation," *IEEE Trans. Microw. Theory Techn.*, vol. 59, no. 7, pp. 1740–1745, Jul. 2011.

[12] J. Butler and R. Lowe, "Beam-forming matrix simplifies design of electrically scanned antennas," *Electron Design*, pp. 170–173, 1961.

[13] J. Butler, "Digital, matrix and intermediate-frequency scanning," *Antennas Propag. Soc. Int. Symp.*, vol. 3, pp. 66–70, Aug. 1965.

[14] K. Tekkouk, J. Hirokawa, R. Sauleau, M. Ettorre, M. Sano, and M. Ando, "Dual-layer ridged waveguide slot array fed by a Butler matrix with sidelobe control in the 60-GHz band," *IEEE Trans. Antennas Propag.*, vol. 63, no. 9, pp. 3857–3867, Sep. 2015.

[15] S. Silver, *Microwave Antenna Theory and Design.* McGraw-Hill Book company, 1949, vol. 1.

[16] W. Rotman, "Wide-angle scanning with microwave double-layer pillboxes," *IRE Trans. Antennas Propag.*, vol. 6, no. 1, pp. 96–105, Jan. 1958.

[17] E. L. Holzman, "Pillbox antenna design for millimeter-wave base-station applications," *IEEE Trans. Antennas Propag. Mag.*, vol. 45, no. 1, pp. 27–37, Feb. 2003.

[18] C. Hemmi, O. Kesler, and R. Dover, "Bifocal pillbox antenna system," US Patent 4 100 548A, Nov. 30, 1976.

[19] M. Ettorre, R. Sauleau, and L. L. Coq, "Multi-beam multi-layer leaky-wave SIW pillbox antenna for millimeter-wave applications," *IEEE Trans. Antennas Propag.*, vol. 59, no. 4, pp. 1093–1100, Apr. 2011.

[20] V. Mazzola and J. E. Becker, "Coupler-type bend for pillbox antennas," *IEEE Trans. Microw. Theory Techn.*, vol. 15, no. 8, pp. 462–468, Aug. 1967.

[21] E. Gandini, M. Ettorre, M. Casaletti, K. Tekkouk, L. L. Coq, and R. Sauleau, "SIW slotted waveguide array with pillbox transition for mechanical beam scanning," *IEEE Antennas and Wireless Propag. Lett.*, vol. 11, pp. 1572–1575, Dec. 2012.

[22] K. Tekkouk, M. Ettorre, L. L. Coq, and R. Sauleau, "SIW pillbox antenna for monopulse radar applications," *IEEE Trans. Antennas Propag.*, vol. 63, no. 9, pp. 3918–3927, Sep. 2015.

[23] K. Tekkouk, M. Ettorre, E. Gandini, and R. Sauleau, "Multibeam pillbox antenna with low sidelobe level and high-beam crossover in SIW technology using the split aperture decoupling method," *IEEE Trans. Antennas Propag.*, vol. 63, no. 11, pp. 5209–5215, Nov. 2015.

[24] K. Tekkouk, M. Ettorre, and R. Sauleau, "Multibeam pillbox antenna integrating amplitude-comparison monopulse technique in the 24 GHz band for tracking applications," *IEEE Trans. Antennas Propag.*, vol. 66, no. 5, pp. 2616–2621, May. 2018.

[25] H. Gent, "The Bootlace Aerial," *Roy. Radar Establishment J.*, pp. 47–57, Oct. 1957.

[26] J. Ruze, "Wide-angle metal-plate optics," *IRE Proc.*, vol. 38, no. 1, pp. 53–59, Jan. 1950.

[27] W. Rotman and R. Turner, "Wide-angle microwave lens for line source applications," *IEEE Trans. Antennas Propag.*, vol. 11, no. 6, pp. 623–632, Nov. 1963.

[28] J. Shelton, "Focusing characteristics of symmetrically configured bootlace lenses," *IEEE Trans. Antennas Propag.*, vol. 26, no. 4, pp. 513–518, Jul. 1978.

[29] T. Katagi, S. Mano, and S. Sato, "An improved design method of Rotman lens antennas," *IEEE Trans. Antennas Propag.*, vol. 32, no. 5, pp. 524–527, May. 1984.

[30] C. M. Rappaport and A. I. Zaghloul, "Multifocal bootlace lens design concepts: a review," *IEEE Antennas Propag. Soc. Int. Symp.*, vol. 2B, pp. 39–42, Jul. 2005.

[31] J. Dong, A. I. Zaghloul, and R. Rotman, "Phase-error performance of multi-focal and non-focal two-dimensional Rotman lens designs," *IET Microw. Antennas Propag.*, vol. 4, no. 12, pp. 2097–2103, Dec. 2010.

[32] N. J. G. Fonseca, "A focal curve design method for Rotman lenses with wider angular scanning range," *IEEE Antennas Wireless Propag. Lett.*, vol. 16, pp. 54–57, Apr. 2016.

[33] O. Kilic and S. J. Weiss, "Rotman lens applications for the US army: A review of history, present, and future," *URSI Radio Science Bulletin*, vol. 2010, no. 332, pp. 10–23, Jun. 2010.

[34] E. O. Rausch, A. F. Peterson, and W. Wiebach, "Electronically scanned millimeter wave antenna using a Rotman lens," *Radar 97*, pp. 374–378, Oct. 1997.

[35] D. Nussler, H. Fuchs, and R. Brauns, "Rotman lens for the millimeter wave frequency range dirk nussler," *European Microw. Conf.*, pp. 696–699, Oct. 2007.

[36] O. Kilic and S. Weiss, "Dielectric Rotman lens design for multi-function RF antenna applications," *IEEE Antennas Propag. Soc. Int. Symp.*, vol. 1, pp. 659–662 Vol.1, Jun. 2004.

[37] L. Schulwitz and A. Mortazawi, "A compact dual-polarized multibeam phased-array architecture for millimeter-wave radar," *IEEE Trans. Microw. Theory Techn.*, vol. 53, no. 11, pp. 3588–3594, Nov 2005.

[38] W. Lee, J. Kim, and Y. J. Yoon, "Compact two-layer Rotman lens-fed microstrip antenna array at 24 GHz," *IEEE Trans. Antennas Propag.*, vol. 59, no. 2, pp. 460–466, Feb. 2011.

[39] K. Tekkouk, M. Ettorre, L. L. Coq, and R. Sauleau, "Multibeam SIW slotted waveguide antenna system fed by a compact dual-layer Rotman lens," *IEEE Trans. Antennas Propag.*, vol. 64, no. 2, pp. 504–514, Feb. 2016.

[40] E. Sbarra, L. Marcaccioli, R. V. Gatti, and R. Sorrentino, "A novel Rotman lens in SIW technology," *European Radar Conf.*, pp. 236–239, Oct. 2007.

[41] R. Luneberg, *Mathematical theory of optics*. Providence, 1944, vol. 1.

[42] R. F. Rinehart, "A solution of the problem of rapid scanning for radar antennas," *Journal of Applied Physics*, vol. 19, pp. 860–862, Oct. 1948.

[43] ——, "A family of designs for rapid scanning radar antennas," *IRE Proc.*, vol. 40, no. 6, pp. 686–688, Jun. 1952.

[44] F. Warren and S. Pinnell, "Tin hat, scanning antennas, RCA victor Co., Montreal, Canada. An analogue of the luneberg lens which has tangents at its periphery, whose directions are in the plane of propagation. lla. KS Kunz:" Generalization of the Rinehart- Luneberg lens "," *J. Appl. Phys*, vol. 25, no. 6, p. 642, 1954.

[45] N. Fonseca, "Compact parallel plate waveguide geodesic lens for line sources with wide scanning range," *Proceedings of the 38th ESA Antenna Workshop*, Oct. 2017.

[46] N. Fonseca, Q. Liao, and O. Quevedo-Teruel, "The water drop lens: a modulated geodesic lens antenna based on parallel curves," *Int. Symp. Antennas Propag. (ISAP)*, Busan, Korea, Oct. 2018.

[47] Q. Liao, N. Fonseca, and O. Quevedo-Teruel, "Compact multibeam fully-metallic geodesic luneburg lens antenna based on non-euclidian transformation optics," *IEEE Trans. Antennas Propag.*, in press.

[48] K. S. Kunz, "Propagation of microwaves between a parallel pair of doubly curved conducting surfaces," *J. Appl. Phys.*, vol. 25, no. 5, pp. 642–653, Mar. 1954.

[49] Y. J. Park and W. Wiesbeck, "Angular independency of a parallel-plate Luneburg lens with hexagonal lattice and circular metal posts," *IEEE Antennas and Wireless Propag. Lett.*, vol. 1, pp. 128–130, Jan. 2002.

[50] O. Quevedo-Teruel, M. Ebrahimpouri, and M. Ng Mou Kehn, "Ultrawideband metasurface lenses based on off-shifted opposite layers," *IEEE Antennas and Wireless Propag. Lett.*, vol. 15, pp. 484–487, Dec. 2016.

[51] S. Maci, G. Minatti, M. Casaletti, and M. Bosiljevac, "Metasurfing: Addressing waves on impenetrable metasurfaces," *IEEE Antennas Wireless Propag. Lett.*, vol. 10, pp. 1499–1502, Jan. 2012.

[52] C. Pfeiffer and A. Grbic, "A printed, broadband Luneburg lens antenna," *IEEE Trans. Antennas Propag.*, vol. 58, no. 9, pp. 3055–3059, Sep. 2010.

[53] M. Bosiljevac, M. Casaletti, F. Caminita, Z. Sipus, and S. Maci, "Non-uniform metasurface Luneburg lens antenna design," *IEEE Trans. Antennas Propag.*, vol. 60, no. 9, pp. 4065–4073, Sep. 2012.

[54] C. D. Diallo, E. Girard, H. Legay, and R. Sauleau, "All-metal Ku-band Luneburg lens antenna based on variable parallel plate spacing fakir bed of nails," *The 11th European Conference on Antennas and Propagation (EuCAP)*, pp. 1401–1404, Mar. 2017.

[55] C. D. Diallo, "Study and design of new multibeam antenna architectures in Ku and Ka bands for broadband satellite communication applications," Ph.D. dissertation, University of Rennes 1, 2016.

[56] H. Legay, S. Tubau, E. Girard, J. P. Fraysse, R. Chiniard, C. Diallo, R. Sauleau, M. Ettorre, and N. Fonseca, "Multiple beam antenna based on a parallel plate waveguide continuous delay lens beamformer," *Int. Symp. Antennas Propag. (ISAP)*, pp. 118–119, Okinawa, Japan, Oct. 2016.

[57] N. J. G. Fonseca, H. Legay, S. Tubau, J. P. Fraysse, E. Girard, M. Ettorre, and R. Sauleau, "Continuous parallel plate waveguide beamformer based on a bifocal constrained lens design," *IEEE Int. Symp. Antennas Propag.*, pp. 1347–1348, Fajardo, Porto Rico, Jun. 2016.

[58] C. A. Balanis, *Antenna Theory: Analysis and Design.* Hoboken: John Wiley, 2005, ch. 7.

[59] ——, *Antenna Theory: Analysis and Design.* Hoboken: John Wiley, 2005, ch. 13.

[60] M. Kline and I. Kay, *Electromagnetic theory and geometrical optics*, ser. Pure and applied mathematics. Interscience Publishers, 1965, ch. 6.

[61] Y. Lo and H. Hsuan, "An equivalence theory between elliptical and circular arrays," *IRE Int. Conv. Rec.*, vol. 12, pp. 200–210, Mar. 1964.

[62] *Ansoft HFSS*, version 15.0, 1984-2016, Ansoft Corporation.

[63] B. Chantraine-Bares, R. Sauleau, L. L. Coq, and K. Mahdjoubi, "A new accurate design method for millimeter-wave homogeneous dielectric substrate lens antennas of arbitrary shape," *IEEE Trans. Antennas Propag.*, vol. 53, no. 3, pp. 1069–1082, Mar. 2005.

[64] R. Sauleau and B. Bares, "A complete procedure for the design and optimization of arbitrarily shaped integrated lens antennas," *IEEE Trans. Antennas Propag.*, vol. 54, no. 4, pp. 1122–1133, Apr. 2006.

[65] S. Kirkpatrick, C. D. Gelatt, and M. P. Vecchi, "Optimization by simulated annealing," *SCIENCE*, vol. 220, no. 4598, pp. 671–680, 1983.

[66] D. Gies and Y. Rahmat-Samii, "Reconfigurable array design using parallel particle swarm optimization," *IEEE Antennas Propag. Society Int. Symp. Digest.*, vol. 1, pp. 177–180 vol.1, Jun. 2003.

[67] D. S. Weile and E. Michielssen, "Genetic algorithm optimization applied to electromagnetics: a review," *IEEE Trans. Antennas Propag.*, vol. 45, no. 3, pp. 343–353, Mar. 1997.

[68] J. M. Johnson and V. Rahmat-Samii, "Genetic algorithms in engineering electromagnetics," *IEEE Antennas Propag. Magazine*, vol. 39, no. 4, pp. 7–21, Aug. 1997.

[69] R. Storn and K. Price, "Differential evolution - a simple and efficient heuristic for global optimization over continuous spaces," *Journal of Global Optimization*, vol. 11, pp. 341–359, Jan. 1997.

[70] "ASTRID-maturation 2016 - projet RAFQO 2016: Active array of quasi optical beamformers," http://www.agence-nationale-recherche.fr/Project-ANR-16-ASMA-0006.

[71] "MIP - Moulage Injection Plastique," https://mip-packaging.net/.

[72] M. J. Maybelle and G. S. Hardie, "EHF waveguide rotman lens for reconfigurable satcom," *Proceedings of the 39th ESA Antenna Workshop on Multibeam and Reconfigurable Antennas for Space Applications*, Oct. 2018.

[73] J. E. Pallesen, S. Pivnenko, and O. Breinbjerg, "First facility comparison campaign," Technical University of Denmark, Tech. Rep., Dec. 2005.

[74] N. J. G. Fonseca, E. Girard, and H. Legay, "Doubly curved reflector design for hybrid array fed reflector antennas," *IEEE Trans. Antennas Propag.*, vol. 66, no. 4, pp. 2079–2083, April 2018.

[75] "The Industry Standard in Reflector Antenna Analysis," https://www.ticra.com/grasp.

List of Publications

Journal papers

- F. Doucet, N.J.G. Fonseca, E. Girard, H. Legay, and R. Sauleau, "Analytical model and study of continuous parallel plate waveguide lens-like multiple beam antennas," *IEEE Trans. Antennas Propag.*, vol. 66, no. 9, pp. 4426-4436, Aug. 2018.

- F. Doucet, N.J.G. Fonseca, E. Girard, X. Morvan, L. Le Coq, H. Legay and R. Sauleau, "Shaped Continuous Parallel Plate Delay Lens with Enhanced Scanning Performance," *IEEE Trans. Antennas Propag.*, under review.

International conference papers

- F. Doucet, N.J.G. Fonseca, E. Girard, H. Legay, and R. Sauleau, "Analysis and design of a continuous parallel plate waveguide multiple beam lens antenna at Ku-band," in *Proc. 11th European Conference on Antennas and Propagation (EUCAP)*, Paris, France, pp. 3631-3635, Mar. 2017.

- F. Doucet, N. J. G. Fonseca, E. Girard, S. Tubau, H. Legay, R. Sauleau, "Design of continuous parallel plate waveguide lens-like beamformers for future low-cost and high-performance multiple beam antennas," in *Proc. 38th ESA Antenna Workshop on Innovative Antenna Systems and Technologies for Future Space Missions*, Noordwijk, The Netherlands, Oct. 2017.

- F. Doucet, N.J.G. Fonseca, E. Girard, H. Legay, and R. Sauleau, "Comparison of Optimization Procedures for the Design of Continuous Parallel Plate Waveguide Multiple Beam Lens Antennas," in *Proc. 12th European Conference on Antennas and Propagation (EUCAP)*, London, United Kingdom, pp. 3631-3635, Apr. 2018.

- F. Doucet, N.J.G. Fonseca, E. Girard, X. Morvan, L. Le Coq, H. Legay and R. Sauleau, "Shaped Continuous Parallel Plate Delay Lens with Enhanced Scanning Performance," in *Proc. 39th ESA Antenna Workshop on Multibeam and Reconfigurable Antennas for Space Applications*, Noordwijk, The Netherlands, Oct. 2018.

- N. Bartolomei, M. G. Vigueras, F. Doucet, D. Blanco, E. Girard, R. Sauleau and M. Ettorre, "Circularly Polarized Parallel Plate Waveguide Multiple-Beam Lens-like Antenna for Satcom Applications," forthcoming in *Proc. 13th European Conference on Antennas and Propagation (EUCAP)*, Krakow, Poland, Mar. 2019.

National conference papers

- S. Tubau, H. Legay, E. Girard, J-P. Fraysse, R. Chiniard, F. Doucet, R. Sauleau, M. Ettorre and N.J.G. Fonseca, "Antenne multifaisceaux réalisée avec un formateur de faisceaux à lentille à retard continu en guide d'onde à plaques parallèles," in *Proc. 20e Journées Nationales Micro-ondes*, Saint-Malo, France, May. 2017.

Biography

François Doucet was born in Vannes, France, in 1992. He received the M.Sc. degree from the Ecole Nationale de l'Aviation Civile (ENAC), Toulouse, France, in 2015 and the Ph.D. degree in electrical engineering from the Institut d'Electronique et de Télécommunications de Rennes, University of Rennes 1, Rennes, France, in 2019.

For six months, he was as an intern with the Research and Technologies Department, Thales Alenia Space, where he carried out his M.Sc.'s thesis project. He holds one patent. During his Ph.D. period he worked in collaboration with the European Space Research and Technology Centre, European Space Agency, Noordwijk, The Netherlands, and Thales Alenia Space, Toulouse, France. His current research interests include millimeter-wave antennas, with an emphasis on numerical modeling for the development of quasi optical beamformers.

Dr. Doucet was a recipient of the Robert Aladenyse ENAC Special Prize, rewarding the best end of studies internship.

UNIVERSITE BRETAGNE LOIRE MATHSTIC

UNIVERSITÉ DE RENNES 1

Titre : Lentilles continues en guide d'ondes à plans parallèles pour des applications multi-faisceaux à bas coût et à haute performance

Mots clés : Formateur de faisceaux, lentille contrainte, optique géométrique (GO), tracé de rayons, antennes multi-faisceaux, guide d'ondes à plans parallèles

Résumé : Les travaux présentés dans cette thèse portent sur l'étude et la conception de lentilles continues en guide d'ondes à plans parallèles (PPW) pour des applications multi-faisceaux. La conversion du front d'onde est assurée par une lentille formée d'une lame et d'une cavité transversale. Ce concept, proposant une approche mécanique simplifiée et possiblement purement métallique, est particulièrement attractif pour les futurs systèmes de communications par satellites (GEO/LEO) requérants des solutions à moindre coût tout en maintenant de hautes performances. La première partie de cette thèse présente la réalisation d'un outil d'analyse numérique basée sur l'optique géométrique (GO). Une prédiction rapide et précise des performances en rayonnement est obtenue. En combinant cet outil avec des processus d'optimisation, des performances en dépointage sur un large secteur angulaire sont ensuite démontrées, incluant une stabilité des diagrammes en rayonnement (ouverture à mi-puissance, niveaux de lobes secondaires et pertes en dépointage). Un prototype fonctionnant dans la bande Ka est réalisé, validant les performances précédemment obtenues. De hautes efficacités de rayonnement sont également mises en avant sur l'ensemble de la plage de fréquence. Enfin un second prototype plus compact basé sur de multiples lentilles est proposé et étudié, démontrant des performances similaires à la première solution fabriquée et mesurée.

Title: Continuous Parallel Plate Waveguide Lenses for Future Low-Cost and High-Performances Multiple Beams Antennas

Keywords: Beamformer, constrained lens, geometrical optics (GO), ray tracing, multiple beam antennas, parallel plate waveguide (PPW)

Abstract: The activities presented in this PhD focus on the study and development of continuous parallel plate waveguide (PPW) lenses for multiple beam applications. The wave front conversion is ensured by a PPW transversal ridge and cavity. The proposed concept, based on a simplified mechanical approach and possibly full-metal, which is particularly suitable for future satellite communication systems (GO/LEO) requiring low-cost antennas while maintaining high performances. The first part of the thesis deals with the development of a numerical analysis tool based on geometrical optics (GO). A fast and accurate prediction of the radiation performance is provided. Combining the tool with optimization processes, large scanning performances have been demonstrated, including a stability of the radiation pattern performance (HPBW, SLL, scan loss). A prototype working at Ka band has been manufactured, validating the performances demonstrated previously. High radiation efficiencies are also proved over the entire frequency range. Finally, a second prototype targeting performances in compactness and based on multiple lenses is proposed and studied, showing similar performances as the first solution fabricated and measured.